Amide-based Donor-acceptor Polymers for Sensor Applications

by

Jenner Ho Loong Ngai

A thesis
presented to the University of Waterloo
in fulfillment of the
thesis requirement for the degree of
Doctor of Philosophy
in
Chemical Engineering (Nanotechnology)

Waterloo, Ontario, Canada, 2021

Examining Committee Membership

The following served on the Examining Committee for this thesis. The decision of the Examining Committee is by majority vote.

External Examiner	Prof. Alex Adronov (Professor)
Supervisor(s)	Prof. Yuning Li (Professor)
Internal Member	Prof. Ting Tsui (Professor)
Internal-external Member	Prof. William Wong (Professor)
Internal-external Member	Prof. Michael Chong (Professor)

Author's Declaration

This thesis consists of material all of which I authored or co-authored: see Statement of Contributions included in the thesis. This is a true copy of the thesis, including any required final revisions, as accepted by my examiners. I understand that my thesis may be made electronically available to the public

Statement of Contribution

This thesis consists of materials from several published or submitted papers, whereby I, Jenner H. L. Ngai, was listed as the principle author. However, the following publications could not be accomplished without the contribution from my colleagues.

The contents in Chapter 3 has been published in:

- Jenner H. L. Ngai, George Y. Chang, Xiguang Gao, Xiaocheng Zhou, Arthur D. Hendsbee and Yuning Li, *RSC Adv.*, **2019**, 9, 26230-26237

The contents in Chapter 4 has been published in:

- Jenner H. L. Ngai, Xiguang Gao, Pankaj Kumar, John Polena, Yuning Li, *Adv. Electron. Mater*. **2021**. *Adv. Electron. Mater.* **2021**, *7,* 2000935.

The contents in Chapter 5 has not yet been published and in near-verbatim state to what is intended for submission. The following is the authorship order:

- Jenner H. L. Ngai, John Polena, Xiguang Gao, Mihir Kapadia, Daniel Afzal, Yuning Li

Abstract

Organic semiconductors, especially polymerized organic semiconductors, are suitable for manufacturing low-cost electronic products on flexible lightweight substrates through a high throughput roll-to-roll printing process. In particular, research into sensor devices based on organic semiconductors has drawn much attention in recent years due to the escalating demands for ubiquitous sensor devices for the Internet of Things (IoTs), smart food packaging, point-of-care devices, etc. Organic semiconductor (or organic)-based sensors have demonstrated promising performance towards a variety of analytes such as volatile organic compounds (VOCs), H^+, biological compounds, temperature, pressure, and metal ions. However, they still have poor long-term stability, unsatisfactory reversibility, and low selectivity.

This thesis aims to address these issues through the development of novel donor-acceptor (D-A) semiconducting and conductive polymers, which contain amide building blocks, namely indigo (ID), diketopyrrolopyrrole (DPP), and hemi-isoindigo (HID), for fluoride ion sensors, volatile organic liquid sensors, and temperature sensors. Several strategies have been used to improve senor performance: 1) Embedding intra- and intermolecular hydrogen bonds to improve the mechanical stability, sensitivity and selectivity; 2) Introducing thermally removable side chains to afford the polymer films excellent solvent resistance through a simple post-deposition thermal treatment; 3) Increasing the HOMO energy levels of polymers to improve the long-term stability of the doped polymers.

First, ID was chosen as the acceptor unit to pair with the bithiophene donor unit to develop an ID-based semiconductor D-A polymer **PIDG-BT-C20**, which is very stable to ambient air and water when used a p-channel semiconductor in organic field effect transistors (OFETs). The remarkable stability of this polymer allows it to be used a channel semiconductor in water-gated organic field-effect transistors (WGOFET), which the polymer is in direct contact with the water gate dielectric. The devices were able to detect halide ions (F^-, Cl^-, Br^-, and I^-) introduced in the water gate dielectric, achieving a low limit of detection (LOD) down to 0.40 mM for fluoride ions. The intramolecular hydrogen bonds in the ID unit were found to play a key role in achieving the high sensitivity and selectivity of fluoride ions.

Then, the strongly electron-withdrawing amide building block DPP was chosen as the acceptor unit and the electron-rich 3,3'-bis(dodecyloxy)-2,2'-bithiophene (C12-BTO) was selected as the

donor unit to make a narrow band-gap D-A polymer **PDEB**, which can be converted into the highly solvent resistant polymer **PDNB** by thermally removing the carbamate side chains in the DPP unit. The intermolecular hydrogen bonds formed between the DPP units in **PDNB** can form a physically cross-linked network to improve the morphological stability of the polymer film, and can also increase the wettability of polymer by polar organic solvents. The very high HOMO energy level (-4.68 eV) of **PDNB** allows it to form a doped polymer complex **PDNB:HCl** with excellent long-term stability (up to 9 moths). This doped film was used as the active layer in low-voltage driven chemiresistive sensors, and distinguish up to 10 different volatile organic liquids with unique current-time profiles.

Lastly, **HID** was selected as the acceptor unit to copolymerize with C12-BTO donor unit and thiophene spacer unit to develop four hemi-isoindigo-based D-A polymers for chemiresistive temperature sensors. The use of thermally removable carbamate side chains on the hemi-isoindigo unit can help forming intermolecular hydrogen bonds, which can afford excellent solvent resistance and morphological stability. Due to their high HOMO energy levels (ranging from -4.69 eV to -4.47 eV), these polymers can be doped by **F4TCNQ** to form moderately conductive films, which are suitable as channel materials for chemiresistive temperature sensors. It was found that the thiophene spacer unit has a great influence on the thermal sensitivity and long-term stability of the doped polymer complex. The doped film **PENB:F4TCNQ** (where **PENB** contains the **EDOT** spacer) has shown the best temperature sensor performance, achieving a high temperature coefficient of resistance (TCR) of up to -1.49 %/^{o}C, high reproducibility/reusability, and excellent long-term stability.

Acknowledgements

I would like to express my sincerest gratitude to my supervisor, Prof. Yuning Li. His expertise and experience have helped me greatly during the course of this research work. His encouragement allowed me to develop my research skills, broadened my horizon in the field of science and engineering. I would also like to thank the Natural Sciences and Engineering Research Council of Canada Green Electronics Network (NSERC-GreEN) for providing the funding support to my research. I would also like to thank the Giga-to-Nano (G2N) centre in UW where device fabrication and characterization took place. The researchers and technicians in the centre provided me with professional opinions and advice to help me with devices design and characterizations, especially to the guidance of Prof. William Wong, Prof. Hany Aziz, Dr. Czang-Ho Lee and Mr. Richard Barber from G2N centre that I was able to attain my goal of device fabrication and characterization. I would like to thank Janet Venne from the Nuclear Magnetic Resonance (NMR) facility in the Chemistry Department of UW, where all NMR analysis took place to confirm the identity of my synthesized compounds. I am also thankful for the Mass Spectrometry (MS) facility especially to Richard Smith and Valerie Goodfellow for helping me with mass analyses. Lastly, I would like to thank Dr. Neil McManus, Dr. Moses George, Ralph Dickhout, and Chris Kleven for their technical support, and assistance in my experiments.

I am indebted to my colleagues Dr. Arthur D. Hendsbee, Dr. Jesse Quinn, Dr. Yinghui He, Dr. Zhong Ma, Dr. Keqiang He, Xiguang Gao, Pankaj Kumar, Yi Yuan, Wuqi Li, Chenyang Guo, Guanlin Wang, John Polena, Daniel Afzal. I would also like to thank the Co-op students George Chang, Ninweh Jeorje, and Geoffrey Siow who helped me with experiments and data analyses, together with all the other previous and present lab members in QNC B503 and B506 for their support, and kind friendship.

I would also like to thank all my committee members, Prof. Alex Adronov, Prof. Yuning Li, Prof. Ting Tsui, Prof. William Wong, and Prof. Michael Chong.

Finally, I would like to acknowledge the indisputable support from my family, especially my parents Sai Ming Ngai, and Connie Chui Han Sun, my brother James Ho Kiu Ngai, and Sarah Au.

Dedication

I dedicate my dissertation work to my family, especially to my parents who always support and encourage me to go on every adventure and journey in my life. Without their love and encouragement, none of my success would be possible.

This thesis is also dedicated to my paternal grandmother Kam Hing Tang Ngai and my maternal grandfather Kai Chi Sun. Although they are no longer of this world, their memories continue to regulate my life.

Table of Contents

List of Figures

List of Tables

List of Abbreviations

AcOH: acetic acid

Acetone-d_6: deuterated acetone

AFM: atomic force microscopy

BGBC: bottom-gate bottom-contact

CB: chlorobenzene

$CDCl_3$: deuterated chloroform

$CHCl_3$: chloroform

CV: cyclic voltammetry

DCM: dichloromethane

DDTS: dodecyltrichlorosilane

DFT: density functional theory

DMF: *N*-*N*-dimethylformamide

DMSO: dimethyl sulfoxide

DMSO-d_6: deuterated dimethyl sulfoxide

DOS: density of states

DPP: diketopyrrolopyrrole

DSC: differential scanning calorimetry

EA: electron affinity

ESR: electron spin resonance

FET: field-effect transistor

HID: hemi-isoindigo

HOMO: highest occupied molecular orbital

hr: hour(s)

FTIR: fourier-transform infrared spectroscopy

LUMO: lowest unoccupied molecular orbital

min: minute(s)

LOD: limit of detection

MO: molecular orbital

MOSFET: metal-oxide semiconductor field-effect transistor

MOx: metal oxide

MPA: methylphosphonic acid

NBS: N-bromosuccinimde

NTC: negative temperature coefficient

OE: organic electronics

OECT: organic electrochemical transistor

OFET: organic field-effect transistor

OLED: organic light emitting diode

OPT: organic phototransistor

OSC: organic semiconductor

OTFT: organic thin film transistor

P3HT: poly(3-hexylthiophene)

PTC: positive temperature coefficient

RFID: radio frequency identification card

rt: room temperature

TCR: temperature coefficient of resistance

TD-DFT: time-dependent density functional theory

TGA: thermogravimetric analysis

TGBC: top-gate bottom-contact

TFT: thin film transistor

UV-Vis: ultraviolet-visible

UV-Vis-NIR: ultraviolet-visible-near-infrared

VOC: volatile organic compound

VRH: variable-range hopping

XRD: x-ray diffraction

List of Symbols

Eg_{opt} optical band gap

I_{DS} drain-source current

$I_{ON/IOFF}$ current ON/OFF ratio

λ_{max} wavelength of incident light with maximum intensity

Mn number-average molar mass

Mw weight-average molar mass

Đ polydispersity index

μ charge carrier mobility

μm microns

V_T threshold voltage

V_{DS} drain-source voltage

V_G gate-source voltage

V_{ON} on voltage

W channel width

L channel length

σ sigma (bonding)

π pi (bonding)

List of Schemes

Chapter 1: Introduction

Organic electronics is a competitive and challenging topic. Research areas in organic electronics are usually carried out in co-operations between different subjects. Therefore, research is often conducted in a multidisciplinary level which may involve collaborations between various subjects such as physics, chemistry and engineering. On account of the accumulation of knowledge and exchange of experience between different subjects, organic electronics have been evolving into a progressively mature subject over the past decades. The rapidly developing research field can lead to numerous applications such as new generation chemical or biological sensors, organic photovoltaics (OPVs), flexible organic light-emitting diode (OLED) displays, radio frequency identification (RFID), organic field-effect transistors (OFETs) and even therapeutic medical devices.[1,2,11–14,3–10]

One of the goals in organic electronics is to provide competing functionalities over traditional electronic devices. Example can be printable and environmentally "green" sensors, which would provide a new alternate solution to generate highly sensitive, low-cost, light-weight, low power driven or even biodegradable sensors used in our daily lives. There can be many other real-life examples of using organic electronic materials as sensors which may include detection of harmful ions in water, toxic substances in food or even harmful gases in our atmosphere.[4–8] These organic-based sensors can be printed on different surfaces, and monitor real-time changes of chemical or physical conditions, which can then give important qualitative or quantitative information in many aspects. Another example can be real-time temperature sensing used in "cold chain logistics" which is a process for the safe transport of temperature-sensitive substances and products such as vaccines, medicines, chemicals, dairy products or fresh produce along the supply chain. Other cutting-edge technologies may include wearable healthcare devices, electronic-nose, electronic-tongue, and disease diagnostic devices.

Studies have also shown that the worldwide organic electronics market size was valued at US$ 33.99 billion back in 2019, and is expected to surpass US$160 billion by 2027.[15] Organic electronics are believed to provide the society with a niche substantial revenue-generating market in the coming future. The forecast for the next several years suggests that the majority of the market growth will fall into the production OLED materials, conductive inks for printable electronics, and sensors. It is believed that there will be increasing research interests and emerging practical applications for organic electronics in the coming future.

1.1. Motivation of Studies

Man-made polymers have been invented for many years, while traditional polymers we use in everyday lives are always considered to be insulators owing to their large energy level differences between their valence and conductive band at the molecular level. Since the discovery of π-conjugated polymers, it was found that polymers can behave like a metal or a semiconductor through proper chemical design and synthesis. This thesis describes full details of some novel amide-based D-A semiconducting or conducting polymers as promising high performance active materials in sensor applications.

Since the discovery of polyacetylene as an organic conductive polymer by Hideki Shirakawa, Alan Heeger, and Alan MacDiarmid in 1970s, scientists and engineers had drawn more attention in organic electronics research, especially the development of new organic semiconducting and conducting materials in the field of organic chemistry.[16] Researchers had been focusing on synthesis and derivatization of conjugated organic materials, trying to explore possible electronic applications based on these compounds. Currently, conjugated organic materials can be mainly divided into polymers and small molecules. These compounds may behave as semiconductors or conductors, and some of them were found to have device performances that are comparable to traditional inorganic semiconductors such as silicon, and metal oxides such as germanium, gallium nitride and zinc oxide.

The intrinsic natures of organic semiconductors or conductors allow electronic engineers to create flexible, lightweight, or even transparent electronic devices used in various areas such as bioelectronics, nanoelectronics, optoelectronics and photovoltaics. For example, conducting polymers such as polypyrrole (PPy), polyaniline (PANI), polythiophene (PTh) and their derivatives, have been used as the active layers for gas sensors since early 1980s. Since then, conducting polymers were believed to be potential active materials used in electronics for the detection of gas molecules. Now, there are many commercially available gas sensors that provide good performances and high accuracies. However, most of the active materials used in these sensors are based on inorganic metal oxides (MOx), which usually require operation at harsh conditions such as high temperatures in the range of 200 − 600 °C.[17–19] High temperature operations involve high power consumptions and could lead to potential safety issues, and such safety concerns may limit the portability of the devices. The production process of MOx

semiconductors also involves the use of harsh conditions such as high vacuum, high temperatures and complicated processing techniques.[20–23] Therefore, there should be a balance between operational temperatures, processing conditions and sensor responses. Organic-based sensor materials may also have high sensitivities and short response time compared to inorganic-based materials, and more importantly they can be operated at much lower temperatures such as room temperatures. As a result, more attentions have been paid in the past few decades to study the use organic semiconductors and conductors as sensing materials.

Despite the numerous advantages of organic-based sensors, there are quite a number of shortcoming issues that may limit the popularity and commercialization of these sensors. The following section may discuss the current challenges in details.

1.1.1. Challenges of Organic Semiconductor or Conductor-based Sensors

1.1.1.1.Long-term Stability Issues

Firstly, many reported organic-based sensors may suffer from long-term stability issues. The stability of the sensors are also seldom studied. For conducting polymer-based sensors, de-doping or over-oxidation of the conductive polymer may occur especially for polyaniline, polypyrroles and polythiophenes when they are exposed in air for a long period of time.[24–26] Oxygen or other oxidants may also cause degradation to the polymer, which may lower the working lifetime of the sensors.

1.1.1.2.Reversibility of the Sensors

Secondly, these sensors may have an irreversible response to analytes. Even though some sensors exhibited high sensitivity and selectivity, the response may not be reversible and the sensor baseline level can barely recover to its original level after one or successive sensing cycles. For example, ammonia sensors using polypyrrole as the channel material are known to have slow baseline recovery. The reason behind the poor sensor reversibility was caused by the irreversible reaction between ammonia the polypyrrole.[25,27] Song et al. also reported an OECT based nanobioelectronic tongue to mimic human taste receptors by using polypyrrole nanotubes and receptor proteins as the active sensing platform. The device demonstrated a good analyte selectivity towards thiourea-group containing compounds, which is responsible for bitterness tastes. However, the current vs. time measurements showed a severe drifting in baseline level after each consecutive testing when analyte was introduced to the sensor.[28] Many other OFET based

sensors also suffer from a similar baseline fluctuation which limited the long-term and repeatable use of these sensors.[29–32] In general, sensors based on physical adsorption or absorption can be used repeatedly, while some other sensors based on chemical interaction can only be used once due to the irreversible nature of certain chemical reactions.

1.1.1.3.Selectivity of the Sensors

Thirdly, organic-based sensors may have a low selectivity in analyte responses. This may also be a major hurdle in all kinds of sensor research, in which the same sensor may not be able to distinguish different analytes, and the responses may be interfered by other interfering analytes or physical parameters such as temperature, pressure and light. Swelling effects or capacitance effect of organic materials may also play a significant role in causing interference to the electrical resistivity of the sensing layer.

1.1.1.4.Lack of Experimental Data to Support Hypothesized Sensing Mechanisms

Furthermore, the sensing mechanisms of many reported highly selective sensors might just be presumptions based on hypothesis and theoretical calculations. The exact working mechanisms of the interactions between analyte and organic semiconductors or conductors need to be supported by experimental observations. For example, spectroscopy methods such as NMR titration, XRD, and ESR can be used to detect changes in chemical/physical environment or polaron concentrations between the analyte and sensing material. These tools can actually help to validate the proposed sensing mechanisms to support the theoretical hypothesis. In order to rationally design a smart functional material for sensors, the sensing mechanism or the analyte recognition sites must be thoroughly understood, so that proper molecular design of the material can be carried out to produce sensors with enhanced stability and selectivity.

In this work, three classes of amide-polymers were developed to address the above mentioned challenges. Detailed reasons for choosing this class of polymer will be discussed in the later sections.

1.2. Research Objectives

The objective of this study aims to resolve the stability, reversibility, and selectivity issues in organic-based materials for sensing technologies. There are also attempts to develop methods for deducing sensing mechanisms to support hypothesized theories. Amide-based donor-acceptor polymers will be used as the candidate materials for the above investigation. The objectives can be split into the following tasks:

- Synthesis and characterization of novel π-conjugated amide-based D-A polymers.
- Engineering the hydrogen-bonds on amide-based polymers as recognition sites which can be used to improve the selectivity of aqueous ions, liquid chemicals or temperature sensors.
- Using hydrogen-bonds in amide-based polymers to change the physical properties of the polymers such as crystallinity, polarity and hydrophobicity to enhance sensor stability and reversibility.
- To examine the performance of sensor devices such as selectivity, long-term stability, and mechanistic study of the sensors using the aforementioned polymers as active sensing materials.
- Using spectroscopic techniques such as NMR titration, XRD, and ESR to support and validate the proposed sensing mechanisms by DFT or other theoretical calculations.

1.3. Thesis Structure

This thesis consists of six chapters and they are organized as follows: The first opening of this thesis provides background information that is crucial for understanding the results and findings in the latter part of this thesis. In Chapter 2, a brief background and theory of organic semiconductors, conductors and examples of the state-of-the-art organic-based sensors are given. Chapter 3 presents a novel D-A semiconductor polymer based on indigo derivatives that exhibits good air and aqueous stability, which can be used as a channeling material for sensing anions. Chapter 4 presents a novel diketopyrrolopyrrole-based D-A polymer with outstanding solvent resistance and long-term ambient stability which can be used as a liquid analyte sensor. Chapter 5 describes a series of novel hemi-isoindigo-based D-A polymers with excellent air stability and cyclability when used as temperature sensors. Finally, conclusions and summary of this thesis and recommended future research directions will be presented in Chapter 6.

Chapter 2: Background and Theory

The first section of this chapter provides a brief background information about organic semiconductors (OSCs) and the subcategories of OSCs in terms of electronic properties and molecular structures. Some important OSC examples and the unique features of amide-based compounds will be discussed, followed by introduction of some state-of-the-art organic-based sensors. The discussion will then go into a more detailed section about device structures, sensing principles, and theories about charge transport mechanism in OSCs.

2.1. Organic Semiconductors

Some examples of early developed OSCs with great performances when used as thin film channel materials can be found in Figure 0.1. Although small molecule materials such as pentacene, rubrene, and C_{60} had all demonstrated promising charge carrier mobilities up to 10^{-2} $cm^2V^{-1}s^{-1}$ order of magnitude, these devices may still suffer from long-term ambient stability issues in ambient condition. Polymeric OSCs such as poly(3-hexylthiophene), poly(p-phenylene vinylene), as well as polyfluorene and its derivatives may possess a better thermal and ambient stability. However, many of these compounds usually consist of simple chemical functionalities such as pure aromatic rings and aliphatic hydrocarbon side chains, which lacks the selectivity to detect analytes when they are used as active materials in sensors. Therefore, materials scientists have been trying to engineer new materials based on these original OSCs, and try to produce novel compounds with extra functionalities for sensing applications while retaining or enhancing their electronic performances.

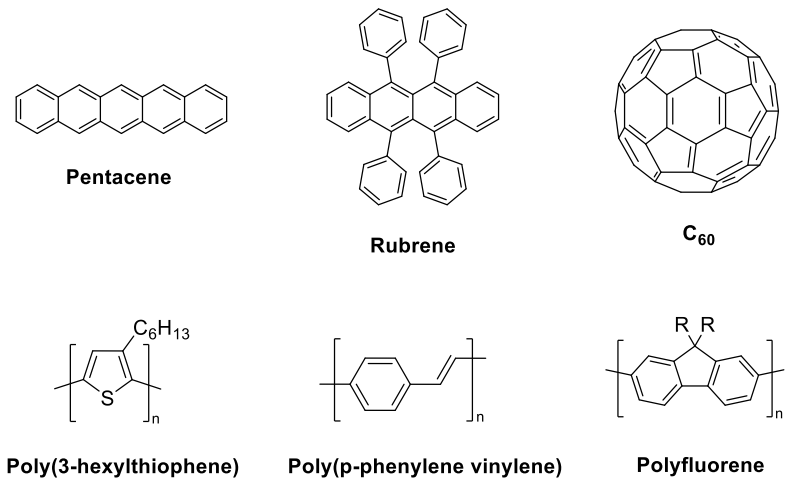

Figure 0.1. Early small molecular and polymeric organic semiconductors

2.1.1.1. P-Type Organic Semiconductors

P-type (positive-type) organic semiconductors are π-conjugated molecules with high highest occupied molecular orbital (HOMO) energy levels. These materials are generally electron-rich species and the electron-donating properties make them good candidates for p-type semiconductors. Many organic semiconductors showed remarkable p-type organic field-effect transistors (OFET) behaviors. In 2009, Hasegawa and Takeya reported that the carrier mobility of a single crystal rubrene can be comparable to polycrystalline silicon with parylene as the gate dielectric.[33] Five years later in 2014, Kim, G. et al reported the carrier mobility of an organic polymer semiconductor could exceed that of an amorphous silicon device using a fluorinated polymer as the gate dielectric.[34] Well known p-type semiconductors are acenes, such as pentacene[35], and heterocyclic oligomers, such as oligothiophenes, and polyconjugated polymers.

In the development of organic semiconductors, pentacene had been used as a model compound for the study of the relative impact of chemical structure on the hole mobility in organic semiconductors.[36] It was reported that by replacing one aromatic ring with thiophene in pentacene exhibited a higher hole mobility and lower threshold voltage (~7V). The stability in air was also improved as compared to pentacene. Therefore, using thiophene compounds were believed to be one method to boost the stability of OE materials in air. Another derivative namely tetracene was synthesized and it has a lower mobility than that of pentacene, indicating that systems with longer π-conjugation showed a higher mobility.[16]

Another factor that affects the performance of a p-type organic semiconductor would be the packing of the thin-film material which is generally governed by the intermolecular forces such as π-stacking and hydrophobic interactions of the material itself and with the substrate surface of the transistor device. For π-stacking interactions, it was reported by Sheraw C.D. et al. that a pentacene derivative containing acetylene units with a bulky chemical substituent adopts a π-stacking columnar structure to avoid steric interactions. The derivative containing isopropyl groups resulted in an OFET with a high mobility as high as 0.4 $cm^2V^{-1}s^{-1}$. This compound was latterly known as the famous TIPS-Pentacene (6,13-Bis(triisopropylsilylethynyl)pentacene), which is always being used as model OFET material for benchmarking mobilities in the development of OFET materials.[37] Another method for constructing π-stacking structures in p-type organic semiconductors is to use intermolecular charge-transfer interaction. When pentacene is

derivatized with an electron-accepting quinone unit, the electron donor-acceptor (D-A) interaction took place and the molecules tended to stack in a tight columnar structure due to the intermolecular pentacene unit which worked as the donor, while the quinone unit acted as an electron charge acceptor.[38] The small molecule based OFET device can reach as mobility of up to 0.05 cm^2Vs^{-1}. The concept of D-A methodology had then become an acceptable and fundamental concept in the development of OSCs, and this type of material will be further discussed in details in the later section.

For hydrophobic interactions, anthracene was an example that it did not exhibit any transistor field-effect in OFET. This is because of its short π-electronic system. Nevertheless, the bisthienyl derivative of anthracene showed good p-type behavior.[39] This is due to the after introduction of two hexyl groups and led to a p-type OFET performance with mobility up to 0.50 $cm^2V^{-1}s^{-1}$. The same tactic can be applied to other heterocyclic compounds such as naphthalene.[40] When the two-membered-ring system naphthalene was derivatized with alkylthienyl groups, the hole mobility can reach 0.14 $cm^2V^{-1}s^{-1}$.[41] Incorporation of aliphatic alkyl chains is an effective way for molecules to adopt an edge-on orientation (plane of aromatic rings facing perpendicularly to the substrates) in OFET devices, especially on SiO_2 substrates for better performance in OFET. Furthermore, it was reported by Halik M. et al. that the alkyl chains in p-type organic semiconductors can also lower the HOMO energy levels. It was also observed that in oligothiophenes, conjugation of four to six thiophene rings with alkyl chains 2–6 carbon units are necessary for high hole mobilities.[42] Many of the aforementioned discoveries helped to build up knowledge in OSC, and act as fundamental concepts to design and develop new functional OE materials.

2.1.1.2. N-Type Organic Semiconductors

N-type (negative-type) OSCs are electron-deficient materials. Interestingly, a p-type organic material can be converted to an n-type material by chemical modifications. One method to prepare n-type organic semiconductors is by introducing electron-withdrawing groups to p-type semiconductors. A famous example is the perfluorinated pentacene.[43] This compound showed electron mobility of 0.11 $cm^2V^{-1}s^{-1}$ under high vacuum conditions. The most famous n-type organic semiconductors are perylenediimide based compounds. The alkylated perylenediimide derivative such as the octyl derivative showed a high electron mobility up to 0.6 cm^2 Vs^{-1}.[44]

However, their OFET devices were not stable in air. In n-type organic semiconductors, radical anions are produced by electron injection. These radical anions are labile to oxygen and the stability is related to the electron-accepting properties of semiconductors. To overcome such problems, cyano groups were introduced to perylenediimides, making it more electron deficient. As expected, the cyano derivative of perylenediimide showed better stability in air as well as a higher electron mobility of 0.64 $cm^2\ Vs^{-1}$.[45] Other electron withdrawing groups have also been introduced to n-type organic semiconductors. For example, the tetrachloro- derivative of perylenediimide also showed a high electron mobility of 0.18 $cm^2\ V^{-1}s^{-1}$ and good air stability.[46] Similarly, the cyano derivatives of naphthalenediimide and anthracenediimide have also been prepared and functioned as n-type materials.[47,48]

Fullerenes, particularly the C_{60} allotrope is another renowned example of n-type organic semiconductor which shows high electron affinity and produced high performance OFETs. Fullerene devices had shown electron mobility of up to 0.56 $cm^2V^{-1}s^{-1}$ in vacuum.[49] Derivatives of C_{60} were also developed to increase their solubility in organic solvents. An example is Phenyl-C_{61}-butyric acid methyl ester ($PC_{61}BM$). The derivative yielded ambipolar OFET using a solution processed method. Its electron and hole mobilities were measured to be 0.01 and 0.008 $cm^2\ V^{-1}s^{-1}$ respectively.[50] Nowadays, $PC_{61}BM$ has been widely employed as the electron acceptor in organic solar cells research. Another amino derivative of C_{60} was also shown to have a high electron mobility of 0.15 $cm^2V^{-1}s^{-1}$ by using solution processing methods.[51] However the production and purification costs of fullerenes are still very high.

2.1.1.3. Donor-Acceptor Polymers

A donor-acceptor (D–A) type conjugated polymer is a kind of alternating copolymer which made up of alternating electron-rich (p-type) and electron-deficient (n-type) building blocks known as the (electron) donor and the acceptor.[52] The highest occupied molecular orbital (HOMO) and the lowest unoccupied molecular orbital (LUMO) energy levels can be adjusted or fine-tuned to obtain the desired energy levels and optoelectronic properties by choosing the appropriate building blocks with specific functional groups.[53–55] In recent years, D–A polymers have been widely studied in advanced and innovative optoelectronic devices[9–14,56] The rise of D-A polymers used in organic electronics research is also greatly attributed to the near mature development of transition metal catalyzed aryl-aryl type carbon-carbon (C-C) bond coupling reactions such as Suzuki, Stille, and

direct arylation coupling reactions.[57] These type of aryl-aryl type coupling reactions are standardized procedures for material chemists to prepare D-A polymers with different donor-acceptor combinations. D-A polymer semiconductors have been found to exhibit excellent charge carrier mobilities and outstanding stability. D-A semiconductor polymer can also be a pure p-type, n-type, or ambipolar material which can be used in various electronic applications. Examples of energy level tuning were demonstrated in the later chapters such as band gap narrowing to afford a p-type OFET polymer semiconductor which will be discussed in Chapter 3. The elevation of HOMO energy of a D-A polymer system to employ a p-type dopable conductive polymer will be discussed in Chapter 4, and matching of energy levels and structure related properties of a polymer:dopant system to obtain extra stability of the sensing devices will be discussed in Chapter 5.

2.1.1.4. Amide-based Organic Electronic Compounds

The amide functional group (Figure 0.2) is an electron-deficient chemical functional group, where R in Figure 0.2 can be different substituents such as hydrogen, alkyl, carbonyl or ester etc... It is well-known that a lot of man-made or natural amide materials demonstrate good chemical and thermal stabilities. Many of these π-conjugated molecules bearing amide or amide analogs such as imides or lactams frameworks have also received considerable attentions of being promising candidates for high-performance optoelectronic materials, particularly for OSCs with high carrier mobilities.[58–63] In this thesis, any materials that consist of carbonyl-nitrogen bonds such as imides, lactams, vinylogous amides, or other similar analogs will be regarded as derivative members under the broad umbrella of the "amide" family for simplicity (Figure 0.2). Otherwise, the enormous combinations and variety of carbonyl-nitrogen functionalities being discussed here may lead to an ambiguous definition for every single chemical structures because of the strict and definitive names for different chemical compounds according to the International Union of Pure and Applied Chemistry (IUPAC) nomenclature system.

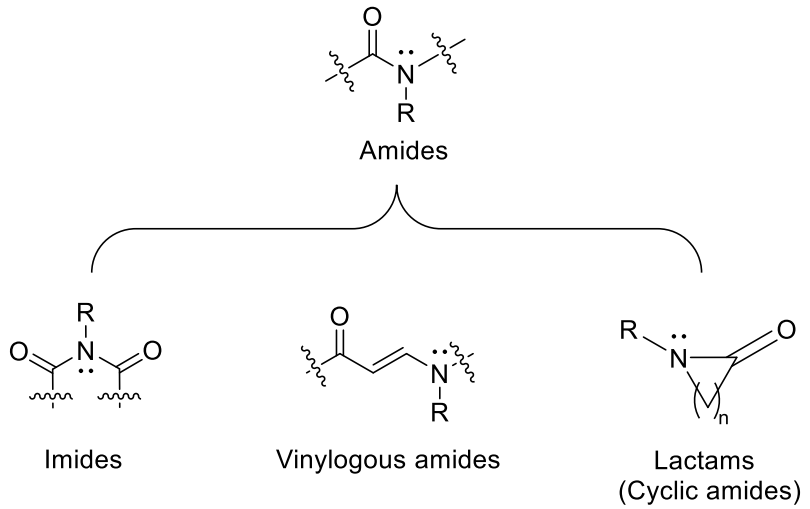

Figure 0.2. Examples of chemical functional groups derived from the amide family.

2.1.2. Basic Chemical Properties of Amides

Nitrogen is a Group V element having an electronic configuration of $1s^2 2s^2 2p^3$ and it has 5 valence electrons, allowing the nitrogen atom to form 3 bonds with its neighboring atoms and leaving behind one set of lone pair electrons in its valence shell. Amide-based compounds can usually provide an anchoring site on the nitrogen atom to give additional functionality to the compound,

which is a very important feature and property for this specific class of material. For instance, the nitrogen atom can be alkylated by long chain hydrocarbons to improve solubility of a compound in solvent. This is exceptionally important in the field of organic electronics, while making a solution soluble semiconductor or conductor ink allows blending of the materials with one another for energy matching and provide an easy way to print or coat the composite materials onto a surface for specific applications. In addition, the nitrogen lone pair electrons in an amide can resonate throughout the amide carbonyl group to gain extra stability of the system by resonance stabilization (Figure 0.3a). Furthermore, when the amide is a primary amide (with R group as hydrogen), the molecules are able to form inter- or intra-molecular hydrogen-bonds with itself or with neighboring molecules. This is an interesting feature in amide that some researchers enable this property to design self-assembled supramolecular structures, or to induce preferred orientation in crystals or thin films for different applications ranging from electronics, sensors to drugs delivery.[60,64–72] Hydrogen-bonds may also provide a considerable amount of photostability of the material due to the presence of intramolecular charge transfer (ICT) or excited state intramolecular proton transfer (ESIPT) of hydrogen-bonds in some systems, as light energy is dissipated as ICT and ESIPT, rather than forming light-induced free radical reactions that could lead to photodegradation of the material.[73–78] Hydrogen-bonds in some amide systems may also lead to a densely packed structure, and are known to be very stable in ambient because the tightly packed structures can prevent moisture and oxidants from getting into the system which can cause oxidation of the materials. Examples of intramolecular and intermolecular hydrogen-bonds are illustrated in Figure 0.3b and 2.3c, and some of their special applications will be discussed in the next section.

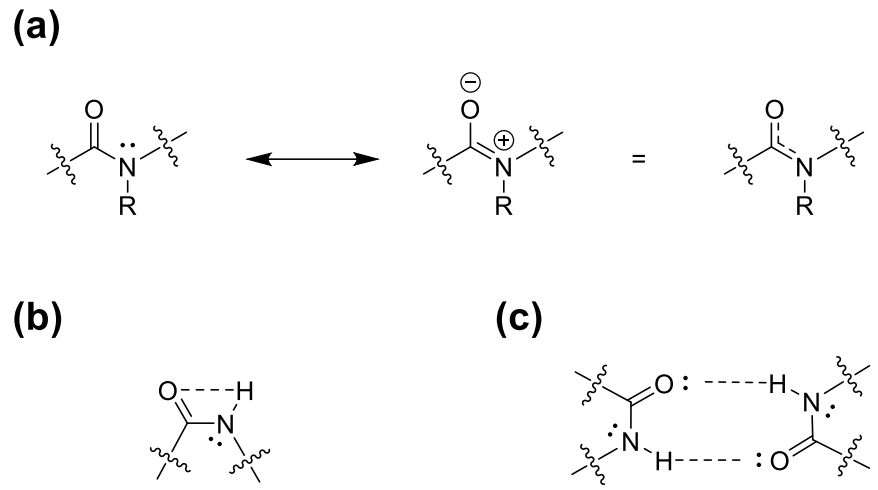

Figure 0.3. (a) Resonance stabilization in amide; (b) Intramolecular hydrogen-bonds in amide; (c) Intermolecular hydrogen-bonds in amide.

2.1.3. Hydrogen-bonds in Amides

George A. Jeffrey first classified the strength of hydrogen-bonds in three levels, where hydrogen-bonds with donor-acceptor distances of 2.2-2.5 Å are considered to be "strong, mostly covalent", 2.5-3.2 Å as "moderate, mostly electrostatic", and 3.2-4.0 Å as "weak, electrostatic" using structural crystallography techniques.[79–81] Some literatures reported the incorporation of weakly held intramolecular "hydrogen-bonds" (or sometimes called chalcogen bonds) using amides or heteroatoms on conjugated polymer backbones, while the hydrogen-bonds can be easily broken down by a solvent and reassembled again in solid state. When these polymers are dissolved in solution, the hydrogen-bonds on the polymers interact with solvent molecules through solvation effect. Breaking down of the intermolecular forces increases the freedom of molecular rotation on the π-conjugated polymer backbone momentarily in solution. This can help to improve solubility of the conjugated polymer, which is an advantage for solution processed device fabrication. Once the polymer solutions are deposited onto the substrate, the solvent molecules slowly leave the substrate surface and the polymer chains undergo a conformational change by self-assembly with the aid of intramolecular hydrogen-bonds from solution to solid state. Finally, the polymer chains would transform into a rigid planar π-conjugated structure which is beneficial for charge transport in organic electronic devices.[59,63,70,82] Examples of using amides or other hydrogen-bonds forming functionality have shown to be a promising tactic to engineer high performance organic

electronic devices such as OFETs, OPTs, and OPVs through self-assembly and supramolecular chemistry.

In many cases, aromatic amides without nitrogen modification would have a poor solubility due to the extensive hydrogen-bonded networks between individual amide molecules. The purification and fabrication of electronic devices using these materials can only be carried out by harsh processes such as sublimation or thermal evaporation in order to deposit uniform thin films on substrate surfaces.[83–89] Despite the harsher fabrication methods of these poorly soluble compounds, their electronic performances were indeed quite excellent. Therefore, in many reported cases for solution processed organic electronic devices, the active materials would have an amide moiety substituted with solubilizing side chains to enable solubility of the material to allow solution processing and printability.

Interestingly, the substitution on the nitrogen atom was also found to have a number of significant impacts to the electronic properties of the semiconductor, such as altering the molecular packing or morphology of thin film material and thus improves the crystallinity for better charge carrier transport in OFETs. The nitrogen atom is also thought to be a good functionalization site for installation of other functional groups such as recognition sites for various chemical or biological analytes for sensing applications. Therefore, there are more emerging studies that focus on side chain engineering of a material, and amide-based compounds could be a good candidate for such investigation due to its intrinsic chemical structure, easy accessibility, low-cost synthetic pathways, and relatively efficient reactivity on the nitrogen atom to allow in-depth structural-electronics studies. Some examples of amide based OSCs will be introduced in the next section.

2.1.4. Examples of Amide-based Electronic Compounds

The first example for some existing amide-based compounds widely used in organic electronics would be the "Imides". Naphthalene diimide (NDI) and perylene diimide (PDI) are two most intensively studied organic conjugated molecules with imide chemical structures for high-performance optoelectronic materials (Figure 0.4).[62,71,90,91] Due to the extensive π-conjugation and the highly electron-deficient imide groups on NDI and PDI, it was found that these materials are good light-absorbing materials and exhibited promising n-type semiconductors even at ambient condition when the nitrogen atom was substituted by a hydrocarbon side chain. This is possibly because of their low-lying LUMO levels and highly reversible redox behavior.[91–93]

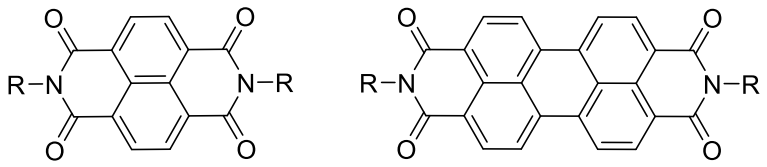

Naphthalene diimides (NDI) Perylene diimides (PDI)

Figure 0.4. General structures of naphthalene diimides and perylene diimides.

The unfunctionalized NDI and PDI showed good n-type charge transport characteristic. However, they showed poor air stability in operation due to their high LUMO energy levels. Another reason for the low stability could also be due to the more hydrophilic nature of the unsubstituted amide which may easily absorb polar impurities from surroundings to induce electronic traps in the devices. Therefore, the radical anions of the unsubstituted amide molecules are believed to be vulnerable to oxygen and water molecule attack. In one example reported to overcome this issue, Würthner et al. modified the PDI core by alkylating the N-position on PDI with fluoroalkyl chains, which is a highly hydrophobic and water repelling side chains that improved the air stability of the OFET devices. The derivative compound **1** demonstrated high electron mobilities up to 1.24 $cm^2V^{-1}s^{-1}$ in air (Figure 0.5).[94]

Alternatively, air stable n-type imide compounds can also be prepared by introducing electron withdrawing groups into the PDI core groups by decreasing the LUMO level. Compound **2** is an example of PDI derivative containing two cyano groups on the PDI core (Figure 0.5). This compound exhibited electron mobilities up to 1.3 $cm^2V^{-1}s^{-1}$ under ambient condition.[95]

Compound **2** also demonstrated a high electron mobility of up to 6.0 $cm^2V^{-1}s^{-1}$ in vacuum on a single crystal OTFT device.[96]

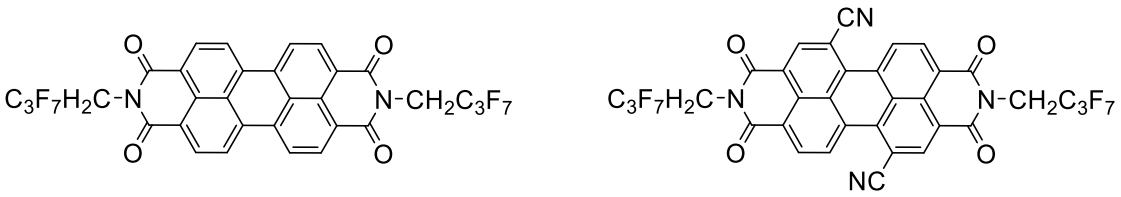

1 **2**

Figure 0.5. Examples of perylene diimide (PDI) derivatives with air stability in OFET devices.

The same strategy can also be applied to NDI-based compounds by adding strong electron withdrawing groups such as fluorine, nitrile, perfluorobenzene, and fluoroalkyl groups on the NDI core or at the nitrogen atom at the imide functionality. The result led to a lowered LUMO level and gaining resistance to ambient oxidation for air-stable n-type transistor devices.

Apart from the aforementioned imide compounds, cyclic aromatic amide compounds such as diketopyrrolopyrrole (DPP) and isoindigo are another two famous building blocks used in many electronic devices (Figure 0.6). Many of its polymeric semiconductors were found to have carrier mobilities greater than 1.0 $cm^2V^{-1}s^{-1}$ when DPP, isoindigo, or their derivatives were used as the acceptor building blocks.[97–103] Indigo is a natural pigment and is the original form of its structural isomer isoindigo (Figure 0.6). Indigo pigment itself was also reported by Mihai Irimia-Vladu et al. to function as an OSC. Their research group showed that other amide-containing natural pigments such as Tyrian Purple, cibalackrot and vat yellow 1 all exhibited good n-type semiconducting properties.[104] Among these natural pigments, indigo and its derivatives such as Tyrian Purple showed a promising electron mobility of up to 0.02 $cm^2V^{-1}s^{-1}$. The long-range hydrogen-bonds and π-stacking within indigo and Tyrian Purple can form highly-ordered crystalline thin films to facilitate charge transport along individual small molecules. In the later chapters, some novel indigo-based, isoindigo-based and DPP-based D-A polymers will be reported. Their properties and potential sensor applications will be further discussed in details.

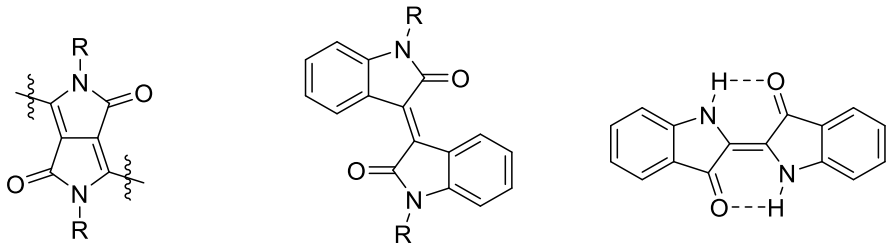

Diketopyrrolopyrrole (DPP) Isoindigo Indigo

Figure 0.6. Examples of heterocyclic aromatic amide compounds with promising electronic properties.

2.2. State-of-the-Art Organic-based Sensors

This section summarizes some of the representative OSCs used in organic-based sensors. Many sensors developed were based on the primitive forms or derivatives of OSC materials discussed in the previous section. The major applications for organic-based sensors are split into three major categories in the discussion below which includes gas sensors, liquid chemical sensors and temperature sensors.

2.2.1. Gas Sensors

For gas sensors, there are always demands and needs for identifying certain gases and monitoring the amount the gas in indoor or outdoor environment. For example, the ingredients of pollutants in atmosphere and the amount of harmful gases such as VOCs in industrial working environments. Many researchers have reported the use of semiconducting or chemiresistive polymers or small molecules to carry out qualitative and quantitative analysis of gases. Using P3HT as an example, Seohyun et al. reported the use of P3HT nanowires to detect ammonia gas (NH_3). The interaction between P3HT and NH_3 can reduce the hole carrier densities in the polymer, which then leads to a decrease of P3HT conductivity. The LOD of P3HT nanowires on NH_3 can reach as low as 8 ppb in concentration.[105] By blending P3HT with a commercially available vinyl polymer PMMA, Yu et al. demonstrated that the microstructures of the blended films can form a vertical phase separation morphology which has a better capability for the adsorption of NH_3 molecules and the LOD can be further lowered down to 0.7 ppb level. Another example is the use of a small molecule semiconductor 5,5'-bis (4-hexylphenyl)-2,2'-bithiophene (6PTTP6) to detect dimethyl methylphosphonate (DMMP) vapours which is a phosphonate nerve agents simulant (Figure 0.7). The OFET-based gas sensor was able to detect DMMP down to 10 ppb level in a controlled gas flow environment.[106]

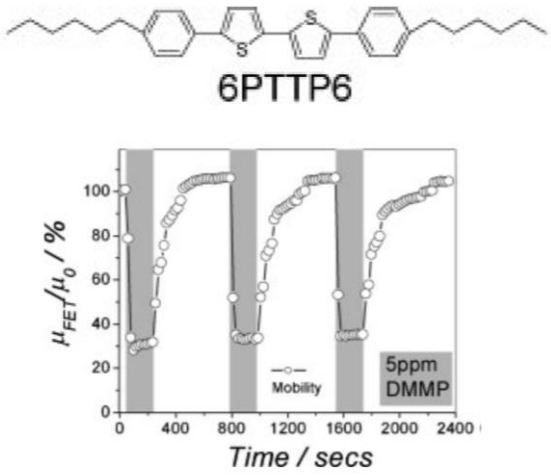

Figure 0.7. Chemical structure of 5,5'-bis (4-hexylphenyl)-2,2'-bithiophene (6PTTP6) and change of the mobility of the OFET device upon exposure to 5 ppm DMMP vapor.

Table 0.1 shows some of the other reported high performance gas sensors using organic small molecules or polymers as sensing materials. Details of redox active gas sensing using OSCs will be discussed in the later section.

Table 0.1. Representative gas sensors based on different organic materials and their general performances[107]

Target gases	Material	Sensitivity	LOD	Response/recovery time	Ref.
NO_2	TIPS-pentcene	1329%/ppm	1.93 ppm	10 min/> 20 min	[108]
	DPP-fluorene-based polymer	614% at 20 ppm	0.5 ppm	5 min/~3 min (40°C)	[109]
	TIPS-pentacene	1181%/ppm	20 ppb	200s/400s	[110]
	CuPc	160000% at 30ppm	400 ppb	400 ppb	[111]
	PQTS-12	410% at 5ppm	1 ppm	15 min/-	[112]
NH_3	P3HT nanowire	~220% at 5 ppm	8 ppb	N/A	[105]
	PDFDT	56% at 10 ppm	1 ppm	>180s	[113]
	DNTT	340%/ppm	10 ppb	95s/200s	[114]
	Pentacene/Gelatin	17.6% at 0.5 ppm	174.0 ppb	15.4s/42.2s	[115]
	P3HT-DPPCN	53% at 0.5 ppm	0.5 ppm	5 min/5min	[116]
	CoPc+TPFB	63% at 4.5 ppm	0.35 ppm	90s/-	[117]
	pDPPBu-BT	45% at 10 ppm	10 ppb	5s/-	[118]
	P3HT-PMMA	1481% at 30 ppm	0.7 ppb	N/A	[119]
DMMP	F_{16}CuPC	10^6 %/ppm	<5 ppm	20 min/180 min	[120]
	6PTTP6	70% at 5 ppm	~10 ppb	40s/-	[106]
SO_2	CuPc nanowire	764% at 20 ppm	0.5 ppm	3 min/8min	[121]
H_2S	BDFTM	11% at 0.1 ppm	10 ppb	5s/-	[122]
	Spirobifluorene-based polymer	95% at 1 ppm	1 ppb	15s/-	[123]

* The contents in this table is adopted from the publication *"Recent progress in chemical gas sensors based on organic thin film transistors"* by Yu et al. The table is slightly modified to match the editing format of this thesis.

2.2.2. Liquid Chemical Sensors

Liquid chemical sensing is another main focus in organic-based sensor research. Using OFET or OECT based device set-ups, various types of thin-film sensors were developed for sensing pH, ions, and other biomolecules such as glucose, DNA, enzymes and antibodies/antigens. It is believed that OSCs may have important applications in chemical and biological sensing when compared to inorganic materials since OSC may have a broad functionalization ability through chemical synthesis techniques.

For example, Roberts et al. demonstrated a low power driven OFET sensor which used ultrathin poly(4-vinylphenol) (PVP) layer as the gate dielectric, and 5,5'-bis-(7-dodecyl-9H-fluoren-2-yl)-2,2'-bithiophene (DDFTTF) as the active sensing layer (Figure 0.8). The sensor showed excellent performance in aqueous solutions and can be used for the detection of pH between 3 and 11 and to detect 2,4,6-trinitrotoluene (TNT) in aqueous solution down to 40 ppm level.[124]

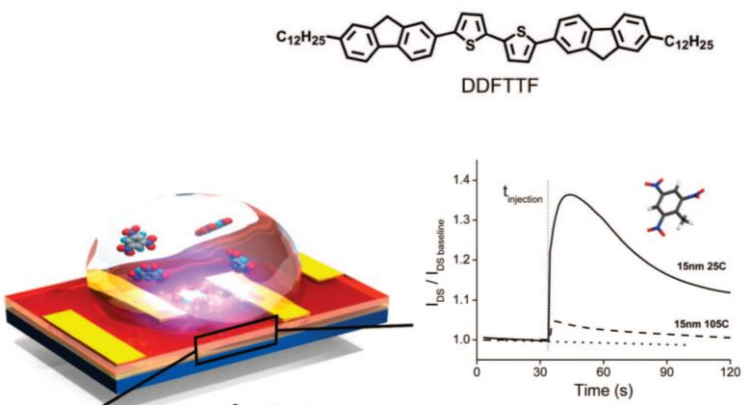

Figure 0.8. Chemical structure of DDFTTF, schematic diagram of a OFET-based aqueous sensor, and the sensing performance of DDFTTF towards TNT at different temperatures.

Apart from small molecules detection, Maddalena et al. reported the use of a multi-layered OFET device with sulfate binding protein (SBP) on maleimide functionalized polystryrene (PSMI) as the top insulator layer, and polymer poly(4,4'-didecylbithiophene-co-2,5-thieno[2,3-b]thiophene) (PDTT) as the semiconductor layer to detect sulfate (SO_4^{2-}) anions in aqueous solution (Figure 0.9). The device is an ion-sensitive OFET, and the detection limit of SO_4^{2-} was found to be as low as 1mM.[125]

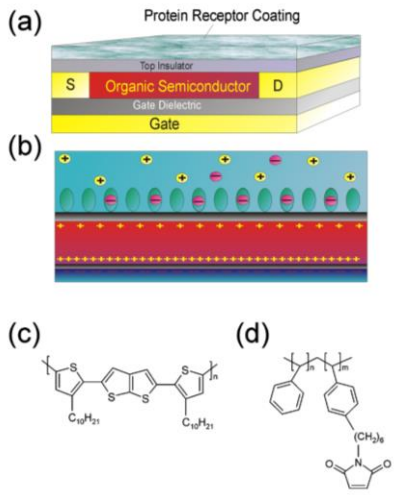

Figure 0.9. (a) Schematic view of the sulfate anion sensor. (b) Operation principle, including the binding of sulfate ions to the receptor and charge compensation in the semiconductor. (c) Chemical structure of the semiconductor, PDTT. (d) Chemical structure of the maleimide functionalized polystryrene, PSMI.

Spijkman et al. reported a dual-gate OFET based pH sensor by using polytriarylamine (PTAA) polymer as the semiconductor. The electrodes are buried underneath the semiconductor to prevent direct contact to the aqueous analytes. The pH sensor was found to have a broad pH detection range from pH = 2 to 10, and the sensitivity of the device could also be fine-tuned by adjusting the capacitance ratio between the top and bottom gates in this type of sensor (Figure 0.10).[126]

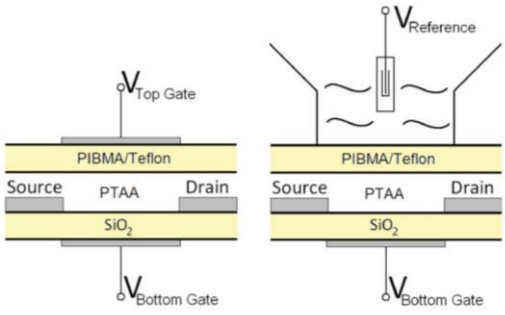

Figure 0.10. Schematic representation of a dual-gate field-effect transistor and the corresponding transducer. PTAA stands for the organic semiconductor polytriaryalamine. The top dielectric consists of a stack of polyisobutylmethacrylate (PIBMA) and the Teflon derivative AF-1600. The gate dielectrics are highlighted in yellow. It shows that the dual-gate transducer is a classical ISFET with an additional gate dielectric to enhance the sensitivity.[126]

Another potential application is the detection of biomolecules, while many biological analytes such as DNA or proteins can only exist in low concentration with specific pH ranges. It is always of great demand to develop low-cost and accurate detection methods to detect biomolecules. Possible applications can be rapid test kits for patients or early diagnosis for certain diseases. Yan et al. demonstrated a label-free DNA sensor by using a PEDOT:PSS OECT set-up (Figure 0.11).[127] Single-strand DNA probes were immobilized on the device and the sensor can detect complementary DNA molecules down to 1 nM. The LOD can be further lowered to 10 pM using pulse-enhanced hybridization process of DNA. The device can also be fabricated on flexible polyethylene terephthalate (PET) substrates and integrated in a microfluidic system.

Other than the previously mentioned liquid sensors, there could be other liquid analytes for detection such as metal ions, amino acids, and proteins. Other representative liquid chemical sensors can be found in **Table 0.2**.

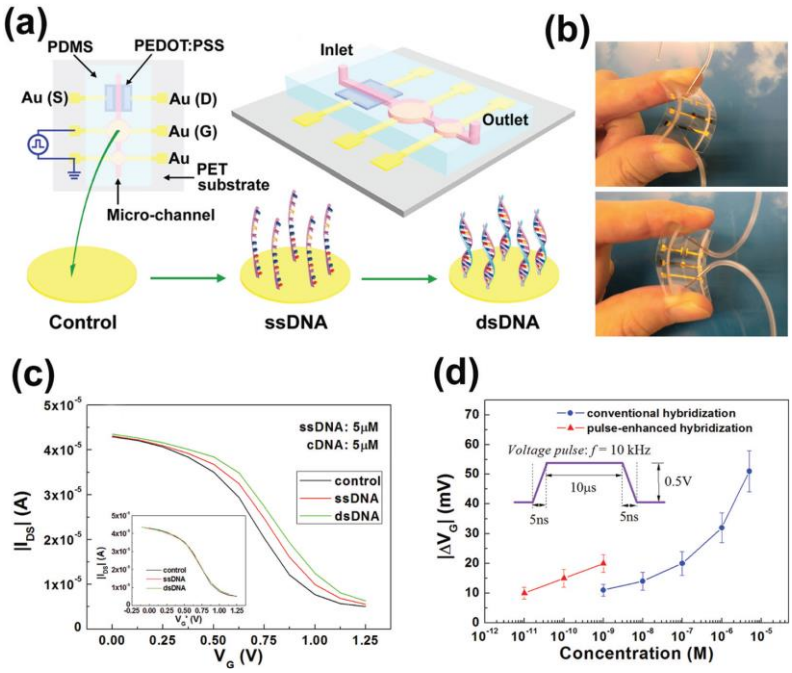

Figure 0.11. (a) Schematic of an OECT-based DNA sensor integrated in a PET flexible microfluidic system. (b) Photographs of the device bent to both sides. (c) Transfer curves of the device before and after the immobilization and the hybridization of DNA. Inset: the three transfer curves are shifted horizontally and merged into a universal curve. (d) $|\Delta V_G|$ as a function of the concentration of DNA targets in PBS solutions. Inset: the electric field pulse (frequency: 104 Hz, voltage: 0.5 V, pulse width: 10 μs, rise/fall time: 5 ns) applied during the hybridization of DNA.[127]

Table 0.2. Representative chemical sensors based on different organic materials and their general performances[3]

Sensor type	Analyte	Active layer	Detection limit	Ref.
Humidity sensor	Humidity	Pentacene	0% - 75%	[128]
	Humidity	C12FTTF	0% - 75%	[129]
	Humidity	C6TFT	0% - 85%	[129]
	Humidity	Pentacene	0% - 75%	[129]
Ion sensor	K^+	P3HT	33 mM	[130]
	Na^+, K^+, Ca^{2+}	P3HT	0.001%	[131]
	SO_4^{2-}	PDTT	1 mM	[125]
pH sensor	pH	P3HT	6.6 - 9.5	[130]
	pH	P3HT	4 - 10	[131]
	pH	P3HT	2 - 10	[132]
	pH	P3HT	3.5 - 5.5	[133]
	pH	Pentacene	4 - 10	[134]
	pH	Pentacene	2.5 - 7	[135,136]
	pH	PTAA	2 - 10	[126]
	pH	DDFTTF	3 - 11	[137]
TNT sensor	TNT	DDFTTF	40 ppm	[124]
Glucose sensor	Glucose	α6T	1 mM	[138]
	Glucose	DDFTTF	10 ppm	[137]
	Glucose	P3HT	10^{-5} M	[139]
	Glucose	PEDOT:PSS	1.1 mM	[140]
DNA sensor	DNA	Pentacene	N/A	[141–143]
	DNA	Pentacene	1 μg/mL	[144]
	DNA	P3HT	N/A	[145]
	DNA	DDFTTF	1 nM	[146]
Lactic acid	Lactic acid	α6T	0.3 mM	[138]
	Lactic acid	DHα6T	N/A	[138]
	Lactic acid	CuPc	10 μM	[138]
Pyruvic acid	Pyruvic acid	CuPc	N/A	[138]
MPA	MPA	DDFTTF	100 ppb	[137]
Cysteine	Cysteine	DDFTTF	100 ppb	[137,147]
	Cysteine	DDFTTF	10 ppb	[124]
1-pentanol	1-pentanol	P3HT	N/A	[148]
Vanillin	Vanillin	P3HT	N/A	[148]
Cell	Cell	P3HT	N/A	[149]
Protein	BSA	Pentacene	500nM	[150]

The contents in this table is adopted from the publication *"Organic Thin-Film Transistors for Chemical and Biological Sensing"* by Yan et al. The table is slightly modified to match the editing format of this thesis.

2.2.3. Temperature sensors

For temperature sensors, many literatures reported the use of conducting polymers or their composite materials to create sensors with high sensitivities. Temperature sensors are of great demands especially for monitoring real-time temperature changes in healthcare or logistic applications. Organic materials especially polymers can provide flexibility to the temperature sensors, allowing the sensors to be attached on human skin surface to monitor temperature changes to give information about health. Many current research aims to improve the temperature measurement range, sensitivity, response time and temperature resolution.

For sensitivity enhancement, it is suggested that the combination of two active materials can give a synergistic effect to increase the sensitivity of temperature sensors. For example, combining the conductive polymer PEDOT:PSS with graphene or CNTs can increase the sensitivity of TCR when compared to their respective single component temperature sensor.[151,152] Using this method, Hong et al. developed a stretchable temperature sensor array membrane of polyaniline nanofibers which can be used as electronic skin.[153] The polymer was combined with single walled carbon nanotube (SWCNT) to create a field-effect transistor system, and temperature was measured in the range between 15 and 45 °C with a 1%/°C TCR. Figure 0.12 shows the fabrication procedures of the flexible E-skin device.

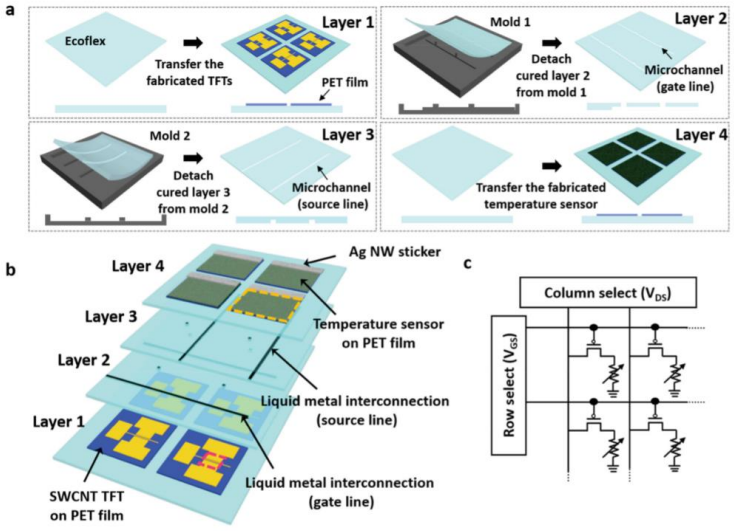

Figure 0.12. Device fabrication of a polyaniline/SWCNT transistor based thermal sensor on PET plastic substrate.

In terms of accuracy, Lee et al. reported a PEDOT:PSS based temperature detection thread for wearable devices.[154] Their devices showed a high linearity towards an increasing temperature gradient and the conductive cotton threads may be stitched into a small-area textile to demonstrate wearable electronics applications (Figure 0.13).

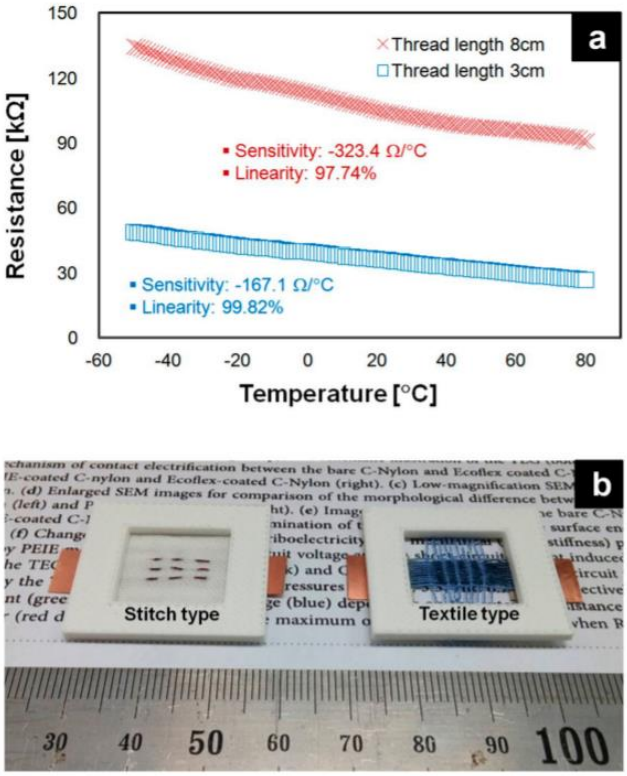

Figure 0.13. a) Resistance and temperature relationship of PEDOT:PSS dyed cotton threads; b) Image of a stitch type and textile type PEDOT:PSS dyed thread.

Salmerón et al. reported the making of a bendable PEDOT:PSS temperature sensor by inkjet printing it on a pre-printed silver nanoparticle (AgNP) electrode on polyethylene terephthalate (PET) substrate (Figure 0.14). The reported device is an all-printed device which demonstrated a proof-of-concept production process in future generation sensor technology. Examples of other representative printable organic temperature sensors with high performances can be seen in Table 0.3.

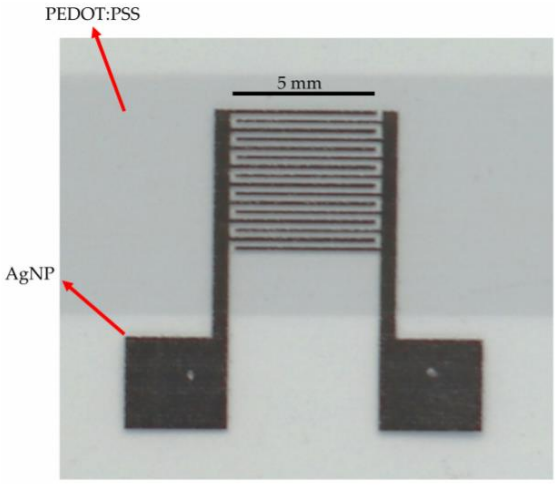

Figure 0.14. Photograph of a fully inkjet-printed sensor module. The photo was recorded from a dry sensor module. Image shows the the AgNP-based interdigitated electrodes, the PEDOT:PSS sensing layer and the bottom polyethylene terephthalate (PET) bendable substrate.

Table 0.3. Representative temperature sensors using different organic materials and their composite materials.

Temperature Sensitive Material	Sensitivity (% $^{o}C^{-1}$)	Working Range (^{o}C)	Response time (Recovery time)	Deposition Method	Ref.
Crosslinked PEDOT:PSS	−0.77	25 – 50	1.5 s (6 s)	Printing	[155]
Gr/PEDOT:PSS	−0.06	35 – 45	20 s (18 s)	Printing	[151]
PEDOT:PSS/CNT	−0.61	22 – 48	18 s	Printing	[156]
pNIPAM /PEODT:PSS/CNT	−2.6	25 – 40	167 s (605 s)	Spin-	[152]
PEDOT:PSS	−0.25	20 – 70	N/A	Printing	[157]
rGO/PET	0.635	30 – 100	1.2 s	Printing	[158]
rGO/PU	1.34	30 – 80	N/A	coating	[159]
pNIPAM/PEDOT:PSS/CNTs/PDMS	2.6	25 – 40	139 s	Coating &	[152]
PEDOT:PSS/PU	0.1	25 – 75	< 2 s	Dipping	[160]
MWCNT/PVDF yarn	0.13	30 – 45	N/A	Dip-coating	[161]
PEDOT:PSS/CNTs/PET	0.85	30 – 55	< 50 ms	Printing	[162]

The contents in this table is adopted from the publications *"Fully Printed PEDOT:PSS-based Temperature Sensor with High Humidity Stability for Wireless Healthcare Monitoring"* by Tokito et al. Copyright 2020, Sci. Rep. *and "Printable, Highly Sensitive Flexible Temperature Sensors for Human Body Temperature Monitoring: A Review"* by Su et al. Copyright 2020, Nanoscale Res Lett. The contents are slightly modified to match the editing format of this thesis.

2.3. Device Structures and Sensing Principles of Organic-based Sensors

This section describes the two type of organic-based sensors that are commonly used in most organic-based sensors namely the organic field-effect transistors (OFET) and the organic resistive device. There may be some differences between the two kinds of sensors in terms of their active channeling layers. Details of the devices structures and sensing principles will be discussed in the following sections.

2.3.1. Organic Field-Effect Transistor (OFET) Sensors

In the next two sections, the basic principles of OFET and the four common geometries of OFET will be discussed. Transistor-based sensors such as the water-gated organic field-effect transistors (WGOFET) anionic sensors will be discussed in the next chapter based on the theories and principles in this section.

2.3.1.1. Basic Principles and Geometries of OFET

OFETs are external field modulated p/n junction that consist of three electrodes. The electrodes are the source (S), the drain (D) and the gate (G) and current flowing through the (S/D) channel can be controlled by the bias voltage applied from the gate (G). The source and the drain electrodes are in direct contact with the semiconductor, while the gate electrode is isolated from the semiconductor via a dielectric layer. An OFET can be fabricated in different geometries (Figure 0.15). The most common OFETs are fabricated with bottom-gate (BG) architecture. In a bottom-gate OFET, the source and the drain electrodes are built on top of (top contact TC) or below (bottom-contact BC) the organic semiconductor layer. Similarly, a top-gate (TG) OFET has an inverted structure of a bottom-gate device. The top-gate architecture may have a positive effect on air-sensitive n-type semiconductors by encapsulating the semiconductor layer from the ambient atmosphere. Different geometries of OFET can be used to construct a sensor device depending on whether the active layer or the dielectric material will be used as the sensing component.

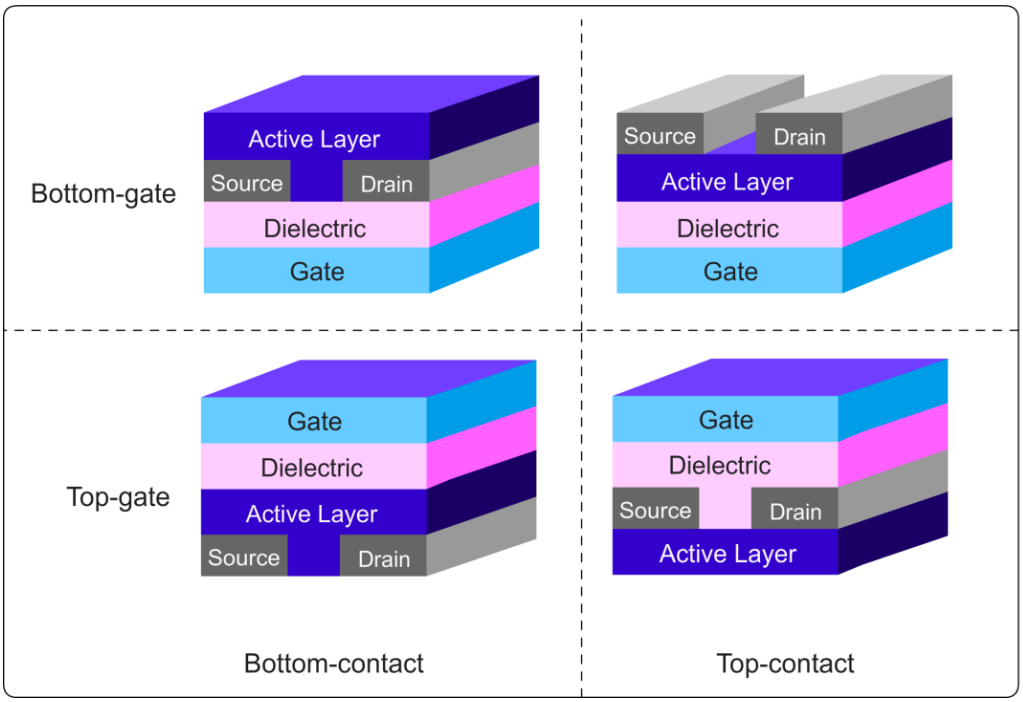

Figure 0.15. The geometry of different OFET devices.

2.3.1.2. General Sensing Principles using OFET

In general, bottom-gate OFETs were used as the common geometry for OFET-based sensors since the active layer would be exposed on top of the device surface. There are also reported OFET sensors using the gate dielectric layer as the sensing material, in which the capacitance change can be used as output signals.[163–166] Regardless of the geometries of the OFET-based sensors, an electrical output signals, such as the output current, threshold voltage, or carrier mobility, would be altered by introducing the analyte to the sensing layer. A general sensing mechanism of an OFET-based chemical sensor is suggested by Oh et al. as follow or is depicted in Figure 0.16 by Mok et al.:[167,168]

1) An analyte is injected onto the sensing layer of the OFET-based sensors.
2) The injected analyte affects the organic semiconducting or dielectric layers depending on the geometry of device. This can include different modes of interactions between the sensing layer and the analyte, by either physical or chemical change at macroscopic or at a molecular level.
3) Finally, a change in charge carrier density may result in a change in the current flow through the channel of the sensor, which gives out an electrical signal for sensing.

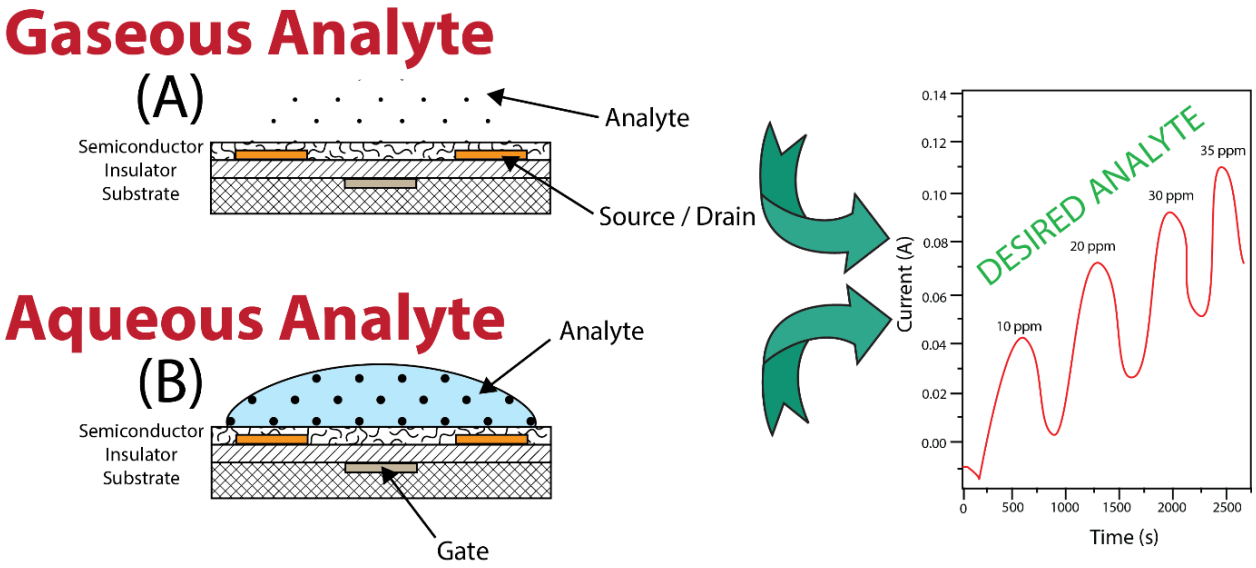

Figure 0.16. Schematic sensing principles of BGTC OFET-based sensor with (A) gaseous analyte and (B) aqueous analyte.[168]

Typically, the sensing mechanisms of chemical sensors may be a mixture of different interactions between the analyte and the sensing layer. In terms of chemistry, such interactions can include hydrogen-bonds, chalcogen bonds, dipole-dipole interactions, hydrophobic/hydrophilic interactions, or formation of charge transfer (CT) complexes. In terms of physics, analyte molecules can diffuse into the grain boundaries and induce a trapping effect to cause a change in charge carrier density (eg. Changing the threshold voltage), or a change in molecular ordering. Nevertheless, the exact mechanism of a working sensor could be explained by the mixture of both chemical and physical effects mentioned.

2.3.2. Organic Resistive Sensors

The device structure of a resistor-type device is simpler than an OFET device described previously, in which only two electrodes are needed. The active material is usually an ohmic conductor and a biased voltage can be applied on the material to assess its conductivity or resistivity changes. Materials used in the active channel of a resistor-type device usually have a reasonably moderate to high conductivity in the order of ~10^{-4} up to 10^{2} S/cm or above. Doped conductive polymers have been demonstrated as promising candidates used as the sensing materials in resistor-type devices.[7,169–174] Similar to OFET-based sensors, recognition of an analyte signal can be converted into an electrical signal by means of intermolecular interactions or physical interactions between

the analyte and the sensing layer. However, a gate terminal is not required to modulate the current flow in resistor-type sensors as the materials used is already intrinsically conductive.

Due to the ease of fabrication and simple design of the device geometry, its applications was always found to be attractive in electronic industries, and the potential applications can range from chemiresistive gas sensors, thermistors, pH sensors, photoresistors, humidity sensors, and other resistor-based sensors used in many currently available electronic modules.[151–154,175–179]

2.3.2.1. Basic Principles of Resistive Devices

The basics of a resistive device follows the Ohm's Law. Ohm's law can be applied to a single component, or a combination of different components. When the current that flows through any part of a circuit is given, the voltage dropped across that part of the circuit is defined by the product of the current and the resistance, also known as the $V = IR$.

Ohm's law states that a combination of voltage and current through a particular conductor determines its resistance. Therefore, if there is a change in physical conditions of a material being used as the conductor, the voltage and current flow of the conductor will also be changed. Examples can be the resistance changes with variations in temperature, which formed the fundaments of a resistance thermometer or sometimes called a thermistor, in which the resistance of this kind of sensor changes with respective to temperature. In organic electronics system, the functional groups on a material can be easily modified by means of chemical synthesis. When conductive polymers were first discovered, researchers have been trying to design and synthesize new functional organic conductive materials that have certain affinities to specific analytes, and give changes to the materials resistance to transduce and amplify a signal when the active layer recognizes the analyte.[167,180–182]

In addition to analyte-sensing layer interactions described above, an analyte can also chemically change the doping state of a conductive polymer in a resistor device if the energy levels are permitted. The physical properties of a conducting polymer are strongly dependent on their doping levels. One example is the changing of doping levels of conducting polymers by redox-active analytes at room temperatures. This process is a kind of redox chemical reaction and the mechanism may involve electron transfer from/to analyte to/from the conductive polymer depending on their difference in energy levels. For example, conductive polymers can be used to

detect redox gases such as O_2, CO, NO_x, SO_x, NH_3, I_2, H_2S…etc. Electron transfer can lead to a change in resistance and work function of the polymer sensing layer.

For instance, polypyrole, polythiophene, or polyaniline are used for sensing redox-active gases such as NH_3, NO_x and H_2S.[183–186]. Oxidizing gases such as NO_2 are highly electron deficient and are able to remove electrons from the electron rich aromatic rings of p-type conducting polymers. When an electron is transferred from the conjugated polymer to the oxidizing gas, radical cation (or polaron) will be generated on the p-type polymer, and the resistance of the polymer will be lowered to give out an increased current flow. Oppositely, when a reducing gas is introduced to the polymer such as NH_3, the process will be reversed. General electron transfer process between a conductive polymer and redox-active gases using NO_2 or NH_3 as examples can be depicted as:

For oxidizing gases such as NO_2,

$$P^0 + NO_2 \rightleftharpoons P^{+\bullet} + NO_2^{-\bullet}$$

For reducing gases such as NH_3,

$$P^{+\bullet} + NH_3 \rightleftharpoons P^0 + NH_3^{+\bullet}$$

where P^0 is the neutral undoped non-conductive polymer, $P^{+\bullet}$ is the doped conductive polymer (polaron). The process can also be seen as an adsorption and desorption process, where the polymer is a solid surface and the gas interacts with the polymer surface. This mechanism would also be regarded as a heterogeneous equilibrium process in chemical kinetics in which the adsorption/desorption process can be a reversible or irreversible process depending on how strongly the analyte can bind to the polymer surface. Using a similar concept, Swager et al. developed a porous conjugated polymer sensor with bulky substituent groups to selectively detect electron deficient nitro-containing molecules. The polymer sensor works by fluorescence quenching, and was found to have highest selectivities towards some explosive compounds such as trinitrotoluene (TNT), dinitrotoluene (DNT), and a number of chloro- and nitro-containing aromatic compounds.[187]

The device geometry of a chemiresistive sensor can be seen in Figure 0.17a. The electrical resistance change of the sensing material is then measured as the output signal, so a simple ohmmeter can be used for data acquisition. Normally, a constant bias current is applied to the

sensor, and the signal measurement can be tested by measuring a current vs. time (*I*-*t*) or a current vs. voltage (*I*-*V*) plot. According to Janata et al., an equivalent circuit diagram of a chemiresistive sensor can be depicted in Figure 0.17b. From the circuit diagram, any change in resistance in any parts of the sensor, either the resistance on the polymer surface ($R_{surface}$), polymer-substrate interface ($R_{interface}$) or polymer-electrode contacts ($R_{contact}$) will cause a substantial change in the overall bulk resistance (R_{bulk}) of the device (Figure 0.17b).[188,189]

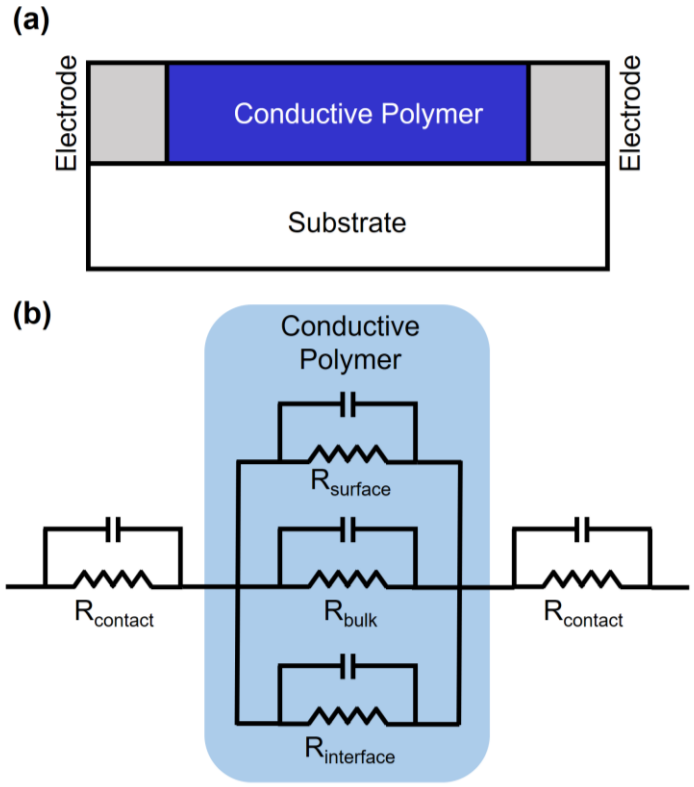

Figure 0.17. (a) Schematic diagram of a cross-section of a chemiresistive sensor and its (b) equivalent circuit diagram.

Since conductivity is inversely proportional to resistivity, the bulk conductivity of a doped conductive polymer system can also be interpreted as a combination of three major components listed in Equation 2.1 below:

$$\frac{1}{\sigma} = \frac{1}{\sigma_c} + \frac{1}{\sigma_h} + \frac{1}{\sigma_i} \qquad \textbf{(Equation 0.1)}$$

where σ is the bulk conductivity, σ_c is the intermolecular conductivity, σ_h is the intramolecular hopping conductivity and σ_i the ionic conductivity, respectively. σ_c can be changed by altering the doping levels of the conductive polymers by both redox electron transfer, acidic/basic doping/dedoping. σ_h is governed by the interchain carrier hopping distance between polymer chains. The hopping factor can be enhanced by swelling of the polymer, crystallinity change, formation of hydrogen-bonds, dipole-dipole interactions or change in grain boundary distances. σ_i is controlled by the carrier mobility of counter ions, which is affected by the interaction between mobile ions and analytes within the conductive grains.[188,189]

2.4. Theory of Organic Semiconductors

The following sections discuss the different mechanisms of electrical transport in the organic system. Over the past 7-8 decades, theoretical physicists, chemists and electronic engineers have developed different charge transport and injection theories and models in the traditional inorganic semiconductor systems. Since the rise of organic electronics in the late 1980s, it has become a maturing area of study in chemistry, physics and engineering during the late 1990s and early 2000s, many theories and models, that were originally developed for inorganic semiconductors, were being fitted into the organic electronic systems to explain charge transport phenomena in organic semiconductors or conductors. Although the theories or models may not be perfectly ideal for organic systems in most cases, the general charge transport mechanisms were widely accepted in in terms of charge hopping and injection theories in the current research field. Details will be discussed in the following sections.

2.4.1. Charge Transport in Organic Systems

In an organic semiconductor, particularly in π-conjugated small molecules or polymers, the carbon atoms in the conjugated system forms σ and π bonds with their adjacent atoms. The σ bonds form strong localized bonds due to its head-to-head orbital overlapping of the atomic orbitals. The σ bonds are rigid and thus forming a structure backbone for the conjugated organic molecules or polymers. The remaining p-orbitals on a carbon atom form π bond with its neighboring carbon atom or sometimes a heteroatom such as nitrogen. The π bond is much weaker due to its sideways overlapping, and the π electrons are considered delocalized. The delocalization of π electrons allows the materials to be charge conducting. Somehow like an inorganic material, whereas the positive charges would transport at the highest bonding π-orbital, which is defined as the highest occupied molecular orbital (HOMO), and electrons would transport at the lowest anti-bonding π*-orbitals, also known as the lowest unoccupied molecular orbital (LUMO). However, the conductivity of an organic semiconductor is considerably lower as its intrinsic free carrier concentration is low. In comparison to inorganic semiconductors, an organic semiconductor would not conduct electricity except when there is a charge injection, doping or when there are photo-generated free carriers.

2.4.1.1. Hopping Transport

2.4.1.1.1. Basic Principles of Hopping in Organic Materials

Charge transport in an organic semiconductor depends on the nature of the materials, particularly on its chemistry, compositions and orientation of molecule in solid state. In some crystalline organic semiconductors, band-like transport can be observed.[190] Similar to inorganic crystalline semiconductor, charge carriers in crystalline organic semiconductor move within delocalized molecular orbitals or "bands". However, lattice vibrations (phonons) can scatter electrons and reduce their mobility. The effect of grain boundary between a polycrystalline interface also lowers the conductivity in organic semiconductors. With increasing number of grain boundaries, the probability of having a higher number of traps would also be higher, and therefore leading to a lower conductivity.[191–194] Lattice vibrations are lower at low temperature. Therefore, higher carrier mobility can be observed for crystalline inorganic semiconductors.

Most semiconducting polymers are usually amorphous and disordered in certain domains. It was first described by L. D. Landau for the presence of charge conduction in a disordered organic material.[195,196] It was suggested that in a disordered organic material, each molecule can be regarded as a discrete and localized energy site, owing to the lack of orbital overlapping. Upon thermal activation or photo-excitation, charge carriers can move from one molecule to another by hopping. This process is assisted by lattice vibrations, and an increase in the temperature would result in a higher mobility which is opposite to that of an inorganic semiconductor. Figure 0.18 shows the schematic diagram of hopping transport in organic systems.

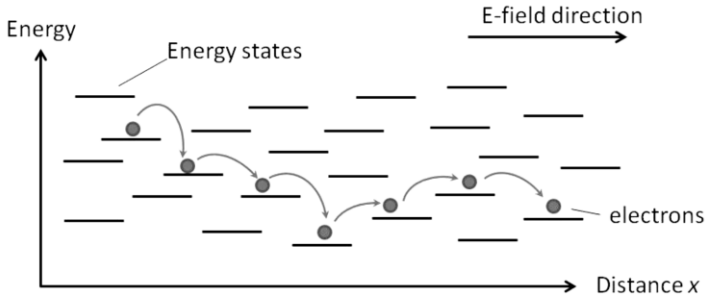

Figure 0.18. Schematic diagram of hopping transport in organic semiconductors.

2.4.1.1.2. Variable-range Hopping (VRH) and Temperature Dependent Hopping Transport

Variable-range hopping (VRH) is a theoretical model first used to describe charge carrier transport in disordered semiconductor or in an amorphous solid by hopping in an extended temperature range. In 1969, Mott first described the VRH model in non-crystalline systems, and his model can be applied in latterly developed π-conjugated conductive organic materials to study temperature related conductivity changes.[197] In the Mott's VRH model, conductivity changes with respect to temperature is described as:

$$\sigma = \sigma_0 \, e \left[-\left(\frac{T_0}{T}\right)^{\alpha}\right] \qquad \textbf{(Equation 0.2)}$$

where σ is the electrical conductivity, σ_0 is the conductivity at infinite temperature, T_0 is the characteristic temperature and α is equal to $1/(1+D)$, where D is dimensionality of the system. The model suggests that the true exponent α in Equation (1.1) was determined at which the correlation coefficient R of the fit of a $ln(\sigma)$-T^{α} plot reached a maximum or close to unity. By then one can determine whether the hopping mechanism in the system follows a certain dimensionality. For example, an α value of ½ would result in $D = 1$, and the hopping transport would be likely to be following a 1-dimensional (1D) hopping. Examples of 1D hopping system can be demonstrated in single-walled carbon nanotubes (SWCNT), graphenes, and some conductive polymers such as sorbitol-doped PEDOT:PSS, and conductive polymer nanowires.[198–203] With the use of Mott's VRH model as a tool, synthetic chemists would be able to correlate structural and charge transport relationship to design and explain appropriate semiconductive or conductive systems. Application of the VRH theory will be further discussed in a Chapter 5 which is about temperature sensors where the VRH theory was used as a theoretical tool to explain certain temperature dependent and stability phenomena of a polyer:dopant complex in terms of hopping dimensionality.

2.4.1.2. Gaussian Disorder Model

Gaussian Disorder Model was first introduced by H. Bässler in 1993 to describe the hopping motion of the carriers within a disorder material that possesses "Gaussian density-of-states". The model relies on a few assumptions as described below:[204,205]

a) The electronic polarization energy of a charge carrier located on a molecule is subject to fluctuations due to the random intermolecular interactions.

b) Charges hop along localized states with a density-of-states (DOS) distribution described by a Gaussian function with a variance σ.

c) Charge transport is a random walk process. The hopping rate v is described by the Miller-Abraham equation:

$$v = v_0 e^{-2\gamma \Delta R_{ij}} e^{-\Delta\varepsilon/kT} \qquad \textbf{(Equation 0.3)}$$

where ΔR_{ij} is the intersite distance and Δε is the energy difference of the sites.

d) In addition to the energetic disorder σ, there exists also a position disorder with a Gaussian distribution Σ.

From Monte-Carlo simulations, Bässler arrived at a universal law relating the mobility to both the energetic disorder σ and the positional disorder Σ:

$$\mu = \mu_0 \, exp\left[-\left(\frac{2}{3}\frac{\sigma}{kT}\right)^2\right] exp\left\{C\left[\left(\frac{\sigma}{kT}\right)^2 - \Sigma^2\right]\sqrt{E}\right\} \qquad \textbf{(Equation 0.4)}$$

where μ_0 is the high temperature limit mobility, C is an empirical constant, E is the external field. According to (Equation 0.4), the mobility depends on both the external field and the temperature. When the external field is absent, the mobility would be temperature dependent only:

$$\mu(T) = \mu_0 \, exp\left[-\left(\frac{2}{3}\frac{\sigma}{kT}\right)^2\right] \qquad \textbf{(Equation 0.5)}$$

2.4.1.3. Charge Injection in Organic Semiconductor

Charge injection is exceptionally important in organic semiconductors since there is no intrinsic mobile carrier for electrical conduction. Charge injection usually occurs at the interface of the organic layer and the metal electrode. The efficiency of charge injection depends on the energetic barrier to transfer free charges from the contact electrode to the organic semiconductor layer. The injection efficiency will be high if the injection barrier is small. Similarly, if there is no charge transfer at the interface, the vacuum levels of both the organic layer and the metal electrode should be aligned. However, if interfacial charge transfer takes place, the process will create interfacial dipoles.[206] The vacuum level of the interface may be altered by these dipoles by a certain energy Δ. Charge-transfer complexes may also be created at the interface at certain circumstances. Because of the interface dipoles, the hole injection barrier Φ_h and the electron injection barrier Φ_e can be defined and modified according to the Schottky-Mott model by the following equations:

$$\phi_h = I_p - \Phi_m + \Delta \qquad \textbf{(Equation 0.6)}$$

$$\phi_e = \Phi_m - A_e - \Delta \qquad \textbf{(Equation 0.7)}$$

where I_p is the ionization energy, A_e is the electron affinity of material, Φ_m is the work function of the specific metal electrode. When the injection barrier is zero, the metal and the organic layer are said to be in ohmic contact. Figure 0.19 illustrates the schematic energy diagram of an organic/metal interface with the presence of an interfacial dipole layer.

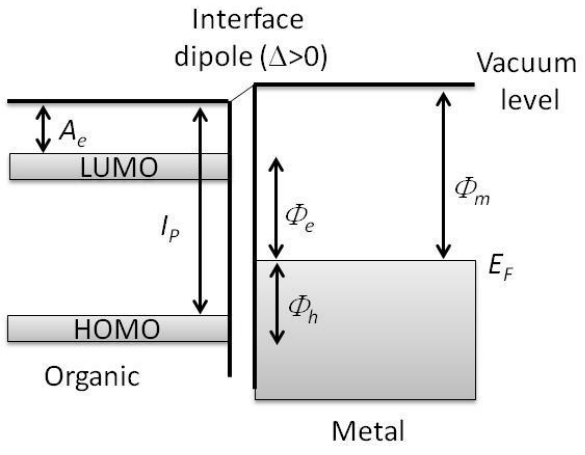

Figure 0.19. Schematic energy diagram of an organic/metal interface with the presence of an interfacial dipole layer.

2.4.1.4. Charge injection mechanism

2.4.1.4.1. Thermionic injection

In thermionic injection, an electron gains sufficient thermal energy and leave the metal surface into the organic layer, overcoming its potential barrier. Thermionic injection occurs at high temperature and low electric field.[207,208] Where there is no electric field, the metal organic Schottky barrier is high (Figure 0.20a). As shown in Figure 0.20b, the detailed thermionic injection process is described as follow: (i) when an electric field is applied, the organic layer acquires a triangular energy level. (ii) image positive charge, which is generated when an electron leaves the metal surface, creating an electrostatic image force that favors charge injection by further reducing the barrier by V_m:

$$V_m = \sqrt{\frac{q^3 F}{4\pi\varepsilon_0\varepsilon_r}} \qquad \textbf{(Equation 0.8)}$$

where ε_0 is the vacuum permittivity and ε_r is the relative permittivity of organic, F is the applied electric field and q is the unit charge. The Richardson-Schottky equation described the field dependent thermionic injection current (J_{RS}):[209]

$$J_{RS} = A^* T^2 e^{-\frac{(\varphi - V_m(F))}{k_B T}} \qquad \textbf{(Equation 0.9)}$$

where T is the absolute temperature, ϕ is the injection barrier height, A^* is the effective Richardson constant:

$$A^* = 4\pi m k_B{}^2 q / h^3 \qquad \textbf{(Equation 0.10)}$$

where m is the electron effective mass, h is the Planck's constant.

2.4.1.4.2. Tunneling

Tunneling is known as field emission. It is another possible mechanism for charge injection. Tunneling refers to carrier injection process in which an electron "tunnels" through the barrier with the assistance of a high external electric field. The tunneled electron in fact did not acquire enough energy to overcome the potential barrier. In other words, this mechanism is a quantum mechanical process. The probability of tunneling injection is directly related to the barrier width.[210] The mechanism of field emission is illustrated in Figure 0.20c. When the applied external electric field is large; the injection barrier width would be much smaller. Therefore, the chance of tunneling would be higher. The tunneling injection current J_{FN} is

described by the Fowler-Nordheim tunneling model:[211]

$$J_{FN} = \frac{q^3 F^2}{8\pi h\varphi} exp\left(-\frac{8\pi\sqrt{2m\varphi^3}}{3hqF}\right) \qquad \textbf{(Equation 0.11)}$$

where q is the unit charge, F is the applied electric field, h is the Planck's constant, m is the effective mass of charge carrier, and ϕ is the injection barrier.

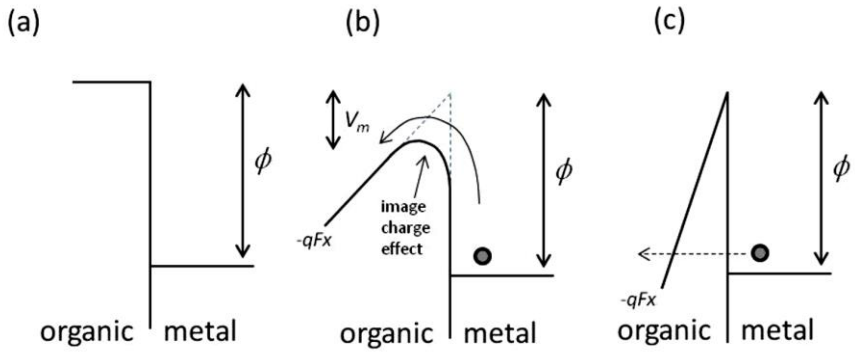

Figure 0.20. Schematic energy level diagram of Schottky barrier: (a) in an absent of an external electric field (b) in thermionic emission, and (c) in Fowler-Nordheim tunneling.

Chapter 3: Indigo-based Amide Polymer as Active Sensing Layer in Water-gated Organic Field-effect Transistor (WGOFET) for Fluoride Sensing[1]

3.1. Introduction

Iindigo was chosen as the first amide-based building block in this study since it is a well-known environmentally stable pigment, with facile synthetic scheme, and low-cost starting materials. The indigo building block reported in this chapter is also a rare example of because it has solubilizing 2-octyldodecyloxy groups at the 7,7'-positions with the hydrogen bonds intact. In this chapter, the design and synthesis of two novel indigo donor-acceptor (D-A) polymers were demonstrated namely, **PIDG-T-C20** and **PIDG-BT-C20**, which comprise an indigo moiety that has intramolecular hydrogen-bonds as the acceptor building block and thiophene (T) and bithiophene (BT) as the donor building block, respectively. **PIDG-T-C20** and **PIDG-BT-C20** exhibited characteristic p-type semiconductor performance, achieving hole mobilities of up to 0.016 and 0.028 $cm^2V^{-1}s^{-1}$, respectively, which are highest values reported for indigo-based polymers. The better performing **PIDG-BT-C20** was used for the fabrication of water-gated organic field-effect transistors (WGOFETs), which showed excellent stability at ambient conditions. The **PIDG-BT-C20**-based WGOFETs exhibited rapid response when fluoride ions were introduced to the water gate dielectric, achieving a limit of detection (LOD) of 0.40 mM. On the other hand, the devices showed much lower sensitivities towards other halide ions with the order of relative response: F^- >> Cl^-> Br^- > I^-. The high sensitivity and selectivity of **PIDG-BT-C20** to fluoride over other halides is considered to be realized through the strong interaction of the hydrogen atoms of the N-H groups in the indigo unit with fluoride ions, which alters the intramolecular hydrogen-bonding arrangement, the electronic structures, and thus the charge transport properties of the polymer.

Fluoride (F^-) is an important component in mammalian biological systems. The uptake of small amount of fluoride ions in drinking water by human can strengthen bones and prevent osteoporosis or tooth decay.[212–214] However, an excess of fluoride ion uptake can lead to

[1] This chapter is a slightly modified version of an accepted manuscript published by Royal Society of Chemistry in RSC Advances on 13th August 2019, available online: https://doi.org/10.1039/C9RA04302K. **Jenner H. L. Ngai**, George Y. Chang, Xiguang Gao, Xiaocheng Zhou, Arthur D. Hendsbee and Yuning Li, "*Design and synthesis of stable indigo polymer semiconductors for organic field-effect transistors with high fluoride sensitivity and selectivity*" The content has been reproduced here with the permission of the copyright holder.

dental and skeletal diseases such as fluorosis, osteosarcoma and nephrolithiasis.[215] Therefore, maintaining the fluoride concentration in drinking water within a proper range through water fluoridation is very important for the public health.[216,217] Existing fluoride sensors rely mainly on a potentiometric working principle with ion selective electrodes (ISE) with the aid of a reference electrode for signal (potential) measurement. Other fluoride sensors under development are colorimetric or fluorescence-based optical chemosensors in which the qualitative and quantitative analyses of fluoride ions are achieved with a UV-Vis spectrophotometer or a fluorimeter. The mechanisms of these optical fluoride sensors involve the interactions between the fluoride ion and the sensing chromophore, which affect the intramolecular charge transfer (ICT) or excited state intramolecular proton transfer (ESIPT) of hydrogen-bonds,[73–78] cleavage of silicon-oxygen or silicon-carbon bonds and binding of fluoride to amides,[218–222] π–π interactions,[223] and aggregation of nanoparticles.[224–228]

Printed organic field-effect transistors (OFETs) based on small molecule or polymer semiconductors have drawn much attention in recent years because of their low fabrication cost, excellent substrate conformity, high mechanical robustness and versatile function tunability of the organic semiconductors. Therefore, OFETs have many potential applications such as flexible displays, radio frequency identification tags, chemical or biological sensors and therapeutic medical devices.[1–3,9–14] Nonetheless, although OFETs have been studied as sensors for the detection of numerous chemical analytes,[3,229–233] there are only a few for sensing ions in aqueous solutions mainly due to the instability of most organic semiconductors towards water and oxygen under device operation. To the best of our knowledge, there has been only one report on the OFET-based fluoride ion sensors,[234] where the gate electrode instead of the polymer semiconductor layer was in direct contact with the aqueous solution containing the analyte fluoride ions.

Indigo is a stable dyestuff, which has been used for textiles for centuries. Indigo and its small molecule[84,104,235–238,238] and polymer [239–242] derivatives have recently demonstrated promising semiconductor properties as channel materials in OFETs. We are particularly interested in the intramolecular hydrogen bonds between the N–H and C=O groups of the two vinylogous amides of indigo, N–H···O=C, which may preferentially interact with

fluoride ions.[73–78] In this work, we prepared two novel indigo donor-acceptor (D-A) polymers, **PIDG-T-C20** and **PIDG-BT-C20** (Scheme 3.1), comprising the hydrogen-bond-containing indigo as the acceptor building block and thiophene (T) or bithiophene (BT) as the donor building block, respectively. **PIDG-T-C20** and **PIDG-BT-C20** exhibited p-type semiconductor performance when used as the active layer in bottom-gate-bottom-contact (BGBC) OFETs, achieving hole mobilities of up to 0.016 and 0.028 $cm^2V^{-1}s^{-1}$, respectively, which are so far highest values reported for indigo-based polymers.[46,48-243] The better performing **PIDG-BT-C20** was chosen for fabricating WGOFET) devices, which showed excellent stability at ambient conditions. When fluoride ions were introduced to the water gate dielectric, a rapid decrease in the drain current (I_{DS}) was observed, achieving a limit of detection (LOD) of 0.40 mM for fluoride ions. On the other hand, the devices showed much lower sensitivities towards other halide ions with the order of relative response: F^- >> Cl^- > Br^- > I^-, indicating the excellent selectivity of these sensors to fluoride ions.

3.2. Results and Discussion

3.2.1. Synthesis of Indigo-based D-A Polymer Semiconductors.

As afore-mentioned, preserving the intramolecular hydrogen bonds, N–H···O=C, for the fluoride sensing is critical in the design of our indigo-based fluoride OFET sensors. However, indigo monomers without solubilizing groups such as Tyrian purple ((*E*)-6,6'-dibromo-[2,2'-biindolinylidene]-3,3'-dione) are insoluble, posing challenges to its purification and polymerization. Therefore, we synthesized a soluble indigo monomer **IDG-C20-Br** (Scheme 3.1), which has solubilizing 2-octyldodecyloxy groups at the 7,7'-positions with the hydrogen bounds intact, following a recently developed synthetic route.[235] Briefly, alkoxylation of 3-hydroxybenzaldehyde (**3-HBA**) formed **1**, which was brominated to afford **2**, followed by nitration to give **3**. The Baeyer–Drewson indigo synthesis using **3** was then carried out to give the indigo monomer **IDG-C20-Br**.[244] Stille coupling polymerization was carried out between **IDG-C20-Br** and 2,5-bis(trimethylstannyl)thiophene or 5,5′-bis(trimethylstannyl)-2,2′-bithiophene to produce two polymers **PIDG-T-C20** and **PIDG-BT-C20**, respectively, which were purified by Soxhlet extraction. Detailed synthesis procedures can be found in Appendix B. The molecular weights of the polymers were measured by high temperature gel permeation

chromatography (HT-GPC) at 140 °C using 1,2,4-trichlorobenzene (TCB) as eluent. **PIDG-T-C20** and **PIDG-BT-C20** have number average molecular weights (M_n) of 21.6 and 18.6 kDa with dispersities ($Đ$) of 2.57 and 2.08, respectively (Figure 3.1). Thermogravimetric analysis (TGA) was performed on **PIDG-T-C20** and **PIDG-BT-C20**, which showed good thermal stability with a 5% weight loss temperature at 315 and 361°C, respectively (Figure 3.2). No noticeable endo- or exothermic transitions were found on their differential scanning calorimetry (DSC) thermograms up to 250 °C (Figure 3.3). Detailed materials characterizations and synthesis procedures can be found in Appendix A and Appendix B.

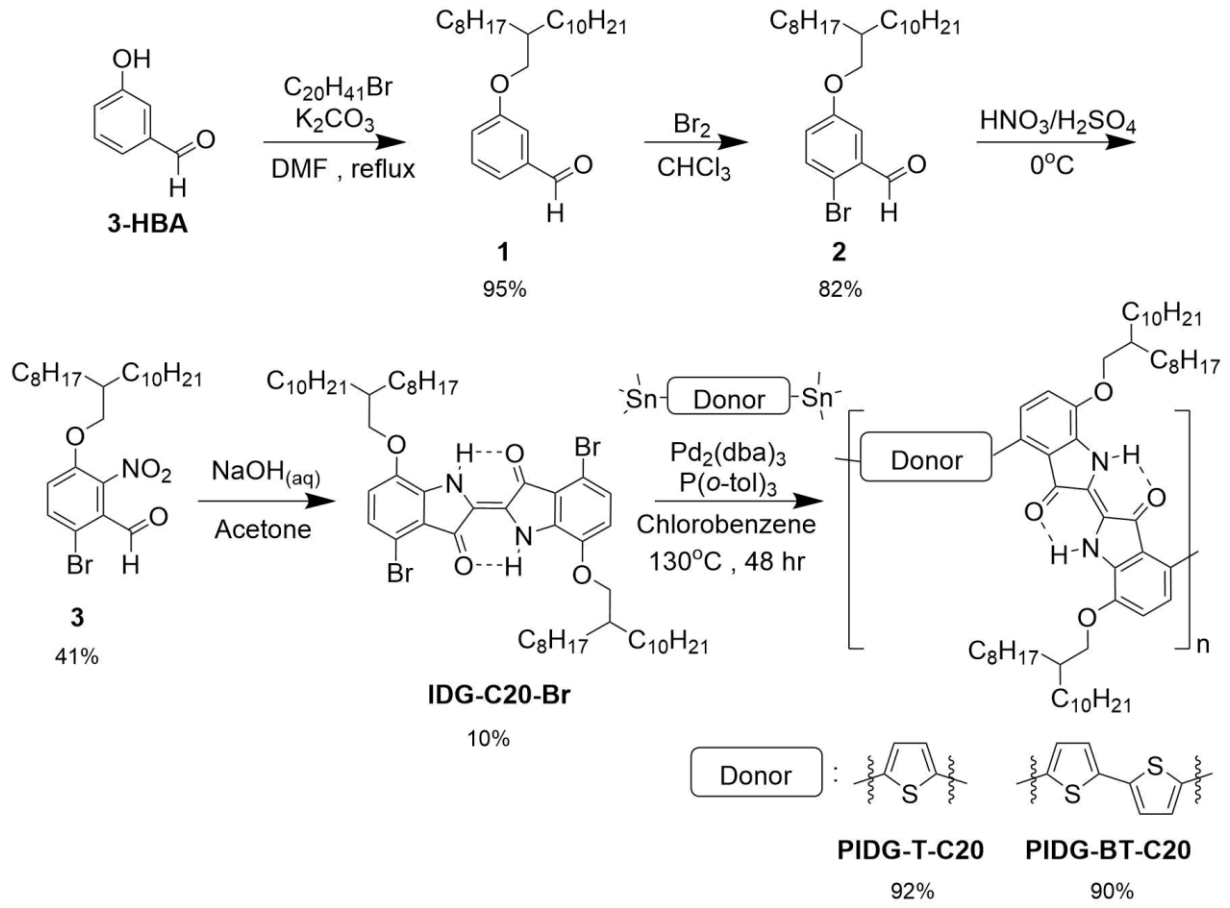

Scheme 3.1. General synthetic scheme of indigo D-A polymers

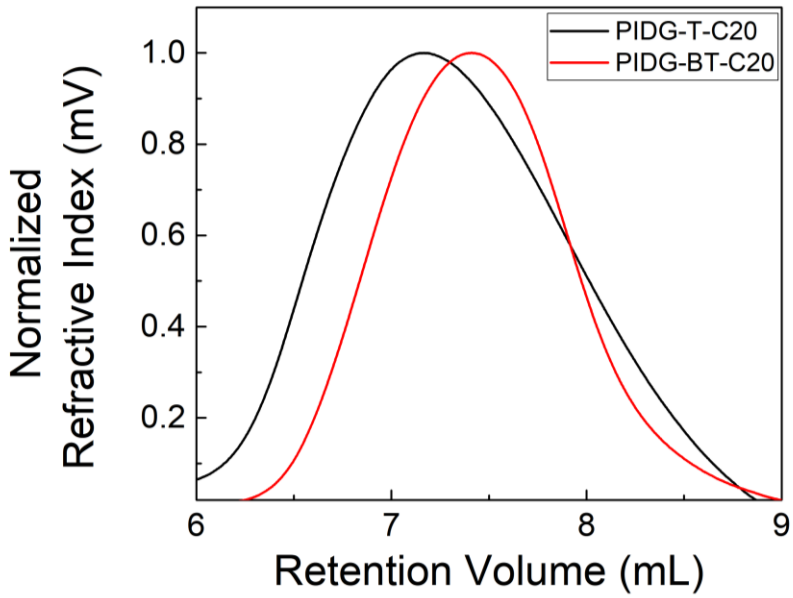

Figure 3.1. GPC chromatograms of **PIDG-T-C20** and **PIDG-BT-C20** measured at 140 °C using 1,2,4-trichlorobenzene as eluent.

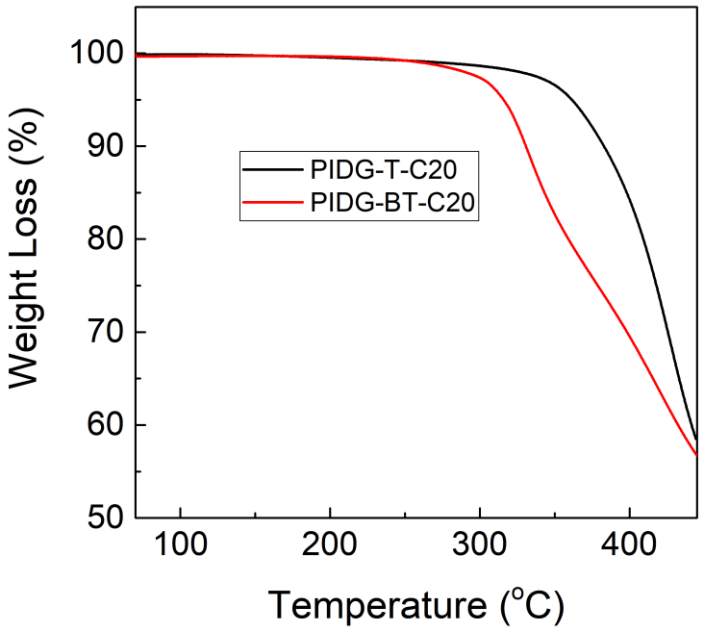

Figure 3.2. TGA graphs of **PIDG-T-C20** and **PIDG-BT-C20** at a heating rate of 20 °C min^{-1} under nitrogen.

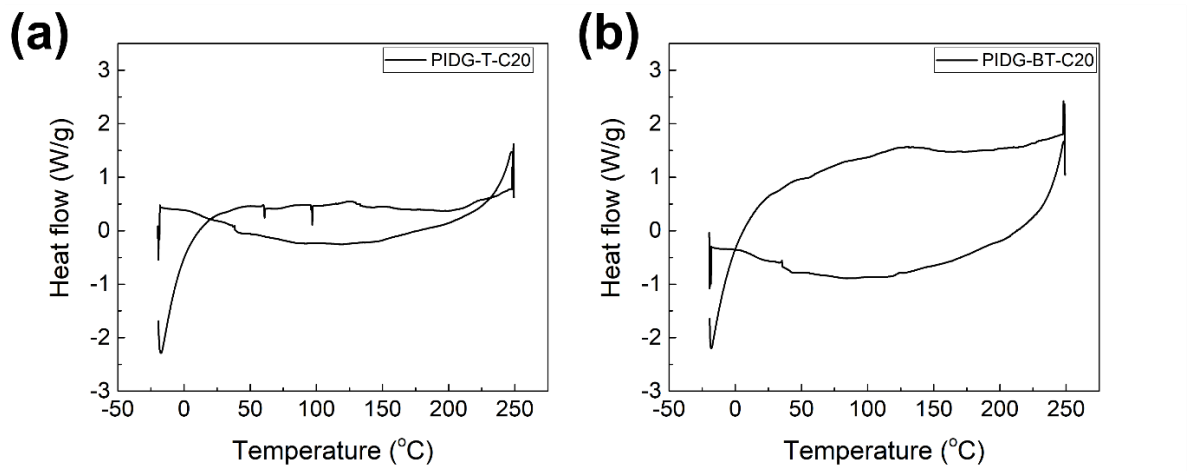

Figure 3.3. DSC thermograms of (a) **PIDG-T-C20** and (b) **PIDG-BT-C20** at a heating/cooling rate of 10 °C min^{-1} under nitrogen.

3.2.2. Optical Properties and Electrochemical Properties.

As shown in Figure 3.4a and Table 3.1, **PIDG-T-C20** and **PIDG-BT-C20** in chloroform solutions exhibited notable red-shifts in the wavelength of maximum absorbance (λ_{max} = 741 nm for **PIDG-T-C20** and 728 nm for **PIDG-BT-C20**) when compared to the indigo monomer **IDG-C20-Br** (λ_{max} = 668 nm). This indicated that the polymers have more extended π-conjugation than the indigo monomer. In thin films, they exhibited broader and further red-shifted absorption spectra (λ_{max} = 762 nm for **PIDG-T-C20** and 758 nm for **PIDG-BT-C20**), which could be attributed to the planarization of polymer backbone and intermolecular interaction in the solid state. Cyclic voltammetry (CV) diagrams of **PIDG-T-C20** and **PIDG-BT-C20** showed oxidative peaks, which were used to calculate their HOMO energy levels to be -5.48 and -5.27 eV, respectively (Figure 3.4b and Table 3.1). On the other hand, no noticeable reduction peaks were observed for both polymers. Therefore, their LUMO energy levels were calculated using the obtained HOMO energy levels and the optical band gaps to be -4.00 eV and -3.80 eV for **PIDG-T-C20** and **PIDG-BT-C20**, respectively. Thermal stability tests were also performed on the **PIDG-T-C20** and **PIDG-BT-C20**, and no observable changes in UV-Vis absorption profiles when the films were heated from rt up to 200°C (Figure 3.5).

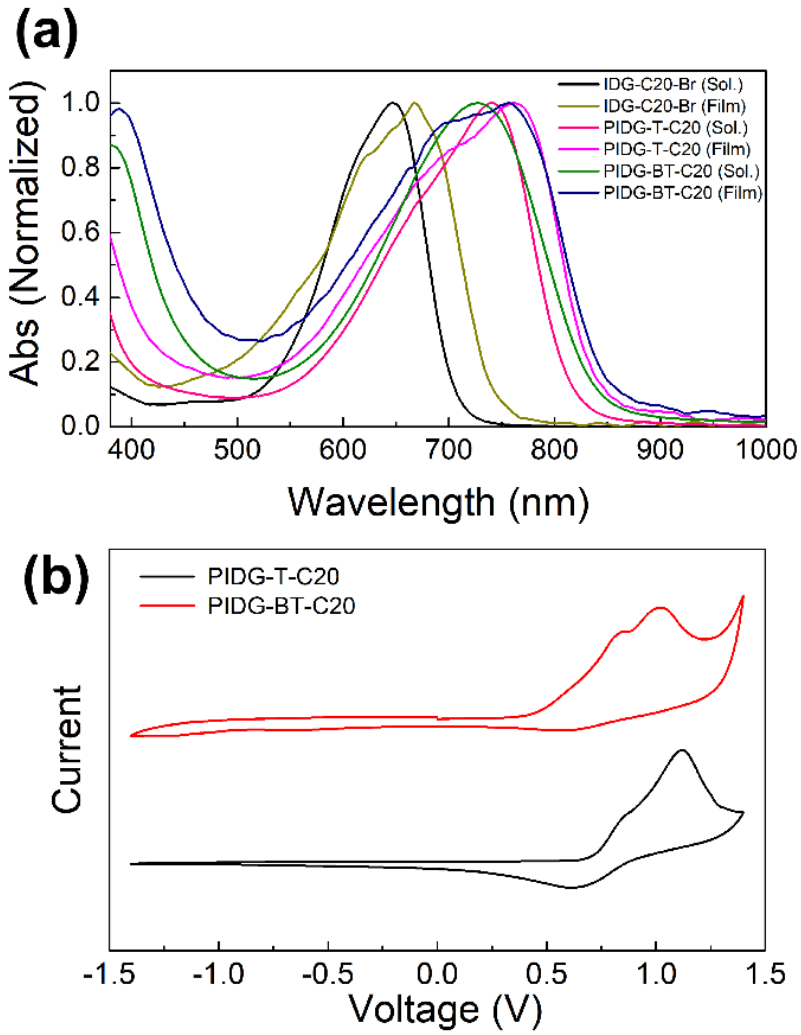

Figure 3.4. (a) UV-Vis absorption spectra of indigo monomers and polymers chloroform solutions and thin films. (b) Cyclic voltammograms of indigo polymers.

Table 3.1. UV-Vis optical and electrochemical information of indigo polymer films

Polymer	$E_{g,opt}$ (eV)	λ_{max} (nm)	λ_{onset} (nm)	$HOMO_{CV}$ (eV)	$LUMO_{opt/CV}$ (eV)
PIDG-T-C20	1.48	762	839	-5.48	-4.00
PIDG-BT-C20	1.47	758	844	-5.27	-3.80

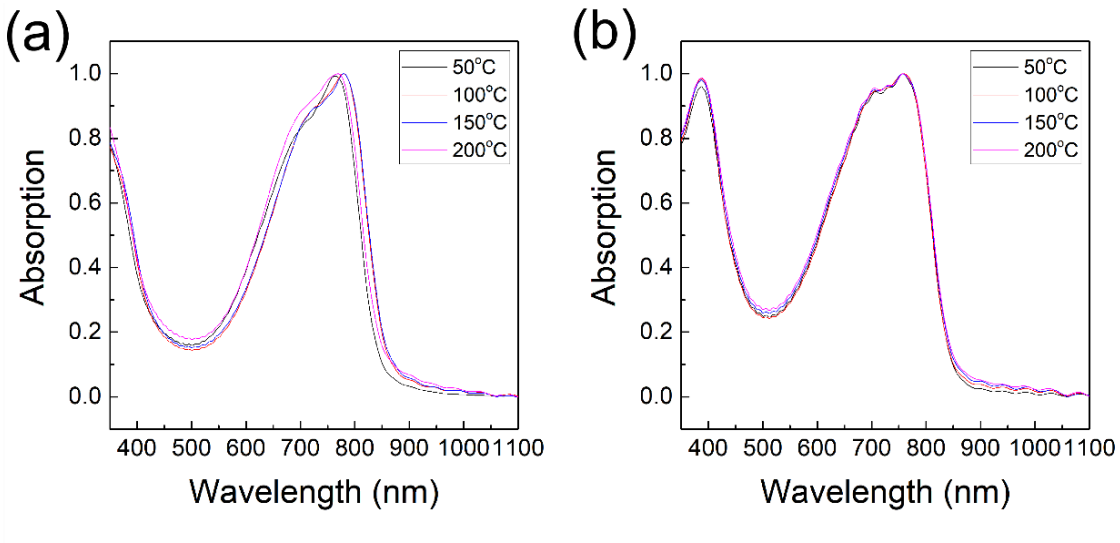

Figure 3.5. UV profiles of polymer thin films: (a) **PIDG-T-C20** and (b) **PIDG-BT-C20** annealed at 50, 100, 150, and 200 °C.

3.2.3. OFET Performance of Polymers

The polymers were used as channel semiconductors in BGBC OFETs. Both polymers exhibited typical p-type semiconductor characteristics with the maximum hole mobilities of up to 0.016 $cm^2V^{-1}s^{-1}$ for **PIDG-T-C20** and 0.028 $cm^2V^{-1}s^{-1}$ for **PIDG-BT-C20** for films annealed at 150 °C (Figure 3.6 and Table 3.2). It is noticed that the devices based on **PIDG-T-C20** showed obvious S-shaped output curves near the origin, indicating the existence of large contact resistances. This might be due to its rather low HOMO energy level that builds up a large hole injection barrier as well as its poor contact with the source/drain electrodes. All the devices exhibited rather large threshold voltages (V_{th} = ca. -30 V ~ -60 V), indicating the presence of a large number of hole traps. A representative **PIDG-BT-C20**-based OFET device showed a hysteresis ΔV_{th} (the difference between forward and reverse) of 7.9 V (Figure 3.7), which is within the typical range for OEFTs.[245–248] However, the **PIDG-T-C20**-based OFET device exhibited a quite large ΔV_{th} of 30.9V, which might be caused by the trap recharging that originated from the large grain boundary resistance.[247,249] The optimal OFET device performance for **PIDG-T-C20** and **PIDG-BT-C20** thin films were the ones annealed at 150 °C, while the OFET transfer and output characteristic of polymer thin films samples annealed at other temperatures can be found in Figure 3.8 and Figure 3.9. Detailed OFET device fabrication procedures can be found in Appendix A.

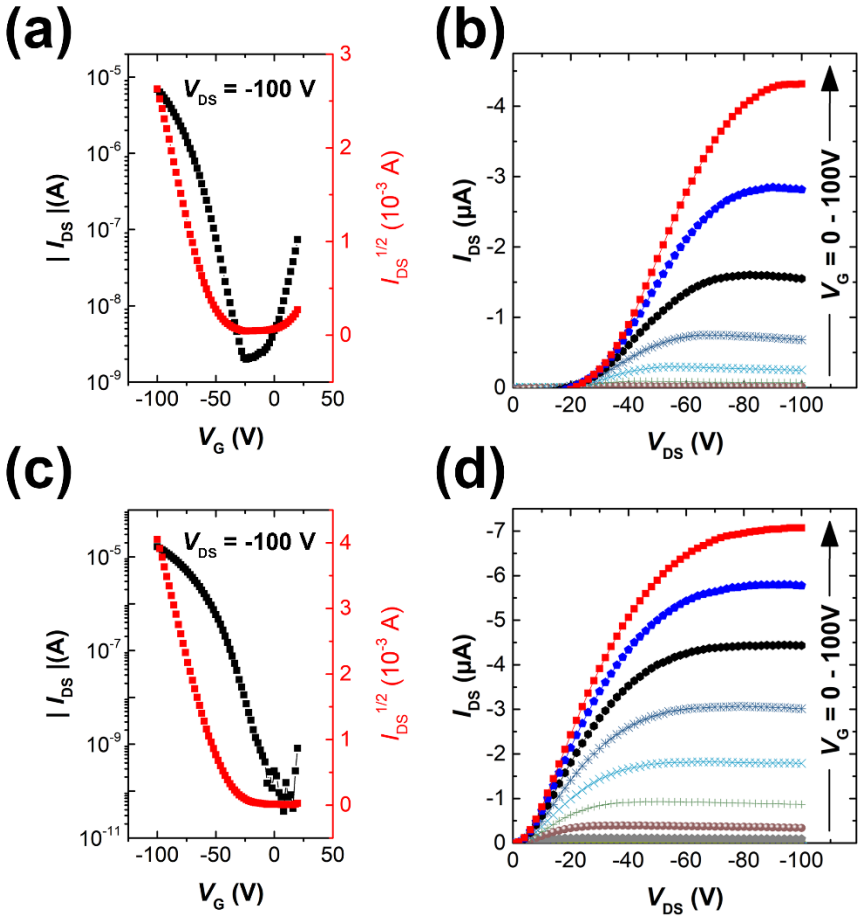

Figure 3.6. Transfer characteristics of (a) **PIDG-T-C20** and (c) **PIDG-BT-C20** films annealed at 150 °C; Output characteristics of (b) **PIDG-T-C20** and (d) **PIDG-BT-C20** films annealed at 150 °C with V_G step voltage = -10 V.

Table 3.2. OFET device data for polymer **PIDG-T-C20** and **PIDG-BT-C20**

Polymer	Annealing Temp. (°C)	Avg. ± Std μ_{sat} ($cm^2V^{-1}s^{-1}$)	Max. mobility ($cm^2V^{-1}s^{-1}$)	V_{th} (V)	$I_{ON/OFF}$
PIDG-T-C20	50	0.0024 ± 0.00093	0.0036	-34.2	1.3×10^4
	100	0.0050 ± 0.00098	0.0059	-58.8	3.1×10^4
	150	0.015 ± 0.00052	0.016	-52.0	3.0×10^3
	200	0.0022 ± 0.00067	0.0029	-63.7	3.0×10^3
PIDG-BT-C20	50	0.0020 ± 0.00034	0.0025	-43.3	1.7×10^4
	100	0.00027 ± 0.00011	0.00037	-39.9	1.3×10^3
	150	0.027 ± 0.00091	0.028	-43.8	1.4×10^5
	200	0.0030 ± 0.00039	0.0035	-43.6	3.3×10^4

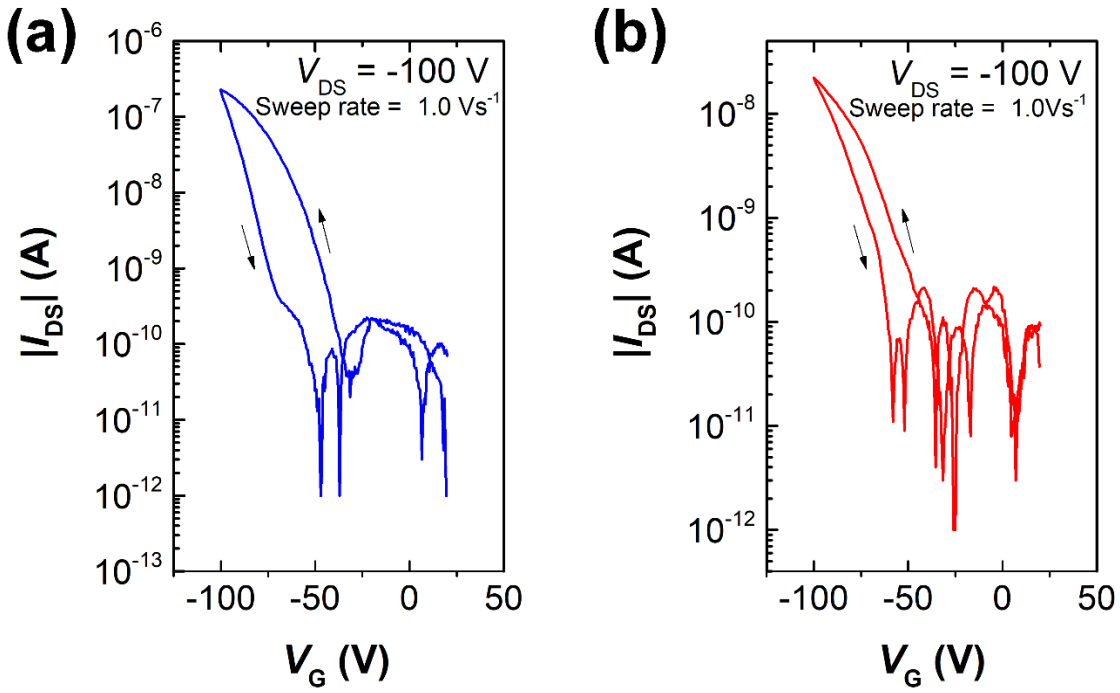

Figure 3.7. Hysteresis behaviors of the transfer characteristics of BGBC OFETs for (a) **PIDG-T-C20** and (b) **PIDG-BT-C20** films annealed at 150 °C by forward and backward V_G scan between +20 to -100 V at a sweep rate of 1.0 Vs^{-1}; The change in threshold voltage (ΔV_{th}) was found to be ΔV_{th} = 30.9V for **PIDG-T-C20** and ΔV_{th} = 7.90V for **PIDG-BT-C20**.

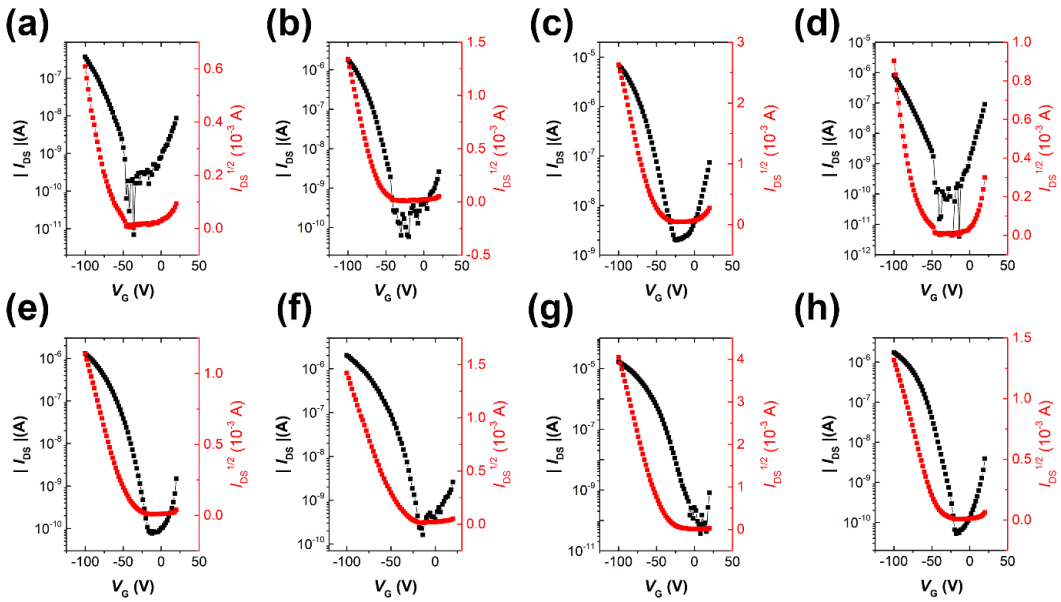

Figure 3.8. OFET transfer characteristics of **PIDG-T-C20** annealed at (a) 50 °C; (b) 100 °C; (c) 150 °C; (d) 200 °C and **PIDG-BT-C20** annealed at (e) 50 °C; (f) 100 °C; (g) 150 °C; (h) 200 °C with V_G step voltage = -10 V.

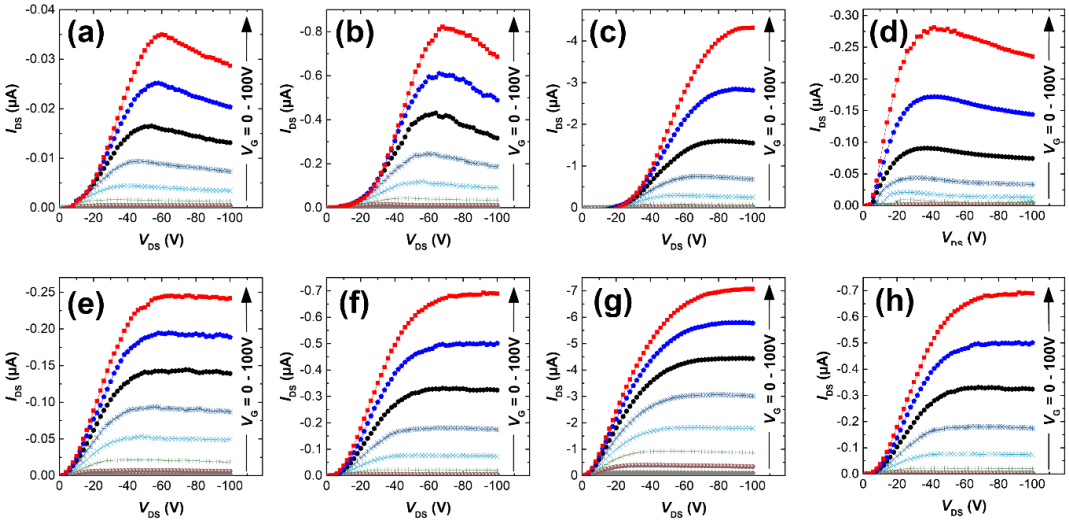

Figure 3.9. OFET output characteristics of **PIDG-T-C20** annealed at (a) 50 °C; (b) 100 ℃; (c) 150 °C; (d) 200 °C and **PIDG-BT-C20** annealed at (e) 50 °C; (f) 100 °C; (g) 150 °C; (h) 200 °C with V_G step voltage = -10 V.

3.2.4. Morphology and Crystallinity of Polymer Films

The atomic force microscopic (AFM) image of the **PIDG-T-C20** film annealed at 50 °C showed some micron-sized particles (bright spots) on the rather smooth film surface (R_q = 1.7 nm) (Figure 3.10a). Upon annealing at 100 °C, fewer but larger particles were seen. At 150 °C, both the number and size of the particles decreased along with a decrease in the film roughness (R_q = 1.1 nm), which may be accounted for the optimum hole mobility achieved at this annealing temperature. Further increasing the annealing temperature to 200 °C led to the formation of more clearly defined aggregates along with larger and deeper cracks. This might create discontinuous regions, resulting in a decrease in mobility. Compared to **PIDG-T-C20**, the 50 °C-annealed **PIDG-BT-C20** film showed larger spherical and rod-like aggregates with a higher roughness (R_q = 2.9 nm). The film became smoother by increasing the annealing temperature to 100 °C (R_q = 1.4 nm) and 150 °C (R_q = 1.1 nm), which might be accounted in part for the improved carrier mobility of **PIDG-BT-C20**. When the film was annealed at 200 °C, larger aggregates with clearer grain boundaries formed, which could explain the significant drop in mobility of this polymer at this annealing temperature.

The crystallinity of the polymer thin films was studied by using XRD in the reflection mode. For the **PIDG-T-C20** film annealed at 50 °C, no diffraction peak was observed, indicating a quite disordered chain packing of this polymer. Upon annealing at 100 °C, a peak at $2\theta = 3.91^{o}$ appeared, which corresponds to a *d*-spacing of 22.6 Å (Figure 3.10b). This peak could be assigned to the (100) diffraction, representing the interlamellar distance. The sole appearance of this peak also suggested that the polymer chains adopted an edge-on orientation, which is favourable for charge transport in OFETs.[250–252] For **PIDG-BT-C20**, a (100) peak at $2\theta = 3.91^{o}$ (*d* = 22.6 Å) was observed at a lower annealing temperature of 50 °C (Figure 3.10b). The peak intensified and shifted to 4.15° (*d* = 21.3 Å) upon annealing at 100 °C, which indicates a closer interlamellar packing distance. For both polymers, the (100) peak disappeared at annealing temperatures higher than 150 °C, suggesting that the polymer chains might have undergone re-organization to form more disordered chain packing. Although both polymers exhibited maximum crystallinity at the annealing temperature of 100 °C, their highest hole mobilities in OFETs were obtained at the

annealing temperature of 150 °C where both polymers were disordered. It has been reported that the film morphology may play a more significant role in charge transport than the crystallinity of the polymer films.[253] Therefore, the observed optimal charge transport performance for the 150 °C annealed films of both polymers may be due to their lower surface roughness as observed in the AFM images at this annealing temperature.

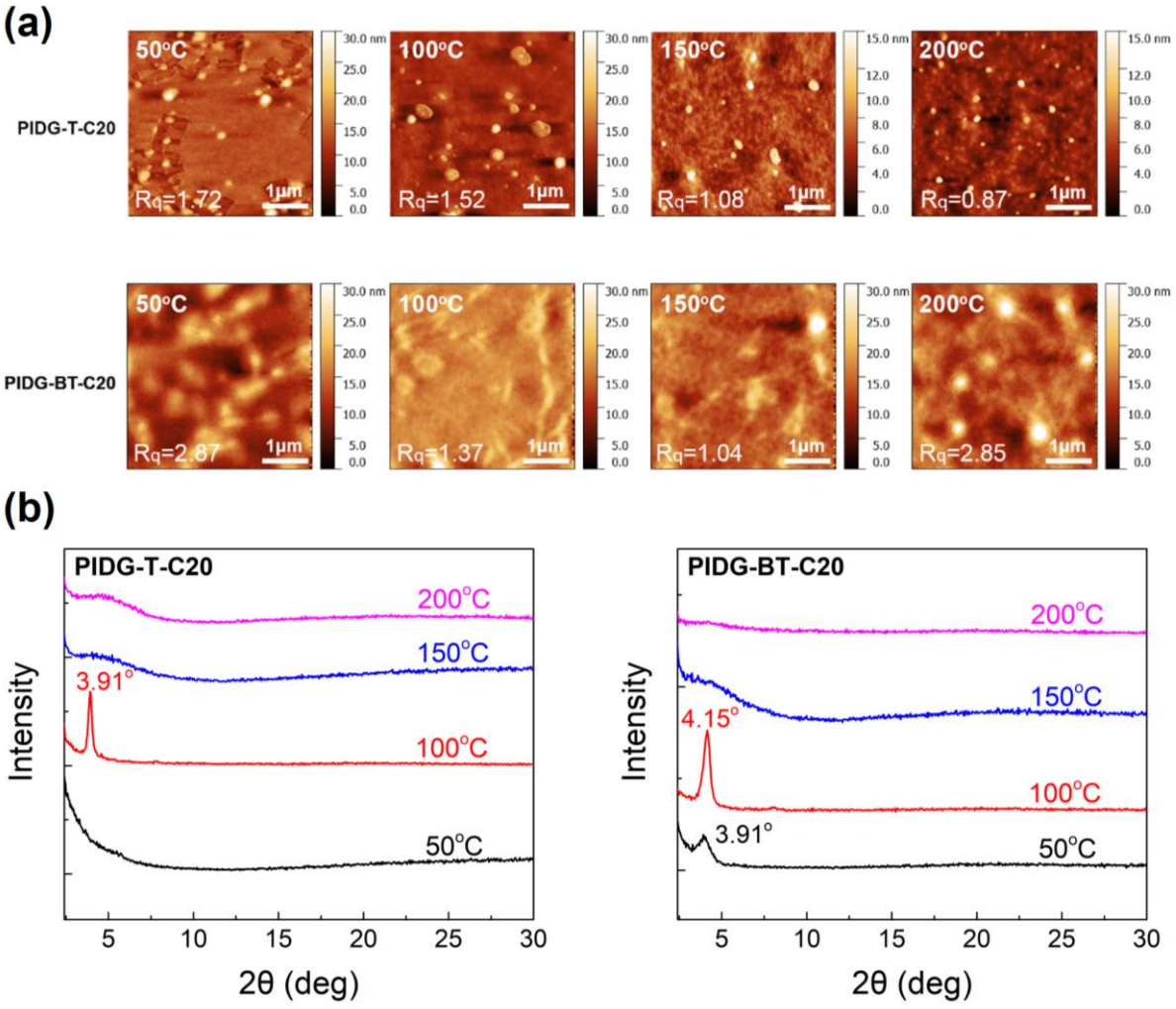

Figure 3.10. (a) AFM images of **PIDG-T-C20**, and **PIDG-BT-C20** annealed at 50, 100, 150, and 200 °C. (b) XRD spectra of **PIDG-T-C20**, and **PIDG-BT-C20**.

3.2.5. Halide Ion Sensing Properties of PIDG-BT-C20-based WGOFET

WGOFETs were fabricated on the bare Si/SiO_2 substrate having interdigitated source and drain electrodes with channel length (L) of 30 µm and channel width (W) of 15.8 mm (Figure 3.11a). **PIDG-BT-C20** was chosen as the active layer for WGOFETs because it showed better OFET performance than **PIDG-T-C20**. For the transistor measurement, 20 µL of 18 MΩ deionized (DI) water was dropped on top of the active layer via a micropipette and a probe needle as the gate electrode was connected to the top of the water droplet. Figure 3.12 shows the analyte injection procedures into the WGOFET device and the actual experimental set-up. Since electrolysis of water would start to occur at a potential difference of 1.23 V,[254] both the gate (V_G) and source-drain (V_{DS}) voltages were kept below an absolute value of 1.23 V. The transfer characteristics of the **PIDG-BT-C20** WGOFET devices at V_{DS} = -1 mV and V_G = 0 – -1.0 V measured in air are shown in Figure 3.11b. A stable signal baseline (measured without analyte) is an important criterion for sensors. As shown in Figure 3.11c, the I_{DS} of the **PIDG-BT-C20** WGOFET device remained relatively steady over time, indicating the excellent stability of this polymer towards water and air. The baseline was found to remain steady after repeated measurements and washing with water multiple times. A reference WGOFET device using regioregular head-to-tail poly(3-hexylthiophene) (**P3HT**) as the active layer was also fabricated and characterized as a comparison. However, the **P3HT** based WGOFET device showed significant deviations in I_{DS} over time (Figure 3.13) and started to degrade a few hours after the measurement. The much better stability of **PIDG-BT-C20** is considered due to its lower HOMO energy level (-5.27 eV) than that of P3HT (ca. -5.0 eV).[255,256] Detailed WGOFET device fabrication procedures can be found in Appendix A.

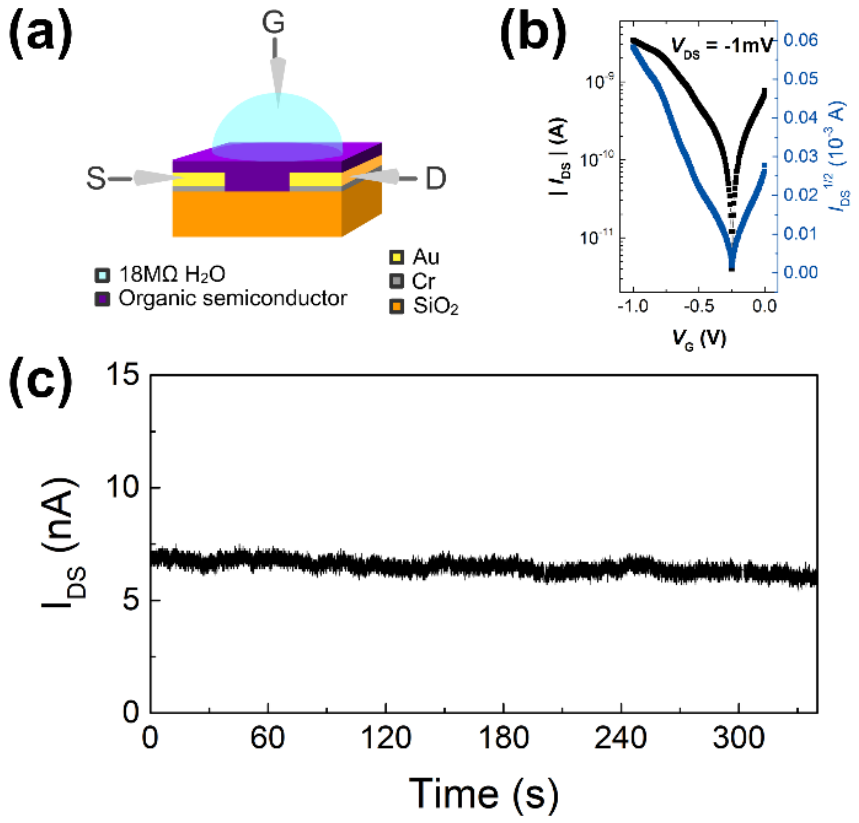

Figure 3.11. (a) Schematic device structure of a WGOFET with a 20 µL 18 MΩ DI water droplet sitting on top of the active later as gate dielectric. (b) WGOFET p-type transfer Characteristic of **PIDG-BT-C20**. (c) Current versus time graph of **PIDG-BT-C20** WGOFET operated at V_{DS} = -1 mV and V_G = -1 V for 340 seconds.

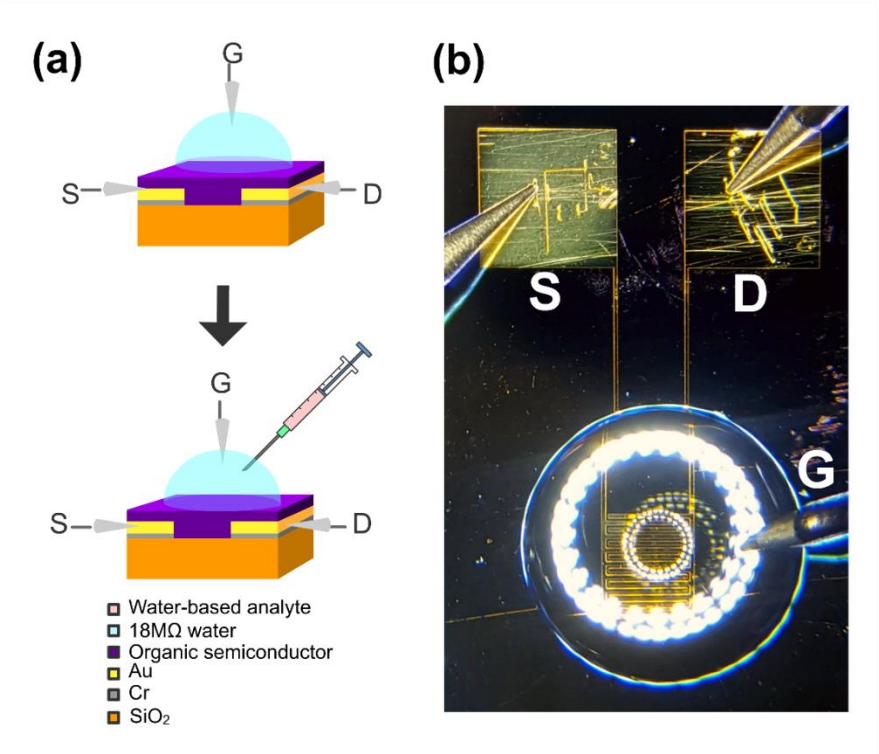

Figure 3.12. (a) Schematic diagram of analyte injection for a WGOFET sensor; (b) top view of a WGOFET sensor with interdigitated source (S) and drain (D) electrodes together with a gate (G) electrode contacting the water-dielectric droplet.

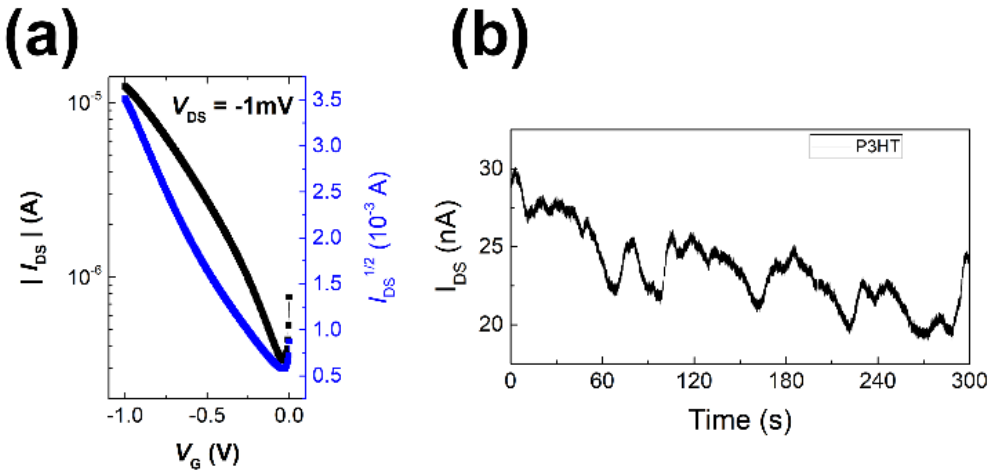

Figure 3.13. (a) Transfer characteristic of P3HT WGOFET without analyte; (b) the current vs time graph of P3HT based WGOFET showing a severe fluctuation.

To study the sensitivity and selectivity of of the **PIDG-BT-C20** WGOFET devices towards F^- over other halide ions (Cl^-, Br^-, and I^-), a series of aqueous solutions of various sodium halides (NaF, NaCl, NaBr, and NaI) with different concentrations were used as analytes. As shown in Figure 3.14a, the device with 20 µL DI water as the dielectric was first operated at V_{DS} = -1 mV and V_G = -1 V. After 60 s, 5 µL of DI water or sodium halide aqueous solution was injected into the water-gate dielectric. Injection of DI water did not cause any change in the drain current, while all halide solutions caused an immediate current drop. The device exhibited the largest current drop when the NaF solution was injected, indicating the highest sensitivity of the device towards the F^- ions. The device also showed a good baseline recovery, which is possibly due to the weak interactions of the halide and the indigoid moiety on the polymer backbone. Such phenomenon will be further discussed in the sensing mechanism section. The differences in drain current before and after halide ion introduction were used to calculate the relative response (S) of the device according to the following Equation 3.1:

$$S = \frac{|I_0 - I_{analyte}|}{|I_0|} \times 100\% \qquad \textbf{(Equation 3.1)}$$

where I_0 is the I_{DS} of the baseline and I_{analye} is the I_{DS} after analyte introduction.

The relative responses for 24 mM NaF, NaCl, NaBr, and NaI solutions were 89%, 53%, 35%, and 32% (Figure 3.14b), indicating the excellent selectivity of this device towards the F^- ions over other halides.

Figure 3.14c shows the current changes $|\Delta I|$ ($|\Delta I| = |I_0 - I_{analyte}|$) with varying halide concentration. A response saturation in the higher concentration range was observed. This is possibly because of the sensor-analyte association-dissociation kinetics had reached an equilibrium state,[257] and is a typical observation for chemical sensors.[258–261] Figure 3.14d shows the linear regression of |ΔI| vs. [NaF] in the NaF range of 0 – 2.4 mM. The slope and coefficient of determination (R^2) of the calibration curve was found to be 2.29 and 0.92, respectively. The limit of detection (LOD) was calculated using Equation 3.2:[262]

$$\mathrm{LOD} = \frac{3.3\sigma}{m} \qquad \textbf{(Equation 3.2)}$$

where, σ is the relative standard deviation of the sensitivity plot of the device in the absence of analyte and m is the slope of the analyte calibration curve. The LOD for fluoride (NaF) was found to be 0.40 mM for the **PIDG-BT-C20** WGOFET device, which is better than the LOD (0.7 mM) of the previously reported OFET-based fluoride ion sensors.[234]

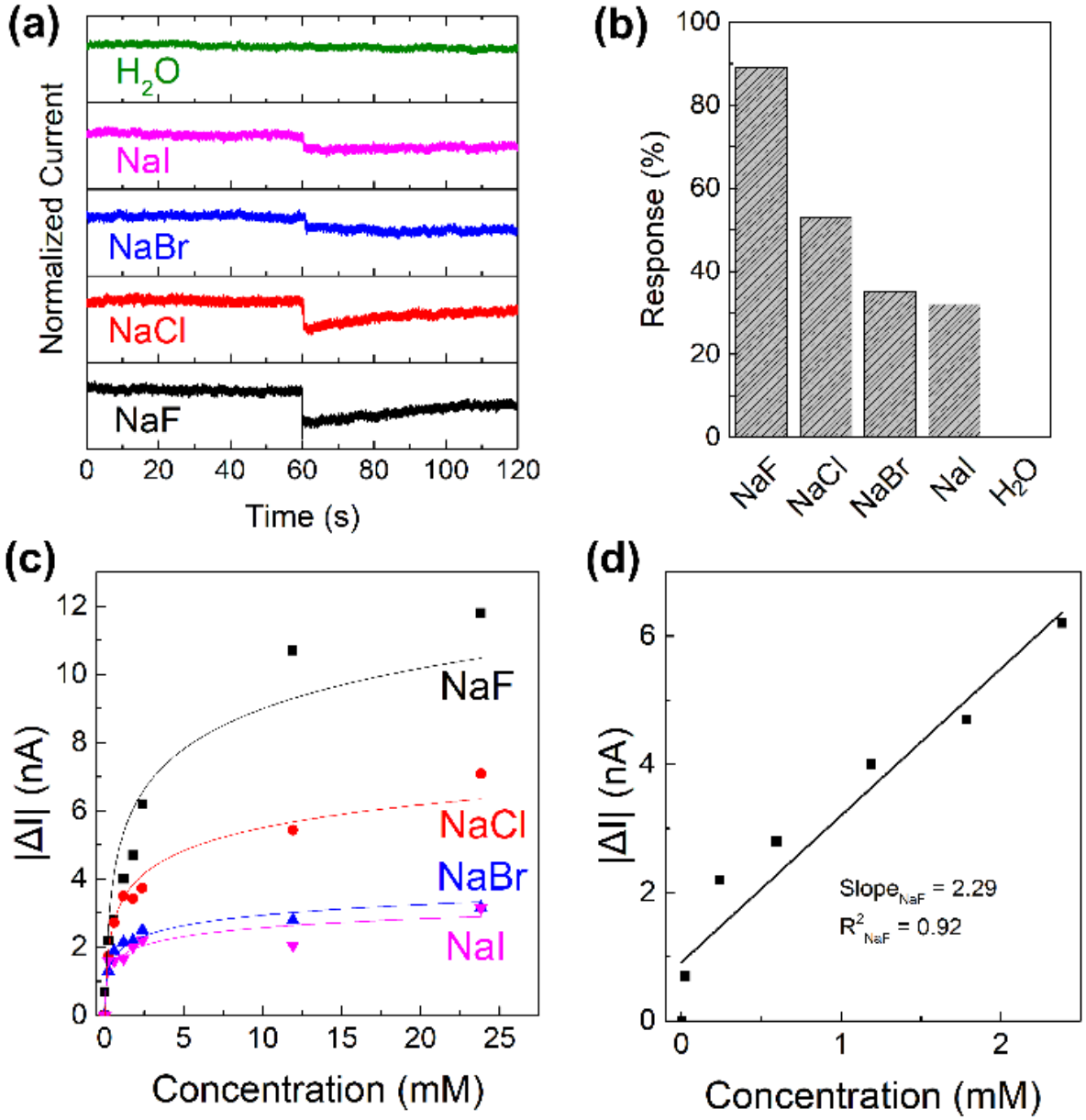

Figure 3.14. (a) Current versus time graph of sodium halide sensing experiment where 5 µL of 24 mM analyte (NaF, NaCl, NaBr, NaI or pure water) was injected into the water-gate droplet at around time = 60s; (b) Histogram showing the relative response of the selectivity of 24 mM halide ion sensing of the **PIDG-BT-C20** WGOFET sensor; (c) Current change versus concentration of analyte graph of sodium halides; (d) Linear region of current change versus concentration of NaF and a best-fitted calibration curve of NaF.

3.2.6. Study of Halide Ion Sensing Mechanism of Polymers

As previously mentioned, the design principle for these indigo-based polymers is to utilize the intramolecular hydrogen bonding of indigo amide N–H···O=C to recognize the fluoride ions. Since fluorine has the highest electronegativity among all elements, the N–H···F^- interaction is expected to be the strongest among all halides. The interaction of the amide hydrogen bonds on **PIDG-BT-C20** with fluoride ions may be similar to that of some previously reported host-guest supramolecular fluoride chemosensors using amide receptors.[263–266] ^{1}H NMR titration[265–267] was adopted as an effective method to verify the N–H···F^- interactions. Using the small molecule **IDG-C20-Br** as the model compound since the ^{1}H NMR signals of polymer **PIDG-BT-C20** were very broad and weak. ^{1}H NMR titration was performed using tetrabutylammonium fluoride (TBAF) in $CDCl_3$. It was observed that the amide proton peak H_a at 9.01 ppm broadened when the ratio of TBAF/**IDG-C20-Br** was increased from 0 to 0.3 molar equiv and disappeared at a 0.5 equiv (Figure 3.15), indicating the strong interaction of H_a with F^-.[268,269] On the other hand, addition of same amounts of tetrabutylammonium chloride (TBAC), bromide (TBAB), or iodide (TBAI) did not result in any observable changes in the H_a signal (Figure 3.16, 3.17 & 3.18).

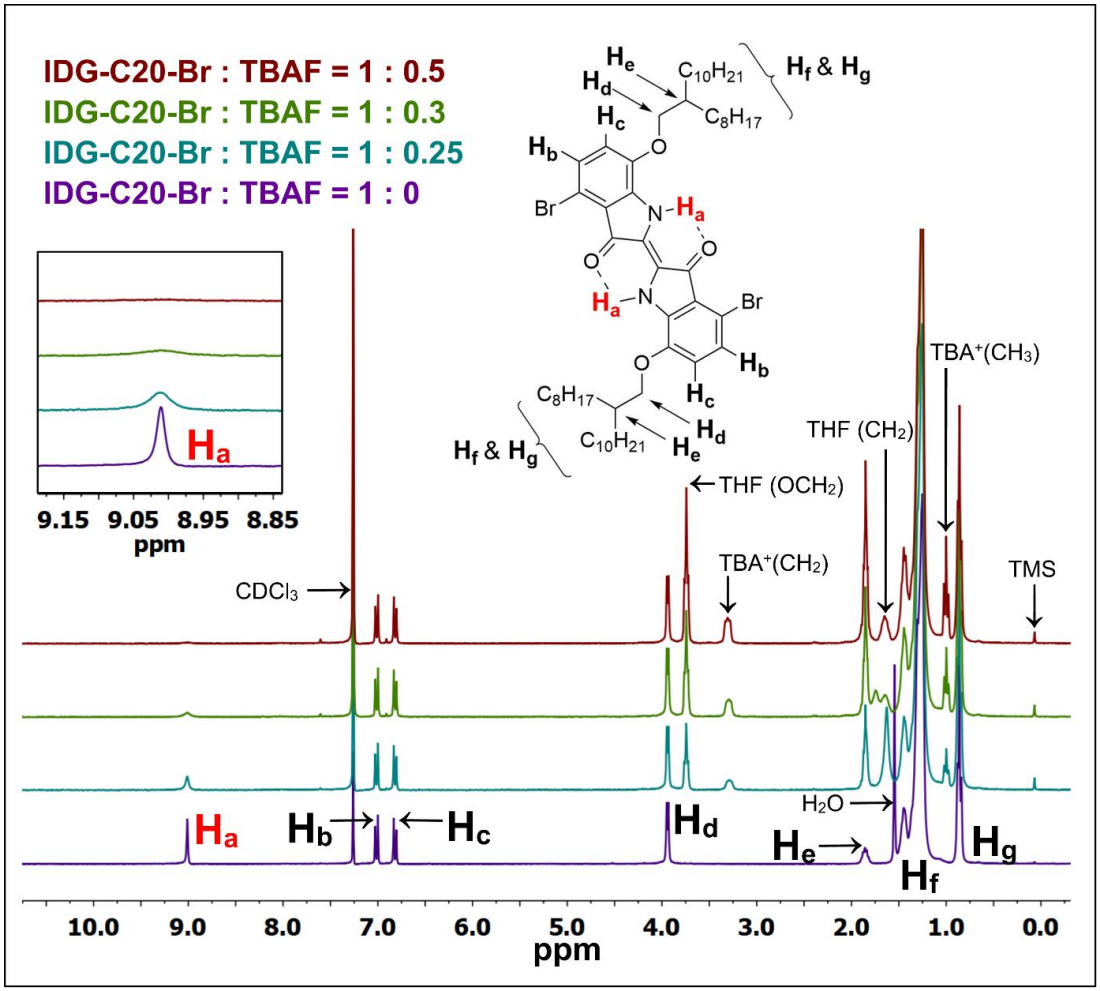

Figure 3.15. [1]HNMR titration of **IDG-C20-Br** with TBAF (0 – 0.5 equiv) in CDCl3

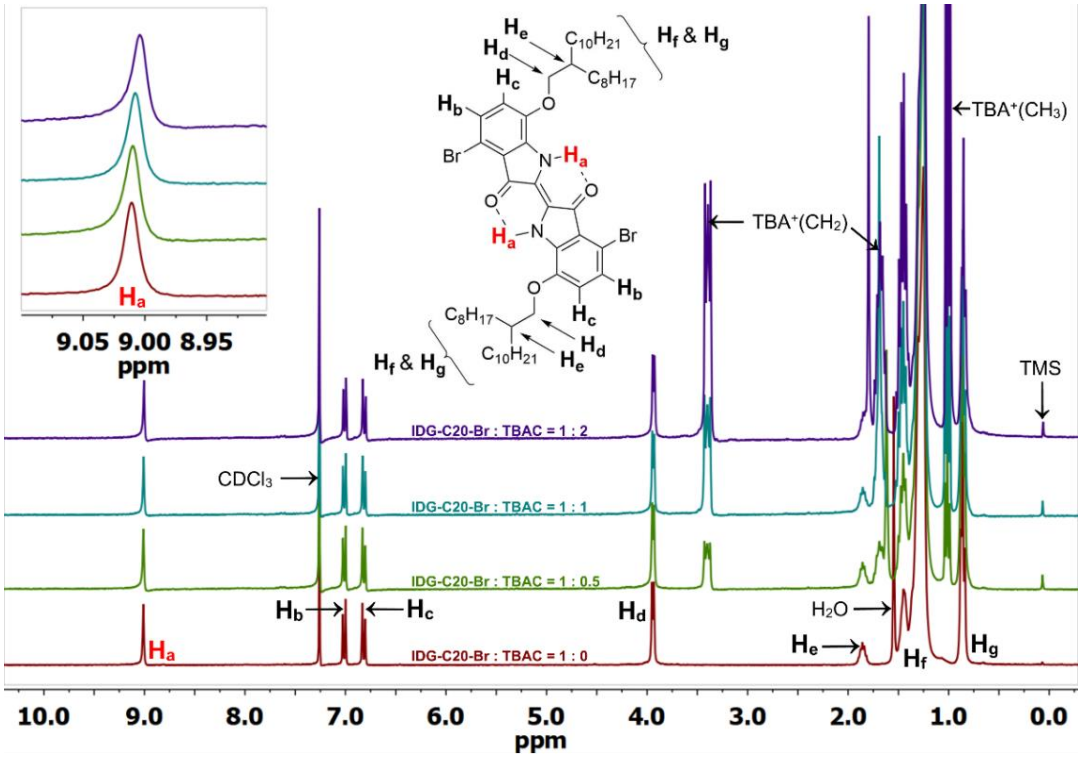

Figure 3.16. 300 MHz ^{1}H NMR titration of **IDG-C20-Br** with TBAC (0 – 2 equiv) in $CDCl_3$.

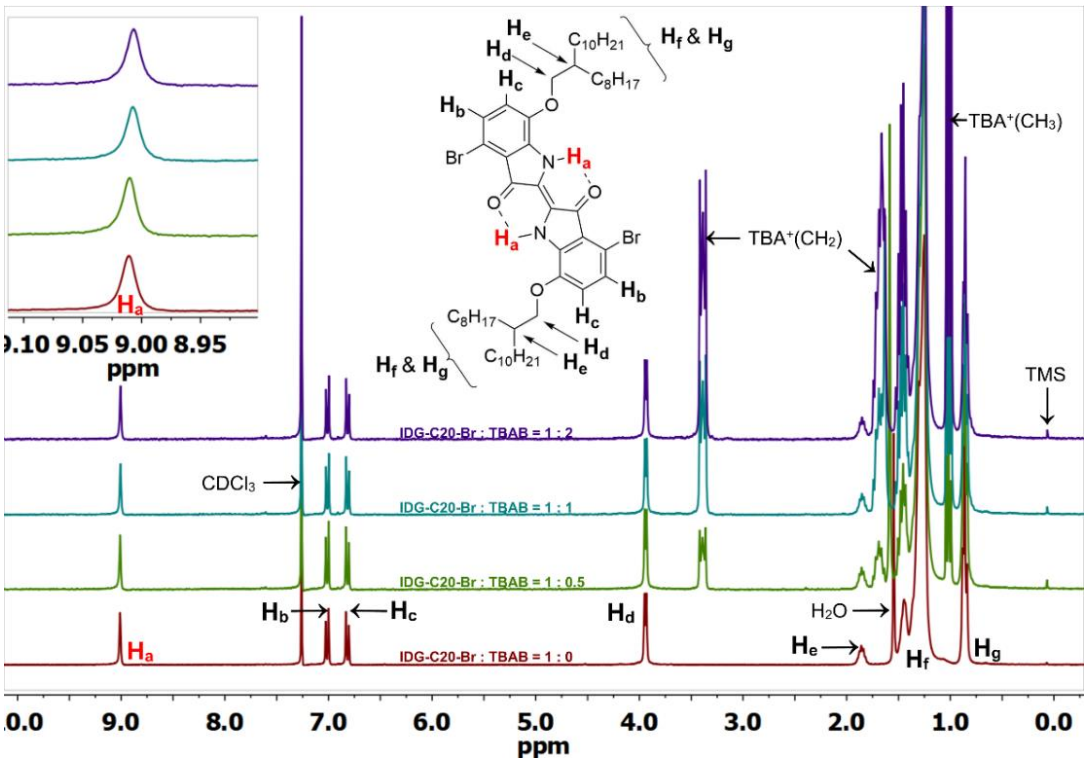

Figure 3.17. 300 MHz ^{1}H NMR titration of **IDG-C20-Br** with TBAB (0 – 2 equiv) in $CDCl_3$.

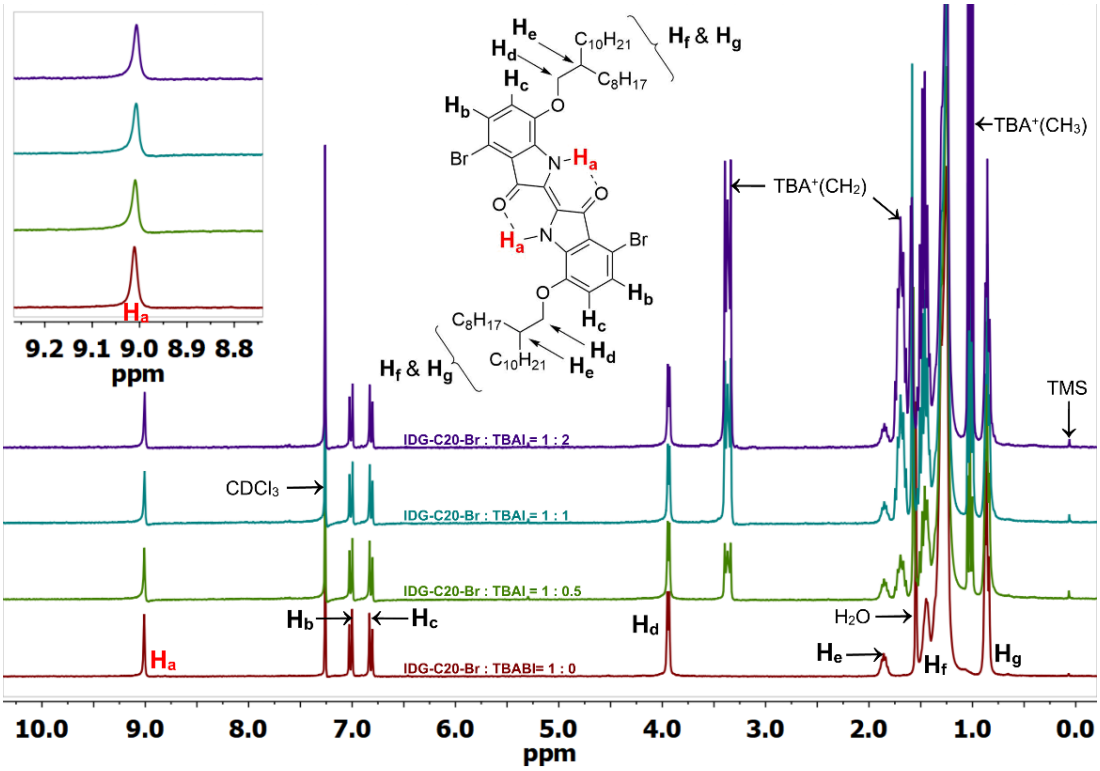

Figure 3.18. 300 MHz ^{1}H NMR titration of **IDG-C20-Br** with TBAI (0 – 2 equiv) in $CDCl_3$.

Thin film UV-Vis spectroscopy was used to further demonstrate the interaction of fluoride ions with the indigo chromophore by measuring the films of **PIDG-BT-C20** or **IDG-C20-Br** blended with 0-3 molar equivalents of TBAF. The peaks representing the π–π* transition at λ_{max} = 713 nm for **PIDG-BT-C20** and 656 nm for **IDG-C20-Br** weakened gradually and a new long wavelength absorption band at λ_{max} = 894 and 862 nm started to appear and intensified with the increasing amount of TBAF from 0 to 3 equivalents (Figure 3.19a and 3.19c). No changes in the absorption spectra were observed when TBAC, TBAB, and TBAI were blended into the **PIDG-BT-C20** and **IDG-C20-Br** films, suggesting the much weaker interactions of Cl^-, Br^-, and I^- with **PIDG-BT-C20** and **IDG-C20-Br**. The significant current decreases observed for WGOFETs as fluoride ions were introduced could be a result of the disruption of hydrogen-bonds in the indigo moiety by fluoride ions (vide supra). Interestingly, it was found that when the **PIDG-BT-C20**/TBAF and **IDG-C20-Br**/TBAF blended film samples were dissolved back into chloroform, the spectra of the obtained

solutions became identical to those of pristine **PIDG-BT-C20** or **IDG-C20-Br** (Figure 3.19b and 3.19d). This observation indicates that the fluoride-indigo interaction was interrupted in solution due to the solvation of fluoride ions and indigo moieties by the large amounts of solvent molecules.

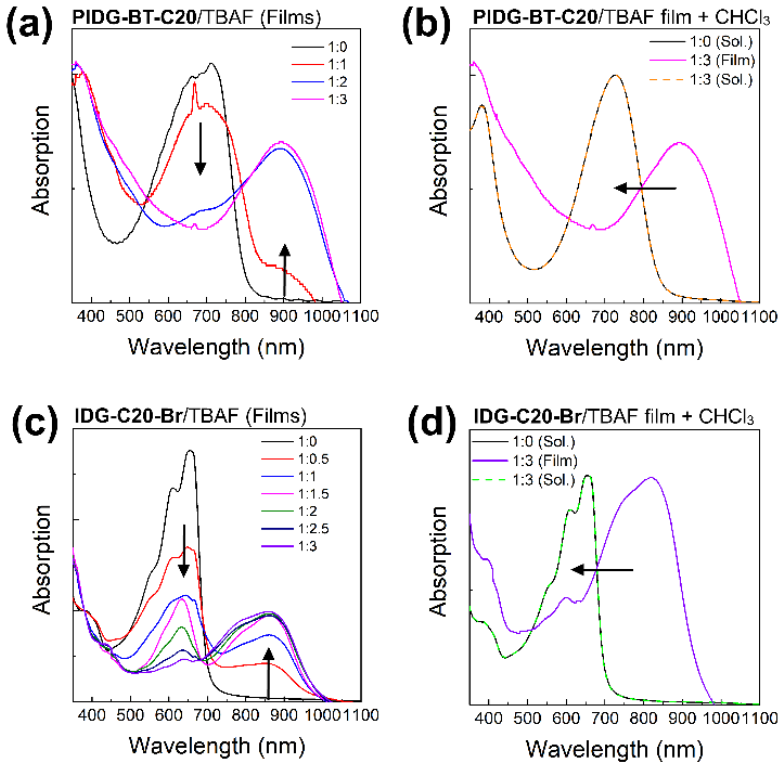

Figure 3.19. (a) and (c) Absorption spectral changes of thin films samples of **PIDG-BT-C20** and **IDG-C20-Br** upon addition of different TBAF molar ratios (0 – 3 equivalent). (b) and (d) Normalized pristine **PIDG-BT-C20** and **IDG-C20-Br** solutions in chloroform (black solid line) and the reversible absorption spectral change (dotted lines) by dissolving the thin film sample of **PIDG-BT-C20** or **IDG-C20-Br : TBAF** = 1 : 3 back into chloroform solutions.

Furthermore, computer simulations of the interaction between the indigo moiety and halide anions were conducted using density functional theory (DFT) with the B3LYP/3-21G* level under tight convergence. The overall charge was set to be -1 and a singlet spin state was used as the initialization parameters for DFT calculations for the model complexes, **IDG-F**, **IDG-Cl**, **IDG-Br** and **IDG-I**. The neutral indigo model compound **IDG** was also simulated as a reference (Figure 3.20a).

The simulation results show that **IDG** has an interatomic distance of 1.02 Å for the $H_a\cdots N$ bond. When a fluoride anion was added, the formed complex **IDG-F** has an increased $H_a\cdots N$ distance of 1.66 Å, while the distance between H_a and F^-, $[H_a\cdots F]$, is very short at 1.00 Å, indicating the formation of a new hydrogen-bond (Figure 3.20b). On the other hand, the amide N-H interatomic distance on the opposite side of indigo was not affected by the fluoride anion ($[H_a'\cdots N'] = 1.02$ Å). For other IDG-halide complexes simulated, the $H_a\cdots N$ distances were only slightly affected ($[H_a\cdots N] = 1.06$ Å for **IDG-Cl**, 1.07 Å for **IDG-Br**, and 1.04 Å for **IDG-I**). Detailed simulation summary can be found in Table 3.3.

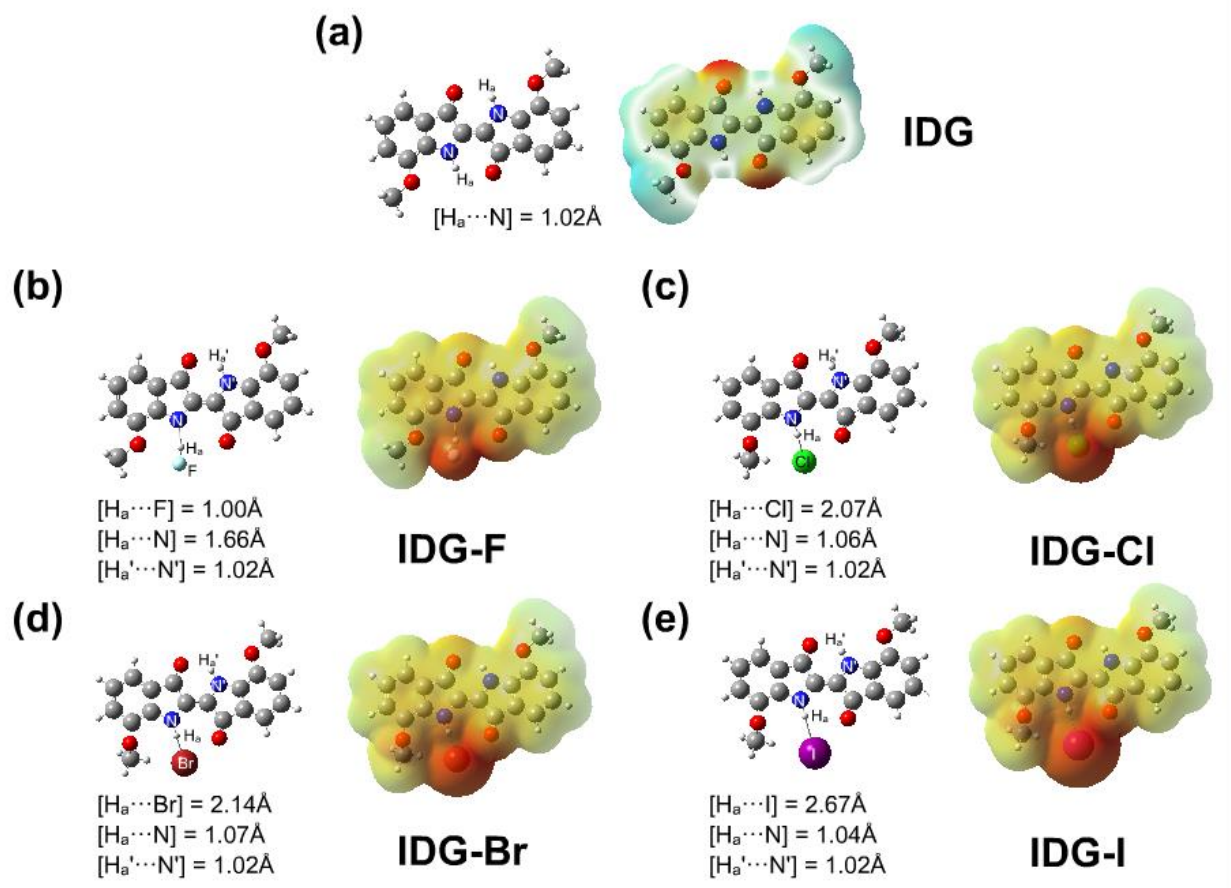

Figure 3.20. DFT calculations results of (a) indigo model compound IDG and indigo-halide model compounds (b) **IDG-F**; (c) **IDG-Cl**; (d) **IDG-Br** and (e) **IDG-I** at the B3LYP/3-21G* level of theory.

Table 3.3. DFT calculation results of model compounds.

Models	Interatomic Distances (Å)			Charge	Spin
	$[H_a \cdots X]$	$[H_a \cdots N]$	$[H_a' \cdots N']$		
IDG	---	1.02	---	0	doublet
IDG-F	1.00	1.66	1.02	-1	singlet
IDG-Cl	2.07	1.06	1.02	-1	singlet
IDG-Br	2.14	1.07	1.02	-1	singlet
IDG-I	2.67	1.04	1.02	-1	singlet

To further demonstrate the importance of the intramolecular amide hydrogen bonding in **PIDG-BT-C20** for the observed high sensing selectivity towards fluoride ions, a known DPP-based D-A polymer semiconductor, PDQT-C20,[245,270] which contains amide moieties (with alkyl substituents at nitrogen atoms), but no N-H groups and intramolecular hydrogen bonds, was used as a channel in a WGOFET for halide ion sensing. It was found that the device showed the relative responses in the order of $F^- < Cl^- < Br^- < I^-$ (Figure 3.21), which is opposite to that of the **PIDG-BT-C20** devices. These results strongly indicate the critical roles of the N-H groups and intramolecular hydrogen bonding in **PIDG-BT-C20** played in the observed high sensitivity and selectivity towards fluoride ions for this polymer.

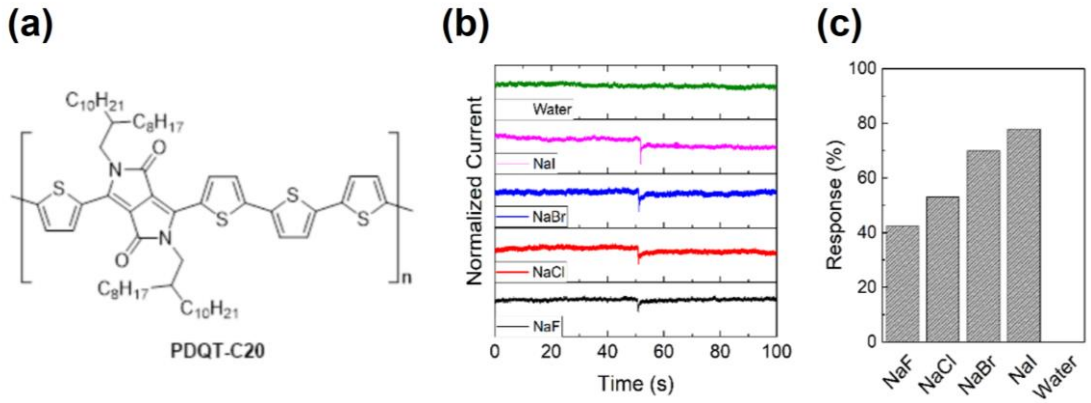

Figure 3.21. (a) Chemical structure of PDQT-C20; (b) current versus time graph (V_{DS} = -1 V and V_G = -1 mV) of sodium halide sensing experiment where 2.4 mM of 5µL analyte (NaF, NaCl, NaBr, NaI) was injected into the water-gate droplet on a **PDQT-C20** WGOFET device at around time = 50s; (c) histogram showing the response of PDQT-C20 towards different sodium halides at 2.4 mM (NaF = 42%, NaCl = 53%, NaBr = 70% and NaI = 78%).

3.3. Conclusion

In this work, two indigo-based donor-acceptor polymers **PIDG-T-C20** and **PIDG-BT-C20**, where the indigo building block has intramolecular hydrogen bonds, were designed and synthesized for use as channel semiconductors in OFETs for fluoride ion sensing. The charge transport performance of **PIDG-T-C20** and **PIDG-BT-C20** was evaluated in BGBC OFETs, demonstrating highest hole mobilities of up to 0.016 and 0.028 $cm^2V^{-1}s^{-1}$, respectively, which are highest values reported for indigo-based polymers. A water-gated organic field-effect transistor was fabricated using **PIDG-BT-C20**, which exhibited excellent stability at ambient conditions. When a small aliquot of aqueous NaF, NaCl, NaBr, or NaI analyte solution was introduced, the device demonstrated the highest sensitivity towards fluoride with the relative response of 89% for NaF, 53% for NaCl, 35% for NaBr, and 32% for NaI at an analyte concentration of 24 mM. The limit of detection (LOD) for NaF was calculated to be 0.40 mM, which is better than the previously reported OFET based fluoride sensors. The mechanism of fluoride selectivity of the WGOFET sensor was studied through ^{1}H NMR, UV-Vis and computer simulations, which indicated the much stronger interaction of fluoride with the intramolecular hydrogen bond N–H···O=C in the indigo unit of the polymer compared with other halides. The disruptive effect of fluoride

on the hydrogen bond would alter the electronic structure and thus the charge transport properties of the polymer, leading to the high sensitivity of the device towards fluoride. Our results demonstrated that the intramolecular hydrogen bond-containing indigo polymers are a promising class of the semiconductors for OFET based fluoride sensors, which showed good field-effect transistor performance, excellent stability at ambient conditions, and high sensitivity and selectivity towards fluoride ions. They have the potential to be printed on flexible plastic substrate as a low-cost, portable alternative or replacement to other types of fluoride sensors.

Chapter 4: Diketopyrrolopyrrole-based Polymer as Active Layer in Chemiresistive Sensors for Volatile Liquid Sensing[2]

4.1. Introduction

The previous chapter reported the use of an indigo-based D-A polymer with intrinsic hydrogen-bonds to achieve good environmental stability and high sensitivity towards halide ions. Installation of hydrogen-bonds in D-A polymers is believed to be an beneficial approach to enhance the stability and performance of other organic-based sensors. Such tactic then led to the design of a new DPP-based polymer with specially designed cleavable side-chains, which can be thermally removed to give a hydrogen-bonds crossed-linked polymer thin film that may have excellent chemical resistance and high selectivity for organic liquid sensing.

This chapter focuses on a new donor-acceptor (D-A) conjugated polymer, poly[bis(2-ethylhexyl) 3-(3",4'-bis(dodecyloxy)-[2,2':5',2"-terthiophen]-5-yl)-1,4-dioxo-6-(thiophen-2-yl)pyrrolo[3,4-c]pyrrole-2,5(1H,4H)-dicarboxylate] (**PDEB**), comprising an electron-accepting carbamate side-chain bearing thiophene-flanked diketopyrrolopyrrole (**DPPTh**), and an electron-donating 3,3'-bis(dodecyloxy)-2,2'-bithiophene (**C12-BTO**) was synthesized. The carbamate side-chains of this soluble precursor polymer can be thermally removed at a moderate temperature, forming an insoluble polymer **PDNB** with high solvent resistance. **PDNB** has a high HOMO energy level of -4.68 eV and a narrow band gap of 1.05 eV, which makes it dopable by HCl to form a stable conductive polymer **PDNB:HCl** with moderate conductivity of 0.24 S cm^{-1}. A chemiresistive sensor based on **PDNB:HCl** can distinguish ten common volatile organic liquids with unique current-time profiles under a low operation voltage of 1 V. Importantly, a single sensor can be used many times and remain functional over a long period of time in air, indicating its extraordinary operational and environmental stability. The results demonstrate that **PDNB** is a promising material for reusable chemiresistive sensors.

π-Conjugated polymers as either conductors or semiconductors have been extensively studied in the past few decades for applications such as logic circuits, sensors, photovoltaics, anti-corrosion,

[2] This chapter is a slightly modified version of an accepted manuscript published by Wiley in Advanced Electronic Materials on 25th January 2021, available online: https://doi.org/10.1002/aelm.202000935 . **Jenner H. L. Ngai**, Xiguang Gao, Pankaj Kumar, John Polena, Yuning Li, "*A Highly Stable Diketopyrrolopyrrole (DPP) Polymer for Chemiresistive Sensors*" The content has been reproduced here with the permission of the copyright holder.

and electrocatalysis.[271–277] Compared to their inorganic counterparts such as silicon,[18,278] conjugated polymer materials can be processed using cost effective techniques such as screen printing, gravure printing, and ink-jetting at milder temperatures, which enables the manufacturing of optoelectronic products at ultralow costs, with high throughputs, and on flexible plastic substrates. In addition, there are a large number of structural variations for polymer materials, which greatly facilitates the realization of new functionalities of the materials and devices, enabling better or new products. Products based on conjugated polymers with these appealing features can complement and replace some existing products that are based on inorganic materials and open up new applications that are unattainable with inorganic materials. In particular, research into polymer based chemical sensors has intensified in recent years largely as a concomitant of the escalating demands for ubiquitous sensor devices for the Internet of Things (IoTs), smart food packaging, point-of-care devices, etc. Polymer-based chemical sensors have demonstrated promising sensitivity and selectivity towards a variety of chemical analytes such as volatile organic compounds (VOCs), H^+, biological compounds, and metal ions.[4–8] Sensing in liquid analytes is very important since a lot of health and safety-related analytes such as biological substances, ions, ingredients in food and beverages are in liquid solutions.

A chemiresistive sensor is a very simple device, which comprises a chemiresisor channel and two electrodes on a substrate, where the resistance of the chemiresisor responds when it is in contact with a chemical analyte. Conductive polymers such as the renowned poly(3,4-ethylenedioxythiophene) doped with polystyrene sulfonate (PEDOT:PSS) has been used as the channel materials for low power driven chemiresistor-based sensors.[151,152,154] However, the dopant PSS in PEDOT is soluble in water and polar solvents, which causes device degradation when the PEDOT:PSS layer in the sensor is in contact with the analyte solution in water or other polar solvents for a long time. Other conductive polymers such as polyacetylene, polythiophene, polypyrrole, and polyaniline were also reported to act as the active materials in gas, thermal, and biological chemiresistive sensors.[169,279–281] However, most of these polymers were fabricated into a sensing film by electrochemical deposition rather than solution processing due to their poor solubility, which is not suitable for high throughput manufacturing. Furthermore, these doped polymers show poor stability in terms of conductivity in air, which is caused by de-doping, whereas the polymer chains and dopant molecules segregate.[18] Another issue associated with conductive polymer based chemiresistive sensors is that the response of sensors weakens and the

signal drifts away from its original baseline after repeated exposure to analytes, which causes damages to the channel polymer.[8,282,283] Therefore, there is a demand for polymer chemiresistors that can offer improved environmental and operational stability to chemiresistive sensors.

In this work, we designed and synthesized a new polymer **PDEB** that can be processed into chemiresistive sensors with greatly enhanced stability. Specifically, **PDEB** is a donor-acceptor (D-A) polymer with a repeat unit consisting of an electron-accepting diketopyrrolopyrrole (DPP) building block and an electron-donating alkoxy bearing 3,3'-bis(dodecyloxy)-2,2'-bithiophene (**C12-BTO**) building block. The primary reason for choosing DPP is because of its outstanding thermal, light and ambient stability. For example, the famous DPP-based cyclic amide pigment "Ferrari Red" is extremely environmentally stable and has been widely used as a colorant in automotive industry. Equally important is that DPP has been a widely used building block for many polymers that have demonstrated outstanding optoelectronic properties in organic field-effect transistors (OFETs), organic photovoltaics (OPVs), organic light-emitting diodes (OLEDs), etc.[77,90,284–288] The electron-donating **C12-BTO** unit coupled with the strong electron-accepting DPP unit in the repeat unit would enable intramolecular charge transfer, which is anticipated to result in a narrow band gap and a high-lying HOMO (highest occupied molecular orbital) energy level of the polymer. These characteristics would help the polymer form an environmentally stable p-doped state. To render the polymer highly solvent resistant, thermally labile carbamate side-chains were introduced to the DPP units in **PDEB**, which could be conveniently removed under rather mild conditions to afford the insoluble polymer **PDNB** through a post-deposition thermal treatment. The chemiresistive sensors based on the doped **PDNB** films have demonstrated remarkable mechanical robustness towards various polar and non-polar solvents, excellent air stability, as well as high sensitivity and selectivity to numerous organic liquid analytes.

4.2. Results and Discussion

4.2.1. Synthesis of Polymers

The synthesis of **PDEB** and **PDNB** were carried out following the steps outlined in Scheme 4.1. Briefly, a carbamation reaction was carried out on 3,6-di(thiophen-2-yl)-2,5-dihydropyrrolo[3,4-c]pyrrole-1,4-dione (**DPPTh**) with 2-ethylhexyl chloroformate under a basic condition to give bis(2-ethylhexyl)1,4-dioxo-3,6-di(thiophen-2-yl)pyrrolo[3,4-c]pyrrole-2,5(1H,4H)-dicarboxylate (**DPPTh-EHC**). Bromination was then performed using *N*-bromosuccinimide (NBS) to afford bis(2-ethylhexyl)3,6-bis(5-bromothiophen-2-yl)-1,4-dioxopyrrolo[3,4-c]pyrrole-2,5(1H,4H)-dicarboxylate (**Br-DPPTh-EHC**) as the acceptor monomer. The donor monomer, (3,3'-bis(dodecyloxy)-[2,2'-bithiophene]-5,5'-diyl)bis(trimethylstannane) (**C12-BTO-TMT**), was synthesized following a previously reported procedure.[272,289] Stille coupling polymerization was then carried out between **C12-BTO-TMT** and **Br-DPPTh-EHC** to afford the D-A polymer poly[bis(2-ethylhexyl)3-(3",4'-bis(dodecyloxy)-[2,2':5',2"-terthiophen]-5-yl)-1,4-dioxo-6-(thiophen-2-yl)pyrrolo[3,4-c]pyrrole-2,5(1H,4H)-dicarboxylate] (**PDEB**). A weight average molecular weight (M_w) of 834,910 and a dispersity ($Đ$) of 34.4 were determined for this polymer by using HT-GPC at 140 °C with 1,2,4-trichlorobenzene (TCB) as eluent (Table 4.1). The very large dispersity is considered due to the partial chain aggregation in solution even at 140 °C, resulting from the strong interchain donor-acceptor interaction. This is evidenced by the GPC diagram that showed a bimodal distribution with the first peak representing the polymer aggregates (Figure 4.1). Similar phenomena were observed for an analogous polymer **PDQT** and some other DPP-based polymers.[245,290,291] Detailed materials characterizations and synthesis procedures can be found in Appendix A and Appendix B.

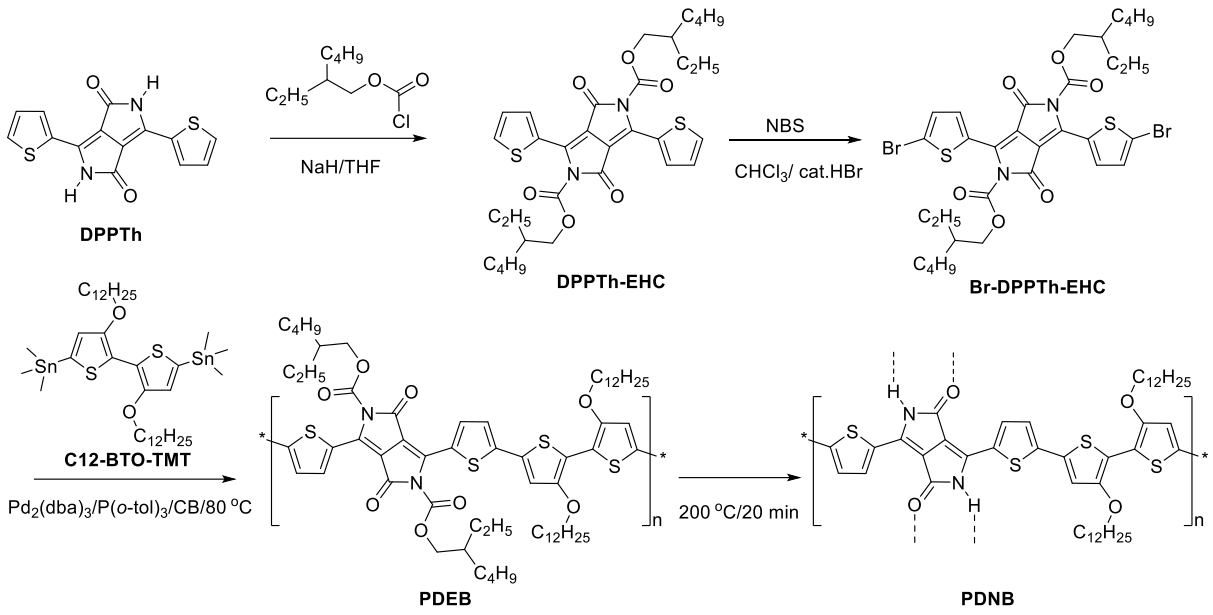

Scheme 4.1. Synthesis of polymers **PDEB** and **PDNB.**

Table 4.1. Molecular weight information of **PDEB**.

PDEB	M_w	M_n	*Đ*
Peak I + II	834,910	24,213	34.4
Peak I	1,759,320	513,071	3.42
Peak II	28,229	13,033	2.17

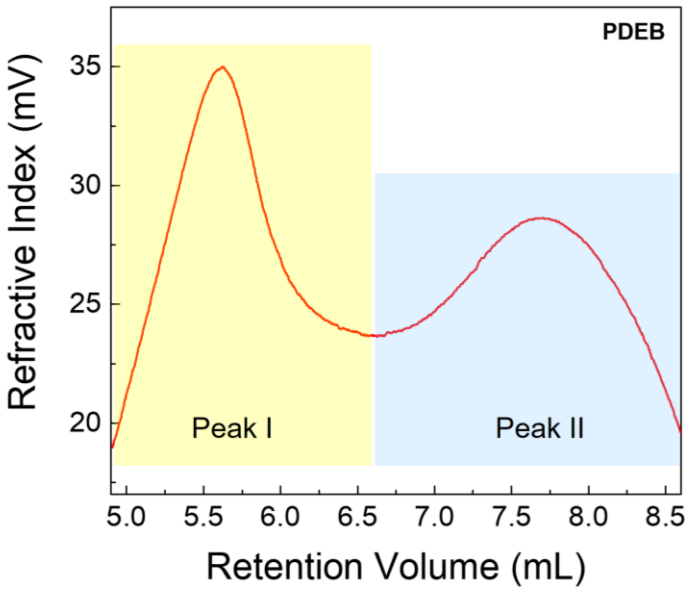

Figure 4.1. GPC chromatogram of **PDEB** measured at 140 °C.

4.2.2. Thermal Removal of Carbamate Side-chains

Alkyl carbamates with *tert*-butyloxycarbonyl (*t*-BOC) as the best example are known for their thermolability, which form carbon dioxide and olefins or alcohols after thermal decomposition under mild temperatures as low as 150 ^{o}C, and have been used as thermally removable side-chains for polymers.[292–294] As stated previously, the purpose of using the carbamate side-chains on **PDEB** is to thermally remove these labile side-chains to form a robust, solvent resistant polymer film for the fabrication of robust liquid chemiresistive sensors.[295,296]

Thermogravimetric analysis (TGA) was used to investigate the thermolability property of the carbamate side-chains on **PDEB**. The polymer was heated in air at a heating rate of 10 ^{o}C min^{-1} from 25 ^{o}C, and held at 200 ^{o}C for 20 min, then heated at 10 ^{o}C min^{-1} until 600 ^{o}C. As shown in Figure 1a, the weight loss at 200 ^{o}C during the 20-min holding time was 3.7%, which is much lower than the anticipated weight loss of 27.3% if all the 2-ethylhexyl carbamate side-chains were removed from the sample. FTIR measurements (to be discussed later) confirmed that this weight loss is attributed to the release of carbon dioxide (CO_2) from the thermal decomposition occurred at the DPP-carbamate junction through hydrolysis,[297–299] while other decomposition by-products such as 2-ethylhexanol from the carbamate side-chains might be trapped in the polymer sample. In fact, the zoomed inset image in Figure 4.2a shows that partial decomposition of carbamate side chains might have started at ca. 100 °C. Since the molecular weight of **PDEB** was measured at 140°C, some of the carbamate side chains might be removed, which would reduce the solubility of the polymer and result in the very large dispersity.

Based on the theoretical weight loss of 4.5% due to the release of CO_2 for a complete decomposition, about 82% of the 2-ethylhexyl carbamate side-chains decomposed when heated at 200 °C for 20 min. As the temperature was further elevated, a more dramatic weight loss stage started at ca. 250 ^{o}C and ended at ca. 340 °C, resulting in a total weight loss of 31%, which agrees with the calculated weight loss of 27.3% assuming that the carbamate side-chains in **PDEB** were fully removed from the sample. The results also suggested that the dodecyloxy side-chains remained almost intact below 340 °C. Beyond this temperature, further degradation continued until ~600 °C when the polymer was completely decomposed.

FTIR spectroscopy was used to further verify the removal of carbamate side-chains and the liberation of the secondary amide groups (-C(=O)NH) on the DPP units by measuring a **PDEB**

film coated on a KBr disc before and after thermal annealing at 200°C for 20 min in air. As can be clearly seen in Figure 4.2b, the absorption bands ν_b = 1694 cm^{-1}, ν_c = 1402 cm^{-1}, ν_d = 1179 cm^{-1}, and ν_e = 1098 cm^{-1}, which can be assigned to the C=O stretching, C-N stretching, C-O stretching and C-N bending of the carbamate groups,[300] respectively, weakened significantly after thermal annealing, indicating that carbamate groups decomposed. The lower frequency of the C=O stretching on the carbamate group (ν_b = 1694 cm^{-1}) than that of the C=O stretching on the DPP core (ν_a = 1742 cm^{-1}) could be caused by the bulky ethyl hexyl side chain, and the possible sulfur-oxygen chalcogen bond interaction, that lowered the oscillation strength of this stretching frequency. For a quantitative analysis, the absorption peak at ν_a = 1742 cm^{-1} that originates from the stretching of DPP's C=O bonds was used as a reference peak since it would remain intact during the annealing process. Accordingly, a 79% decrease in the integral of the carbamate C=O stretching peak at ν_b = 1694 cm^{-1} after annealing was calculated, which indicates that the majority of the carbamate side-chains decomposed under the selected annealing conditions. The degree of decomposition of the carbamate groups determined by FTIR agrees well with that (82%) obtained by the TGA data. In addition, a small absorption peak at ν_e = 3068 cm^{-1} appeared after annealing, which can be assigned to the stretching associated with the secondary amide N-H bond.[243,301] It is noticed that the peaks originated from the C-H stretching at 2800-3000 cm^{-1} almost remain unchanged, which suggests that the by-products from 2-ethylhexyl moieties from the decomposition of the carbamate side-chains were trapped inside the film, which corroborates the TGA data as discussed previously.

Based on the above TGA and FTIR results, the annealing conditions of 200 °C for 20 min in air were chosen to cleave the majority of the carbamate side-chains in the polymer thin film and prevent the polymer backbone from oxidation that may occur at higher temperatures. Since the purpose of removing the carbamate side-chains is to make the resultant polymer insoluble in solvents, the solubility of the annealed polymer sample was evaluated. Specifically, a **PDEB** solution in chlorobenzene was spin coated onto a glass substrate, which was annealed under the above conditions to decompose the carbamate side-chains. The resultant polymer film **PDNB** was soaked in various solvents. It was found that the obtained **PDNB** film is insoluble in all solvents tested, polar or nonpolar (see discussion on the UV-vis data), demonstrating its excellent solvent resistance. The insolubility of **PDNB** is attributed to the loss of most solubilizing carbamate side-chains (ca. 80%) as well as the possible formation of an extensive network through hydrogen-

bonds between the secondary amide groups at the DPP units of the neighboring polymer chains.[61,302]

It was expected that the resulting **PDNB** comprising secondary amide groups would be more hydrophilic than **PDEB**. Water contact angles of a **PEDB** film were measured before and after the thermal removal of side-chains. The **PDEB** film had a water contact angle of $\theta = 87°$. After thermal annealing, the contact angle of the resultant **PDNB** film reduced to $\theta = 69°$ (Figure 4.3), indicating an increase in hydrophilicity of the film. The increased hydrophilicity for **PDNB** would be a desirable property for sensing polar analytes.

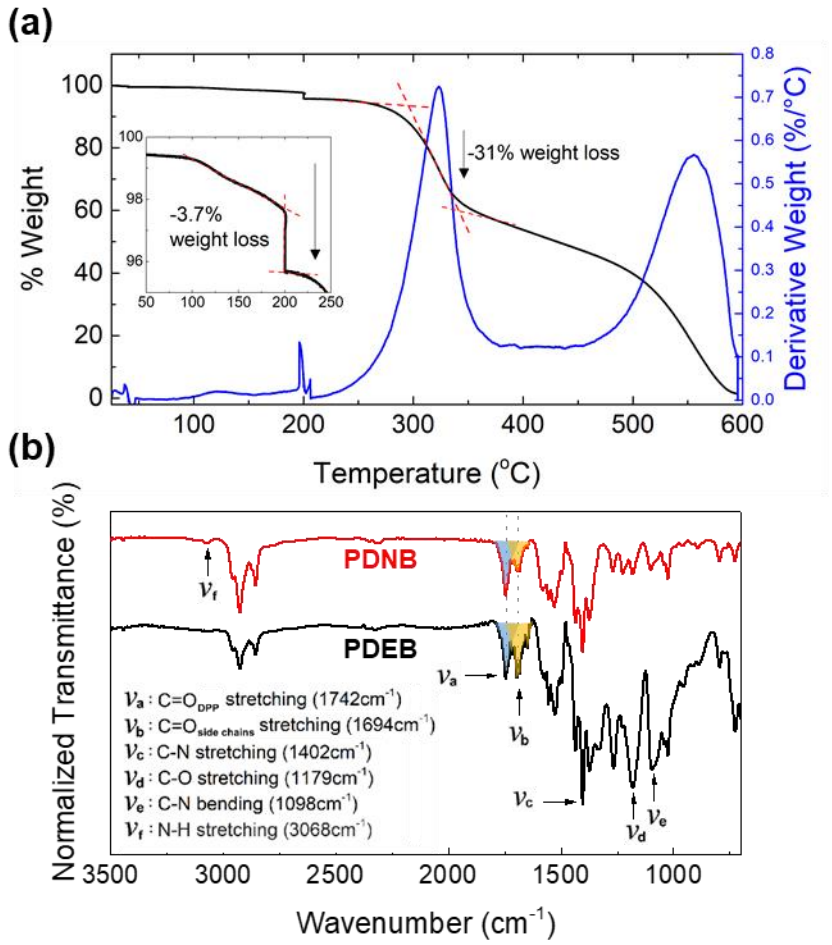

Figure 4.2. (a) TGA diagram showing the transition of **PDEB** to **PDNB** by thermal removal of carbamate side-chains on the polymer. (b) FTIR spectra of **PDEB** and **PDNB** (obtained by heating **PDEB** at 200 °C for 20 min in air), whereas the spectra are normalized using the DPP's C=O stretching (ν_a) frequency and blue and orange shaded areas represent the integrals of DPP and carbamate C=O stretching frequencies, which are used for quantitative analysis of side-chains content on **PDNB**.

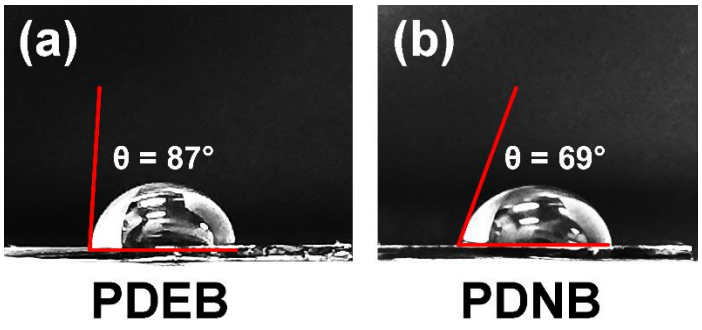

Figure 4.3. Photograph showing the water contact angle of(a) **PDEB** film & (b) **PDNB** film.

4.2.3. Optical and Electrochemical Properties of Polymers

Ultraviolet-Visible-Near-Infrared (UV-Vis-NIR) spectroscopy was used to study the absorption properties of **PDEB** and **PDNB**. As shown in Figure 4.4a and Table 4.2, a **PDEB** solution in chloroform exhibited a dramatic red-shifted absorption profile (λ_{max} = 926 nm) compared to the monomer **Br-DPPTh-EHC** (λ_{max} = 506 nm). This originates from the much more extended π-conjugation of the polymer backbone than that of the DPP monomer as well as the strong intramolecular charge transfer effect between the donor **C12-BTO** and acceptor DPP units. The UV-Vis-NIR spectrum of the **PDEB** thin film exhibited a large blue shift (60 nm) in λ_{max} compared to its solution. This is possibly due to the strong intermolecular donor-donor (D-D) and acceptor-acceptor (A-A) packing in the solid state, leading to the formation of H-aggregates.[303–305] The optical band gap of the polymer film calculated from the onset absorption wavelength was found to be 0.94 eV. When the carbamate side-chains on **PDEB** were removed by annealing at 200 °C for 20 min in air, the resultant **PDNB** exhibited a slightly red-shifted λ_{max} at 871 nm, but a shorter onset absorption wavelength at 1181 nm, corresponding to a slightly enlarged bandgap of 1.05 eV. Nonetheless, the results indicate that **PDNB** remained highly conjugated after the removal of carbamate side-chains.

The solvent resistance of the **PDNB** film was evaluated by treating the polymer film with some common polar (methanol and acetone) and non-polar (toluene, chlorobenzene, and chloroform) solvents. Specifically, a 40-60 nm **PDNB** thin film on a glass substrate was soaked in a solvent in a covered petri dish for 10 min. The sample was taken out, dried, and subjected to the UV-Vis-NIR measurement. For all solvents tested, the film showed a superimposed absorption profile compared to the untreated film (Figure 4.5), indicating that the **PDNB** film has superior solvent resistance without dissolution or delamination from the substrate, which is very desirable for sensing various organic liquids.

Cyclic voltammetry (CV) measurements of **PDEB** and **PDNB** films were carried out using transparent conductive ITO glass as the substrate (Figure 4.4b). **PDEB** exhibited a reversible oxidation process within the potential range from -1.40 V to +1.40 V. The onset oxidation potential is ca. 0.00 V vs. Ag/AgCl, which corresponds to a HOMO energy level of -4.80 V using ferrocene as the standard, which has a HOMO energy value of -4.80 eV.[306] The **PDNB** sample showed a much different oxidation loop, in which both the oxidation and the charge release processes were

retarded. The HOMO energy level of **PDNB** was calculated to be -4.68 eV, which is slightly higher than that of its parent polymer **PDEB** (-4.80 eV). The lowest unoccupied molecular orbital (LUMO) energy levels were calculated using the HOMO energy levels and optical bandgaps to be -3.84 eV for **PDEB** and -3.63 eV for **PDBN**.

The rather high HOMO energy levels observed for both **PDEB** and **PDBN** films (-4.80 and -4.68 eV) could be attributed to the strong electron donating effect of the **C12-BTO** units in the polymer backbone. In addition, the energy levels of an analogous polymer **PDQT**[245,270,307] having a non-substituted bithiophene donor building block was also measured. Figure 4.4c shows the comparison of frontier energy levels of **PDQT**, **PDEB** and **PDNB**. It is believed that the electron rich **C12-BTO** units in **PDEB** and **PDNB** increase the HOMO energy levels, which is the main factor in reducing their band gaps. The high HOMO energy level and narrow band gap would make **PDNB** easily doped by p-type dopants to become a stable conductive polymer for use in chemiresistor-type sensors.

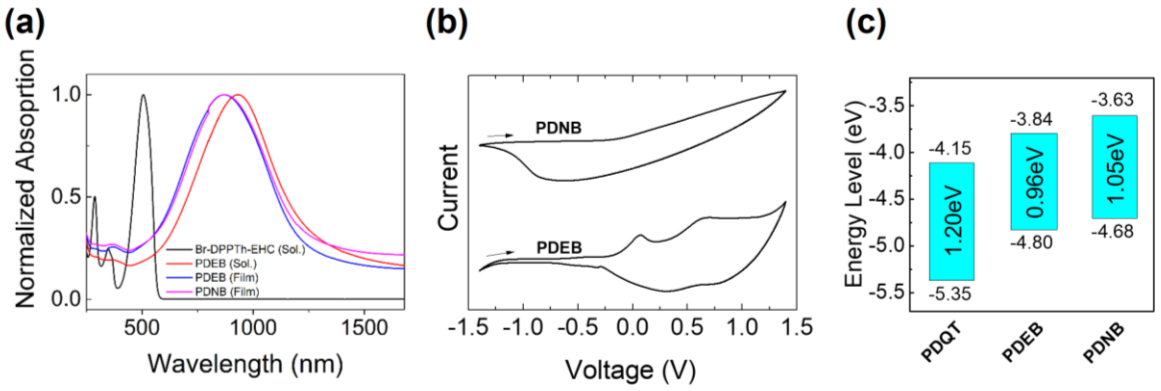

Figure 4.4. (a) Normalized UV-Vis-NIR spectra of **Br-DPPTh-EHC**, **PDEB** and **PDNB** in chloroform solutions and thin films. (b) Cyclic voltammogram of **PDEB** and **PDNB** using Ag/AgCl as the reference electrode, indium-tin oxide (ITO) on glass as the working electrode and platinum disk as the reference electrode. The measurement was carried out in a 0.1 M tetrabutylammonium hexafluorophosphate solution in anhydrous acetonitrile at a scan rate of 50 mV s^{-1}. (c) Energy levels and band gaps of the polymers calculated from CV and UV-Vis-NIR data.

Table 4.2. Optical and electrochemical properties of **PDEB** and **PDNB**.

	λ_{max} [nm]		λ_{onset} [nm]		$HOMO_{CV}$ [eV]	$LUMO_{opt/CV}$ [eV]	$E_{g,opt}$ [eV]
	sol.	film	sol.	film	film	film	film
PDEB	926	866	1392	1319	-4.80	-3.84	0.94
PDNB	---	871	---	1181	-4.68	-3.63	1.05

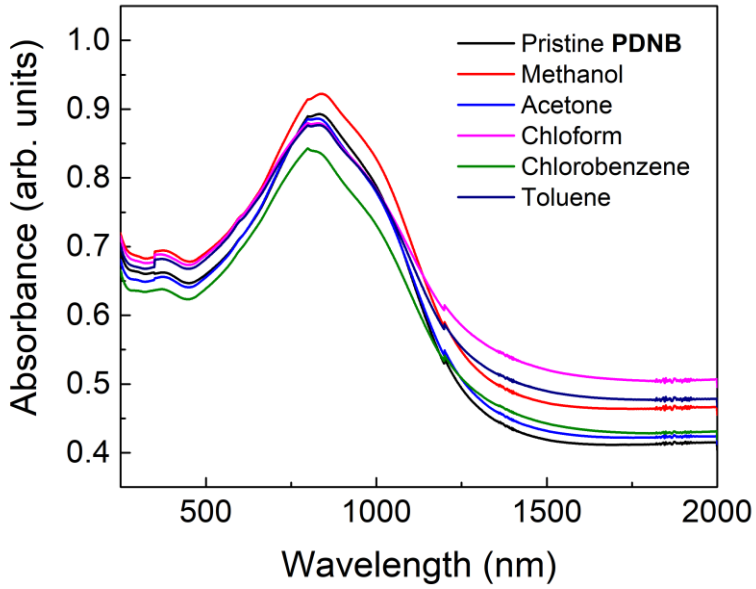

Figure 4.5. UV-Vis-NIR absorption profiles of the pristine **PDNB** film and the solvent-treated **PDNB** films.

4.2.4. Doping of PDNB

Six common p-type dopants including iodine (I_2, sublimation method), *p*-toluenesulfonic acid (*p*-TSA, 5N), acetic acid (AcOH, 5N), sulfuric acid (H_2SO_4, 5N), hydrobromic acid (HBr, 5N) and hydrochloric acid (HCl, 5N)[308–317] were used to dope **PDNB**. Figure 4.6a shows a schematic diagram of the device for conductivity measurement using an interdigitated two-electrode resistor. A silicon wafer substrate with a 300 nm thermally grown SiO_2 top layer was pre-patterned by conventional lithography and thermal evaporation, which has a pair of interdigitated gold electrodes having a channel length (L) of 30 μm and a total channel width (W) of 15.8 mm with a

W/L ratio of 527. A **PDEB** film was first deposited on the substrate by spin coating a **PDEB** solution in chlorobenzene, followed by thermal annealing at 200 °C for 20 min in air to form the **PDNB** film (~30 nm thick). Then the device was swept by changing the bias from -1 to +1 V to obtain an *I-V* curve. Subsequently, the **PDNB** film was doped with a dopant and the *I-V* curve of the device was collected again. Based on the *I-V* curves (Figure 4.6b), the conductivities of the **PDNB** film with different dopants were calculated, which follow the order of I_2 (5.64 S cm^{-1}) > HCl (0.24 S cm^{-1}) > *p*TSA (0.01 S cm^{-1}) > HBr (6.56×10^{-3} S cm^{-1}) > H_2SO_4 (2.16×10^{-4} S cm^{-1}) ≈ AcOH (1.83×10^{-4} S cm^{-1}) (Figure 4.6c). For doped samples **PDNB:H_2SO_4** and **PDNB:AcOH**, their conductivities are close to that of the pristine **PDNB** (2.79×10^{-4} S cm^{-1}), indicating that H_2SO_4 (5N or at other concentrations including 98% H_2SO_4) and AcOH are not good dopants for **PDNB**. The high polarity and large size of H_2SO_4 and low acidity of AcOH might be accounted for the poor doping capabilities of these two dopants to **PDNB**. Accordingly, these two dopants were excluded for the subsequent stability study of the doped **PDNB** films.

As shown in Figure 4.6d, the conductivity of **PDNB:I_2** dropped to the level of the pristine **PDNB** within 3 days (subset of Figure 4.6d). The fast conductivity decay was probably caused by the volatile nature of I_2, which is a common observation for the I_2-doped polymers.[318–320] **PDNB:pTSA** and **PDNB:HBr** are much more stable, but their conductivities started to decay rapidly after 2-3 months. On the other hand, **PDNB:HCl** exhibited the best stability, maintaining a conductivity at ~10^{-2} S cm^{-1} even after 9 months of prolonged exposure to the ambient air.

It was found that all the polymer films with decayed conductivity could be re-doped by HCl to reach a conductivity level comparable to that of a freshly prepared **PDNB:HCl** film. This is a strong evidence that **PDNB** itself did not degrade and the decay of conductivity of the doped polymer films is simply due to a gradual loss (evaporation) of dopant molecules over time. The fact that **PDNB:HCl** showed the best stability might be due to the smaller dopant counter ions Cl^- that can be deeply and tightly embedded between polymer chains.

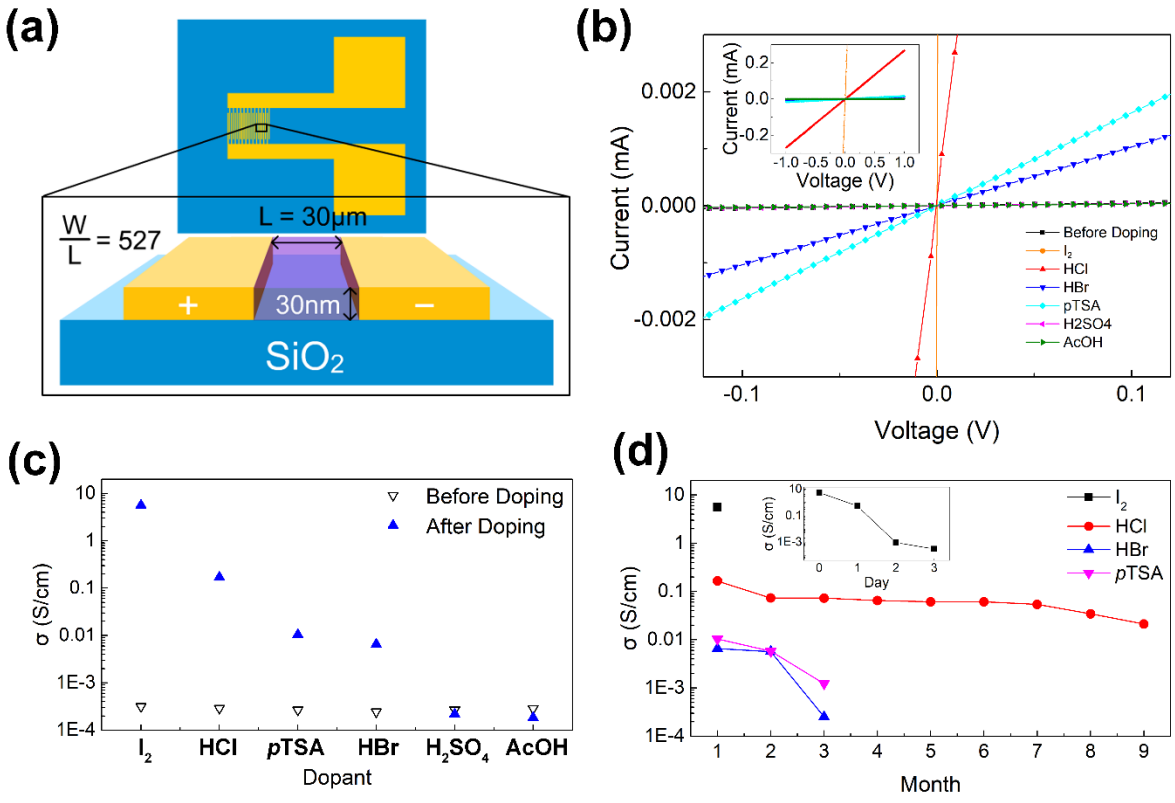

Figure 4.6. (a) Schematic diagram of the conductivity measurement set-up. (b) *I-V* characteristics showing the resistor behavior of **PDNB** before and after doping by different dopants (subset image showing the full scanning range from -1.0 to 1.0 V). (c) Conductivities of the **PDNB** films before and after doping with different dopants. (d) Conductivity-time curves of **PDNB** films doped with different dopants (the subset shows the conductivity decay of **PDNB:I2** within 3 days). Samples were stored in ambient at 25°C and 65% relative humidity.

4.2.5. Microstructures of Polymer Thin Films

Atomic force microscopy (AFM) was used to study the morphology of **PDEB**, **PDNB**, and **PDNB:HCl** thin films (Figure 4.7a-c). The as-spun **PDEB** polymer on an SiO_2/Si substrate showed a smooth surface with a root mean square roughness (R_q) of 0.75 nm. After thermal removal of carbamate side-chains, the surface of the resultant **PDNB** film showed a decrease in roughness to R_q = 0.58 nm and appearance of small pores (Figure 4.7b). Figure 4c shows the AFM image of the **PDNB:HCl** film that has an increased roughness of R_q = 1.84 nm and the disappearance of the small pores possibly as a result of incorporating the HCl dopant molecules.

The crystallinity of the polymer thin films was studied by using X-ray diffractometry (XRD). In the reflection mode (Figure 4.7d), a very weak diffraction peak at $2\theta = 3.96^{o}$ is observed for the as-spun **PDEB** film, indicating the rather disordered chain packing in this sample. This peak can be assigned to the (100) plane, representing an interlamellar distance of 22.3 Å of the polymer crystal structure. Upon annealing at 50, 100, and 150 ^{o}C, the polymer film remained poorly crystalline although the film annealed at 150 ^{o}C showed a slightly intensified (100) peak. When **PDEB** was annealed at 200 ^{o}C, the diffraction angle increased notably to 4.23^{o}, corresponding to a shrinkage of the interchain d-spacing to 20.9 Å. This abrupt change manifests the thermal removal of most of the carbamate side-chains on the polymer to form **PDNB** as discussed earlier. It is also noticed that the (100) peak intensity increased sharply, indicating the formation of a more ordered chain packing. Both the detachment of the sterically bulky side-chains from the polymer backbone to allow for chain motion and the formation of hydrogen-bonds between polymer chains might aid the re-organization of polymer chains into a more ordered structure. The slight red shift of the film UV-Vis-NIR absorption from **PDEB** to **PDNB** (from 866 nm to 871 nm) is another evidence for the improved chain packing after removal of the carbamate side-chains. Once **PDNB** was doped with HCl, the (100) peak of the resulting **PDNB:HCl** film shifted slightly to $2\theta = 4.15°$ (Figure 4.7d), which corresponds to a *d*-spacing of 21.3 Å, a slight increase compared to the undoped **PDNB** due to the accommodation of HCl molecules in the film.

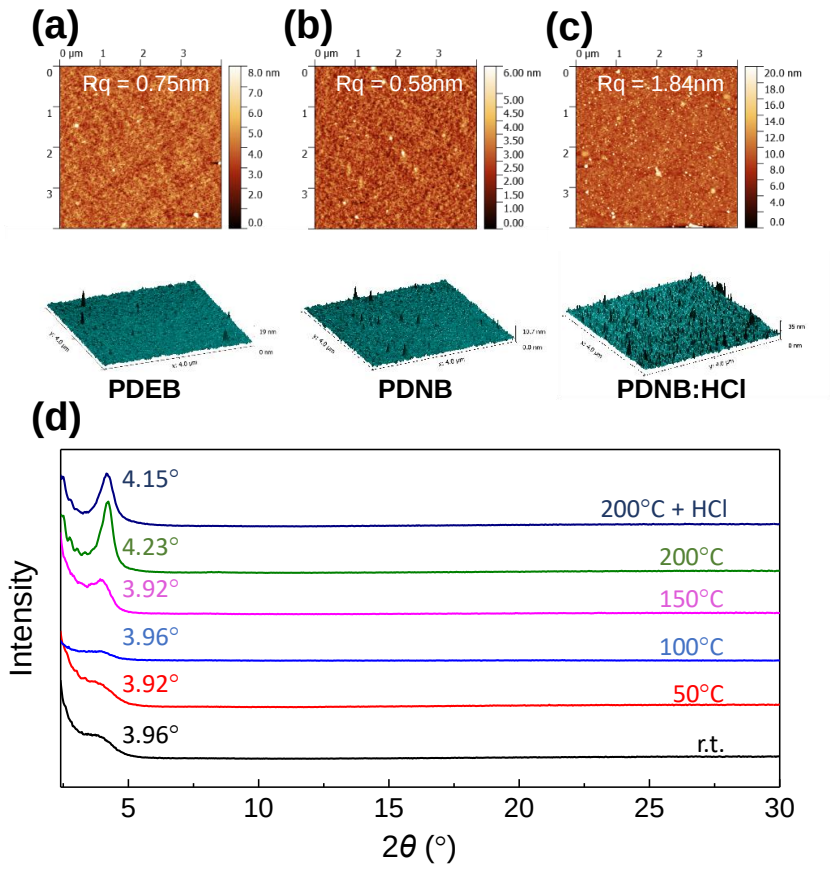

Figure 4.7. Two-dimensional (2D) and three-dimensional (3D) AFM surface morphology of (a) **PDEB**, (b) **PDNB** and (c) **PDNB**:**HCl** films on SiO_2/Si substrates and XRD spectra (d) of the films of **PDEB** annealed for 20 min at different temperature in air, **PDBN**, and **PDNB:HCl** films on SiO_2/Si substrates.

The XRD patterns acquired in the reflection mode only exhibited the (100) peak of the lamellar crystal structure, indicating that the polymer chains in the film adopted an edge-on orientation.[250–252] To reveal the in-plane π-π stacking distance, free-standing film samples were measured using the transmission mode XRD. As shown in Figure 4.8a, **PDEB** exhibited a strong diffraction peak at 3.78°, which can be assigned to the (100) planes as described previously, while the broad peak at 19.5° with a *d*-spacing of 4.55 Å might be the amorphous halo from the disordered phase. A peak appeared at 25.3°, which can be assigned to the (010) planes originated from the main chain π-π stacking. A very short π-stacking distance of 3.52 Å was calculated from this peak, indicating the very strong intermolecular interaction and high coplanarity of the polymer backbone, compared to its analogous polymer **PDQT**, which has a π-stacking distance of 3.68-3.86 Å.[50] When the

carbamate side-chains were removed, the (100) peak of the resultant **PDNB** is significantly weakened, while the (010) peak becomes sharper. The more dramatically different intensities of the (100) peak in the in-plane and out-of-plane modes for **PDNB** suggest that the polymer chains are more dominantly oriented in the edge-on motif compared to the **PDEB** film. The doped sample **PDNB:HCl** showed very similar diffraction patterns (Figure 4.8b & 4.8c) as **PDNB**, indicating that the chain packing, particularly the π-π stacking, was negligibly influenced by HCl doping.

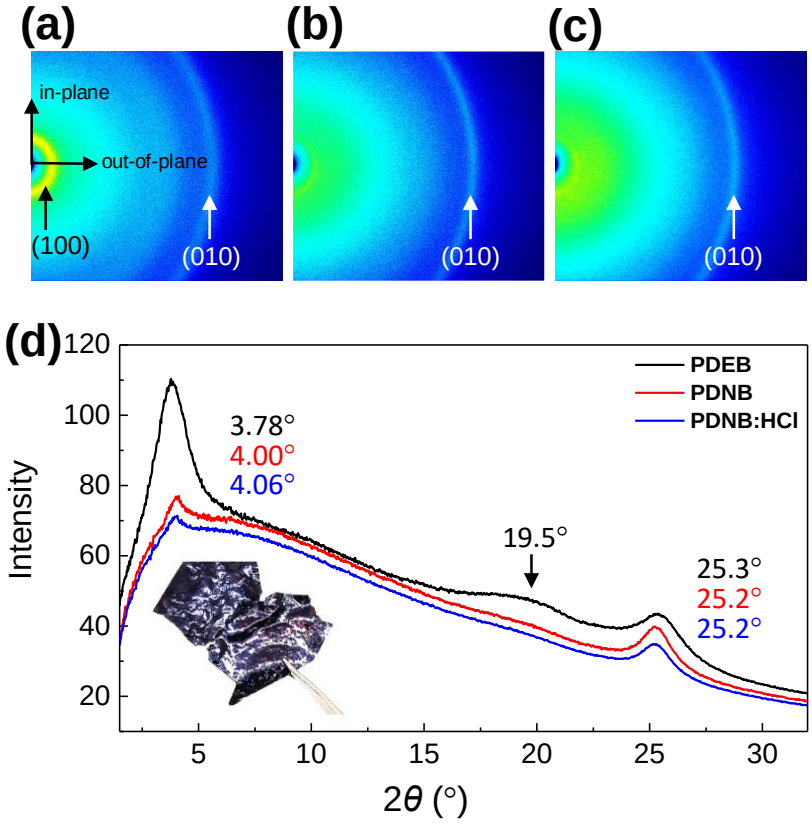

Figure 4.8. 2D transmission mode XRD spectra of flake samples of (a) **PDEB** (as-spun), (b) **PDNB** and (c) **PDNB:HCl**, as well as their integrated one-dimensional (1D) XRD spectra (d) (insert image shows the actual appearance of the **PDEB** polymer film).

4.2.6. Chemiresistive Sensors based on PDNB:HCl

PDNB:HCl was used as a channel chemiresistor for a simple low power driven, two-electrode chemiresistor-type sensor for detecting volatile organic liquids because of its appropriate conductivity, excellent stability in air, good solvent resistance and long shelf life. The structure of the sensor and the testing procedure are illustrated in Figure 4.9a, while the top view of the actual sensor is shown in Figure 4.9b. Under an electrical bias of 1 V, an organic liquid (5.0 μL) was introduced with a micropipette onto the surface of the **PDNB:HCl** film at the channel, while the current signal was recorded as a function of time until the baseline recovered to obtain an *I-t* profile for the given liquid. The sensor was then used for the next testing cycle with the same or a different liquid. As shown in Figure 4.9c, all ten common volatile organic liquids tested showed different signature profiles, which can be easily distinguished visually. More importantly, the shape of the *I-t* profile for each liquid maintained the same characteristics during repeated testing (only results for three tests are shown), which functions as a "fingerprint' for each liquid.

The attainment of different *I-t* profiles for different volatile liquids may involve multiple mechanisms. First, it is known that the electrical current of a chemiresistor may change in response to the analyte that has a different chemical nature from that of the channel polymer material.[321–323] Therefore, the direction and magnitude of the current change may vary with different liquids. For example, the liquids in the first row (chloroform, hexane, diethyl ether, etc.) caused a drop in current, while the liquids in the second row (acetone, acetonitrile, methanol, etc.) resulted in an increase in current immediately after the liquid was introduced. On the other hand, the current drop observed for chloroform was much more significant (almost to zero) compared to hexane and ethyl acetate. These differences would have originated from their different interactions with the polymer (**PDNB**) and/or the dopant (HCl). For instance, the non-polar liquids, chloroform and hexane, may interact with the polymer backbone and the dodecyloxyl side-chains to alter the conformation of the polymer, which changes the π-conjugation and interchain distance, leading to a change in conductivity. The O and N containing liquids such as diethyl ether, acetonitrile, and esters may interact with the N-H bond of the secondary amide in the DPP unit. For alcohols the O-H groups may form hydrogen bonds with the O-containing moieties, the secondary amide and dodecyloxyl, in the polymer. The polar solvents such as alcohols may also interact with the dopant HCl. Second, the diffusion rate of different liquids may differ due to their different molecular size and geometry

as well as polarity, which causes changes in the rate and magnitude of the current. Furthermore, the different volatility of the liquids would influence the recovery time and the shape of the *I-t* curve. For example, diethyl ether showed a very short recovery time due to its high volatility compared to ethyl acetate that is less volatile and showed a much longer recovery time. The recovery time is also influenced by the interaction of the liquid molecules and the polymer. For example, chloroform has a slightly lower boiling point (61 °C) than that of hexane (68 °C), but the device tested with chloroform took a much longer time to recover, which might be due to the stronger interaction of chloroform molecules with the polymer. The *I-t* profiles of the liquid analytes tested were quantitatively analyzed by dividing each sensing cycle into three stages: infiltration, absorption (or diffusion), and desorption of the liquid analyte (Figure 4.10). The maximum changes in current ($\left(\frac{\Delta I}{I_o}\right)_{max}$ %) and time durations for the infiltration ($\tau_{infiltration}$), absorption ($\tau_{absorption}$), and desorption ($\tau_{desorption}$) of the analytes on the sensor are summarized in Table 4.3. The lowest $\left(\frac{\Delta I}{I_o}\right)_{max}$ % of 8.7% or the weakest response was observed for acetonitrile, while the highest $\left(\frac{\Delta I}{I_o}\right)_{max}$ % of 1230 % or the strongest response was observed for ethyl formate. For the rest liquids, the $\left(\frac{\Delta I}{I_o}\right)_{max}$ % values fall in ~20-70%. For all the organic liquid tested, it took less than 5 min to complete one sensing cycle.

It should be mentioned that one sensor could be used to test the ten organic liquids with measurements conducted hundreds of times during a period of several months. The results are highly repeatable and reproducible, demonstrating that the **PDNB:HCl** based chemiresistive sensor has remarkable solvent resistance, together with long-term storage and operational stability under ambient conditions. Detailed chemiresistive device fabrication procedures and chemical sensing procedures can be found in Appendix A.

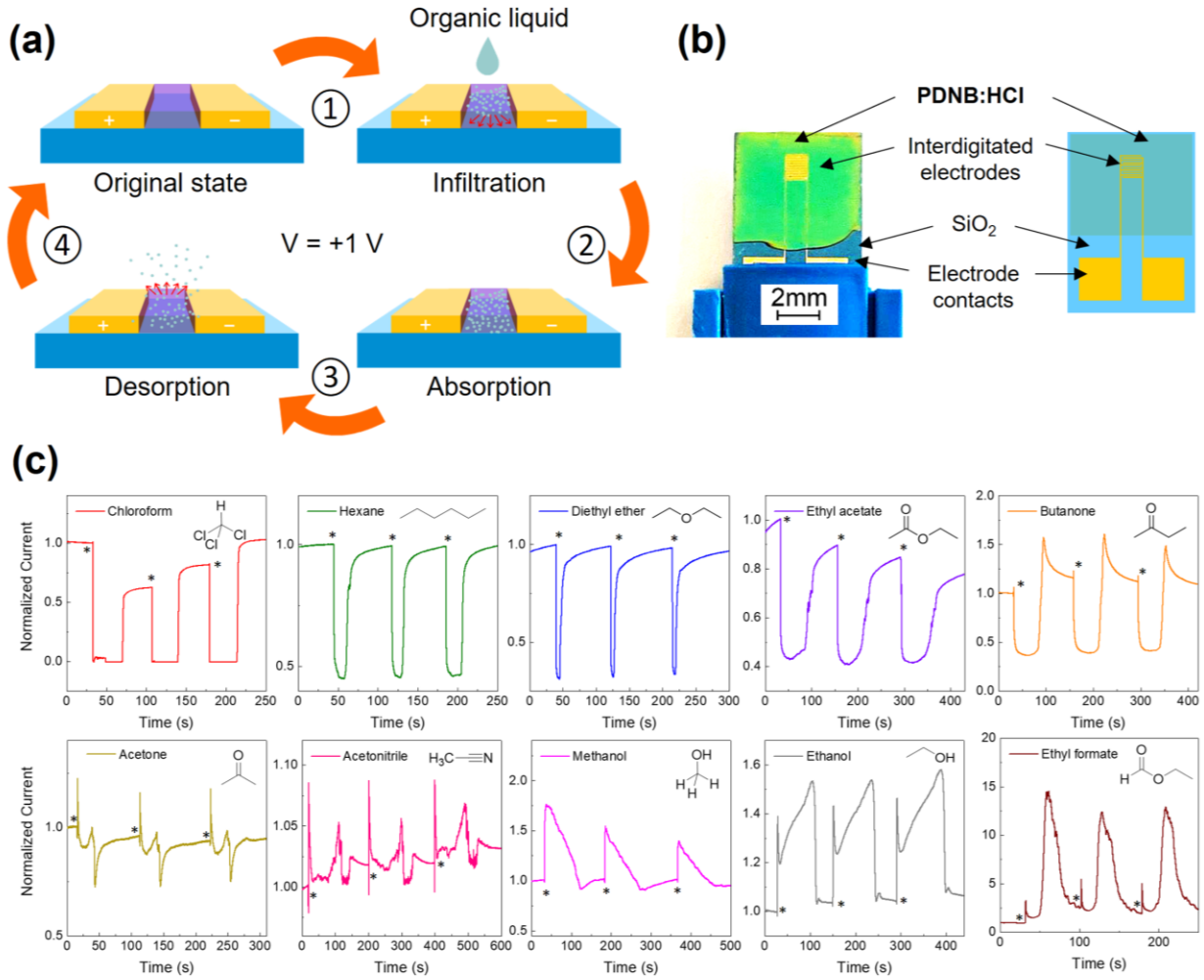

Figure 4.9. (a) Structure of the chemiresistor-type liquid sensor and testing procedure: Step 1: Liquid analyte introduction; Step 2: Organic molecules diffussion into polymer; Step 3: Desorptin of organic molecules from polymer; Step 4: Recovery of polymer to original state after evaporation of the solvent. (b) Left: top view of an actual chemiresistive liquid sensor device using **PDNB:HCl** as the channel layer on a SiO_2/Si substrate; Right: the schematic drawing of the device. (c) Normalized current versus time (*I*-*t*) profiles of ten different volatile organic liquids measured at V_{DS} = +1.0 V. The asterisk (*) represents the time when a droplet of 5.0 μL liquid analyte was introduced to the channel.

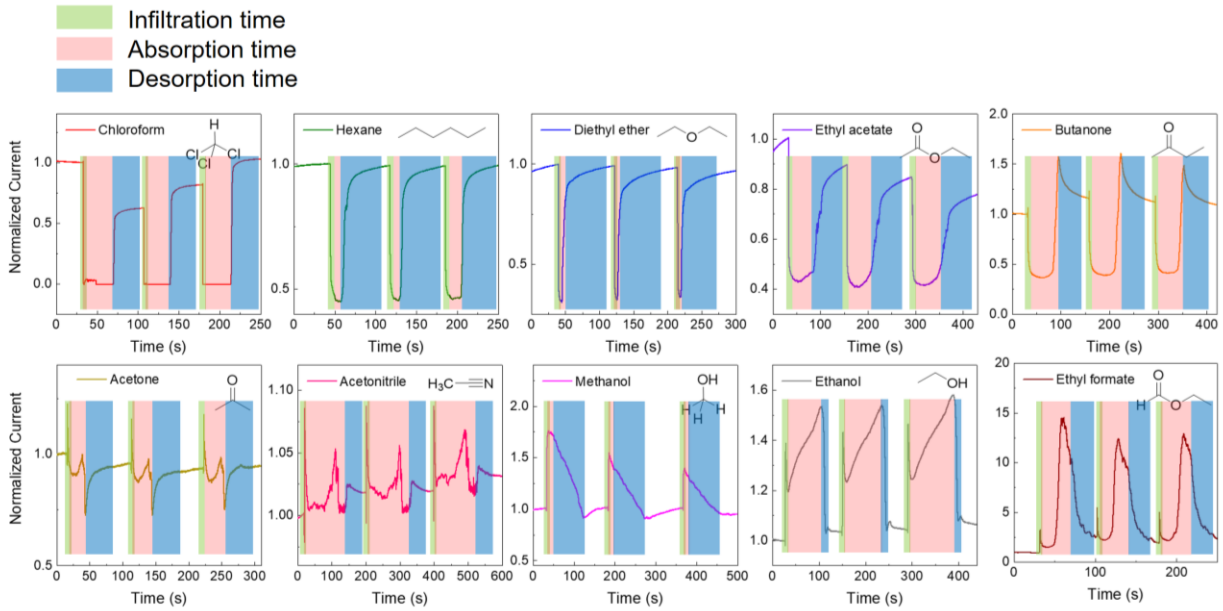

Figure 4.10. Defined infiltration, absorption and desorption stages in the *I-t* profiles of ten different volatile organic liquids measured using a **PDNB:HCl** based chemiresistor (same data shown in Figure 6 in the main text). The colored areas indicate different stages during which the liquid analyte infiltrates the surface of the channel polymer (green), the absorption stage during which the liquid analyte is being absorbed (red), and the desorption stage during which the liquid analyte is desorbed from the channel polymer (blue) in each sensing cycle.

Table 4.3. Quantitative data of the *I-t* graphs of volatile organic liquid analytes measured using a **PDNB:HCl** based chemiresistor.

Analyte	$\left(\frac{\Delta I}{I_o}\right)_{max}$ (%)[a]	$\tau_{infiltration}$ (s)[b]	$\tau_{absorption}$ (s)[c]	$\tau_{desorption}$ (s)[d]	τ_{total} (s)[e]
Chloroform	-100[f]	0.417 ± 0.177	34.2 ± 2.10	29.4 ± 2.69	64.0 ± 3.42
Hexane	-45.6 ± 0.436	7.73 ± 1.60	9.53 ± 1.99	37.7 ± 4.69	55.0 ± 5.34
Diethyl ether	-67.9 ± 1.25	1.33 ± 0.236	2.65 ± 0.580	62.3 ± 5.50	66.3 ± 5.53
Ethyl acetate	-58.3 ± 1.04	1.91 ± 0.512	49.7 ± 2.09	70.8 ± 4.44	122 ± 4.93
Butanone	-61.2 ± 2.81	4.95 ± 0.718	56.4 ± 2.56	62.0 ± 1.74	123 ± 3.18
Acetone	+18.6 ± 3.08	0.783 ± 0.390	30.1 ± 2.51	61.6 ± 7.10	92.5 ± 7.54
Acetonitrile	+8.67 ± 0.140	1.28 ± 0.140	132 ± 4.69	58.1 ± 6.55	191 ± 8.06
Methanol	+56.8 ± 18.5	4.79 ± 1.12	2.94 ± 0.335	86.7 ± 2.19	94.4 ± 2.48
Ethanol	+55.3 ± 2.55	2.26 ± 3.76	85.7 ± 9.84	10.3 ± 0.925	98.3 ± 10.6
Ethyl formate	+1230 ± 109	10.6 ± 0.253	24.8 ± 3.23	31.3 ±1.94	66.7 ± 3.78

[a] $\left(\frac{\Delta I}{I_o}\right)_{max}$ is the maximum percentage current change (in magnitude) in each sensing cycle in the *I-t* graph shown in Figure 4.10, where $\Delta I = I_H$ (or I_L) $- I_0$, and I_0 is the baseline current just before the analyte liquid is introduced, I_H and I_L are the highest or lowest current measured after the analyte liquid is introduced. I_H and I_L may occur during the infiltration or absorption stage. In case that there are both I_H and I_L, such as acetone, the one with the largest absolute value is chosen.

[b] $\tau_{infiltration}$ is the infiltration time during which the liquid analyte infiltrate the surface of the channel polymer. It is the duration measured right after the analyte liquid is introduced until the current signal reaches the maximum absolute value (green areas in Figure 4.10).

[c] $\tau_{absorption}$ is the absorption time during which the analyte liquid is being absorbed by the channel polymer. This stage gives the unique *I-t* profile/fingerprint for each analyte. It is the time measured between the end of infiltration stage and the start of the desorption stage (red areas in Figure 4.10).

[d] $\tau_{desorption}$ is the desorption time during which the channel polymer completes the absorption of the liquid analyte, and the absorbed analyte is desorbed from the channel polymer until the current signal reaches the baseline level (blue areas in Figure 4.10).

e $\tau_{total} = \tau_{infiltration} + \tau_{absorption} + \tau_{desorption}$, which is the total time required to complete one sensing cycle.

[f] A value of -100% indicates that the current dropped to zero.

4.3. Conclusion

We reported the design and synthesis of a new multifunctional DPP-based D-A polymer **PDEB** with a low band gap and a high HOMO energy level. **PDEB** consists of a strong electron-withdrawing DPP building block and a strong electron-donating **C12-BTO** building block in its repeat unit, which endows this polymer with a high-lying HOMO energy level of -4.80 eV and a narrow band gap of 0.94 eV owing to the strong intramolecular charge transfer effect between the D and A unit. Furthermore, **PDEB** contains thermally labile carbamate side-chains on the DPP units, which can be thermally removed under rather mild temperatures to produce insoluble polymer **PDNB** that is resistant to all common solvents tested. The HOMO energy level of **PDNB** is even higher at -4.68 eV, which is desirable to convert this polymer into a conductive polymer via p-doping.

It was found that **PDNB** could be doped by some common p-dopants, achieving a conductivity of up to 5.64 S cm^{-1} with iodine as a dopant. When **PDNB** was doped by HCl, the resulting doped polymer **PDNB:HCl** showed a conductivity of 0.24 S cm^{-1} and an excellent stability with the conductivity maintained at ~10^{-2} S cm^{-1} even after being stored for 9 months under ambient conditions.

A chemiresistive sensor with a simple two-electrode bottom contact structure was constructed using **PDNB:HCl** as the channel, which can be driven by a low operating voltage of 1.0 V. The sensor was used to test ten different common volatile organic liquids. A unique current versus time fingerprint profile was obtained for each liquid, which can be used to easily distinguish these liquids. The device can be repeatedly used for hundreds of times over months with the same or different liquids and still afford reproducible results, demonstrating that **PDEB** is a very promising solution processable/printable precursor polymer for the fabrication of robust chemiresistor-type chemical sensors with excellent air stability, solvent resistance, and selectivity. The sensor may also be useful for sensing other analytes such as gases and aqueous solutions, which is under investigation.

Chapter 5: Hemi-isoindigo-based Polymers as Temperature Sensor[3]

5.1. Introduction

The pristine, semiconducting π-conjugated polymers have been widely studied for applications including logic circuits, sensors, photovoltaics, anti-corrosion, and electrocatalysis.[271–277] The physical properties of polymeric materials also allow stretchable, bendable and implantable electronics in future applications. In addition, polymer materials can be readily functionalized by means of chemical modifications on the materials and band gap tuning to enable better or novel technologies. After doping, the conductivity of a π-conjugated polymer increases. When the conductivity is high, the doped polymer can be used as an electrode in electronic device, and when the conductivity is low to medium, it can be used as a channel material in a resistor-type sensor.[18,278][311,324,325]

Temperature sensors have been one of the most common and demanding sensors used in various areas, especially in the medical field for vital sign monitoring. There is also a potential demand for flexible temperature sensors that can be incorporated onto human skin to monitor skin temperature. Such skin thermometer may have possible applications to monitor cardiovascular health, physical activity, ulcer prediction for disease prevention and early diagnosis.[175,176] Conductive polymer-based temperature sensors are particularly suitable for these applications because of their excellent mechanical properties, low costs, as well as lower operating voltage ranges (below 1 V).[326–328]

In the previous chapters, hydrogen-bonds in amide-based D-A conjugated polymers were found to be advantageous for enhancing the environmental stability, sensitivity, and selectivity of sensor devices. It is believed that through a rational design of the backbone and functional substituent groups on D-A polymers, the environmental stability and performance of organic-based sensors can be greatly improved. This chapter uses these strategies to develop hemi-isoindigo-based polymers for high-performance chemiresistive temperature sensors.

Many sensors that use conductive polymers as active materials can only be used for a few days or weeks, which makes them impossible for long-term applications. The charge transfer complex formed between the polymer and the dopant (polymer:dopoant) may undergo phase segregation,

[3] This chapter is not yet published and in near-verbatim at which it is intended for submission. The following is the authorship order: **Jenner H. L. Ngai**, John Polena, Xiguang Gao, Mihir Kapadia, Daniel Afzal, Yuning Li.

the coupling reaction between polymer polarons, and the counterion coupling reaction between polymer and dopant,[329] which reduces the number of polarons and causes the conductivity to drop over time. To improve the stability of the p-doped polymer, the polymer should have a high HOMO (highest occupied molecular orbital) energy level (E_{HOMO}), so that the polymer can form strongly bound polymer:dopant complexes.[330] On the other hand, a dopant that is non-volatile and stable towards the sensing environment such as the moisture in air is desirable for improving the long-term stability of the doped polymer. For example, the sensing performance of PEDOT is severely affected by air humidity and will rapidly degrade in a short period of hours and days.[331] The water-soluble PSS counterion swells when it comes in contact with moisture, causing the distance between adjacent PEDOT grains to increase, so the conductivity of PEDOT:PSS decreases.[152,332] Therefore, it is very important to develop stable conductive polymers used in temperature sensors for practical applications long-term durability is critical.

In this report, several novel HID polymers consist of thermally cleavable side chains that can be partially removed at a later stage to create a polar hydrogen-bonds locked polymer chains. This cross-linking effect helps connecting all the adjacent conjugated polymers in a more rigid manner, and as a result minimizing the irreversible distancing of neighboring polymers by changing environment, which could lead to poor sensitivity, stability and cyclability during sensing. The hydrogen-bonded environment also created a high polarity environment for dopant molecules to accommodate within the polymer film, thus creating more stable polymer:dopant complexes compared to purely hydrocarbon side chained polymers. In our study, the novel doped HID polymers were found to behave as negative temperature coefficient (NTC) materials in a variable working temperature range from 20–70^{o}C, in which the resistivity of the material decreases with an increasing temperature, opposite to that of metals. In NTC-type temperature sensors, an increasing thermal energy would facilitate the charge carrier hopping and tunneling processes between individual polymers and the neighboring polymers in the nanoscopic level according to the variable range hopping (VRH) theory and the charge transfer model.[201,333–335] Therefore the materials would have a negative value in which is opposite to that of positive temperature coefficient (PTC) materials such as metals. There are also very little reported literatures about printable polymer-based NTC-type materials that have favorable human body temperature sensing ranges, especially operated at low-power.[336] Most of these NTC materials were composite materials made up of an insulator and a conductor such as PEDOT:PSS, carbon nanotubes (CNTs)

or graphene derivatives.[151,337–339] Many of these composites might only have an NTC effect below ambient temperatures which make bio-related applications intangible.[340,341] Herein, we report the synthesis and preparation of four new asymmetric conductive hemi-isoindigo (HID) polymers, that three of them when being fabricated into temperature sensors can possess high thermal sensing performance with TCR up to -1.04 %/^{o}C, with excellent stability, high thermal sensitivity and reversibility. We also demonstrated the fabrication of an all-solution processed flexible temperature sensor using HID polymers as the sensing element with high TCR up to -1.49 %/^{o}C with good stability and temperature sensing reversibility.

5.2. Results and Discussion

5.2.1. Synthesis of Polymers

Four polymers **PTEB, PMEB, PEEB** and **PPEB**, which contain a 2-ethylhexyloxyl carbonyl substituted HID, a 3,3'-bis(dodecyloxy)-2,2'-bithiophene (**DDOBT**), and a thiophene without or with different alkoxy substituents at its 3- and 4-positions were synthesized following the routes outlined in Scheme 5.1. The **DDOBT** unit is very electron-rich, while the HID unit is electron deficient, both of which would form donor-acceptor (D-A) electron transfer, reducing the bandgap and elevating the E_{HOMO} of the polymer. In comparison to **PTEB** (R = H), the electron-donating short alkoxy substituents on the thiophene spacer in **PMEB** (R = $–OCH_3$), **PEEB** (R+R = $–OCH_2CH_2O–$), and **PPEB** (R+R = $–OCH_2CH_2CH_2O–$) are expected to further raise the E_{HOMO} of these polymers to improve the stability of the polymer:dopant complex. Furthermore, 2-ethylhexyloxyl carbonyl at the nitrogen atom (a carbamate group) of the HID unit is introduced to render these polymers soluble, which is crucial for solution processing of these polymers, while it can also be readily thermally removed to form polymers **PTNB**, **PMNB**, **PENB**, and **PPNB**.[330] The removal of the side chain on HID would create voids to easy access of the dopant molecules to the polymer backbone. The amide group (-C(=O)NH-) on the non-substituted HID unit is expected to form strong hydrogen bonding, which can lock polymer chains to form a stable cross-linked network.

Briefly, the respective monomer compounds **M1-4** for **PTEB**, **PMEB**, **PEEB**, and **PPEB** were synthesized from various thiophene compounds to anchor formyl groups at the α-position, following by Knoevenagel condensation reactions to produce the core structures comprising HID and thiophene. Bromination with *N*-bromosuccinimide (NBS) was carried out before (for **M1**, **M3**,

and **M4**) or after (for **M2**) the Knoevenagel condensation to attach the bromo functionality for the final Stille coupling polymerization. The thermally removable 2-ethylhexyloxyl carbonyl group was introduced to the HID unit by carbamation of these compounds with ethylhexyl chloroformate. The full synthetic details are provided the Supporting Information. It should be mentioned that monomers **M1**, **M3**, and **M4** are predominantly the *Z*-form geometric isomers and there were no *E*-isomers detected in the Knoevenagel condensation and carbamation steps. On the other hand, for **M2**, although only the *Z*-isomer formed in the Knoevenagel condensation step, the following carbamation produced a mixture of *Z*- and *E*-form isomers at a ratio of ~1:1, which could not be separated by column chromatography. Therefore, a *Z*:*E* isomer ratio of ~1:1 remained in **M2**.

Stille polymerization was then carried out between **M1**, **M2**, **M3**, or **M4** and (3,3'-bis(dodecyloxy)-[2,2'-bithiophene]-5,5'-diyl)bis(trimethylstannane) (**M5**) in the presence of $Pd_2(dba)_3$/P(*o*-tolyl)$_3$ as the catalyst in chlorobenzene at 80 °C to afford **PTEB**, **PMEB**, **PEEB**, or **PPEB**. After purification by using Soxhlet extraction with methanol, acetone, and chloroform, final polymers were obtained from the chloroform fractions. The molecular weights of the polymers were analyzed using high-temperature gel-permeation chromatography (HT-GPC) at 140 °C using 1,2,4-trichlorobenzene (TCB) as eluent (**Figure 5.1** & Table 5.1). Detailed materials characterizations and synthesis procedures can be found in Appendix A and Appendix B.

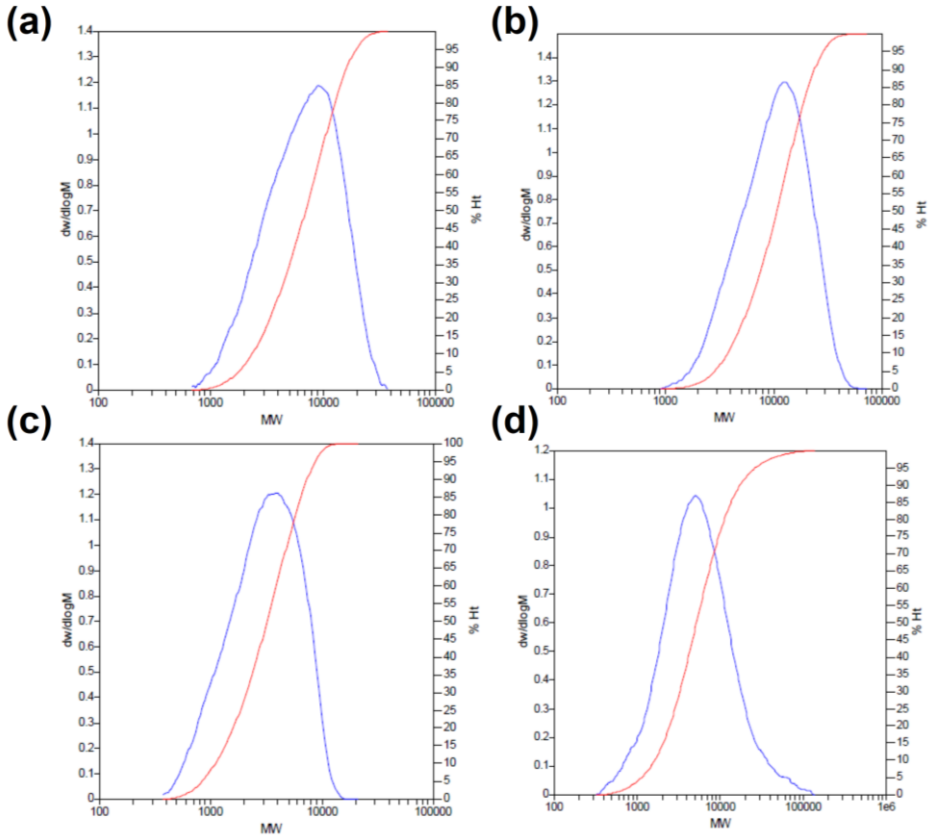

Figure 5.1. Molecular weight distribution of (a) **PTEB**; (b) **PMEB**; (c) **PEEB**; and (d) **PPEB** obtained from HT-GPC.

Table 5.1. Molecular weight information of the asymmetric HID polymers

Polymer	M_w	M_n	$Đ$
PTEB	8,319	4,879	1.71
PMEB	12,389	7,635	1.62
PEEB[a]	3,757	2,286	1.64
PPEB	8,373	3,432	2.44

[a] The measured molecular weight of **PEEB** indicated that this compound should be a mixture of short oligomers.

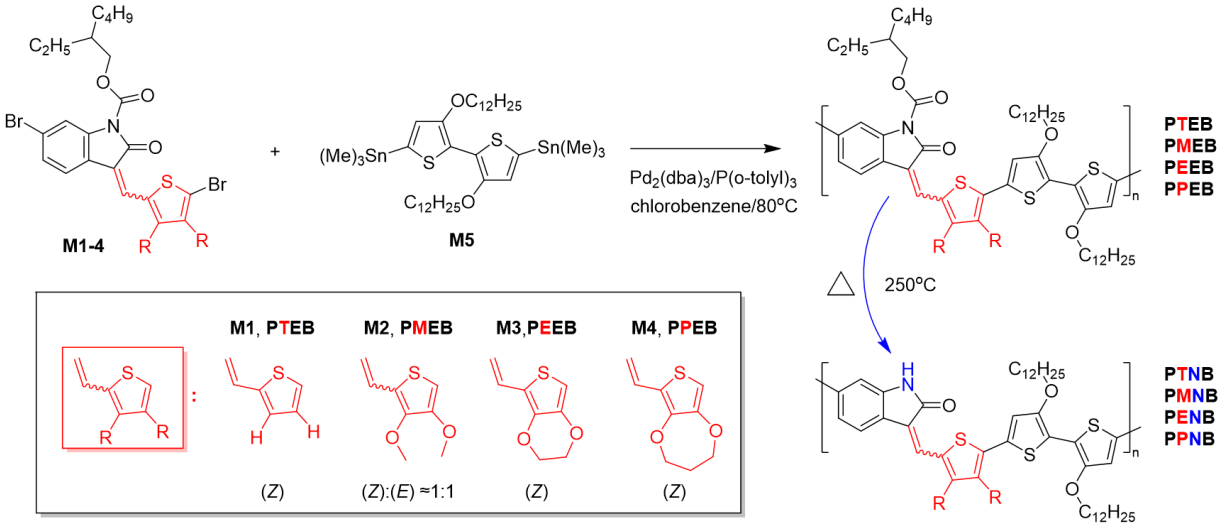

Scheme 5.1. General scheme of the synthesis of asymmetric hemi-isoindigo (HID) polymers **PTEB**, **PMEB**, **PEEB** and **PPEB**.

5.2.2. Optical and Electrochemical Properties

Ultraviolet-Visible-Near-Infrared (UV-Vis-NIR) spectroscopy was used to study the optical properties of the polymers. As shown in Figure 5.2a and Table 5.2, **PTEB**, **PMEB**, **PEEB** and **PPEB** solutions in chloroform exhibited a dramatic red-shifted absorption at (λ_{max} = 674, 688, 695 and 700 nm) when compared to their monomers **M1**, **M2**, **M3** and **M4** (λ_{max} = 420, 420, 440 and 430 nm) respectively (Figure 5.2 and Table 5.2). This indicated that the polymers consist of a much more extended π-conjugation length than that of the corresponding monomers. The film UV-Vis-NIR spectra of **PTEB**, **PMEB**, and **PPEB** exhibited a red shift of 12, 6, and 5 nm in λ_{max},

respectively, compared to their solutions (Figure 5.2a, 5.1b & 5.1d). This indicated the formation of J-aggregates in the solid state. However, the film of **PEEB** exhibited a blue shift of 9 nm in λ_{max} from its solution (Figure 5.2c). This phenomenon is likely due to the stronger donor-donor (D-D) and acceptor-acceptor (A-A) attractions between the polymer chains in the **PEEB** film, leading to the formation of H-aggregates in the solid state.[303–305] Among the four polymers, **PEEB** was found to have the lowest molecular weight and the poorest solubility in organic solvents, which is possibly caused by the aforementioned strong H-aggregation in **PEEB**. This phenomenon seems to be a beneficial feature for better charge carrier hopping in this system, which will be discussed later. The optical band gaps for **PTEB**, **PMEB**, **PEEB** and **PPEB** in the solid state were estimated based on their onset absorption wavelengths to be 1.41, 1.35, 1.36 and 1.24 eV. The lower band gaps for **PMEB**, **PEEB** and **PPEB** are likely due to the electron donating effect of the alkoxy substituents (methoxy on **PMEB**, ethylenedioxy on **PEEB** and propylenedioxy **PPEB**) on the thiophene spacer. The more electron rich thiophene spacer would result in a stronger donor-acceptor push-pull effect or charge transfer interaction with the adjacent electron accepting HID unit, narrowing the band gap of the polymers.[342] After the **PTEB**, **PMEB**, **PEEB** and **PPEB** films were heated at 250 °C for 20 min in air to remove the carbamate side chains on the HID units, the absorption spectra of the resultant polymers **PTNB**, **PMNB**, **PENB** and **PPNB** remained almost identical, indicating that the removal of carbamate side chains did not have a noticeable impact on the π-conjugation length of the polymer backbone.

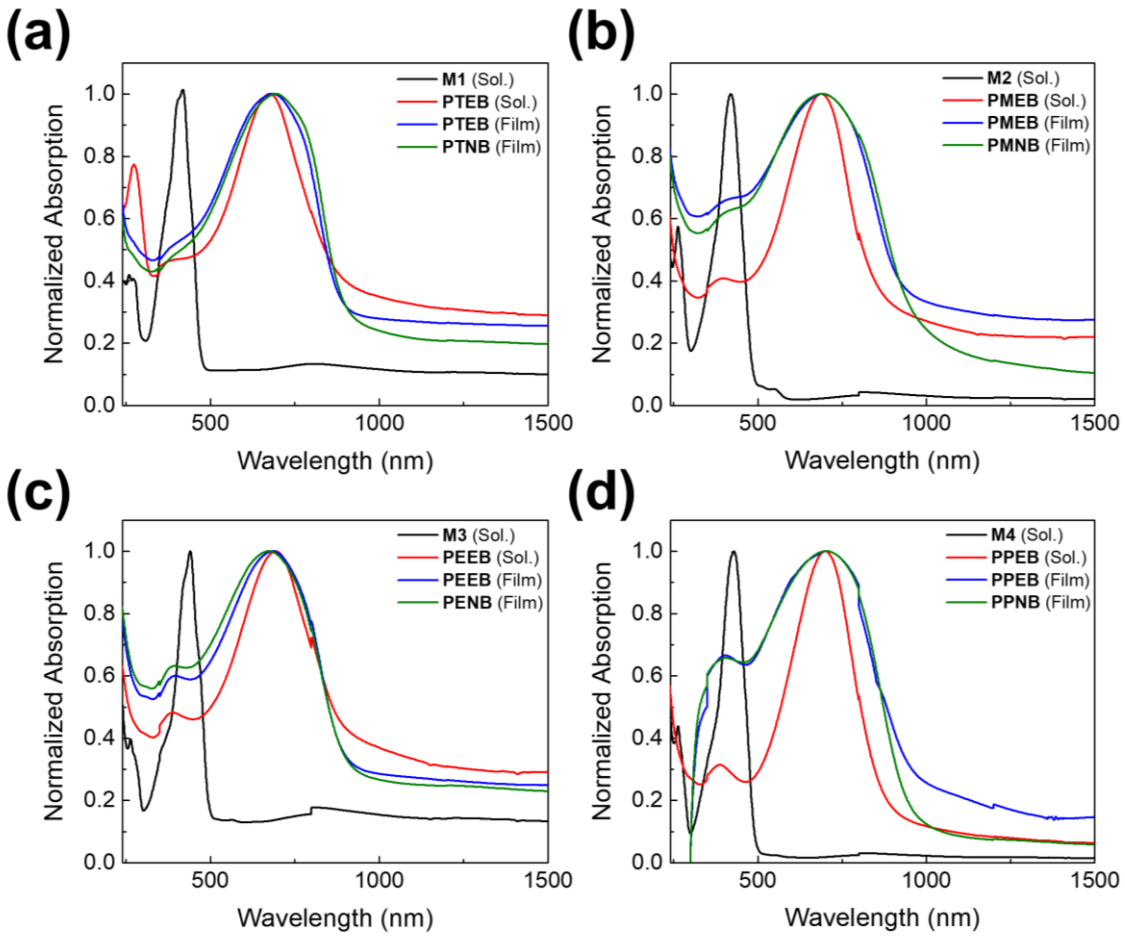

Figure 5.2. Solution and film UV-Vis-NIR absorption spectra of (a) **PTEB**, **PTNB** and its monomer **M1**; (b) **PMEB**, **PMNB** and its monomer **M2**; (c) **PEEB**, **PENB** and its monomer **M3**; (d) **PPEB**, **PPNB** & its monomer **M4**.

Cyclic voltammetry (CV) measurements of the polymer films before and after removal of side chains were carried out using conductive indium-doped tin oxide (ITO) electrode coated on glass. All polymers exhibited a reversible two-electron oxidation process within the potential range from -1.4 V to +1.4 V (Figure 5.3a-d). Ferrocene, which has an E_{HOMO} of -4.8 eV,[306] was used as the internal standard to calculate the E_{HOMO}'s of **PTEB**, **PMEB**, **PEEB** and **PPEB** to be -4.83, -4.74, -4.74 and -4.57 eV respectively (Figure 5.3c and Table 5.2). The E_{HOMO}'s of **PTNB**, **PMNB**, **PENB** and **PPNB** are -4.69, -4.55, -4.68 and -4.47 eV, respectively, which are higher compared to their parent polymers due to the removal of the electron-withdrawing carbamate side chains. The lowest unoccupied molecular orbital (LUMO) energy level (E_{LUMO}) of a typical p-dopant 7,7,8,8-tetracyanoquinodimethane (**F4TCNQ**) was measured to be -5.01 eV, which is deeper than

the E_{HOMO}'s of these polymers and would allow the electron transfer from the HOMO of the polymers to the LUMO of **F4TCNQ** to form charge transfer complexes, namely, p-doping.

Doping of a polymer or the formation of an electron transfer complex between the polymer and the dopant can be considered the "trapping" of charge carriers (electrons in the case of a p-dopant, e.g., **F4TCNQ**). The difference between the E_{HOMO} of the polymer and the E_{LUMO} of **F4TCNQ** is the energy well or the trap energy (E_T).[343,344] Previous studies show that traps with a trap energy greater than ~0.25 eV are deep traps,[344,345] indicating that the electron transfer complex would be quite stable. Based on the E_{HOMO}'s of these polymers and the E_{LUMO} of **F4TCNQ** (Figure 5.3c), all the polymer:**F4TCNQ** complexes should be quite stable.

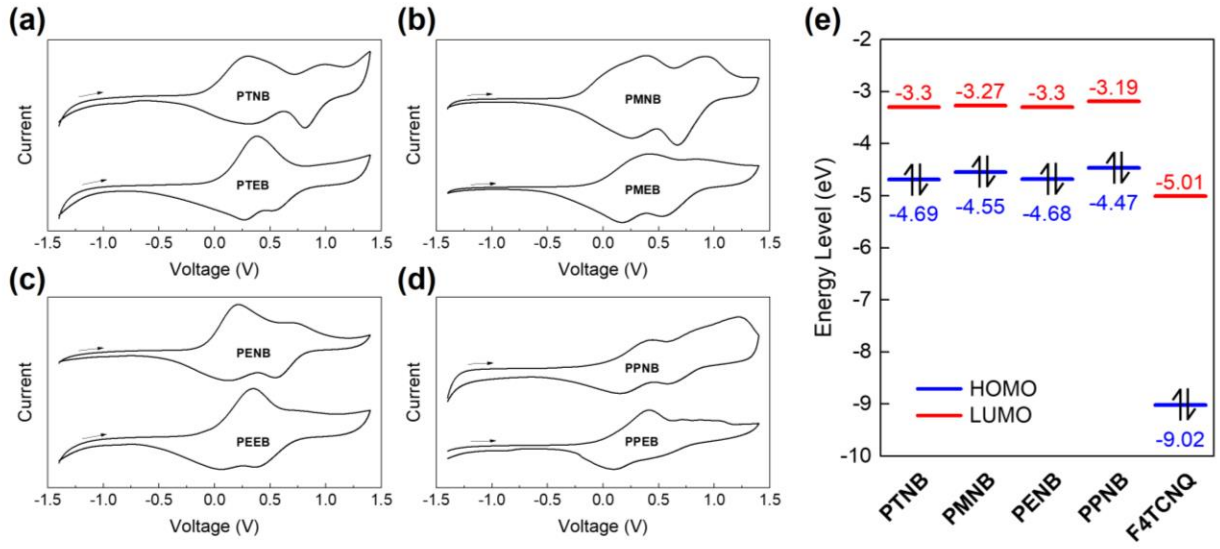

Figure 5.3. (a-d) Cyclic voltammograms of HID polymers using Ag/AgCl as the reference electrode and ferrocene as the internal standard; (e) Energy level diagram of HID polymers and **F4TCNQ** calculated from the CV measurements.

Table 5.2. Optical and electrochemical properties of HID polymers and **F4TCNQ**.

Material	λ_{max} (nm)		λ_{onset} (nm)		E_g^{opt} (eV)[a]	E_{HOMO} (eV)[b]	E_{LUMO} (eV)[b]
	sol.	film	sol.	film	film	film	film
PTEB	674	686	875	879	1.41	-4.83	-3.42
PTNB	---	694	---	892	1.39	-4.69	-3.30
PMEB	688	694	867	919	1.35	-4.74	-3.39
PMNB	---	691	---	969	1.28	-4.55	-3.27
PEEB	695	686	896	912	1.36	-4.74	-3.38
PENB	---	674	---	899	1.38	-4.68	-3.30
PPEB	700	705	873	1000	1.24	-4.57	-3.33
PPNB	---	702	---	969	1.28	-4.47	-3.19
F4TCNQ	---	270	---	309	4.01	-9.02	-5.01

[a] Optical bandgaps (E_g^{opt}'s) calculated from the onset absorption wavelengths of the thin films; [b] E_{HOMO}'s of polymers and E_{LUMO} of **F4TCNQ** were calculated using their onset oxidation and reduction potentials, respective, with ferrocene as a reference (E_{HOMO} = -4.8 eV), while E_{LUMO}'s of polymers and E_{HOMO} of **F4TCNQ** were calculated using the equation: $E_{LUMO} = E_g^{opt} + E_{HOMO}$.

5.2.3. Fabrication and Characterization of Doped Polymer Films

The general procedure for preparing the polymer conductive films is depicted in Scheme 5.2. A solution of **PTEB**, **PMEB**, **PEEB** or **PPEB** with a concentration of 5 mg mL^{-1} in chlorobenzene was spin-coated onto a glass substrate at 700 rpm for 80 s. The substrate was then thermally annealed in air at 250 ^{o}C for 20 min to partially remove the carbamate side chains on the HID units to form **PTNB**, **PMNB**, **PENB** or **PPNB**, which are insoluble in any solvent. Thermal gravimetric analysis (TGA) of the polymers can be found in Figure 5.4 which shows the drop in percentage mass when annealing the precursor polymers at high temperature, demonstrating the partial removal of the carbamate side chains on the polymers. These polymer films were then doped by spin-coating a **F4TCNQ** solution (1mg mL^{-1}) in acetonitrile at 2000 rpm for 60 s. The obtained doped polymer:**F4TCNQ** films were subsequently annealed at 60 ^{o}C for an additional 20 min and subjected to the UV-Vis-NIR measurement.

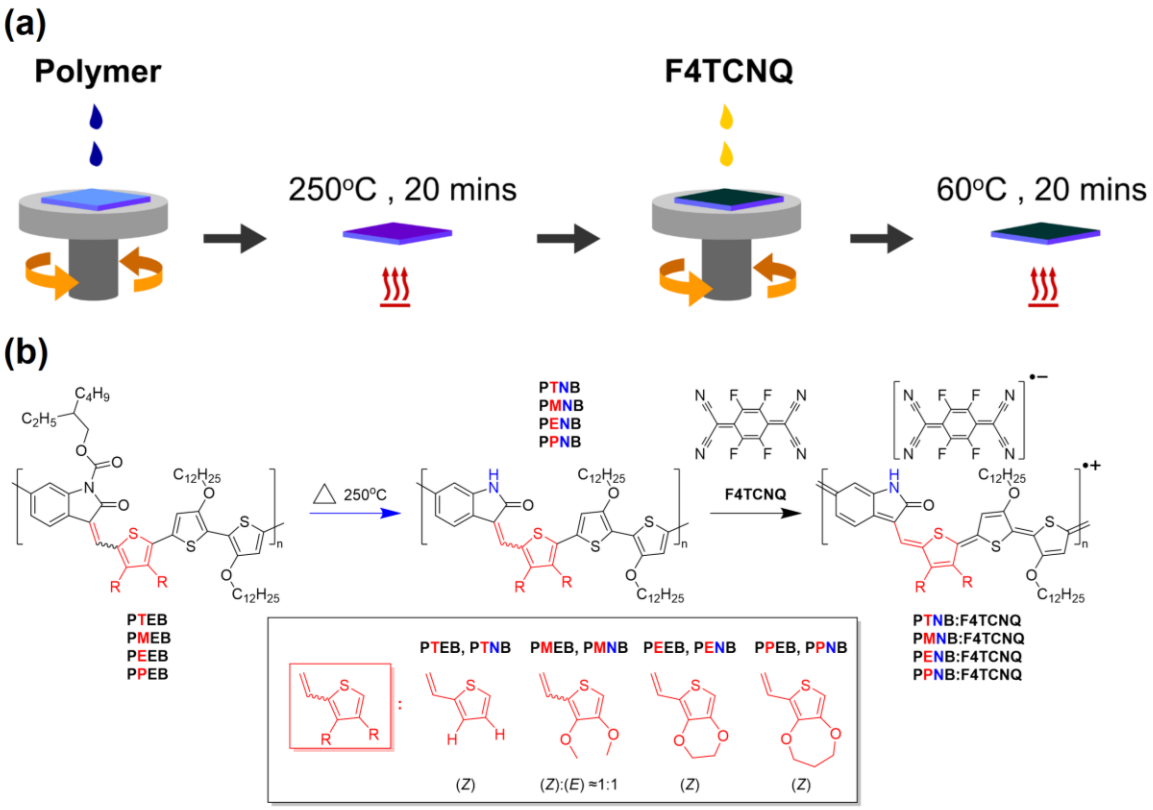

Scheme 5.2. (a) Graphical Schematics for preparing the doped HID conductive polymer films. (b) Chemical transformation of side chain cleavage and doping of HID polymers.

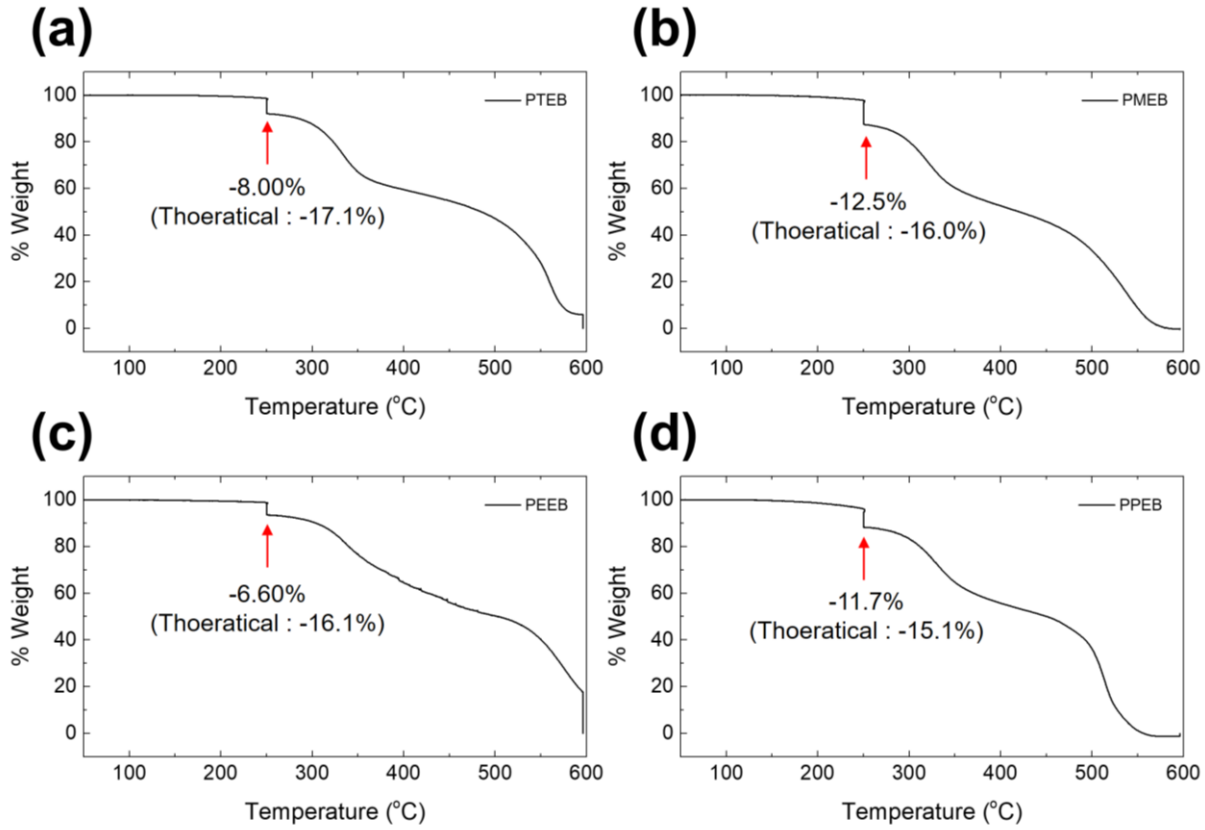

Figure 5.4. TGA diagram showing the transition of soluble polymer to the solvent resistant hydrogen-bonded polymers by thermal removal of carbamate side chains (a) **PTEB** to **PTNB**; (b) **PMEB** to **PMNB**; (c) **PEEB** to **PENB;** & (a) **PPEB** to **PPNB**. The polymer was heated in air at a heating rate of 10 °C min^{-1} from 25 °C, and held at 250 °C for 20 min, then heated at 10 °C min^{-1} until 600 °C.

UV-Vis-NIR spectroscopy was used to determine the change of optical absorption profiles of the polymer films before and after doping. Figure 5.5 shows that all polymer films exhibited a red shift in optical absorption spectra after doping with **F4TCNQ**. The red shifted λ_{max} values of **PTNB**, **PMNB**, **PENB**, and **PPNB** were found to be 138, 164, 100, and 179 nm respectively after treatment with the dopant. The optical band gaps of the polymers were found to be significantly lowered with a new emerging broad peak found in the near-IR region (1200 – 2200 nm), which should be associated to the quinoidal doped polymers with better π-delocalized structures. The λ_{max} absorption peaks of the undoped polymers were also almost completely disappeared in the polymer:**F4TCNQ** spectra (Figure 5.5a-d). Time-dependent Density functional theory (TD-DFT) was used to simulate the UV-Vis-NIR spectra of the neutral polymer models and the doped models

(polaron). It was found that when a single electron is removed from the neutral models **TNB**, **(*Z*)-MNB** & **(*E*)-MNB**, **ENB**, and **PNB**, the polaron species **TNB**$^{+\bullet}$, **(*Z*)-MNB**$^{+\bullet}$ & **(*E*)-MNB**$^{+\bullet}$, **ENB**$^{+\bullet}$, and **PNB**$^{+\bullet}$ resulted in a red-shift in absorption and an emerging peak at ~1500nm which this should be associated to the new band gap of the +1 charged doublet state of the polaron (Figure 5.5e-h). In general, the UV-Vis-NIR experimental results agreed very well with the TD-DFT results. This evidence indicated that a large portion of the neutral polymers has been transformed into their doped states by the **F4TCNQ** dopant, and the electron transfer should be a single electron transfer from polymers to the **F4TCNQ** dopant.

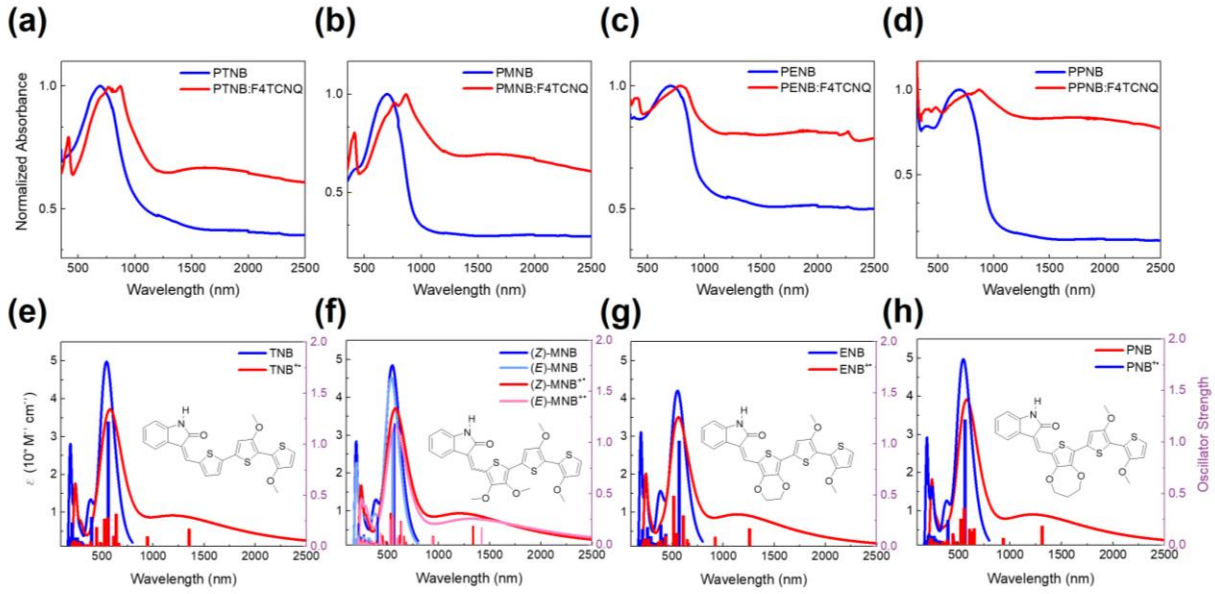

Figure 5.5. UV-Vis-NIR spectra of the neutral and doped polymer of (a) **PTNB**, **PTNB:F4TCNQ**; (b) **PMNB**, **PMNB:F4TCNQ**; (c) **PENB**, **PENB:F4TCNQ**; and (d) **PPNB**, **PPNB:F4TCNQ**; TD-DFT simulation of the UV-Vis-NIR spectra and the chemical strucutres of model compounds (a) **TNB** & **TNB**$^{+\bullet}$;(b) **(*Z*)-MNB**, **(*E*)-MNB**$^{+\bullet}$ & **(*Z*)-MNB**$^{+\bullet}$; (c) **ENB** & **ENB**$^{+\bullet}$; (d) **PNB** & **PNB**$^{+\bullet}$.

Resistor-type devices were then fabricated by depositing the polymer films onto SiO_2 (300 nm) / Si wafer substrates with an interdigitated gold (Au) electrode pair, and doping the films in a similar manner described previously. The resistor has a channel length (L) of 30 μm and a total channel width (W) of 15.8 mm with a W/L ratio of 527 (Figure 5.6a). The current versus voltage (*I-V*) relationships of the doped polymers were measured by sweeping a biased voltage from -1.0 to +1.0 across the electrodes to obtain the electrical conductivity of the doped polymers. The straight lines of the *I-V* curves indicate that all doped polymers behave as ohmic conductors (Figure 5.6b). The conductivities of the as-doped (Day 0) polymer films are in the order of **PENB:F4TCNQ** (0.735 S/cm) > **PMNB:F4TCNQ** (0.335 S/cm) > **PTNB:F4TCNQ** (0.179 S/cm) > **PPNB:F4TCNQ** (0.00364 S/cm). The doped polymers were stored in ambient air (at 22 °C and a relative humidity of 55%) and their electrical conductivities were measured intermittently within 30 days to study their stability. As shown in Figure 5.6c, the conductivity of **PTNB:F4TCNQ** dropped rapidly after about 5 days and only retained 4% of its initial value after 30 days. On the other hand, the conductivities of the other three doped polymers were found to be comparable to the as-doped ones after 30 days.

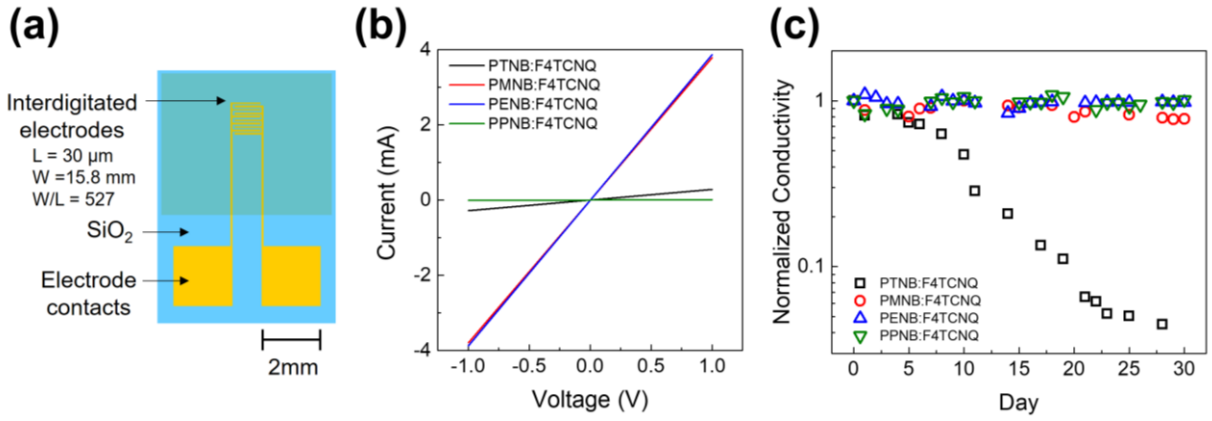

Figure 5.6. (a) Dimensions and pattern structure of the interdigitated resistor substrate used for conductivity measurement; (b) Current versus voltage (*I-V*) relationships of as-doped polymers; (c) Conductivity vs. time of doped HID polymers.

The anomaly of the long-term stability observed for **PTNB:F4TCNQ** was unexpected since the trap energy of **F4TCNQ** with respect to **PTNB** is 0.32 eV. In particular, the E_{HOMO} of **PENB** (-4.68 eV) is only slightly higher than that of **PTNB** (-4.69 eV), but **PENB:F4TCNQ** exhibited excellent stability. Therefore, it is difficult to explain the poor long-term stability of **PTNB:F4TCNQ** by its E_{HOMO}. Instead, we believe that the ethylenedioxy substituent on the HID unit of **PENB** helps to significantly improve the stability of **PENB:F4TCNQ**. The electron-rich ethylenedioxy substituents may strongly attract the electron-deficient **F4TCNQ** dopant molecules, thereby preventing the dopant molecules from separating from the polymer chains. Similarly, the excellent stability of **PMNB:F4TCNQ** and **PPNB:F4TCNQ** can be explained by their electron rich methoxy and propylenedioxy substituents in their HID units, respectively.

Density functional theory (DFT) was again used to determine the dipole moments of the polymer model compounds **TNB**, **MNB**, **ENB** and **PNB** (Figure 5.7a) in order to investigate the relationship of polarity and the polymer:dopant stability. From the DFT results, the dipole moment magnitudes of the model compounds **TNB**, **MNB**, **ENB** and **PNB** were found to be 2.12, 3.85, 4.18 and 4.14 debye. The weakest dipole **TNB** showed the highest conductivity decaying rate, while the conductivity decaying rate of polymer **PMNB:F4TCNQ**, **PENB:F4TCNQ** and **PPNB:F4TCNQ** were found to be very similar with almost no loss in conductivity (Figure 5.7a). The DFT calculated dipole moments were found to be in good agreement with the conductivity decay rate observed for the actual polymer:dopant complexes. The results suggest an obvious correlation between the polarity of the polymer backbone and the conductivity stability of the doped polymers.

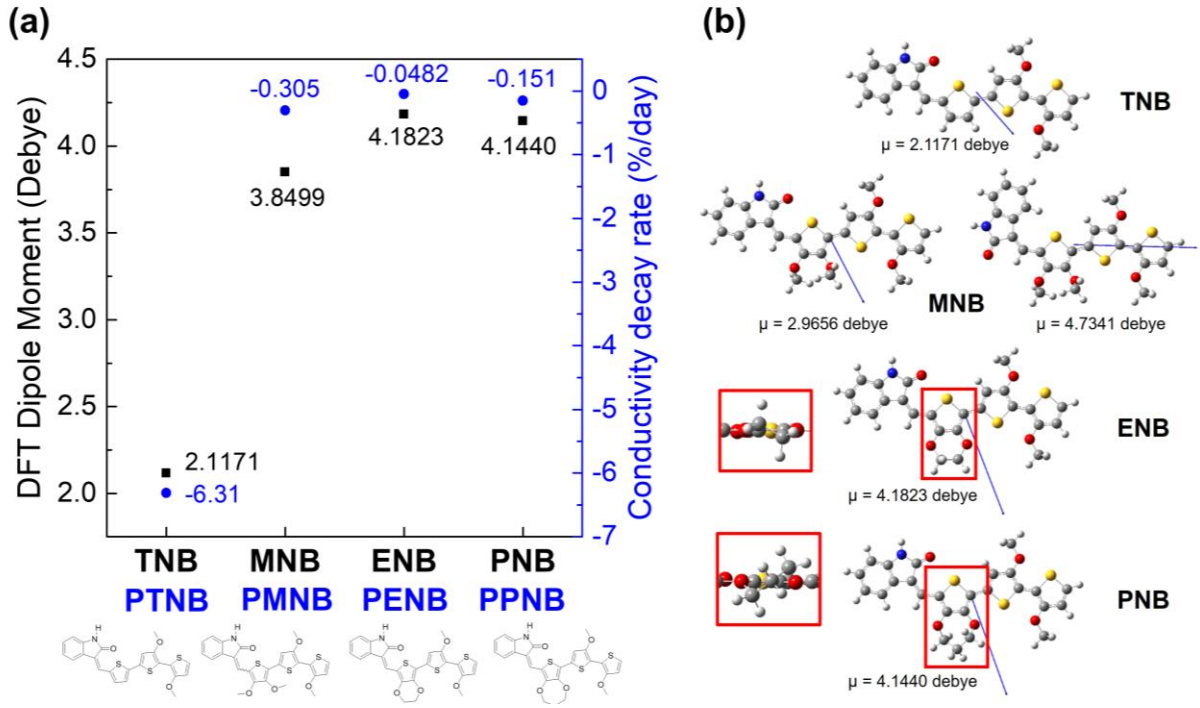

Figure 5.7. (a) The corresponding structures of model compounds of the polymers for DFT calculation; The DFT simulated dipole moments of model compounds **TNB**, **MNB**, **ENB** and **PNB**; and the measured conductivity decay rate of polymer **PTNB**, **PMNB**, **PENB** and **PPNB**. (b) The DFT results of the model compounds dipole moment with arrows showing the dipole vector and their respective dipole magnitude. (Two **MNB** models were simulated since **PMEB** and **PMNB** were made up of a 1:1 *Z:E* isomeric monomers); The aromatic core structures of all DFT models were found to be highly co-planar, while the ether bridges on the thiophene spacer in models **ENB** and **PNB** were found to be misaligned from the co-plane of the mainchain backbone due to the presence of sp^3 carbon units on their respective ethylenedioxy and propylenedioxy groups.

X-ray diffraction (XRD) spectroscopy was used to examine the effects of doping on crystallinity of the HID polymer films on the SiO_2/Si substrates. As shown in Figure 5.8a, the pristine **PTEB** exhibits a (100) diffraction peak at $2\theta = 4.27°$ corresponds to a *d*-spacing of 20.7 Å, which can be assigned to the interchain distance of the lamellar crystal structure of this polymer. Since there is no observable (010) peak that represents the π−π stacking distance, which should appear at ~20-25°, it suggests that the polymer chains adopted an anisotropic edge-on orientation. Upon thermal annealing at 250 °C, the resulting **PTNB** showed a sharper and more intense (100) peak at $2\theta = 4.48^{o}$, which corresponds to a *d*-spacing of 19.8 Å, manifesting a shrinkage of the interchain

distance due the removal of carbamate side chains. When **PTNB** was doped by **F4TCNQ**, the (100) diffraction peak shifted notably to 2θ = 4.16° (*d*-spacing = 21.2 Å), while the (010) diffraction peak remained the same in intensity and position. The enlarged interchain distance compared to that of the non-doped sample is most likely due to the insertion of the dopant molecules into the interlamellar spaces. Similar observations were reported when doping highly crystalline conjugated polymers with edge-on polymer chains orientation. It has been believed that the dopant molecules are inserted in the interlamellar space and are not into the π-π stacks of the polymer, thus only changing the intensity and position of the (100) peak.[346,347] Figure 5.9 shows the XRD spectra of the undoped **PTNB** and **PTNB:F4TCNQ** films in day 0, 5 and 10, in which the (100) peak position slowly shifted back to the original undoped film, with *d*-spacing decreased from *d*-spacing (day 0) of 21.3 Å to *d*-spacing (day 5) of 20.8 Å and then back to *d*-spacing (day 10) of 20.2 Å that is close to that of the undoped **PTNB** film (19.8 Å). The results indicate that the **F4TCNQ** dopant molecules have escaped from the interlamellar spaces over time, which agrees well with the decaying electrical conductivity mentioned earlier.

In sharp contrast with **PTEB**, the crystallinity of **PMEB**, **PEEB** and **PPEB** films is much lower, and there are no obvious (100) lamellar peaks (Figure 5.8b-d). Rather, they showed broad peaks at 2θ = 22.2° (*d*-spacing = 4.00 Å) for **PMEB**, 22.6° (*d*-spacing = 3.94 Å) for **PEEB**, and 20.4° (*d*-spacing = 4.35 Å) for **PPEB**. While these peaks may comprise of the amorphous halo, they may also be partially attributed to the (010) diffraction associated with the co-facial π-π stacking of the polymer main chains since their quite different positions. After removal of the carbamate side chains, the XRD pattern of the resulting **PMNB** remained similar, but shifted to 2θ = 21.5° (*d*-spacing = 4.13 Å), indicating a slight increase in π-π stacking distance. On the other hand, the peak intensities for both **PENB** and **PPNB** decreased significantly

The broad peak of the doped samples indicated enlarged π-π stacking distances due to the accommodation of the dopant molecules, with 2θ = 20.4° (*d*-spacing = 4.35 Å) for **PMNB:F4TCNQ**, 21.1° (*d*-spacing = 4.20 Å) for **PENB:F4TCNQ**, and 20.0° (*d*-spacing = 4.44 Å) for **PPNB:F4TCNQ**. For **PPNB:F4TCNQ**, the much weaker peak intensities could be due to the sterically bulkier propylenedioxy groups in **PPNB** than the ethylenedioxy groups in **PENB** or the dimethoxy groups in **PMNB** that might prevent the polymer backbones from close π-π stacking or even weaker intermolecular interactions, which this might be a reason to explain the

significantly lower conductivity of **PPNB:F4TCNQ** compared with **PENB:F4TCNQ**.[348] In addition, the absence of substituents on the thiophene spacer in **PTNB** might promote its chain packing, leading to a higher degree of crystallinity, but also drive the dopant molecules out of the polymer phase, which might be another reason for the poor long-term stability of **PTNB:F4TCNQ**.

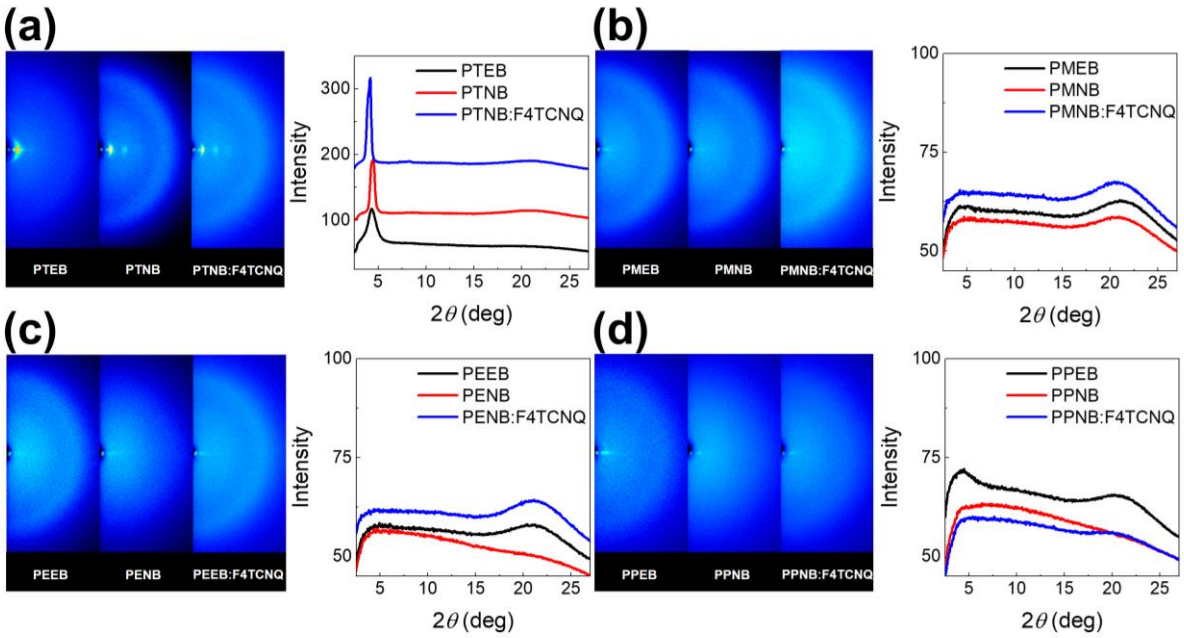

Figure 5.8. Two-dimensional and one-dimensional XRD spectra of (a) **PTEB**, **PTNB** & **PTNB:F4TCNQ**; (b) **PMEB**, **PMNB** & **PMNB:F4TCNQ**; (c) **PEEB**, **PENB** & **PENB:F4TCNQ** and (d) **PPEB**, **PMNB** & **PPNB:F4TCNQ**.

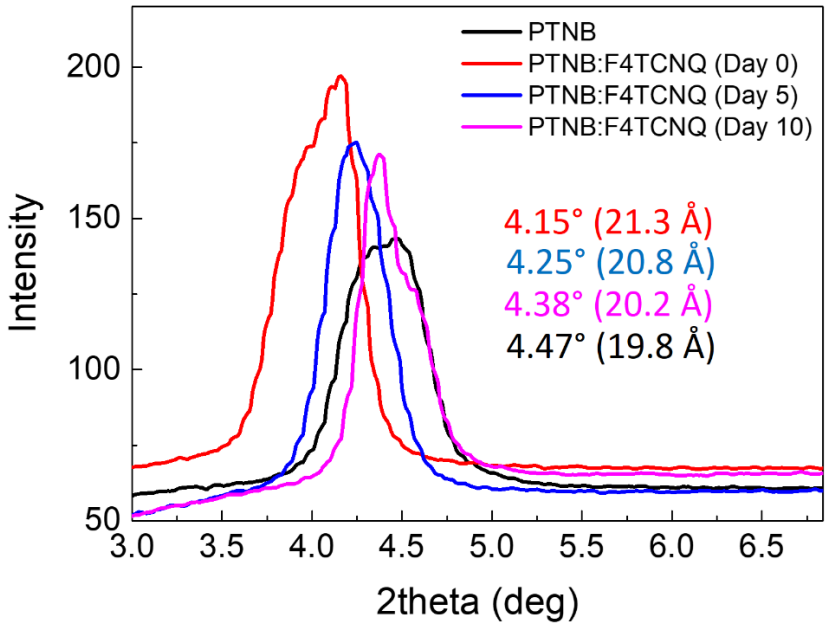

Figure 5.9. XRD diffraction pattern of the undoped **PTNB**, **PTNB:F4TCNQ** films in day 0, day 5, and day 10; Value in brackets show the interlamellar distances.

5.2.4. Temperature Sensors Based on HID polymers

PMNB, **PENB** and **PPNB** were chosen as the active layer in resistor-type temperature sensors owing to their excellent stability in their doped states. The active layers of the sensors were fabricated using the **F4TCNQ** doped polymers on a similar interdigitated two-electrode substrate mentioned in the previous section. On top of the device, a thin layer of polymethymethacrylate (PMMA) was used to encapsulate the polymer:**F4TCNQ** layer to minimize atmospheric interference during the temperature sensitivity measurements due to its low water and VOC permeability.[349–352] The general device structure is shown in Figure 5.10a. A constant bias voltage of 1.0V was then applied on two electrodes until a stable baseline current was established. In order to measure the temperature-dependent conductance of the sensor, the device was placed on a heating stage that is connected to a temperature controller. The device was insulated from the surroundings and measured in the temperature range of 20-70 ^{o}C, which is compatible with many practical applications such as storage or delivery for food and drugs; biomedical, physiological and health monitoring of human body temperatures.[353–356] A thermocouple was in contact with the surface of the polymer layer to monitor the temperature change. Figure 5.10b-d shows the real-time current as a function of time (*I*-*t*) for devices with the three doped polymers. All devices

exhibited a current increment upon increasing temperature. The **PMNB:F4TCNQ** device showed a gradual decrease in sensitivity when the temperature was beyond 40°C, while **PENB:F4TCNQ** and **PPNB:F4TCNQ** exhibited a more linear relationship between current and temperature. However, the current change of the **PPNB:F4TCNQ** device fluctuated seriously with changing temperatures due to the very low current (or low conductivity of this doped polymer).

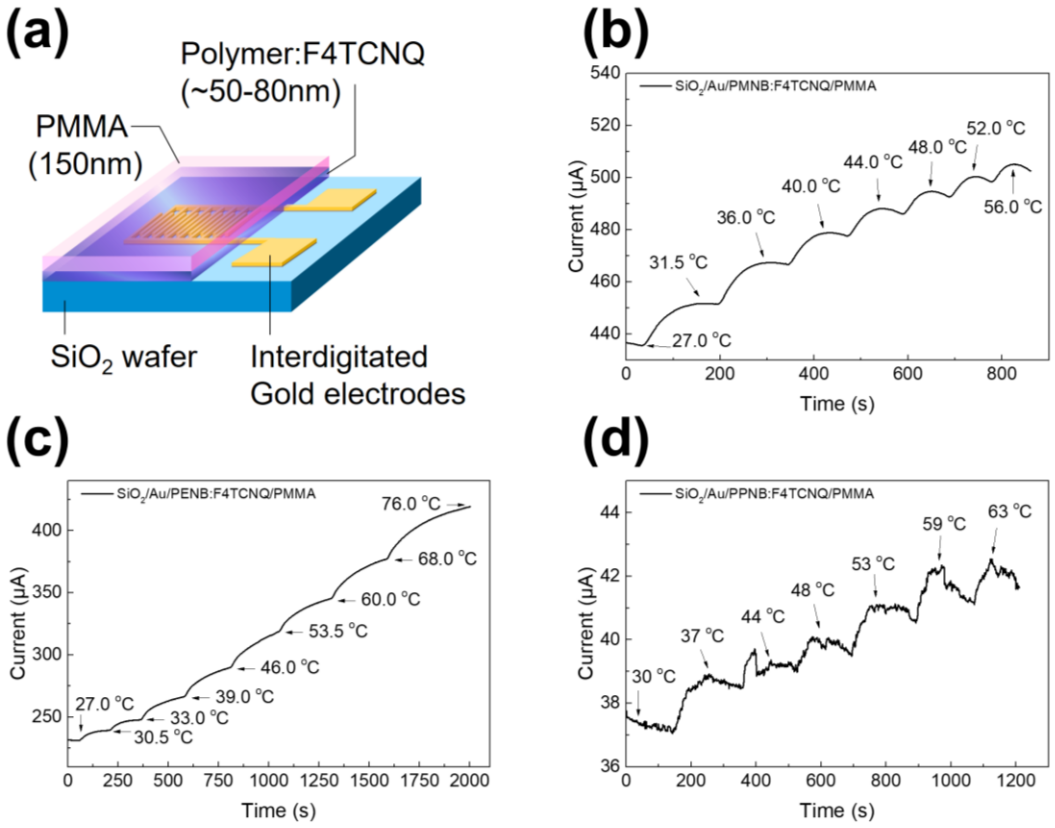

Figure 5.10. (a) Schematic diagram of the device structure of the HID polymer temperature sensor; Real-time current versus time (*I-t*) graphs at varying temperatures for (b) **PMNB:F4TCNQ**; (c) **PENB:F4TCNQ** and (d) **PPNB:F4TCNQ**.

The thermal sensitivities of the sensors are defined by the temperature coefficient of resistance (TCR), which can be calculated using Equation 5.1:[155]

$$\mathrm{TCR} = \frac{R - R_0}{R_0} \times \frac{1}{\Delta T} \times 100\% \qquad \textbf{(Equation 5.1)}$$

where R is the resistance at a specific sensing temperature, R_0 is the resistance at the reference temperature, and ΔT is the temperature difference between the sensing and reference temperatures. The response time of the device is defined by the time required for the sensor to reach 90% of the signal saturation, where a shorter time represents a faster response and higher sensitivity.

Figure 5.11a-c shows the relative resistance-temperature (R/R_0–T) curves of the devices. All doped polymer films showed a decrease in R/R_0 with respect to increasing temperature. The **PMNB:F4TCNQ** device exhibited a non-linear temperature dependent resistance change, having a TCR of -0.793%/^{o}C at 20 - 40^{o}C and a TCR of -0.330%/^{o}C at 40 - 60^{o}C. On the other hand, the **PENB:F4TCNQ** and **PPNB:F4TCNQ** devices showed more linear relationships between the R/R_0 and temperature changes in the range of 20 - 70 ^{o}C (Figure 5.11b & 5.11c). One possible reason for the nonlinearity of the R/R_0–T curve or the decrease in TCR at ca. 40^{o}C for the **PMNB:F4TCNQ** device might be due to the rather amorphous nature of **PMNB** due to the presence of two geometric isomers in this polymer as verified by the XRD data. The highly disordered polymer chains might be prone to move at a temperature higher than 40^{o}C, resulting in a larger distance between the conductive polymer backbones and/or polymer grains. This is a PTC competing factor that has been often observed in NTC-type sensors.[154,157,336,357,358]

The TCR values of the **PENB:F4TCNQ** and **PPNB:F4TCNQ** sensors are -1.04 %/^{o}C and -0.390 %/^{o}C, respectively. The higher TCR of **PENB:F4TCNQ** was likely due to its much shorter π-stacking distance of **PENB** than that of **PPNB**, which can promote the charge carrier hopping more significantly when temperature increases according to the VHR theory.

As a comparison, a PEDOT:PSS sensor was also fabricated using the similar procedure. The I-V graph of the PEDOT:PSS sensor can be seen in Figure 5.12a. During the initial baseline establishment phase, the sensor showed fluctuating current signals, which led to large variations when the temperature-dependent resistance measurement was carried out (Figure 5.12b). The device also showed a slightly nonlinear R/R_0–T graph with a turning point at ca. 50^{o}C (Figure

5.12c), which is typical for the PEDOT:PSS temperature sensors.[152,332] It has been interpreted that the insulating PSS dopant counterions expand at higher temperatures, which would notably enlarge the distance between the conductive PEDOT chains and/or grains, making the charge carrier hopping more difficult.[152,332] This serious PTC effect offsets the NTC effect at high temperatures (ca. 50^{o}C or above). The TCR values of PEDOT:PSS are -0.884 %/^{o}C in the range of 20-80^{o}C (Table 3), which was found to be a comparable value to some reported PEDOT:PSS based temperature sensors.[152,332,359] It should also be noted that although the freshly prepared PEDOT:PSS temperature sensor showed a reasonably high TCR, the baseline current tended to fluctuate after successive measurements and the resistance changes among individual devices were found to be highly inconsistent. The deviation of TCR values measured from the same material PEDOT:PSS could be originated from the imbalance charge transport mechanism within the polymer. PEDOT:PSS is a composite material that comprises of a hole transporting PEDOT polymer and an ions transporting PSS counterpart,[360] PSS electrolytic mobile ions could migrate and give changes to the macroscopic morphology when an electric current is passed through the polymer-dopant system for a long enough of time. It is also possible for the redox active PEDOT:PSS to undergo redox reactions in the presence of PSS electrolyte at opposite electrodes. In addition, there is also a known capacitive effect in PEDOT:PSS that could accumulate charges in the polymer composites,[361] especially in our study whereas the charge accumulation process would be quite severe in the current vs time measurement in our temperature sensors. All of these could influence the baseline current and the sensitivity of the sensor. Such phenomena may hinder the use of PEDOT:PSS for making practical, long-term stable sensors with reliable sensing accuracy.

The **PENB:F4TCNQ** temperature sensor was also tested for a warming-cooling cycle in between 20 – 24^{o}C The real-time *I-t* response can be seen in Figure 5.11d in which the sensor was cycled from 20 ↔ 22 ↔ 24^{o}C back and forth. The baseline current could be easily returned to the original level at each temperature cycle, showing an excellent reversibility of the temperature sensor. As the heat sensitivity of the sensor is greatly dependent on the thickness of the material and substrate,[362–365] the substrate of the device should also be as thin as possible to minimize any interference with measurements caused by the intrinsic thermal conductivity and heat capacity of the substrate. There have also been many reported high performance temperature sensors using thin polymer sheets such as polyethylene terephthalate (PET) as device substrates.[366–369] In order

to further optimize the temperature sensing performance of **PENB:F4TCNQ** and to demonstrate the possibility of printable and flexible electronics using the HID polymers, an all-solution processed temperature sensor was fabricated by blade-coating a thin film of **PENB:F4TCNQ** (20nm) as the thermal sensing layer on top of silver interdigitated electrodes printed on a flexible PET substrate. The flexible sensor was also passivated by blade-coating a thin layer of PMMA on top. The device responded to human body temperature when a finger was placed at the back of the PET substrate. The response to the skin temperature (ca. 33^{o}C) demonstrated a response time of as short as 9.2 seconds until the sensor reached 90% of the signal saturation with fast recovery back to the original background temperature (Figure 5.11e). The TCR of this device was found to be as high as 1.49 %/^{o}C. The higher TCR obtained from the flexible PET-based temperature sensor may be related to the thinner substrate, which allows heat to be transferred from the heat source to the **PENB:F4TCNQ** layer more effectively compared with the sensors on thick SiO_2 substrates. In general, all HID-based temperature sensors showed almost instant responses to small heat changes with good recovery. Other details such as device structures of the temperature sensors are summarized in Table 5.3.

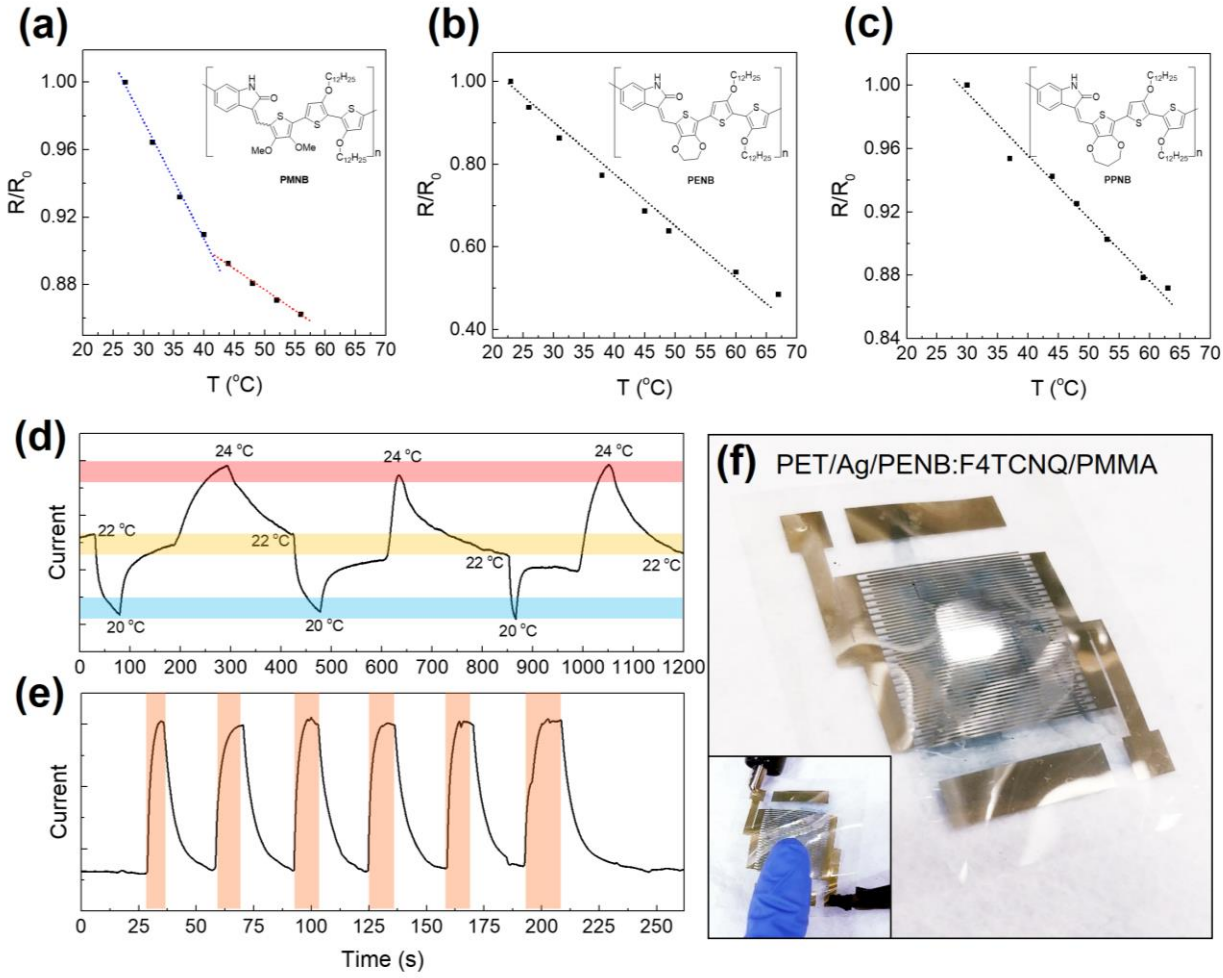

Figure 5.11. Temperature-dependent relative resistance changes of (a) **PMNB:F4TCNQ**; (b) **PENB:F4TCNQ** and (c) **PPNB:F4TCNQ**; (d) Real-time *I-t* curve of **PENB:F4TCNQ** temperature sensor device with temperature cycling between 20 – 24 ºC; (e) Real-time *I-t* curve of blade-coated **PENB:F4TCNQ** (20nm) on PET flexible interdigitated silver electrode platform for near body temperature sensing (~20-40 °C). Orange shaded areas represented the time when the back of the PET substrate was being touched by a human finger. (f) Photography of the all-solution processed flexible temperature sensor with 200µm channel length and W/L = 5000; bottom right hand corner shows the operating sensor being touched.

Table 5.3. Temperature sensor device properties and performances.

Polymer	Thickness (nm)	Substrate & electrodes	Working Range (°C)	TCR ± Std (%/°C)	Response Time ± Std (s)
PMNB:F4TCNQ	55	SiO_2/Cr/Au	25 - 40	-0.792 (± 0.112)	66.7 (± 13.3)
PMNB:F4TCNQ	55	SiO_2/Cr/Au	40 - 60	-0.330 (± 0.0560)	45.8 (± 4.30)
PENB:F4TCNQ	83	SiO_2/Cr/Au	25 - 70	-1.04 (± 0.120)	91.6 (± 1.41)
PPNB:F4TCNQ	62	SiO_2/Cr/Au	25 - 60	-0.390 (± 0.0423)	57.3 (± 16.2)
PEDOT:PSS	30	SiO_2/Cr/Au	25 - 80	-0.884 (± 0.275)	79.8 (± 10.9)
PENB:F4TCNQ	20	PET/Ag	20 - 40	-1.49 (± 0.0416)	14.6 (± 4.65)

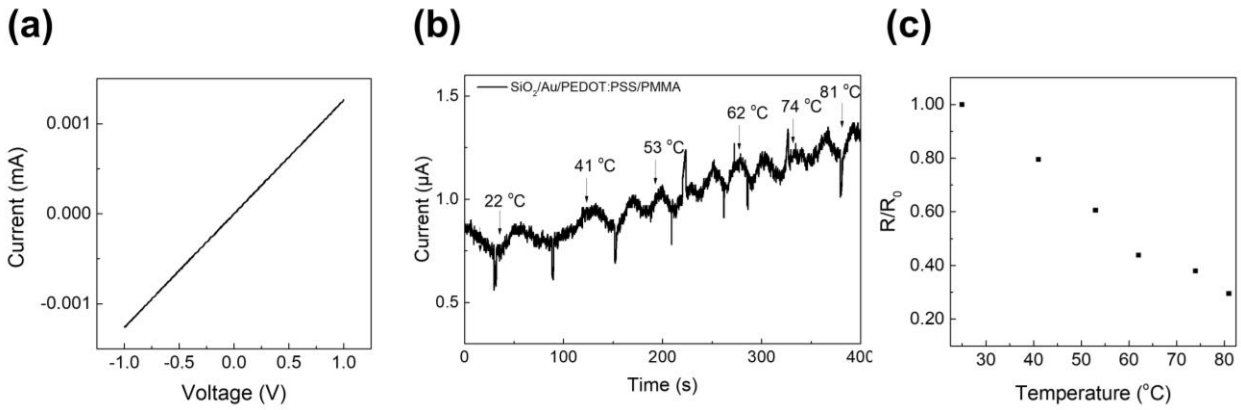

Figure 5.12. (a) Current versus voltage (I-V) scanning of PEDOT:PSS based temperature sensor from -1 to +1 V at 25°C; (b) Real-time current versus time (I-t) graphs at varying temperatures for PEDOT:PSS based temperature sensor; (c) Temperature-dependent relative resistance changes of PEDOT:PSS.

5.2.5. Hypothesized Charge Transport Mechanism

In order to further investigate the charge transport mechanisms, we employed the Mott's variable range hopping theory (VRH) to investigate the charge transport mechanism of the HID polymers, together with PEDOT:PSS as a reference. The general equation for temperature dependent conductivity is depicted in Equation 5.2:[333]

$$\sigma = \sigma_0 \, e \left[-\left(\frac{T_0}{T}\right)^{\alpha}\right] \qquad \textbf{(Equation 5.2)}$$

where σ is the electrical conductivity, σ_0 is the conductivity at infinite temperature, T_0 is the characteristic temperature and α is equal to $1/(1+D)$, where D is dimensionality of the system.

According to different reported literatures, the charge transport of PEDOT:PSS followed different mechanisms and were found to have debatable dimensionalities.[201,370,371] In our study, the encapsulated PEDOT:PSS temperature sensor was found to have α = ½ , when the correlation coefficient of the $ln(\sigma)$-T^{α} plot was found to be the highest among the other 2D and 3D models (Figure 5.13a). The 1D transport was believed to have a structure of parallel straight conductive chains in polymers (eg. rigid conjugated linear backbone of the PEDOT polymer). When there is no blocking of charge carriers, the transport is unidirectional and behaved like granular metals.[372–374] It was also found that the best fit correlation for the $ln(\sigma)$-T^{α} plot of **PMNB:F4TCNQ** would be α = ½, where this system should also follow a 1D transport mechanism (Figure 5.13b). In contrary, the best fit lines of $ln(\sigma)$-T^{α} plots with highest correlation coefficient for **PENB:F4TCNQ** and **PPNB:F4TCNQ** were found to have α = ¼ where these systems should follow a 3-dimensional charge hopping mechanism (Figure 5.13c and 5.13d). Despite the dimensionality of each F4TCNQ doped HID polymers can be estimated by the VRH model, the exact relationship between the polymer chemical structure, bulk morphology, film crystallinity, processing conditions and their hopping transport dimensionality may still need to be further investigated.

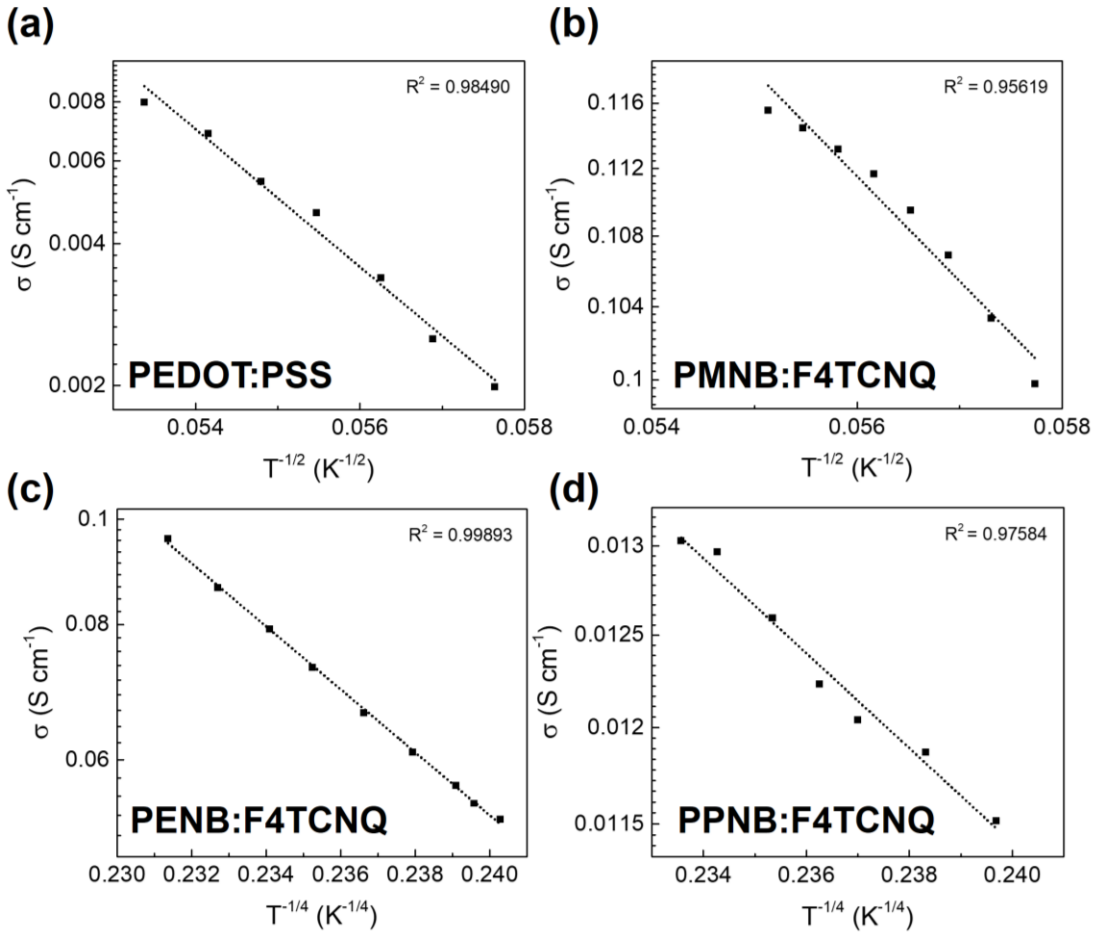

Figure 5.13. Temperature dependent conductivity of (a) PEDOT:PSS; (b) **PMNB:F4TCNQ**; (c) **PENB:F4TCNQ**; & (e) **PPNB:F4TCNQ**.

5.3. Conclusion

We reported the synthesis of four new asymmetric donor-acceptor polymers **PTEB**, **PMEB**, **PEEB** and **PPEB**, that when heated at elevated temperature can be converted to hydrogen-bonds cross-linked polymers **PTNB**, **PMNB**, **PENB** and **PPNB** with high E_{HOMO} up to -4.69, -4.55, -4.68 and -4.47eV.

The hydrogen-bonds cross-linked polymers can be doped by a p-type dopant **F4TCNQ**, converting them into conductive DA polymers **PTNB:F4TCNQ**, **PMNB:F4TCNQ**, **PENB:F4TCNQ** and **PPNB:F4TCNQ**. The hydrogen-bonds in the polymers create a connected network between individual polymer chains, decreasing the distances to facilitate charge carrier hopping during electrical conduction. In other words, the hydrogen-bonds minimized the PTC-effect by reducing

the volume expansion especially at high temperature which could increase the resistance of the sensing element, while enhancing the NTC-effect in the conductive polymer-based temperature sensors.

Three of the doped polymers **PMNB:F4TCNQ**, **PENB:F4TCNQ** and **PPNB:F4TCNQ** exhibited excellent polymer:dopant stability with almost no or little decay in electrical conductivity after 1 month of storage in ambient. NTC-type temperature sensors were fabricated using these three doped polymers as the sensing element. The devices can be operated at low operational power (1 volt) with stable and reversible temperature sensitivity. The highest TCR in this series polymers was obtained from the **PENB:F4TCNQ** temperature sensor fabricated on silicon dioxide wafer having TCR = -1.04 (± 0.120) %/^{o}C at 25 – 70 ^{o}C, while the sensor fabricated on flexible PET substrate can reach up to -1.49 (± 0.0416) %/^{o}C at 20 – 40 ^{o}C which is in the range of near body temperature with only 2.79% deviation in TCR value.

The charge transport mechanisms of the conductive polymer **PMNB:F4TCNQ**, **PENB:F4TCNQ**, and **PPNB:F4TCNQ** were found to follow a 1D, 3D, and 3D charge hopping mechainsm in the VRH theory. The introduction of asymmetric structures and an appropriate degree of steric hindrance induced by substituent units resulted the doped HID polymers to be high performance NTC-type temperature sensors profoundly seen in the representative amorphous conductive **PENB:F4TCNQ** polymer that can minimize the effect of phase segregation of polymer:dopant. The relationship of the structural or morphological dependence dimensionality of charge hopping mechanism in F4TCNQ doped HID polymers will be further investigated.

The device showed excellent real-time sensitivity and cyclability, and the novel HID-polymers and their thin film temperature sensors may find useful applications in accurate real-time temperature monitoring applications. Further investigation will be carried out to look into the potential development of wearable electronics for skin temperature monitoring in healthcare, medical devices. Other potential applications may also include thermal array used in tactile sensing for artificial skin technologies in the future.

Chapter 6: Conclusion and Future Outlook

6.1. Conclusions

The major contributions in this study are summarized as follows:

- Using hydrogen-bonds containing D-A polymers to enhance the selectivity in OFET or chemiresistive based sensors to detect chemical analytes or physical parameters such as fluoride anions, volatile organic liquids and temperature changes.
- NMR and UV-Vis-NIR titration was used to support the DFT simulated sensing mechanism in fluoride anion detection in indigo-based D-A polymer semiconductor.
- Using an indigo-based amide D-A polymer to achieve a highly fluoride ion selective aqueous sensor with LOD of 0.40 mM.
- Development of semiconducting or conducting polymer systems which enable fast and stable sensing baseline establishment, together with high sensitivity and recovery rate with the use of polar functional groups such as amides, carbamates and ethers.
- Using asymmetric building blocks such as hemi-isoindigo and supramolecular interactions such as hydrogen-bonds to induce randomness in polymer morphologies, which can create amorphous conductive polymers with high polarity for achieving long-term polymer:dopant environmental stability.
- Using the hemi-isoindigo-based amide D-A polymers to achieve a high TCR value up to -1.49 %/^{o}C on flexible substrate with fast response and accuracy.

In Chapter 3, two new indigo-based D-A semiconductor polymers **PIDG-T-C20** and **PIDG-BT-C20** were synthesized. These polymers were found to be fluoride or anionic sensor in aqueous sensing owing to the hydrophilic nature of the free N-H moieties on the amide functionality of the polymer backbone. With the aid of ^{1}HNMR titration, UV-Vis spectroscopy and DFT calculations, it is hypothesized that the amide moieties on **PIDG-BT-C20** act as recognition sites for anions and the hydrogen-bonds are responsible for anions recognition, with high fluoride ions sensitivity when operated as a WGOFET. The OFET of these polymers were also shown to have hole mobilities up to a magnitude of 10^{-2} $cm^2V^{-1}s^{-1}$. The starting material for synthesizing the indigo-based polymers is 3-hydroxybenzaldehyde, which is an abundant, low-cost and easily accessible starting material.

In Chapter 4, a new diketopyrrolopyrrole-based D-A polymer **PDEB** was synthesized which acts as a precursor polymer to yield the chemical resistant **PDNB** polymer. **PDEB** can be easily converted to **PDNB** by thermal annealing at 250^{o}C to release N-H moieties on the DPP backbone with intermolecular hydrogen-bonds. The intermolecular hydrogen-bonds are believed to form a cross-linked network which resulted the polymer thin film (~30nm) to be completely insoluble in most organic solvents, and at the same time retaining the electrical conductivity of the polymer when it is doped by a low-cost hydrochloric acid (HCl) dopant. A single conductive polymer **PDNB:HCl** used in the chemiresistive sensor as the sensing element is able to distinguish up to 10 different volatile organic liquids with unique fingerprint current vs. time (*I-t*) profiles powered at as low as 1V, and is reported to be a novel concept for liquid chemical sensing.

In Chapter 5, a series of novel hemi-isoindigo-based D-A polymers were reported namely **PTEB**, **PMEB**, **PEEB**, and **PPEB**. These reported polymers can also have their side chains thermally removed to yield hydrogen-bonds cross-linked polymers **PTNB**, **PMNB**, **PENB**, and **PPNB**. The **F4TCNQ** doped polymers **PMNB:F4TCNQ**, **PENB:F4TCNQ**, and **PPNB:F4TCNQ** were found to be negative-type coefficient (NTC) conductive materials with working temperature range from 20–70^{o}C powered at 1V, in which the resistivity of the material decreases with an increasing temperature, opposite to that of metals. In this case, the cross-linked amide hydrogen-bonds minimized the PTC-effect when the materials are used as NTC temperature sensors by reducing the volume expansion effect of insulating moieties within the polymer when the sensor is operated at high temperatures. At the same time, the polar hydrogen-bonds and polar units in the thiophene spacer are able to trap dopant molecules in the amorphous regions of the polymer to prevented phase segregation of the polymers and dopant to improve the polymer:dopant stability. The investigation also included engineering of the substituent effects on the thiophene spacer on the HID core of the HID-based polymers, and it was found by stability experiments and DFT calculations that the higher the polarity and dipole magnitude of the HID-polymers, the higher the stability of the polymer:dopant complexes. Therefore, in one of the best engineered HID polymer:dopant systems, **PENB:F4TCNQ** were found to have a TCR value as high as -1.04%/^{o}C on rigid substrate and -1.49%/^{o}C on flexible substrate, together with a long-term ambient stability.

6.2. Recommended Future Research and Future Outlook

6.2.1. Using a Continual Flow System in WGOFET

In chapter 3, the WGOFET sensor was constructed by placing a drop of 20 μL of 18 MΩ deionized (DI) water droplet on top of the channeling area on the transistor as the water-gate dielectric. However, this method may have a drawback that when analyte was injected into the droplet, the volume and concentration of the water-gate droplet would be different. This limits the number of uses for the sensor as the water-gate droplet expands or the accumulation of analyte may alter the concentration of the droplet and changes its capacitance. This makes repeatable measurement or quantitative analysis using a single device less accurate and less convenient. A way to solve this issue is by creating a continual liquid flow system as the water-gate dielectric that can carry both the water-gate dielectric and the anionic analyte for detection. By tuning the flow rate in the flow cell, the analyte can be washed away easily after a sensing cycle so that the baseline of the device can be recalibrated immediately for repeatable sensing.

6.2.2. Testing I-t Fingerprints for Non-volatile Compounds

In chapter 4, the liquid analyes used for the chemiresistive sensor are limited to volatile organic liquids. The later part of the *I-t* fingerprints was based on the time-of-desorption (TOD) of the chemical desorbing from the surface of sensor. The desorption rate of a liquid analyte is proportional to its vapor pressure or boiling point of the compound. For non-volatile compounds, the sensor may not be able to observe a unique desorption pattern in a short period of time, and the time required for complete desorption may be very long or would be infinite for non-volatile compounds. Therefore, adding a heating element at the sensor chip or carrying out the sensing at a low pressure may be able to test for *I-t* fingerprints of some non-volatile compounds or even solids, so as to break through the current limitation of this type of sensor.

6.2.3. Establishing an I-t Fingerprint Database and Testing of Mixture of Compounds

In chapter 4, ten pure volatile liquids were tested for their *I-t* fingerprints. Since the *I-t* fingerprints were found to be very unique for different analytes and the testing can be repeated to give almost identical *I-t* patterns, it is possible to repeatedly collect *I-t* profiles for different known compounds and establish a collection of *I-t* database for each unique compound. By employing artificial intelligence (AI) and machine learning techniques, the database can be used for unknown

compounds deduction. Different features from the signal can also be extracted using principal component analysis (PCA) by computational calculations. Later on, *I-t* signals of mixture of compounds with unknown contents can be analyzed using the sensor and the big data from the *I-t* database by deconvolution methods. Such technology may lead to the development of potential smart electronic nose or electronic tongue used in various areas.

6.2.4. Testing of HID-based Polymer Temperature Sensors in Wide Temperature Ranges

In chapter 5, the temperature sensors were tested in temperature ranges from ~20-100ºC. Temperature dependent conductivity measurements in a wider range shall be tested in order to extract more accurate information such as charge hopping dimensionality and thermal activation energy of the hopping mechanisms. In particular, conductivity of the polymer at low temperatures should also be tested as this type of sensor may find useful applications in real-time temperature monitoring used in "cold chain logistics" which is a process for the safe transport of temperature-sensitive substances and products.

6.2.5. Density Functional Theory (DFT) and Natural Bond Order (NBO) Analyses

For the HID-based polymers synthesized in chapter 5, DFT and NBO analyses can be performed to study the stability of the conductive polymers in term of electronic effect. From the previous results, DFT was used to simulate the physical properties of the polymers only such as direction of dipole moment, dipole magnitude, UV-Vis-NIR absorption and charge distribution of the neutral or polaronic model compounds. Using NBO analysis in DFT, it would be possible to simulate the electronic environment in a model compound by identifying donor-acceptor molecular orbitals (MOs) in the compound. As the substituent effects played a significant role in the HID-polymer system, NBO analysis would be able to distinguish small differences of electronic distributions in terms of chemical bonding between each bonded atoms in the model compound in order to find out the highest energy (most unstable) or lowest energy (most stable) bonds. Electronic and charge distribution can then be simulated to look into polarons stability and study the feasibility of any polaron dissociation reactions that can occur at any particular bonds. The study can possibly lead to development of a systematic tool for designing stable polymer:dopant complexes for organic chemists by rationally engineering the substituents on a conductive polymer backbone with the aid of quantum mechanical tools.

6.2.6. Electron Spin Resonance (ESR) Spectroscopy

For the conductive polymers synthesized in Chapter 4 and 5, ESR spectroscopy can used to measure the concentration of delocalized radical cations (polarons) present in the doped polymers. This may give additional information to the stability of polymer:dopant complexes in terms of polaron stability, doping states, polaron concentration and other quantum mechanical information.

Bibliography

[1] A. Facchetti, M. H. Yoon, T. J. Marks, *Adv. Mater.* **2005**, *17*, 1705.

[2] Y. Wen, Y. Liu, Y. Guo, G. Yu, W. Hu, *Chem. Rev.* **2011**, *111*, 3358.

[3] P. Lin, F. Yan, Organic thin-film transistors for chemical and biological sensing. *Adv. Mater.* **2012**, *24*, 34–51.

[4] O. Y. Kweon, M. Y. Lee, T. Park, H. Jang, A. Jeong, M. K. Um, J. H. Oh, *J. Mater. Chem. C* **2019**, *7*, 1525.

[5] C. Zhang, P. Chen, W. Hu, Organic field-effect transistor-based gas sensors. *Chem. Soc. Rev.* **2015**, *44*, 2087–2107.

[6] H. Li, W. Shi, J. Song, H. J. Jang, J. Dailey, J. Yu, H. E. Katz, *Chem. Rev.* **2019**, *119*, 3.

[7] D. Elkington, M. Wasson, W. Belcher, P. C. Dastoor, X. Zhou, *Appl. Phys. Lett.* **2015**, *106*, 263301.

[8] O. Knopfmacher, M. L. Hammock, A. L. Appleton, G. Schwartz, J. Mei, T. Lei, J. Pei, Z. Bao, *Nat. Commun.* **2014**, *5*, 2954.

[9] L. Sims, H. J. Egelhaaf, J. A. Hauch, F. R. Kogler, R. Steim, *Compr. Renew. Energy* **2012**, *1*, 439.

[10] D. P. Hagberg, J. H. Yum, H. J. Lee, F. De Angelis, T. Marinado, K. M. Karlsson, R. Humphry-Baker, L. Sun, A. Hagfeldt, M. Grätzel, M. K. Nazeeruddin, *J. Am. Chem. Soc.* **2008**, *130*, 6259.

[11] N. Stutzmann, R. H. Friend, H. Sirringhaus, *Science (80-.).* **2003**, *299*, 1881.

[12] R. H. Friend, R. W. Gymer, A. B. Holmes, J. H. Burroughes, R. N. Marks, C. Taliani, D. D. C. Bradley, D. A. Dos Santos, J. L. Brédas, M. Lögdlund, W. R. Salaneck, *Nature* **1999**, *397*, 121.

[13] L. Schmidt-Mende, A. Fechtenkötter, K. Müllen, E. Moons, R. H. Friend, J. D. MacKenzie, *Science (80-.).* **2001**, *293*, 1119.

[14] D. D. Li, J. X. Wang, Y. Ma, H. S. Qian, D. Wang, L. Wang, G. Zhang, L. Qiu, Y. C. Wang, X. Z. Yang, *ACS Appl. Mater. Interfaces* **2016**, *8*, 19312.

[15] Organic Electronics Market Size, Share Report 2020 to 2027. *https://www.precedenceresearch.com/organic-electronics-market*.

[16] H. Shirakawa, E. J. Louis, A. G. MacDiarmid, C. K. Chiang, A. J. Heeger, *J. Chem. Soc. Chem. Commun.* **1977**, 578.

[17] S. J. Choi, B. H. Jang, S. J. Lee, B. K. Min, A. Rothschild, I. D. Kim, *ACS Appl. Mater. Interfaces* **2014**, *6*, 2588.

[18] A. Dey, Semiconductor metal oxide gas sensors: A review. *Mater. Sci. Eng. B Solid-State Mater. Adv. Technol.* **2018**, *229*, 206–217.

[19] C. Wang, L. Yin, L. Zhang, D. Xiang, R. Gao, *Sensors* **2010**, *10*, 2088.

[20] A. Ponzoni, E. Comini, I. Concina, M. Ferroni, M. Falasconi, E. Gobbi, V. Sberveglieri, G. Sberveglieri, *Sensors (Switzerland)* **2012**, *12*, 17023.

[21] K. K. Makhija, A. Ray, R. M. Patel, U. B. Trivedi, H. N. Kapse, *Bull. Mater. Sci.* **2005**, *28*, 9.

[22] E. Comini, G. Faglia, G. Sberveglieri, Z. Pan, Z. L. Wang, *Appl. Phys. Lett.* **2002**, *81*, 1869.

[23] Z. Liu, T. Yamazaki, Y. Shen, T. Kikuta, N. Nakatani, Y. Li, *Sensors Actuators, B Chem.* **2008**, *129*, 666.

[24] Z. Jin, Y. Su, Y. Duan, *Sensors Actuators, B Chem.* **2000**, *71*, 118.

[25] M. Šetka, J. Drbohlavová, J. Hubálek, *Sensors (Switzerland)* **2017**, *17*.

[26] Y. Wen, J. Xu, *J. Polym. Sci. Part A Polym. Chem.* **2017**, *55*, 1121.

[27] I. Lähdesmäki, A. Lewenstam, A. Ivaska, *Talanta* **1996**, *43*, 125.

[28] H. S. Song, O. S. Kwon, S. H. Lee, S. J. Park, U. K. Kim, J. Jang, T. H. Park, *Nano Lett.* **2013**, *13*, 172.

[29] W. Shi, X. Yu, Y. Zheng, J. Yu, *Sensors Actuators, B Chem.* **2016**, *222*, 1003.

[30] H. Fan, S. Han, Z. Song, J. Yu, H. E. Katz, *Org. Electron.* **2019**, *67*, 247.

[31] R. Song, Z. Wang, X. Zhou, L. Huang, L. Chi, *Chempluschem* **2019**, *84*, 1222.

[32] D. Khim, G. S. Ryu, W. T. Park, H. Kim, M. Lee, Y. Y. Noh, *Adv. Mater.* **2016**, *28*, 2752.

[33] T. Hasegawa, J. Takeya, *Sci. Technol. Adv. Mater.* **2009**, *10*.

[34] G. Kim, S. J. Kang, G. K. Dutta, Y. K. Han, T. J. Shin, Y. Y. Noh, C. Yang, *J. Am. Chem. Soc.* **2014**, *136*, 9477.

[35] H. Klauk, M. Halik, U. Zschieschang, F. Eder, G. Schmid, C. Dehm, *Appl. Phys. Lett.* **2003**, *82*, 4175.

[36] M. L. Tang, T. Okamoto, Z. Bao, *J. Am. Chem. Soc.* **2006**, *128*, 16002.

[37] C. D. Sheraw, T. N. Jackson, D. L. Eaton, J. E. Anthony, *Adv. Mater.* **2003**, *15*, 2009.

[38] Q. Miao, M. Lefenfeld, T. Q. Nguyen, T. Siegrist, C. Kloc, C. Nuckolls, *Adv. Mater.* **2005**, *17*, 407.

[39] S. Ando, J. I. Nishida, E. Fujiwara, H. Tada, Y. Inoue, S. Tokito, Y. Yamashita, *Chem. Mater.* **2005**, *17*, 1261.

[40] H. Meng, F. Sun, M. B. Goldfinger, G. D. Jaycox, Z. Li, W. J. Marshall, G. S. Blackman, *J. Am. Chem. Soc.* **2005**, *127*, 2406.

[41] K. Oikawa, H. Monobe, K. I. Nakayama, T. Kimoto, K. Tsuchiya, B. Heinrich, D. Guillon, Y. Shimizu, M. Yokoyama, *Adv. Mater.* **2007**, *19*, 1864.

[42] M. Halik, H. Klauk, U. Zschieschang, G. Schmid, S. Ponomarenko, S. Kirchmeyer, W. Weber, *Adv. Mater.* **2003**, *15*, 917.

[43] Y. Sakamoto, T. Suzuki, M. Kobayashi, Y. Gao, Y. Fukai, Y. Inoue, F. Sato, S. Tokito, *J. Am. Chem. Soc.* **2004**, *126*, 8138.

[44] P. R. L. Malenfant, C. D. Dimitrakopoulos, J. D. Gelorme, L. L. Kosbar, T. O. Graham, A. Curioni, W. Andreoni, *Appl. Phys. Lett.* **2002**, *80*, 2517.

[45] B. A. Jones, M. J. Ahrens, M. H. Yoon, A. Facchetti, T. J. Marks, M. R. Wasielewski, *Angew. Chemie - Int. Ed.* **2004**, *43*, 6363.

[46] M. M. Ling, P. Erk, M. Gomez, M. Koenemann, J. Locklin, Z. Bao, *Adv. Mater.* **2007**, *19*, 1123.

[47] B. A. Jones, A. Facchetti, T. J. Marks, M. R. Wasielewski, *Chem. Mater.* **2007**, *19*, 2703.

[48] Z. Wang, C. Kim, A. Facchetti, T. J. Marks, *J. Am. Chem. Soc.* **2007**, *129*, 13362.

[49] S. Kobayashi, T. Takenobu, S. Mon, A. Fujiwara, Y. Iwasa, *Appl. Phys. Lett.* **2003**, *82*, 4581.

[50] T. D. Anthopoulos, G. C. Anyfantis, G. C. Papavassiliou, D. M. De Leeuw, *Appl. Phys. Lett.* **2007**, *90*.

[51] P. H. Wöbkenberg, J. Ball, D. D. C. Bradley, T. D. Anthopoulos, F. Kooistra, J. C. Hummelen, D. M. De Leeuw, *Appl. Phys. Lett.* **2008**, *92*.

[52] H. A. M. Van Mullekom, J. A. J. M. Vekemans, E. E. Havinga, E. W. Meijer, *Mater. Sci. Eng. R Reports* **2001**, *32*, 1.

[53] T. Abidin, Q. Zhang, K. L. Wang, D. J. Liaw, *Polymer (Guildf).* **2014**, *55*, 5293.

[54] G. Gunbas, L. Toppare, *Chem. Commun.* **2012**, *48*, 1083.

[55] C. M. Amb, A. L. Dyer, J. R. Reynolds, *Chem. Mater.* **2011**, *23*, 397.

[56] A. Liscio, G. De Luca, F. Nolde, V. Palermo, K. Müllen, P. Samorì, *J. Am. Chem. Soc.* **2008**, *130*, 780.

[57] *Synthetic Methods for Conjugated Polymers and Carbon Materials*; Leclerc, M.; Morin, J.-F., Eds.; Wiley-VCH Verlag GmbH & Co. KGaA: Weinheim, Germany, 2017.

[58] Z. Liu, G. Zhang, Z. Cai, X. Chen, H. Luo, Y. Li, J. Wang, D. Zhang, *Adv. Mater.* **2014**, *26*, 6965.

[59] M. U. Ocheje, B. P. Charron, Y. H. Cheng, C. H. Chuang, A. Soldera, Y. C. Chiu, S. Rondeau-Gagné, *Macromolecules* **2018**, *51*, 1336.

[60] A. Pron, M. Leclerc, *Prog. Polym. Sci.* **2013**, *38*, 1815.

[61] J. Lee, A. R. Han, J. Hong, J. H. Seo, J. H. Oh, C. Yang, *Adv. Funct. Mater.* **2012**, *22*, 4128.

[62] P. Gawrys, D. Boudinet, M. Zagorska, D. Djurado, J. M. Verilhac, G. Horowitz, J. Pécaud, S. Pouget, A. Pron, *Synth. Met.* **2009**, *159*, 1478.

[63] C. Zhu, A. U. Mu, C. Wang, X. Ji, L. Fang, *ACS Macro Lett.* **2018**, *7*, 801.

[64] G. R. Desiraju, *Acc. Chem. Res.* **1996**, *29*, 441.

[65] C. B. Aakery, A. M. Beatty, B. A. Helfrich, *Angew. Chemie - Int. Ed.* **2001**, *40*, 3240.

[66] C. B. Aakeröy, A. M. Beatty, *Chem. Commun.* **1998**, 1067.

[67] Z. F. Liu, X. Chen, Z. F. Mou, W. J. Jin, *J. Mater. Chem. C* **2020**, *8*, 16100.

[68] J. Dhar, D. P. Karothu, S. Patil, *Chem. Commun.* **2015**, *51*, 97.

[69] B. Liu, J. Li, W. Zeng, W. Yang, H. Yan, D. C. Li, Y. Zhou, X. Gao, Q. Zhang, *Chem. Mater.* **2021**, *33*, 580.

[70] H. Huang, L. Yang, A. Facchetti, T. J. Marks, *Chem. Rev.* **2017**, *117*, 10291.

[71] Y. Wang, T. Hasegawa, H. Matsumoto, T. Michinobu, *J. Am. Chem. Soc.* **2019**, *141*, 3566.

[72] T. Maeda, A. Liess, A. Kudzus, A. M. Krause, M. Stolte, H. Amitani, S. Yagi, H. Fujiwara, F. Würthner, *Chem. Commun.* **2020**, *56*, 9890.

[73] K. Liu, X. Zhao, Q. Liu, J. Huo, B. Zhu, S. Diao, *Beilstein J. Org. Chem.* **2015**, *11*, 563.

[74] Y. Wu, X. Peng, J. Fan, S. Gao, M. Tian, J. Zhao, S. Sun, *J. Org. Chem.* **2007**, *72*, 62.

[75] H. S. Jung, H. J. Kim, J. Vicens, J. S. Kim, *Tetrahedron Lett.* **2009**, *50*, 983.

[76] J. Y. Li, X. Q. Zhou, Y. Zhou, Y. Fang, C. Yao, *Spectrochim. Acta - Part A Mol. Biomol. Spectrosc.* **2013**, *102*, 66.

[77] C. Guo, W. Hong, H. Aziz, Y. Li, *Rev. Adv. Sci. Eng.* **2012**, *1*, 200.

[78] S. Goswami, S. Maity, A. C. Maity, A. K. Das, B. Pakhira, K. Khanra, N. Bhattacharyya, S. Sarkar, *RSC Adv.* **2015**, *5*, 5735.

[79] M. J. Minch, *J. Chem. Educ.* **1999**, *76*, 759.

[80] J. J. Dannenberg, *J. Am. Chem. Soc.* **1998**, *120*, 5604.

[81] G. A. Jeffrey, W. Saenger, *Hydrogen Bonding in Biological Structures*; 1991.

[82] C. Zhu, A. J. Kalin, L. Fang, *Acc. Chem. Res.* **2019**, *52*, 1089.

[83] E. D. Głowacki, M. Irimia-Vladu, M. Kaltenbrunner, J. Gsiorowski, M. S. White, U. Monkowius, G. Romanazzi, G. P. Suranna, P. Mastrorilli, T. Sekitani, S. Bauer, T. Someya, L. Torsi, N. S. Sariciftci, *Adv. Mater.* **2013**, *25*, 1563.

[84] I. V. Klimovich, L. I. Leshanskaya, S. I. Troyanov, D. V. Anokhin, D. V. Novikov, A. A. Piryazev, D. A. Ivanov, N. N. Dremova, P. A. Troshin, *J. Mater. Chem. C* **2014**, *2*, 7621.

[85] E. D. Głowacki, H. Coskun, M. A. Blood-Forsythe, U. Monkowius, L. Leonat, M. Grzybowski, D. Gryko, M. S. White, A. Aspuru-Guzik, N. S. Sariciftci, *Org. Electron.* **2014**, *15*, 3521.

[86] E. Daniel Głowacki, L. Leonat, M. Irimia-Vladu, R. Schwödiauer, M. Ullah, H. Sitter, S.

Bauer, N. Serdar Sariciftci, *Appl. Phys. Lett.* **2012**, *101*.

[87] E. D. Głowacki, G. Romanazzi, C. Yumusak, H. Coskun, U. Monkowius, G. Voss, M. Burian, R. T. Lechner, N. Demitri, G. J. Redhammer, N. Sünger, G. P. Suranna, S. Sariciftci, *Adv. Funct. Mater.* **2015**, *25*, 776.

[88] E. D. Glowacki, L. Leonat, G. Voss, M. Bodea, Z. Bozkurt, M. Irimia-Vladu, S. Bauer, N. S. Sariciftci, *Org. Semicond. Sensors Bioelectron. IV* **2011**, *8118*, 81180M.

[89] D. Berg, C. Nielinger, W. Mader, M. Sokolowski, *Synth. Met.* **2009**, *159*, 2599.

[90] J. T. E. Quinn, J. Zhu, X. Li, J. Wang, Y. Li, *J. Mater. Chem. C* **2017**, *5*, 8654.

[91] J. Yang, B. Xiao, K. Tajima, M. Nakano, K. Takimiya, A. Tang, E. Zhou, *Macromolecules* **2017**, *50*, 3179.

[92] S. V. Bhosale, C. H. Jani, S. J. Langford, *Chem. Soc. Rev.* **2008**, *37*, 331.

[93] L. Zang, Y. Che, J. S. Moore, *Acc. Chem. Res.* **2008**, *41*, 1596.

[94] R. Schmidt, J. H. Oh, Y. Sen Sun, M. Deppisch, A. M. Krause, K. Radacki, H. Braunschweig, M. Könemann, P. Erk, Z. Bao, F. Würthner, *J. Am. Chem. Soc.* **2009**, *131*, 6215.

[95] J. Soeda, T. Uemura, Y. Mizuno, A. Nakao, Y. Nakazawa, A. Facchetti, J. Takeya, *Adv. Mater.* **2011**, *23*, 3681.

[96] A. S. Molinari, H. Alves, Z. Chen, A. Facchetti, A. F. Morpurgo, *J. Am. Chem. Soc.* **2009**, *131*, 2462.

[97] J. Huang, Z. Mao, Z. Chen, D. Gao, C. Wei, W. Zhang, G. Yu, *Chem. Mater.* **2016**, *28*, 2209.

[98] J. Shin, H. A. Um, D. H. Lee, T. W. Lee, M. J. Cho, D. H. Choi, *Polym. Chem.* **2013**, *4*, 5688.

[99] G. E. Park, J. Shin, D. H. Lee, M. J. Cho, D. H. Choi, *J. Polym. Sci. Part A Polym. Chem.* **2015**, *53*, 1226.

[100] M. J. Cho, J. Shin, T. R. Hong, H. A. Um, T. W. Lee, G. W. Kim, J. H. Kwon, D. H. Choi, *Polym. Chem.* **2015**, *6*, 150.

[101] J. S. Ha, K. H. Kim, D. H. Choi, *J. Am. Chem. Soc.* **2011**, *133*, 10364.

[102] Y. Gao, Y. Deng, H. Tian, J. Zhang, D. Yan, Y. Geng, F. Wang, *Adv. Mater.* **2017**, *29*, 1606217.

[103] R. Stalder, J. Mei, K. R. Graham, L. A. Estrada, J. R. Reynolds, *Chem. Mater.* **2014**, *26*, 664.

[104] E. D. Głowacki, G. Voss, L. Leonat, M. Irimia-Vladu, S. Bauer, N. S. Sariciftci, *Isr. J. Chem.* **2012**, *52*, 540.

[105] S. Mun, Y. Park, Y. E. K. Lee, M. M. Sung, *Langmuir* **2017**, *33*, 13554.

[106] J. Huang, J. Sun, H. E. Katz, *Adv. Mater.* **2008**, *20*, 2567.

[107] M. Wu, S. Hou, X. Yu, J. Yu, *J. Mater. Chem. C* **2020**, *8*, 13482.

[108] B. Shao, Y. Liu, X. Zhuang, S. Hou, S. Han, X. Yu, J. Yu, *J. Mater. Chem. C* **2019**, *7*, 10196.

[109] T. Mukhopadhyaya, J. S. Wagner, H. Fan, H. E. Katz, *ACS Appl. Mater. Interfaces* **2020**, *12*, 21974.

[110] Z. Wang, L. Huang, X. Zhu, X. Zhou, L. Chi, *Adv. Mater.* **2017**, *29*, 1703192.

[111] W. Huang, X. Zhuang, F. S. Melkonyan, B. Wang, L. Zeng, G. Wang, S. Han, M. J. Bedzyk, J. Yu, T. J. Marks, A. Facchetti, *Adv. Mater.* **2017**, *29*, 1701706.

[112] H. Li, J. Dailey, T. Kale, K. Besar, K. Koehler, H. E. Katz, *ACS Appl. Mater. Interfaces* **2017**, *9*, 20501.

[113] B. Nketia-Yawson, A. R. Jung, Y. Noh, G. S. Ryu, G. D. Tabi, K. K. Lee, B. Kim, Y. Y. Noh, *ACS Appl. Mater. Interfaces* **2017**, *9*, 7322.

[114] J. Lu, D. Liu, J. Zhou, Y. Chu, Y. Chen, X. Wu, J. Huang, *Adv. Funct. Mater.* **2017**, *27*, 1700018.

[115] X. Zhuang, D. Zhang, X. Wang, X. Yu, J. Yu, *Appl. Phys. Lett.* **2018**, *113*, 263301.

[116] K. Besar, J. Dailey, X. Zhao, H. E. Katz, *J. Mater. Chem. C* **2017**, *5*, 6506.

[117] W. Huang, K. Besar, R. Lecover, A. M. Rule, P. N. Breysse, H. E. Katz, *J. Am. Chem. Soc.* **2012**, *134*, 14650.

[118] Y. Yang, G. Zhang, H. Luo, J. Yao, Z. Liu, D. Zhang, *ACS Appl. Mater. Interfaces* **2016**, *8*, 3635.

[119] S. Hou, J. Yu, X. Zhuang, D. Li, Y. Liu, Z. Gao, T. Sun, F. Wang, X. Yu, *ACS Appl. Mater. Interfaces* **2019**, *11*, 44521.

[120] R. D. Yang, J. Park, C. N. Colesniuc, I. K. Schuller, J. E. Royer, W. C. Trogler, A. C. Kummel, *J. Chem. Phys.* **2009**, *130*, 164703.

[121] T. Shaymurat, Q. Tang, Y. Tong, L. Dong, Y. Liu, *Adv. Mater.* **2013**, *25*, 2269.

[122] H. Luo, S. Chen, Z. Liu, C. Zhang, Z. Cai, X. Chen, G. Zhang, Y. Zhao, S. Decurtins, S. X. Liu, D. Zhang, *Adv. Funct. Mater.* **2014**, *24*, 4250.

[123] A. Lv, M. Wang, Y. Wang, Z. Bo, L. Chi, *Chem. - A Eur. J.* **2016**, *22*, 3654.

[124] M. E. Roberts, S. C. B. Mannsfeld, M. L. Tang, Z. Bao, *Chem. Mater.* **2008**, *20*, 7332.

[125] F. Maddalena, M. J. Kuiper, B. Poolman, F. Brouwer, J. C. Hummelen, D. M. De Leeuw, B. De Boer, P. W. M. Blom, *J. Appl. Phys.* **2010**, *108*, 124501.

[126] L. Ma, S. Liang, X. L. Liu, D. J. Yang, L. Zhou, Q. Q. Wang, *Adv. Funct. Mater.* **2015**, *25*, 898.

[127] P. Lin, X. Luo, I. M. Hsing, F. Yan, *Adv. Mater.* **2011**, *23*, 4035.

[128] Z. T. Zhu, J. T. Mason, R. Dieckmann, G. G. Malliaras, *Appl. Phys. Lett.* **2002**, *81*, 4643.

[129] D. Li, E. J. Borkent, R. Nortrup, H. Moon, H. Katz, Z. Bao, *Appl. Phys. Lett.* **2005**, *86*, 042105.

[130] S. K. Hau, H. L. Yip, H. Ma, A. K. Y. Jen, *Appl. Phys. Lett.* **2008**, *93*, 233304.

[131] G. Scarpa, A. L. Idzko, A. Yadav, S. Thalhammer, *Sensors* **2010**, *10*, 2262.

[132] C. Bartic, B. Palan, A. Campitelli, G. Borghs, *Sensors Actuators, B Chem.* **2002**, *83*, 115.

[133] S. Ritjareonwattu, Y. Yun, C. Pearson, M. C. Petty, *Org. Electron.* **2010**, *11*, 1792.

[134] A. Loi, I. Manunza, A. Bonfiglio, *Appl. Phys. Lett.* **2005**, *86*, 1.

[135] A. Caboni, E. Orgiu, M. Barbaro, A. Bonfiglio, *IEEE Sens. J.* **2009**, *9*, 1963.

[136] A. Caboni, E. Orgiu, E. Scavetta, M. Barbaro, A. Bonfiglio, *Appl. Phys. Lett.* **2009**, *95*, 123304.

[137] M. E. Roberts, S. C. B. Mannsfeld, N. Queraltó, C. Reese, J. Locklin, W. Knoll, Z. Bao, *Proc. Natl. Acad. Sci. U. S. A.* **2008**, *105*, 12134.

[138] T. Someya, A. Dodabalapur, A. Gelperin, H. E. Katz, Z. Bao, *Langmuir* **2002**, *18*, 5299.

[139] C. Bartic, A. Campitelli, S. Borghs, *Appl. Phys. Lett.* **2003**, *82*, 475.

[140] J. Liu, M. Agarwal, K. Varahramyan, *Sensors Actuators, B Chem.* **2008**, *135*, 195.

[141] Q. Zhang, V. Subramanian, *Biosens. Bioelectron.* **2007**, *22*, 3182.

[142] L. Jagannathan, V. Subramanian, *Biosens. Bioelectron.* **2009**, *25*, 288.

[143] G. J. Zhang, G. Zhang, J. H. Chua, R. E. Chee, E. H. Wong, A. Agarwal, K. D. Buddharaju, N. Singh, Z. Gao, N. Balasubramanian, *Nano Lett.* **2008**, *8*, 1066.

[144] P. Stoliar, E. Bystrenova, S. D. Quiroga, P. Annibale, M. Facchini, M. Spijkman, S. Setayesh, D. de Leeuw, F. Biscarini, *Biosens. Bioelectron.* **2009**, *24*, 2935.

[145] F. Yan, S. M. Mok, J. Yu, H. L. W. Chan, M. Yang, *Biosens. Bioelectron.* **2009**, *24*, 1241.

[146] H. U. Khan, M. E. Roberts, O. Johnson, R. Förch, W. Knoll, Z. Bao, *Adv. Mater.* **2010**, *22*, 4452.

[147] M. E. Roberts, S. C. B. Mannsfeld, R. M. Stoltenberg, Z. Bao, *Org. Electron.* **2009**, *10*, 377.

[148] L. Wang, D. Fine, S. I. Khondaker, T. Jung, A. Dodabalapur, *Sensors Actuators, B Chem.* **2006**, *113*, 539.

[149] G. Scarpa, A. L. Idzko, A. Yadav, E. Martin, S. Thalhammer, *IEEE Trans. Nanotechnol.* **2010**, *9*, 527.

[150] H. U. Khan, J. Jang, J. J. Kim, W. Knoll, *Biosens. Bioelectron.* **2011**, *26*, 4217.

[151] T. Vuorinen, J. Niittynen, T. Kankkunen, T. M. Kraft, M. Mäntysalo, *Sci. Rep.* **2016**, *6*, 1.

[152] J. H. Oh, S. Y. Hong, H. Park, S. W. Jin, Y. R. Jeong, S. Y. Oh, J. Yun, H. Lee, J. W. Kim, J. S. Ha, *ACS Appl. Mater. Interfaces* **2018**, *10*, 7263.

[153] S. Y. Hong, Y. H. Lee, H. Park, S. W. Jin, Y. R. Jeong, J. Yun, I. You, G. Zi, J. S. Ha, *Adv. Mater.* **2016**, *28*, 930.

[154] J. W. Lee, D. C. Han, H. J. Shin, S. H. Yeom, B. K. Ju, W. Lee, *Sensors (Switzerland)* **2018**, *18*, 2996.

[155] Y. F. Wang, T. Sekine, Y. Takeda, K. Yokosawa, H. Matsui, D. Kumaki, T. Shiba, T. Nishikawa, S. Tokito, *Sci. Rep.* **2020**, *10*, 1.

[156] W. Honda, S. Harada, T. Arie, S. Akita, K. Takei, *Adv. Funct. Mater.* **2014**, *24*, 3299.

[157] C. Bali, A. Brandlmaier, A. Ganster, O. Raab, J. Zapf, A. Hübler, *Mater. Today Proc.* **2016**, *3*, 739.

[158] G. Liu, Q. Tan, H. Kou, L. Zhang, J. Wang, W. Lv, H. Dong, J. Xiong, *Sensors (Switzerland)* **2018**, *18*.

[159] T. Q. Trung, S. Ramasundaram, B. U. Hwang, N. E. Lee, *Adv. Mater.* **2016**, *28*, 502.

[160] F. Zhang, Y. Zang, D. Huang, C. A. Di, D. Zhu, *Nat. Commun.* **2015**, *6*.

[161] M. Sibinski, M. Jakubowska, M. Sloma, *Sensors* **2010**, *10*, 7934.

[162] J. Shin, B. Jeong, J. Kim, V. B. Nam, Y. Yoon, J. Jung, S. Hong, H. Lee, H. Eom, J. Yeo, J. Choi, D. Lee, S. H. Ko, *Adv. Mater.* **2020**, *32*, 1905527.

[163] H. Tang, F. Yan, P. Lin, J. Xu, H. L. W. Chan, *Adv. Funct. Mater.* **2011**, *21*, 2264.

[164] C. Liao, M. Zhang, L. Niu, Z. Zheng, F. Yan, *J. Mater. Chem. B* **2014**, *2*, 191.

[165] C. H. Mak, C. Liao, Y. Fu, M. Zhang, C. Y. Tang, Y. H. Tsang, H. L. W. Chan, F. Yan, *J. Mater. Chem. C* **2015**, *3*, 6532.

[166] W. Huang, J. Yu, X. Yu, W. Shi, *Org. Electron.* **2013**, *14*, 3453.

[167] Y. H. Lee, M. Jang, M. Y. Lee, O. Y. Kweon, J. H. Oh, *Chem* **2017**, *3*, 724.

[168] F. Yan, J. Li, S. M. Mok, *J. Appl. Phys.* **2009**, *106*, 074501.

[169] H. Bai, G. Shi, *Sensors* **2007**, *7*, 267.

[170] L. Pan, A. Chortos, G. Yu, Y. Wang, S. Isaacson, R. Allen, Y. Shi, R. Dauskardt, Z. Bao, *Nat. Commun.* **2014**, *5*.

[171] S. Pirsa, In *Materials Science and Engineering: Concepts, Methodologies, Tools, and Applications*; 2017; Vol. 1–3, pp. 543–574.

[172] Y. He, Q. Gui, Y. Wang, Z. Wang, S. Liao, Y. Wang, *Small* **2018**, *14*.

[173] C. Yang, L. Li, J. Zhao, J. Wang, J. Xie, Y. Cao, M. Xue, C. Lu, *ACS Appl. Mater. Interfaces* **2018**, *10*, 25811.

[174] X. Feng, W. Gu, X. Zhang, H. Jiang, *Cailiao Daobao/Materials Rev.* **2019**, *33*, 1243.

[175] R. C. Webb, A. P. Bonifas, A. Behnaz, Y. Zhang, K. J. Yu, H. Cheng, M. Shi, Z. Bian, Z. Liu, Y. S. Kim, W. H. Yeo, J. S. Park, J. Song, Y. Li, Y. Huang, A. M. Gorbach, J. A. Rogers, *Nat. Mater.* **2013**, *12*, 938.

[176] S. Li, Y. Zhang, Y. Wang, K. Xia, Z. Yin, H. Wang, M. Zhang, X. Liang, H. Lu, M. Zhu, H. Wang, X. Shen, Y. Zhang, *InfoMat* **2020**, *2*, 184.

[177] A. Feteira, *J. Am. Ceram. Soc.* **2009**, *92*, 967.

[178] W. Honda, S. Harada, T. Arie, S. Akita, K. Takei, *Proc. IEEE Sensors* **2014**, *2014-Decem*, 2227.

[179] W. Hong, Y. Xu, G. Lu, C. Li, G. Shi, *Electrochem. commun.* **2008**, *10*, 1555.

[180] L. Torsi, G. M. Farinola, F. Marinelli, M. C. Tanese, O. H. Omar, L. Valli, F. Babudri, F. Palmisano, P. G. Zambonin, F. Naso, *Nat. Mater.* **2008**, *7*, 412.

[181] A. N. Sokolov, M. E. Roberts, O. B. Johnson, Y. Cao, Z. Bao, *Adv. Mater.* **2010**, *22*, 2349.

[182] M. Y. Lee, H. J. Kim, G. Y. Jung, A. R. Han, S. K. Kwak, B. J. Kim, J. H. Oh, *Adv. Mater.* **2015**, *27*, 1540.

[183] V. C. Nguyen, K. Potje-Kamloth, *Thin Solid Films* **1999**, *338*, 142.

[184] C. Nguyen Van, K. Potje-Kamloth, *Thin Solid Films* **2001**, *392*, 113.

[185] N. V. Bhat, A. P. Gadre, V. A. Bambole, *J. Appl. Polym. Sci.* **2003**, *88*, 22.

[186] S. Virji, J. D. Fowler, C. O. Baker, J. Huang, R. B. Kaner, B. H. Weiller, *Small* **2005**, *1*, 624.

[187] J. S. Yang, T. M. Swager, *J. Am. Chem. Soc.* **1998**, *120*, 11864.

[188] J. Janata, *Proc. IEEE* **2003**, *91*, 864.

[189] H. Chen, M. Josowicz, J. Janata, K. Potje-Kamloth, *Chem. Mater.* **2004**, *16*, 4728.

[190] V. Podzorov, E. Menard, A. Borissov, V. Kiryukhin, J. A. Rogers, M. E. Gershenson, *Phys. Rev. Lett.* **2004**, *93*.

[191] I. Vladimirov, M. Kühn, T. Geßner, F. May, R. T. Weitz, *Sci. Rep.* **2018**, *8*.

[192] G. Horowitz, *Adv. Funct. Mater.* **2003**, *13*, 53.

[193] M. Mladenović, N. Vukmirović, *Adv. Funct. Mater.* **2015**, *25*, 1915.

[194] L. G. Kaake, P. F. Barbara, X. Y. Zhu, *J. Phys. Chem. Lett.* **2010**, *1*, 628.

[195] *Collect. Pap. L.D. Landau* **1965**.

[196] N. Tessler, Y. Preezant, N. Rappaport, Y. Roichman, *Adv. Mater.* **2009**, *21*, 2741.

[197] N. F. Mott, *Philos. Mag.* **1969**, *19*, 835.

[198] N. Wang, Z. K. Tang, G. D. Li, J. S. Chen, *Nature* **2000**, *408*, 50.

[199] A. Troisi, *Nat. Mater.* **2009**, *8*, 538.

[200] V. N. Do, T. H. Pham, *Adv. Nat. Sci. Nanosci. Nanotechnol.* **2010**, *1*.

[201] A. M. Nardes, R. A. J. Janssen, M. Kemerink, *Adv. Funct. Mater.* **2008**, *18*, 865.

[202] H. Cordes, S. D. Baranovskii, K. Kohary, P. Thomas, S. Yamasaki, F. Hensel, J. H. Wendorff, *Phys. Rev. B - Condens. Matter Mater. Phys.* **2001**, *63*.

[203] A. N. Aleshin, *Phys. Solid State* **2007**, *49*, 2015.

[204] H. Bässler, *Phys. Status Solidi* **1993**, *175*, 15.

[205] R. Coehoorn, P. A. Bobbert, *Phys. Status Solidi Appl. Mater. Sci.* **2012**, *209*, 2354.

[206] H. Ishii, K. Sugiyama, E. Ito, K. Seki, *Adv. Mater.* **1999**, *11*, 605.

[207] M. E. Kiziroglou, X. Li, A. A. Zhukov, P. A. J. de Groot, C. H. de Groot, *Solid. State. Electron.* **2008**, *52*, 1032.

[208] *Handb. Charg. Part. Opt.* **2017**.

[209] P. R. Emtage, J. J. O'Dwyer, *Phys. Rev. Lett.* **1966**, *16*, 356.

[210] S. M. Sze, K. K. Ng, *Physics of Semiconductor Devices*; 2006.

[211] M. Lenzlinger, E. H. Snow, *J. Appl. Phys.* **1969**, *40*, 278.

[212] M. Mousny, S. Omelon, L. Wise, E. T. Everett, M. Dumitriu, D. P. Holmyard, X. Banse, J. P. Devogelaer, M. D. Grynpas, *Bone* **2008**, *43*, 1067.

[213] E. T. Everett, *J. Dent. Res.* **2011**, *90*, 552.

[214] L. S. Kaminsky, M. C. Mahoney, J. Leach, J. Melius, M. J. Miller, *Crit. Rev. Oral Biol. Med.* **1990**, *1*, 261.

[215] C. H. Turner, M. P. Akhter, R. P. Heaney, *J. Orthop. Res.* **1992**, *10*, 581.

[216] S. Peckham, N. Awofeso, *Sci. World J.* **2014**, *2014*, 1.

[217] C. M. Carey, *J. Evid. Based. Dent. Pract.* **2014**, *14*, 95.

[218] M. R. Rao, S. M. Mobin, M. Ravikanth, *Tetrahedron* **2010**, *66*, 1728.

[219] H. Lu, Q. Wang, Z. Li, G. Lai, J. Jiang, Z. Shen, *Org. Biomol. Chem.* **2011**, *9*, 4558.

[220] B. Qiu, Y. Zeng, L. Cao, R. Hu, X. Zhang, T. Yu, J. Chen, G. Yang, Y. Li, *RSC Adv.* **2016**, *6*, 49158.

[221] S. Elsayed, A. Agostini, L. E. Santos-Figueroa, R. Martínez-Máñez, F. Sancenón, *ChemistryOpen* **2013**, *2*, 58.

[222] S. Y. Xu, X. Sun, H. Ge, R. L. Arrowsmith, J. S. Fossey, S. I. Pascu, Y. B. Jiang, T. D. James, *Org. Biomol. Chem.* **2015**, *13*, 4143.

[223] S. Guha, S. Saha, *J. Am. Chem. Soc.* **2010**, *132*, 17674.

[224] J. Liu, X. Yang, K. Wang, R. Yang, H. Ji, L. Yang, C. Wu, *Chem. Commun.* **2011**, *47*, 935.

[225] R. C. Mulrooney, N. Singh, N. Kaur, J. F. Callan, *Chem. Commun.* **2009**, 686.

[226] J. F. Callan, R. C. Mulrooney, S. Kamila, B. McCaughan, *J. Fluoresc.* **2008**, *18*, 527.

[227] R. Velu, V. T. Ramakrishnan, P. Ramamurthy, *J. Photochem. Photobiol. A Chem.* **2011**, *217*, 313.

[228] R. Velu, E. J. Padma Malar, V. T. Ramakrishnan, P. Ramamurthy, *Tetrahedron Lett.* **2010**, *51*, 5680.

[229] J. T. Mabeck, G. G. Malliaras, *Anal. Bioanal. Chem.* **2006**, *384*, 343.

[230] M. E. Roberts, A. N. Sokolov, Z. Bao, *J. Mater. Chem.* **2009**, *19*, 3351.

[231] L. Torsi, M. Magliulo, K. Manoli, G. Palazzo, *Chem. Soc. Rev.* **2013**, *42*, 8612.

[232] C. Liao, F. Yan, *Polym. Rev.* **2013**, *53*, 352.

[233] D. Elkington, N. Cooling, W. Belcher, P. Dastoor, X. Zhou, *Electronics* **2014**, *3*, 234.

[234] T. Minami, T. Minamiki, S. Tokito, *Chem. Commun.* **2015**, *51*, 9491.

[235] J. H. L. Ngai, L. M. Leung, S. K. So, H. K. H. Lee, *Org. Electron.* **2016**, *32*, 258.

[236] M. Irimia-Vladu, E. D. Gåowacki, P. A. Troshin, G. Schwabegger, L. Leonat, D. K. Susarova, O. Krystal, M. Ullah, Y. Kanbur, M. A. Bodea, V. F. Razumov, H. Sitter, S. Bauer, N. S. Sariciftci, *Adv. Mater.* **2012**, *24*, 375.

[237] E. D. Głowacki, G. Voss, N. S. Sariciftci, *Adv. Mater.* **2013**, *25*, 6783.

[238] O. Pitayatanakul, K. Iijima, M. Ashizawa, T. Kawamoto, H. Matsumoto, T. Mori, *J. Mater. Chem. C* **2015**, *3*, 8612.

[239] C. Guo, B. Sun, J. Quinn, Z. Yan, Y. Li, *J. Mater. Chem. C* **2014**, *2*, 4289.

[240] B. He, A. B. Pun, D. Zherebetskyy, Y. Liu, F. Liu, L. M. Klivansky, A. M. McGough, B. A. Zhang, K. Lo, T. P. Russell, L. Wang, Y. Liu, *J. Am. Chem. Soc.* **2014**, *136*, 15093.

[241] C. Guo, J. Quinn, B. Sun, Y. Li, *J. Mater. Chem. C* **2015**, *3*, 5226.

[242] C. Guo, J. Quinn, B. Sun, Y. Li, *Polym. Chem.* **2015**, *6*, 6998.

[243] C. Liu, S. Dong, P. Cai, P. Liu, S. Liu, J. Chen, F. Liu, L. Ying, T. P. Russell, F. Huang, Y. Cao, *ACS Appl. Mater. Interfaces* **2015**, *7*, 9038.

[244] A. Baeyer, V. Drewsen, *Berichte der Dtsch. Chem. Gesellschaft* **1882**, *15*, 2856.

[245] Y. Li, P. Sonar, S. P. Singh, M. S. Soh, M. Van Meurs, J. Tan, *J. Am. Chem. Soc.* **2011**, *133*, 2198.

[246] S. H. Kim, W. M. Yun, O. K. Kwon, K. Hong, C. Yang, W. S. Choi, C. E. Park, *J. Phys. D. Appl. Phys.* **2010**, *43*.

[247] W. Huang, W. Shi, S. Han, J. Yu, *AIP Adv.* **2013**, *3*.

[248] W. Xu, S. W. Rhee, *J. Mater. Chem.* **2009**, *19*, 5250.

[249] J. H. Schön, B. Batlogg, *J. Appl. Phys.* **2001**, *89*, 336.

[250] H. Sirringhaus, P. J. Brown, R. H. Friend, M. M. Nielsen, K. Bechgaard, B. M. W. Langeveld-Voss, A. J. H. Spiering, R. A. J. Janssen, E. W. Meijer, P. Herwig, D. M. De Leeuw, *Nature* **1999**, *401*, 685.

[251] Y. Li, P. Sonar, L. Murphy, W. Hong, *Energy Environ. Sci.* **2013**, *6*, 1684.

[252] B. S. Ong, Y. Wu, Y. Li, P. Liu, H. Pan, *Chem. - A Eur. J.* **2008**, *14*, 4766.

[253] R. J. Kline, M. D. McGehee, E. N. Kadnikova, J. Liu, J. M. J. Fréchet, M. F. Toney, *Macromolecules* **2005**, *38*, 3312.

[254] E. Zoulias, E. Varkaraki, N. Lymberopoulos, C. N. Christodoulou, G. N. Karagiorgis, *Tcjst* **2004**, *4*, 41.

[255] W. C. Tsoi, S. J. Spencer, L. Yang, A. M. Ballantyne, P. G. Nicholson, A. Turnbull, A. G. Shard, C. E. Murphy, D. D. C. Bradley, J. Nelson, J. S. Kim, *Macromolecules* **2011**, *44*, 2944.

[256] Y. Qin, M. A. Uddin, Y. Chen, B. Jang, K. Zhao, Z. Zheng, R. Yu, T. J. Shin, H. Y. Woo, J. Hou, *Adv. Mater.* **2016**, *28*, 9416.

[257] S. Xu, J. Zhan, B. Man, S. Jiang, W. Yue, S. Gao, C. Guo, H. Liu, Z. Li, J. Wang, Y. Zhou, *Nat. Commun.* **2017**, *8*.

[258] P. Lin, F. Yan, H. L. W. Chan, *ACS Appl. Mater. Interfaces* **2010**, *2*, 1637.

[259] D. A. Bernards, D. J. MacAya, M. Nikolou, J. A. Defranco, S. Takamatsu, G. G. Malliaras, *J. Mater. Chem.* **2008**, *18*, 116.

[260] L. Zhang, G. Wang, D. Wu, C. Xiong, L. Zheng, Y. Ding, H. Lu, G. Zhang, L. Qiu, *Biosens. Bioelectron.* **2018**, *100*, 235.

[261] Q. He, Z. Zeng, Z. Yin, H. Li, S. Wu, X. Huang, H. Zhang, *Small* **2012**, *8*, 2994.

[262] A. Shrivastava, V. Gupta, *Chronicles Young Sci.* **2011**, *2*, 21.

[263] T. Kundu, A. D. Chowdhury, D. De, S. M. Mobin, V. G. Puranik, A. Datta, G. K. Lahiri, *Dalt. Trans.* **2012**, *41*, 4484.

[264] Z. J. Chen, L. M. Wang, G. Zou, L. Zhang, G. J. Zhang, X. F. Cai, M. S. Teng, *Dye. Pigment.* **2012**, *94*, 410.

[265] B. Liu, H. Tian, *J. Mater. Chem.* **2005**, *15*, 2681.

[266] Y. Ma, Y. Zhao, F. Zhang, T. Jiang, X. Wei, H. Shen, R. Wang, Z. Shi, *Sensors Actuators, B Chem.* **2017**, *241*, 735.

[267] A. Sarkar, S. Bhattacharyya, A. Mukherjee, *Dalt. Trans.* **2016**, *45*, 1166.

[268] S. Ghosh, M. A. Alam, A. Ganguly, N. Guchhait, *Spectrochim. Acta - Part A Mol. Biomol. Spectrosc.* **2015**, *149*, 869.

[269] S. Wang, Y. Zhao, C. Zhao, L. Liu, S. Yu, *J. Fluor. Chem.* **2013**, *156*, 236.

[270] S. Chen, B. Sun, W. Hong, H. Aziz, Y. Meng, Y. Li, *J. Mater. Chem. C* **2014**, *2*, 2183.

[271] R. M. Rosa, R. L. Szulc, R. W. C. Li, J. Gruber, *Macromol. Symp.* **2005**, *229*, 138.

[272] Y. He, J. T. E. Quinn, D. Hou, J. H. L. Ngai, Y. Li, *J. Mater. Chem. C* **2017**, *5*, 12163.

[273] L. Dai, P. Soundarrajan, T. Kim, *Pure Appl. Chem.* **2002**, *74*, 1753.

[274] A. F. Frau, R. B. Pernites, R. C. Advincula, *Ind. Eng. Chem. Res.* **2010**, *49*, 9789.

[275] A. Malinauskas, *Synth. Met.* **1999**, *107*, 75.

[276] O. Winther-Jensen, B. Winther-Jensen, D. R. MacFarlane, *Electrochem. commun.* **2011**, *13*, 307.

[277] Y. I. Kurys, D. O. Mazur, V. G. Koshechko, V. D. Pokhodenko, *Theor. Exp. Chem.* **2016**, *52*, 163.

[278] N. Joshi, T. Hayasaka, Y. Liu, H. Liu, O. N. Oliveira, L. Lin, *Microchim. Acta* **2018**, *185*, 213.

[279] B. Li, G. Sauvé, M. C. Iovu, M. Jeffries-El, R. Zhang, J. Cooper, S. Santhanam, L. Schultz, J. C. Revelli, A. G. Kusne, T. Kowalewski, J. L. Snyder, L. E. Weiss, G. K. Redder, R. D. McCullough, D. N. Lambeth, *Nano Lett.* **2006**, *6*, 1598.

[280] J. Huang, S. Virji, B. H. Weiller, R. B. Kaner, *Chem. - A Eur. J.* **2004**, *10*, 1314.

[281] J. H. Yoon, S. B. Hong, S. O. Yun, S. J. Lee, T. J. Lee, K. G. Lee, B. G. Choi, *J. Colloid Interface Sci.* **2017**, *490*, 53.

[282] C. Hua, Y. Shang, Y. Wang, J. Xu, Y. Zhang, X. Li, A. Cao, *Appl. Surf. Sci.* **2017**, *405*, 405.

[283] J. H. Yoon, S. B. Hong, S. O. Yun, S. J. Lee, T. J. Lee, K. G. Lee, B. G. Choi, *J. Colloid Interface Sci.* **2017**, *490*, 53.

[284] L. Lu, T. Zheng, Q. Wu, A. M. Schneider, D. Zhao, L. Yu, *Chem. Rev.* **2015**, *115*, 12666.

[285] O. Inganäs, *Adv. Mater.* **2018**, *30*, 1800388.

[286] H. Sirringhaus, *Adv. Mater.* **2014**, *26*, 1319.

[287] C. Liu, Y. Xu, Y. Y. Noh, *Mater. Today* **2015**, *18*, 79.

[288] R. P. Xu, Y. Q. Li, J. X. Tang, *J. Mater. Chem. C* **2016**, *4*, 9116.

[289] X. Guo, J. Quinn, Z. Chen, H. Usta, Y. Zheng, Y. Xia, J. W. Hennek, R. P. Ortiz, T. J. Marks, A. Facchetti, *J. Am. Chem. Soc.* **2013**, *135*, 1986.

[290] J. Li, Y. Zhao, H. S. Tan, Y. Guo, C. A. Di, G. Yu, Y. Liu, M. Lin, S. H. Lim, Y. Zhou, H. Su, B. S. Ong, *Sci. Rep.* **2012**, *2*, 754.

[291] J. Chang, P. Sonar, Z. Lin, C. Zhang, J. Zhang, Y. Hao, J. Wu, *Org. Electron.* **2016**, *36*, 113.

[292] J. Ji, D. Zhou, Y. Tang, P. Deng, Z. Guo, H. Zhan, Y. Yu, Y. Lei, *J. Mater. Chem. C* **2018**, *6*, 13325.

[293] S. Mula, T. Han, T. Heiser, P. Lévêque, N. Leclerc, A. P. Srivastava, A. Ruiz-Carretero, G. Ulrich, *Chem. - A Eur. J.* **2019**, *25*, 8304.

[294] M. Shaker, B. Park, J. H. Lee, W. Kim, C. K. Trinh, H. J. Lee, J. W. Choi, H. Kim, K. Lee, J. S. Lee, *RSC Adv.* **2017**, *7*, 16302.

[295] J. Freudenberg, D. Jänsch, F. Hinkel, U. H. F. Bunz, *Chem. Rev.* **2018**, *118*, 5598.

[296] Y. Yang, Z. Liu, G. Zhang, X. Zhang, D. Zhang, *Adv. Mater.* **2019**, *31*, 1903104.

[297] G. L. Stahl, R. Walter, C. W. Smith, General Procedure for the Synthesis of Mono-N-acylated 1,6-Diaminohexanes. *J. Org. Chem.* **1978**, *43*, 2285–2286.

[298] J. Wang, Y. L. Liang, J. Qu, *Chem. Commun.* **2009**, 5144.

[299] M. Prashad, D. Har, B. Hu, H. Y. Kim, M. J. Girgis, A. Chaudhary, O. Repič, T. J. Blacklock, W. Marterer, *Org. Process Res. Dev.* **2004**, *8*, 330.

[300] B. Berns, B. Tieke, *Polym. Chem.* **2015**, *6*, 4887.

[301] Z. H. Guo, N. Ai, C. R. McBroom, T. Yuan, Y. H. Lin, M. Roders, C. Zhu, A. L. Ayzner, J. Pei, L. Fang, *Polym. Chem.* **2016**, *7*, 648.

[302] B. Sun, W. Hong, H. Aziz, Y. Li, *J. Mater. Chem.* **2012**, *22*, 18950.

[303] F. C. Spano, C. Silva, *Annu. Rev. Phys. Chem.* **2014**, *65*, 477.

[304] B. Heyne, *Photochem. Photobiol. Sci.* **2016**, *15*, 1103.

[305] S. Siddiqui, F. C. Spano, *Chem. Phys. Lett.* **1999**, *308*, 99.

[306] J. Pommerehne, H. Vestweber, W. Guss, R. F. Mahrt, H. Bässler, M. Porsch, J. Daub, *Adv. Mater.* **1995**, *7*, 551.

[307] B. Sun, W. Hong, H. Aziz, N. M. Abukhdeir, Y. Li, *J. Mater. Chem. C* **2013**, *1*, 4423.

[308] D. W. Hatchett, M. Josowicz, J. Janata, *J. Phys. Chem. B* **1999**, *103*, 10992.

[309] A. G. Macdiarmid, J. C. Chiang, A. F. Richter, A. J. Epstein, *Synth. Met.* **1987**, *18*, 285.

[310] M. Gizdavic-Nikolaidis, G. A. Bowmaker, *Polymer (Guildf).* **2008**, *49*, 3070.

[311] T. H. Le, Y. Kim, H. Yoon, *Polymers (Basel).* **2017**, *9*, 150.

[312] M. Naseri, L. Fotouhi, A. Ehsani, *Chem. Rec.* **2018**, *18*, 599.

[313] S. Bhadra, N. K. Singha, D. Khastgir, *Polym. Int.* **2007**, *56*, 919.

[314] B. Pasela, A. Castillo, R. Simon, M. Pulido, H. Mana-ay, M. Abiquibil, R. Montecillo, K. Thumanu, D. von Tumacder, K. Taaca, *Biomimetics* **2019**, *4*, 15.

[315] M. V. Kulkarni, A. K. Viswanath, R. Marimuthu, T. Seth, *J. Polym. Sci. Part A Polym. Chem.* **2004**, *42*, 2043.

[316] E. J. Jelmy, S. Ramakrishnan, M. Rangarajan, N. K. Kothurkar, *Bull. Mater. Sci.* **2013**, *36*, 37.

[317] X. Wang, X. Zhang, L. Sun, D. Lee, S. Lee, M. Wang, J. Zhao, Y. Shao-Horn, M. Dincă, T. Palacios, K. K. Gleason, *Sci. Adv.* **2018**, *4*.

[318] S. C. Hobaica, *J. Polym. Sci. Part B Polym. Phys.* **2003**, *41*, 807.

[319] X. R. Zeng, T. M. Ko, *Polymer (Guildf).* **1998**, *39*, 1187.

[320] S. Radhakrishnan, S. G. Joshi, *J. Polym. Sci. Part C, Polym. Lett.* **1989**, *27*, 127.

[321] C. Baker, J. L. Gole, *ACS Sensors* **2016**, *1*, 235.

[322] Y. Tahara, K. Toko, *IEEE Sens. J.* **2013**, *13*, 3001.

[323] X. Jiang, T. Yang, C. Li, R. Zhang, L. Zhang, X. Zhao, H. Zhu, *Glob. Challenges* **2017**, *1*, 1700037.

[324] N. Basescu, Z. X. Liu, D. Moses, A. J. Heeger, H. Naarmann, N. Theophilou, *Nature* **1987**, *327*, 403.

[325] G. Wegner, *Angew. Chemie Int. Ed. English* **1981**, *20*, 361.

[326] J. H. L. Ngai, G. Y. Chang, X. Gao, X. Zhou, A. D. Hendsbee, Y. Li, *RSC Adv.* **2019**, *9*, 26230.

[327] E. Stucchi, G. Dell'Erba, P. Colpani, Y. H. Kim, M. Caironi, *Adv. Electron. Mater.* **2018**, *4*, 1800340.

[328] T. Wang, M. Farajollahi, Y. S. Choi, I. T. Lin, J. E. Marshall, N. M. Thompson, S. Kar-Narayan, J. D. W. Madden, S. K. Smoukov, *Interface Focus* **2016**, *6*.

[329] N. C. Billingham, P. D. Calvert, P. J. S. Foot, F. Mohammad, *Polym. Degrad. Stab.* **1987**, *19*, 323.

[330] J. H. L. Ngai, X. Gao, P. Kumar, J. Polena, Y. Li, *Adv. Electron. Mater.* **2021**, *7*, 2000935.

[331] M. Kuş, S. Okur, *Sensors Actuators, B Chem.* **2009**, *143*, 177.

[332] L. Bießmann, L. P. Kreuzer, T. Widmann, N. Hohn, J. F. Moulin, P. Müller-Buschbaum, *ACS Appl. Mater. Interfaces* **2018**, *10*, 9865.

[333] H. Shi, C. Liu, Q. Jiang, J. Xu, *Adv. Electron. Mater.* **2015**, *1*, 1500071.

[334] C. Liu, K. Huang, W. T. Park, M. Li, T. Yang, X. Liu, L. Liang, T. Minari, Y. Y. Noh, *Mater. Horizons* **2017**, *4*, 608.

[335] A. M. Nardes, M. Kemerink, R. A. J. Janssen, *Phys. Rev. B - Condens. Matter Mater. Phys.* **2007**, *76*.

[336] L. Dan, A. L. Elias, *Adv. Healthc. Mater.* **2020**, *9*, 2000380.

[337] T. Q. Trung, H. S. Le, T. M. L. Dang, S. Ju, S. Y. Park, N. E. Lee, *Adv. Healthc. Mater.* **2018**, *7*, 1800074.

[338] S. Zhao, D. Lou, P. Zhan, G. Li, K. Dai, J. Guo, G. Zheng, C. Liu, C. Shen, Z. Guo, *J. Mater. Chem. C* **2017**, *5*, 8233.

[339] F. Liu, X. Zhang, W. Li, J. Cheng, X. Tao, Y. Li, L. Sheng, *Compos. Part A Appl. Sci. Manuf.* **2009**, *40*, 1717.

[340] M. Aggarwal, S. Khan, M. Husain, T. C. Ming, M. Y. Tsai, T. P. Perng, Z. H. Khan, *Eur. Phys. J. B* **2007**, *60*, 319.

[341] Y. Zhang, C. J. Sheehan, J. Zhai, G. Zou, H. Luo, J. Xiong, Y. T. Zhu, Q. X. Jia, *Adv. Mater.* **2010**, *22*, 3027.

[342] F. Bureš, *RSC Adv.* **2014**, *4*, 58826.

[343] H. T. Nicolai, M. Kuik, G. A. H. Wetzelaer, B. De Boer, C. Campbell, C. Risko, J. L. Brédas, P. W. M. Blom, *Nat. Mater.* **2012**, *11*, 882.

[344] C. Li, L. Duan, H. Li, Y. Qiu, *J. Phys. Chem. C* **2014**, *118*, 10651.

[345] B. Sun, W. Hong, C. Guo, S. Sutty, H. Aziz, Y. Li, *Org. Electron.* **2016**, *37*, 190.

[346] D. Nava, Y. Shin, M. Massetti, X. Jiao, T. Biskup, M. S. Jagadeesh, A. Calloni, L. Duo, G. Lanzani, C. R. Mcneill, M. Sommer, M. Caironi, *ACS Appl. Energy Mater.* **2018**, *1*, 4626.

[347] D. T. Scholes, P. Y. Yee, J. R. Lindemuth, H. Kang, J. Onorato, R. Ghosh, C. K. Luscombe, F. C. Spano, S. H. Tolbert, B. J. Schwartz, *Adv. Funct. Mater.* **2017**, *27*.

[348] R. P. Fornari, A. Troisi, *Phys. Chem. Chem. Phys.* **2014**, *16*, 9997.

[349] J. Peng, J. I. Khan, W. Liu, E. Ugur, T. Duong, Y. Wu, H. Shen, K. Wang, H. Dang, E. Aydin, X. Yang, Y. Wan, K. J. Weber, K. R. Catchpole, F. Laquai, S. De Wolf, T. P. White, *Adv. Energy Mater.* **2018**, *8*.

[350] J. Peng, Y. Wu, W. Ye, D. A. Jacobs, H. Shen, X. Fu, Y. Wan, T. Duong, N. Wu, C. Barugkin, H. T. Nguyen, D. Zhong, J. Li, T. Lu, Y. Liu, M. N. Lockrey, K. J. Weber, K. R. Catchpole, T. P. White, *Energy Environ. Sci.* **2017**, *10*, 1792.

[351] F. Wang, A. Shimazaki, F. Yang, K. Kanahashi, K. Matsuki, Y. Miyauchi, T. Takenobu, A. Wakamiya, Y. Murata, K. Matsuda, *J. Phys. Chem. C* **2017**, *121*, 1562.

[352] A. Roy, A. Ghosh, S. Bhandari, S. Sundaram, T. K. Mallick, *Ind. Eng. Chem. Res.* **2020**, *59*, 11063.

[353] M. M. Rodgers, V. M. Pai, R. S. Conroy, *IEEE Sens. J.* **2015**, *15*, 3119.

[354] K. Kim, B. Kim, C. H. Lee, *Adv. Mater.* **2020**, *32*.

[355] H. R. Lim, H. S. Kim, R. Qazi, Y. T. Kwon, J. W. Jeong, W. H. Yeo, *Adv. Mater.* **2020**, *32*.

[356] Y. Liu, M. Pharr, G. A. Salvatore, *ACS Nano* **2017**, *11*, 9614.

[357] Y. He, S. Yang, H. Liu, Q. Shao, Q. Chen, C. Lu, Y. Jiang, C. Liu, Z. Guo, *J. Colloid Interface Sci.* **2018**, *517*, 40.

[358] W. P. Shih, L. C. Tsao, C. W. Lee, M. Y. Cheng, C. Chang, Y. J. Yang, K. C. Fan, *Sensors* **2010**, *10*, 3597.

[359] S. Harada, W. Honda, T. Arie, S. Akita, K. Takei, *ACS Nano* **2014**, *8*, 3921.

[360] S. Fabiano, N. Sani, J. Kawahara, L. Kergoat, J. Nissa, I. Engquist, X. Crispin, M. Berggren, *Sci. Adv.* **2017**, *3*.

[361] A. V. Volkov, K. Wijeratne, E. Mitraka, U. Ail, D. Zhao, K. Tybrandt, J. W. Andreasen, M. Berggren, X. Crispin, I. V. Zozoulenko, *Adv. Funct. Mater.* **2017**, *27*.

[362] P. Adhyapak, R. Aiyer, S. R. Dugasani, H. U. Kim, C. K. Song, A. Vinu, V. Renugopalakrishnan, S. H. Park, T. Kim, H. Lee, D. Amalnerkar, *R. Soc. Open Sci.* **2018**, *5*.

[363] G. Dijk, H. J. Ruigrok, R. P. O'Connor, *Adv. Mater. Interfaces* **2020**, *7*.

[364] R. Montazami, S. Liu, Y. Liu, D. Wang, Q. Zhang, J. R. Heflin, *J. Appl. Phys.* **2011**, *109*.

[365] Y. Xu, L. Zheng, C. Yang, W. Zheng, X. Liu, J. Zhang, *ACS Appl. Mater. Interfaces* **2020**, *12*, 20704.

[366] M. D. Dankoco, G. Y. Tesfay, E. Benevent, M. Bendahan, *Mater. Sci. Eng. B Solid-State Mater. Adv. Technol.* **2016**, *205*, 1.

[367] D. Briand, A. Oprea, J. Courbat, N. Bârsan, *Mater. Today* **2011**, *14*, 416.

[368] D. Briand, F. Molina-Lopez, A. V. Quintero, C. Ataman, J. Courbat, N. F. De Rooij, *Procedia Eng.* **2011**, *25*, 8.

[369] A. Rivadeneyra, M. Bobinger, A. Albrecht, M. Becherer, P. Lugli, A. Falco, J. F. Salmerón, *Polymers (Basel).* **2019**, *11*.

[370] H. Shi, C. Liu, Q. Jiang, J. Xu, *Adv. Electron. Mater.* **2015**, *1*, 1500017.

[371] A. N. Aleshin, S. R. Williams, A. J. Heeger, *Synth. Met.* **1998**, *94*, 173.

[372] I. S. Beloborodov, A. V. Lopatin, V. M. Vinokur, *Phys. Rev. B - Condens. Matter Mater. Phys.* **2005**, *72*.

[373] P. Sheng, *Phys. Rev. B* **1980**, *21*, 2180.

[374] P. Sheng, B. Abeles, Y. Arie, *Phys. Rev. Lett.* **1973**, *31*, 44.

Appendix

Appendix A: Materials Characterization

Materials

All chemicals used were purchased from Sigma-Aldrich, VWR, TCI, Fluka and Armstrong. Other solvents were analytical grade for organic synthesis or used as received. The solvents used for fabrication of solution process electronic devices, UV-Vis-NIR, CV and HT-GPC experiments were HPLC grades. Poly[2,5-bis(2-octyldodecyl)pyrrolo[3,4-c]pyrrole-1,4(2H,5H)-dione -3,6-diyl)-alt-(2,2';5',2'';5'',2'''-quaterthiophen-5,5'''-diyl)] (PDQT-C20), 3,6-Di(thiophen-2-yl)-2,5-dihydropyrrolo[3,4-c]pyrrole-1,4-dione[251] (**DPPTh)** and (3,3'-bis(dodecyloxy)-[2,2'-bithiophene]-5,5'-diyl)bis(trimethylstannane)[289] (**C12-BTO-TMT**) were synthesized by following a previously reported procedures. .[270] Arsenic n-doped silicon dioxide wafer (6-inch) with 300nm polished oxide layer was purchased from University Wafer. Chromium rods and gold ingots (99.9%) used for thermal evaporation was purchased from Angstrom Engineering and Royal Canadian Mint. Column chromatography was performed on silica gel (230-400 mesh).

Nuclear Magnetic Resonance (NMR) Spectroscopy

^{1}H NMR and ^{13}C NMR spectroscopy were used for routine structural identification of the intermediates and the final products. The samples were dissolved in deuterated solvents such as $CDCl_3$ (ALDRICH, 99.8 atom % D, contains 0.1 % (v/v) TMS), Acetone-d_6 (ALDRICH, 99.9 atom % D, contains 0.1 % (v/v) TMS) or DMSO-d_6 (ALDRICH, 99.5 atom % D, contains 0.1 % (v/v) TMS). The spectroscopies were recorded on a FT-NMR, 300 MHz (Bruker 300 UltraShield) spectrometer.

Matrix-assisted laser desorption/ionization (MALDI)

Matrix-assisted laser desorption/ionization (MALDI) experiment was performed using a Bruker Autoflex Speed MALDI-TOF mass spectrometer using red phosphorus clusters as mass calibration.

Ultraviolet-Visible (UV-VIS) Spectroscopy

UV-VIS absorption spectroscopy was used to obtain optical properties of the materials synthesized. All spectra were recorded on a Thermo Scientific GENESYS™ 10S VIS spectrophotometer, or using the Cary 7000 UMS UV-Vis-NIR spectrophotometer. The thin film samples were prepared either by spin-coating or drop-casting a sample solution on a microscope glass slide.

Optical information such as the absorption maximum wavelength and absorption onset which relates to the electronic transistion of from $\pi \rightarrow \pi^*$ orbitals can be obtained. The optical bandgaps can then be estimated by extracting information from the material UV/Vis profile.

Cyclic Voltammetry (CV)

CV was employed for the determination of the oxidative and reductive potentials for the synthesized materials. The determination was carried out on a CHI600E electrochemical analyser. The samples of interest were casted on a platinum working electrode disc as a thin film. The analysis was performed in a 0.1M tetrabutylammonium hexafluorophosphate (Bu_4NPF_6) solution in acetonitrile (ACN) as the electrolyte at a scan rate of 50 mVs^{-1}. Ferrocene was used as the internal standard and the HOMO level of ferrocene was assumed to be -4.80 eV. Silver/silver chloride was used as the reference electrode, while a platinum wire was used as the auxilary electrode and another platinum rod was used as the working electrode.

The measureable change in current for the sample would be calculated with respect to the oxidative potential of ferrocene. The highest occupied molecular orbital (HOMO) and lowest unoccupied molecular orbital (LUMO) of the samples were then estimated from the cyclic votammograms.[306]

High Temperature Gel Permeation Chromatography (HT-GPC)

HT-GPC analysis was performed to obtain molecular weight information of the synthesized polymers. The weight average molecular weight and the number average molecular weight can be found from the GPC chromatograms and the polydispersity index can be calculated from the molecular weight information collected. HT-GPC measurements were performed on a Viscotek Malvern 350 HT-GPC system with a 300 mm Jordi Gel DVB Mixed Bed liquid chromatography column using 1,2,4-trichlorobenzene as eluent and polystyrene as standards at 140 °C. The polymer samples were detected by a refractive index (RI) detector.

Fabrication of OFET and WGOFET Devices

The heavily n-doped Si substrate with a 300 nm SiO_2 layer was cleaned by submerging in isopropanol and sonicated for 15 min. The cleaning procedure was repeated with acetone and chloroform. The substrates were then dried with compressed nitrogen and was exposed to O_2 plasma for 2 min. The substrate surface was then modified with a self-assembled monolayer (SAM) by submerging the substrates into a toluene solution of trichlorododecylsilane (DDTS) (~10 mM) for 20 minutes. The substrates were then washed with toluene and dried with compressed nitrogen.

A polymer solution of known concentration (5mg mL^{-1} in solvent) was spin-coated (3000 rpm) on top of the substrate for 80 s to deposit a 30 nm thick polymer layer. The transistor was then placed on a hotplate and annealed for 20 min at different temperatures (50, 100, 150 or 200 °C) in an argon-filled glovebox prior to the transistor measurements. Carrier mobility was calculated in the saturation regime according to the following equation:

$$I_{DS} = \left(\frac{WC_i}{2L}\right)\mu(V_G - V_T)^2$$

where I_{DS} is the source-drain current, μ is the charge carrier mobility, C_i is the capacitance per unit area of the dielectric (11.6 nF cm^{-2} for DDTS modified SiO_2), W (1000 μm) and L (30 μm) are OTFT channel width and length, V_G is the gate voltage, and V_T is the threshold voltage.

The fabrication of WGOFETs were similar to that of OFETs except bare SiO_2 was used instead of DDTS modified SiO_2 transistor substrates and a longer channel width (W) of 15.8 mm was used. A water droplet was then added on top of the semiconductor layer as the gate dielectric and a probe tip was positioned on top of the water droplet as the gate electrode.

Fabrication of Chemiresistors and Chemical Sensing

The **PDNB:HCl** chemiresistors were fabricated using a SiO_2 (300 nm)/Si wafer substrate with pre-patterned bottom-contact gold (Au) interdigitated electrodes which have a channel length (L) of 30 μm and a total channel width (W) of 15.8 mm with a W/L ratio of 527. The bare substrate was first cleaned by sonication in DI water, acetone and chloroform for 15 min each. The substrate then dried by a N_2 flow, followed by air-plasma cleaning for 2 min. A **PDEB** film was then deposited on the substrate by spin coating a 10 mg mL^{-1} **PDEB** solution in chlorobenzene at 700 rpm for 80 s to afford a 30 nm film, followed by thermal annealing at 200 °C in air for 20 min to form **PDNB**. The sample was then washed by ethanol, acetone and hexane. Doping of the film was done using 5N HCl followed by the previously described submersion technique. The **PDNB:HCl** chemiresistor was then rinsed with DI water (18 MΩ) and air-dried for testing.

Chemical sensing of the **PDNB:HCl** chemiresistor was performed in ambient. The sensor was placed horizontally with its face up on a testing platform. The two electrodes of the sensor were connected to an Agilent B2912A Precision Source/Measure Unit. A 1.0 V constant voltage was applied to the chemiresistor. A current versus time (I-t) measurement was carried out to establish

a stable baseline before chemical sensing. Once a stable baseline was obtained (typically around 1-2 min), a liquid analyte (5.0 μL) was introduced with a micropipette onto the surface of the **PDNB:HCl** film at the channel with the channel area fully covered with the analyte soliton. The *I-t* measurement was continued during the evaporation of the analyte. The data was recorded until the sensor was completely dried and the baseline is recovered to the original level. A subsequent measurement with the same or different liquid may be followed with the same manner.

Atomic Force Microscopy (AFM)

Atomic force microscopy (AFM) images were taken with a Dimension 3100 scanning probe microscope. AFM analysis was used for the determination of surface morphology, thickness, and roughness of the thin film samples. AFM images were taken on polymer thin films spin-coated on a bare or dodecyltrichlorosilane modified SiO_2/p++Si substrates with a Dimension 3100 scanning probe microscope.

X-ray Diffraction (XRD)

X-ray diffraction (XRD) measurements were carried out on a Bruker D8 Advance diffractometer with Cu Ka radiation (λ = 0.15418 nm) using polymer films spin coated on SiO_2/Si substrates and polymer flakes.

Mask Aligner Photolithography

The Karl Suss MA6 mask aligner is used in part of the photolithography process to prepare substrates for transistors and sensors. A negative photoresist nLOF 2035 was spin-coated onto a 6-inch p-doped silicon dioxide wafer. A shadow mask with the transistor electrodes pattern was put on top of the substrate. The wafer was then put into the mask aligner and an ultraviolet irradiation with a power of 1 mW/cm^2 was exposed on the substrate for 11 seconds. The process would then create a pattern according to the shadow mask on top of the substrate. Finally, the uncured negative photoresist was the lifted off submerging the patterned wafer in a developer solution AZ726 for 3 min. The wafer was then submerged in 18MΩ water for 1 min and washed successively with deionized water. The wafer was then dried by compressed nitrogen gas. The silicon wafer with transistor or resistor pattern was then put into nitrogen storage for the later metal evaporation process to deposit metal electrodes for transistor, resistor or sensor substrates.

Thermal Evaporation of Metals

Thermal evaporation of metals was carried out using the Angstrom Covap PVD system to deposit metal electrodes for transistor, resistor or sensor substrates. The silicon wafer substrate which has been pre-patterned by photolithography process was put into the vacuum chamber in the vacuum thermal evaporator. The chamber was then put into high vacuum until a pressure of ~10^{-7} Torr was reached. A Chromium adhesion layer (2nm) was then deposited onto the substrate surface at a rate of ~ 2Å/s at a power of 14-18% from the PVD system. Gold was then deposited as the second layer at a rate of ~ 0.15 – 0.2 Å/s. After the deposition process, the substrate was then submerged in HPLC grade acetone/chloroform and sonicated at 40ºC for 60 min or until no metal or photoresist solid particles were present in the solution. The substrate was then dried by compressed nitrogen and stored in a tightly sealed storage box for later use.

Appendix B: Syntheses

Synthesis of 3-((2-octyldodecyl)oxy)benzaldehyde (1)

To a 500 mL round-bottom flask, 3-hydroxybenzaldehyde (3-HBA) (10 g, 0.082 mol) was dissolved in dimethylformamide (150 mL). Potassium carbonate (22.6 g , 0.164 mol) was added to the solution of 3-HBA. 9-(Bromomethyl)nonadecane (17.4 g , 0.090 mol) was added in one portion to the reaction mixture. The mixture was equipped with a condenser and was heated to reflux for 18 h under nitrogen. The reaction mixture was cooled down to room temperature, and water and hexane were added to the mixture. The solution was then stirred at room temperature until the excess potassium carbonate powder was dissolved in the aqueous layer. The crude product was extracted with hexane and washed with water and saturated NaCl solution. The organic layer was collected and anhydrous Na_2SO_4 was added to remove residual water in the organic solution. The solution was filtered and solvent was removed by rotary evaporation. The crude product was then purified by a short silica column using pure hexane as eluent to afford compound **1** as a colorless liquid (18.2 g, 95%). ^{1}H NMR (300 MHz, Chloroform-*d*) δ 9.97 (s, 1H), 7.43 (d, *J* = 4.9 Hz, 2H), 7.39 (s, 1H), 7.17 (m, 1H), 3.89 (d, *J* = 5.6 Hz, 2H), 1.98 (t, *J* = 7.8 Hz, 1H), 1.57 – 1.10 (m, 27H), 0.88 (t, *J* = 6.5 Hz, 6H). ^{13}C NMR (300 MHz, Chloroform-*d*) δ 192.25, 159.98, 137.77, 129.93, 123.21, 121.99, 112.84, 71.23, 37.92, 31.92, 31.34, 30.00, 29.65, 29.35, 26.84, 22.69, 14.11. (Figure B-1 & B-2)

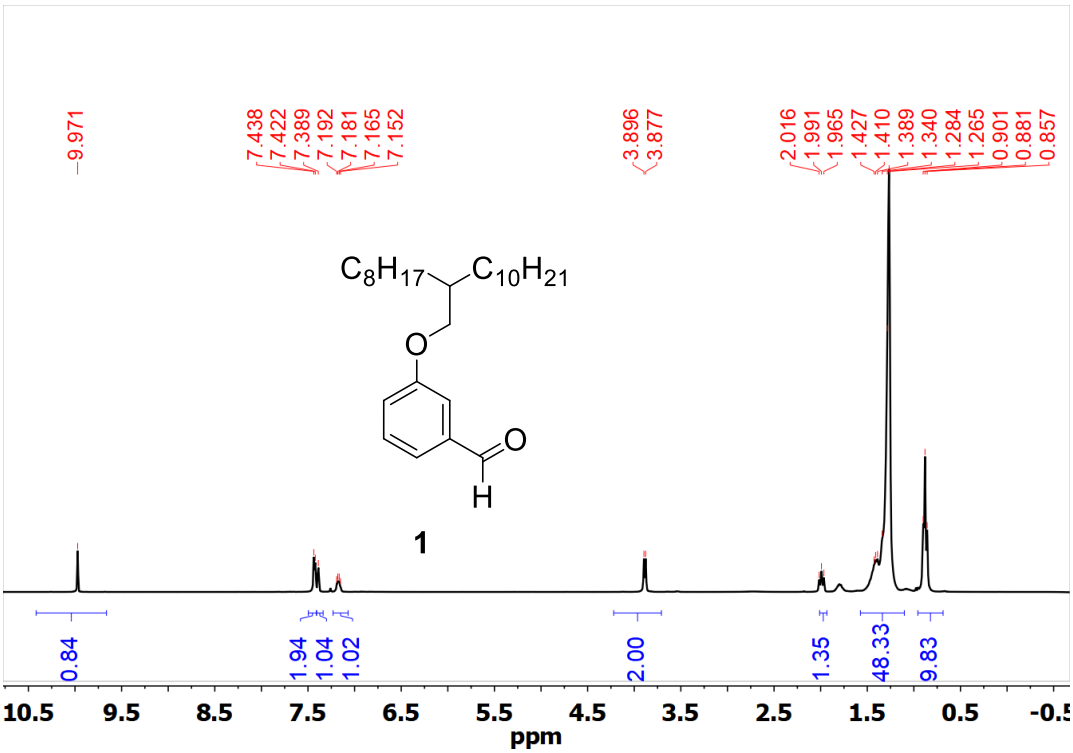

Figure B-1. 300 MHz ^{1}H NMR of Compound **1** in $CDCl_3$.

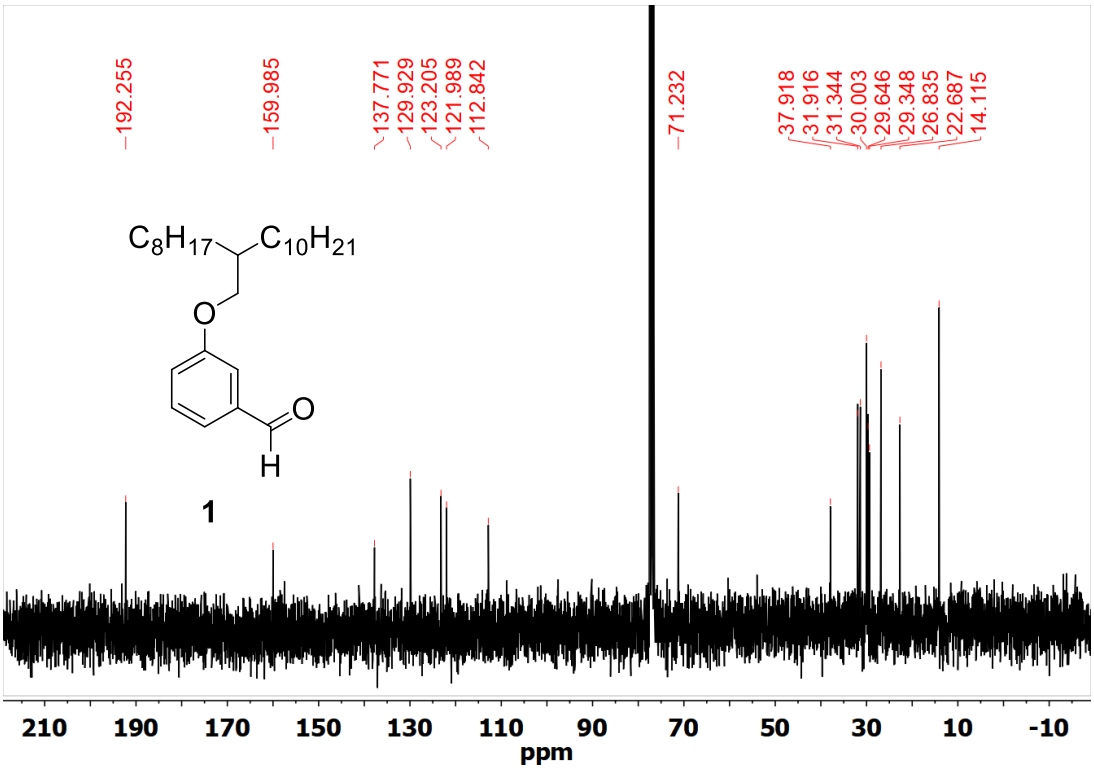

Figure B-2. 75 MHz ^{13}C NMR of Compound **1** in $CDCl_3$.

Synthesis of 2-bromo-5-((2-octyldodecyl)oxy)benzaldehyde (2)

To a two-necked 500 mL round-bottom flask, compound **1** (6.0 g, 0.015 mol) was dissolved in chloroform (100 mL). A solution of bromine (0.92 mL, 0.018 mol) in chloroform (10 mL) was added dropwise into the reaction mixture with a syringe through the rubber septum in 20 min. The reaction mixture was then stirred for an additional 40 min. Cold water was added to the mixture followed by sodium bisulfite solution to eliminate the unreacted bromine. The reaction mixture was then extracted with hexane and washed with water and saturated NaCl solution. The organic layer was collected and anhydrous Na_2SO_4 was added to remove residue of water in the organic solution. The solution was filtered, and solvent was removed by rotary evaporation. The crude product was then purified by a short silica column using pure hexane as eluent to afford compound **2** as a colorless liquid (5.9 g, 82%). ^{1}H NMR (300 MHz, Chloroform-*d*) δ 10.31 (s, 1H), 7.51 (d, *J* = 8.8 Hz, 1H), 7.40 (d, *J* = 3.1 Hz, 1H), 7.03 (dd, *J* = 8.8, 3.2 Hz, 1H), 3.85 (d, *J* = 5.6 Hz, 2H), 1.94 – 1.68 (m, 1H), 1.46 – 1.09 (m, 32H), 0.88 (t, *J* = 6.6 Hz, 6H). ^{13}C NMR (300 MHz, Chloroform-*d*) δ 191.92, 159.07, 134.45, 123.50, 113.42, 71.52, 37.85, 31.92, 31.28, 29.98, 29.66, 29.57, 29.35, 26.81, 22.69, 14.12. (Figure B-3 & B-4)

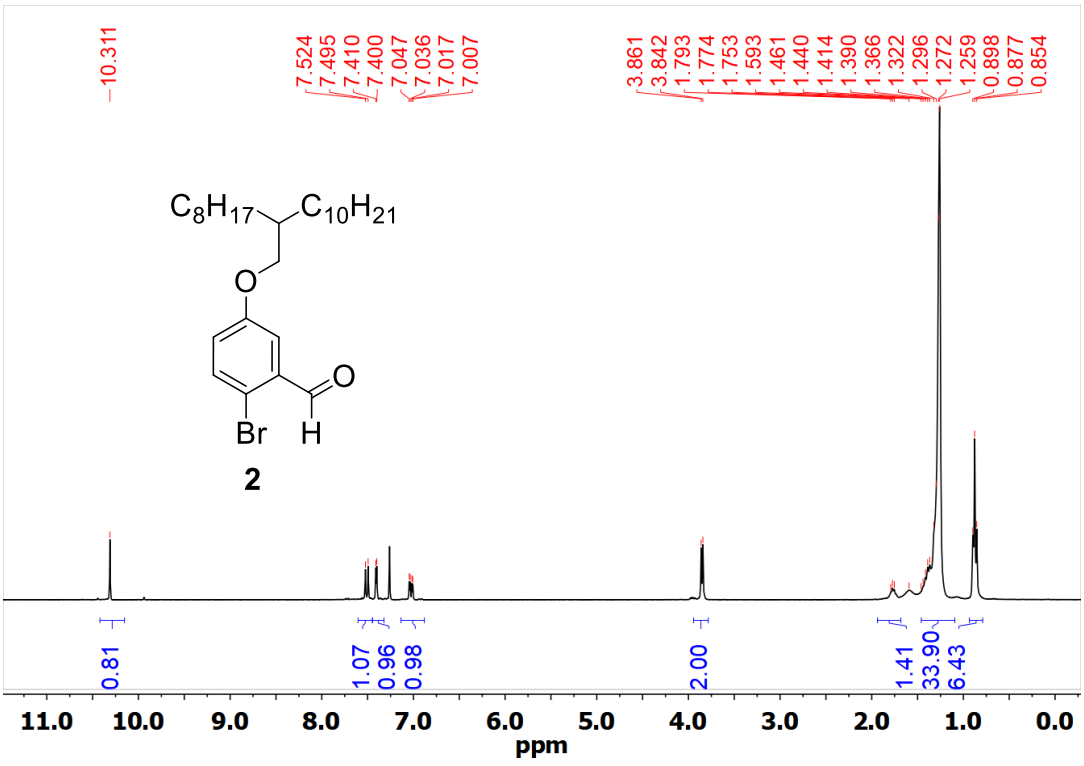

Figure B-3. 300 MHz ^{1}H NMR of Compound **2** in $CDCl_3$.

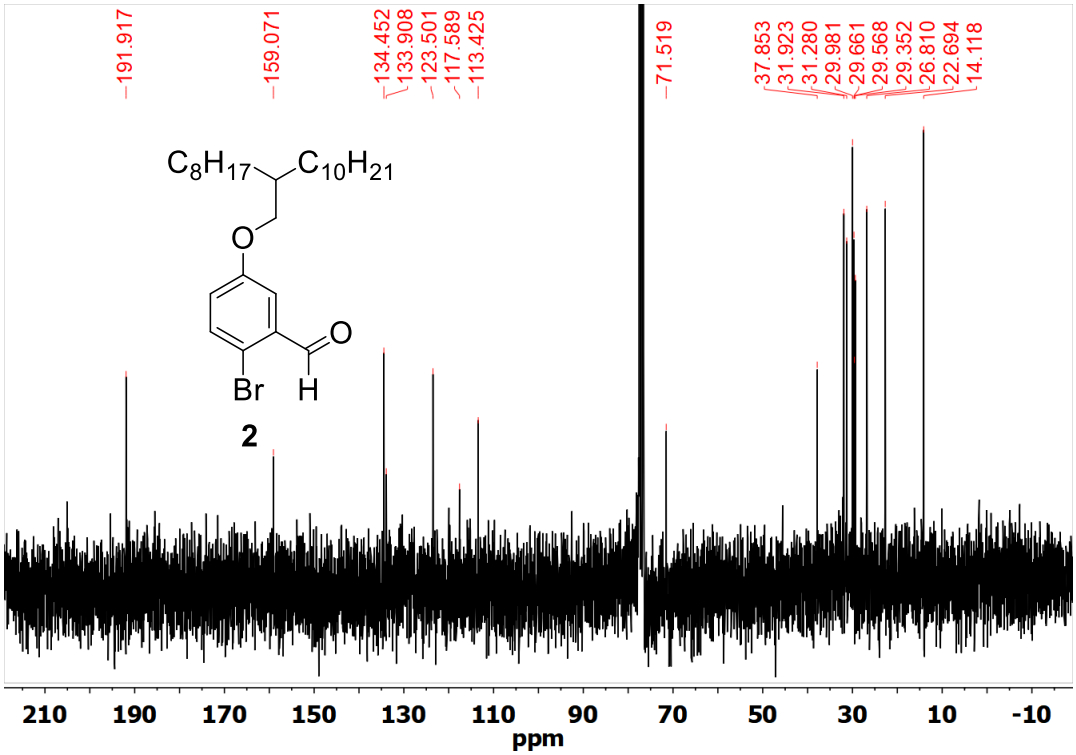

Figure B-4. 75 MHz ^{13}C NMR of Compound **2** in $CDCl_3$.

Synthesis of 6-bromo-2-nitro-3-((2-octyldodecyl)oxy)benzaldehyde (3)

To a 100 mL round-bottom flask, 65% nitric acid (1.40 mL, 0.0201 mol) was slowly added to 96% concentrated sulfuric acid (18 mL, 0.334 mol) at 0 °C and the mixture was stirred for 10 min to form the nitrating reagent. Compound **2** (7.5 g , 0.0155 mol) was added dropwise to the nitrating reagent in 10 min. The solution was kept stirring at 0 °C for 30 min. Crushed ice was added directly to the reaction mixture to precipitate the nitration product. The crude product was collected by suction filtration and washed with cold water until the filtrate is neutral as monitored by pH paper. The crude product was recrystallized in acetone/water solution and dried in vacuum at room temperature to obtain a yellow sticky paste of compound **3** (3.3 g, 41%). The crude product was used directly in the next step without further purification.

Synthesis of (E)-4,4'-dibromo-7,7'-bis((2-octyldodecyl)oxy)-[2,2'-biindolinylidene]-3,3'-dione (IDG-C20-Br)

To a 100 mL two-necked round-bottom flask, compound **3** (7 g, 0.0133 mol) was dissolved in acetone (105 mL). One neck of the flask was connected to argon atmosphere and the other neck was stoppered with a rubber septum. The mixture was stirred in an ice bath in argon atmosphere for 10 min. A solution of 0.2 N sodium hydroxide (14 mL) solution was added slowly to the acetone solution with a syringe through the rubber septum at moderate stirring. When color of the solution turned deep red, a 0.4 N sodium hydroxide solution (105 mL) was added slowly. The reaction mixture was stirred for another 15 min. The temperature of the reaction mixture was then raised to room temperature. When the mixture turned deep green, the temperature of the reaction mixture was further increased to refluxing temperature and stirred for an additional hour. The temperature was lowered to room temperature and chloroform was added to the mixture. The mixture was separated with a separating funnel and the organic portion was collected and washed with water three times. The organic portion was concentrated and poured into a short plug of silica. The filtration cake was then washed with toluene and the filtrate was collected. The solvent in the filtrate was reduced to minimum and isopropanol was added. The solution was cooled to 0 °C for crystallization. The final precipitate was collected by suction filtrate and washed successively with isopropanol and methanol. The final product of **IDG-C20-Br** was a dark blue powder (678 mg , 10%) ^{1}H NMR (300 MHz, Chloroform-*d*) δ 9.01 (s, 2H), 7.01 (d, *J* = 8.3 Hz, 2H), 6.81 (d, *J* = 8.4 Hz, 2H), 3.94 (d, *J* = 5.5 Hz, 4H), 1.98 – 1.77 (m, 2H), 1.45 – 1.21 (m, 64H), 0.86 (t, *J* = 6.4 Hz, 12H). ^{13}C NMR (300 MHz, Chloroform-*d*) δ 186.56, 145.08, 144.00, 124.89, 121.58, 120.90, 117.53, 109.21, 72.05, 37.83, 37.83, 31.94, 31.25, 30.00, 29.69, 29.39, 26.81, 22.71, 14.13. Matrix assisted laser desorption ionization time-of-flight mass spectrometry (MALDI-TOF-MS) was used to characterize the mass of the monomer **IDG-C20-Br**. The mass spectrum is shown in Figure S16. Calculated [M+H^{+}]: 1013.52; Found: 1013.37. (Figure B-5, B-6, & B-7)

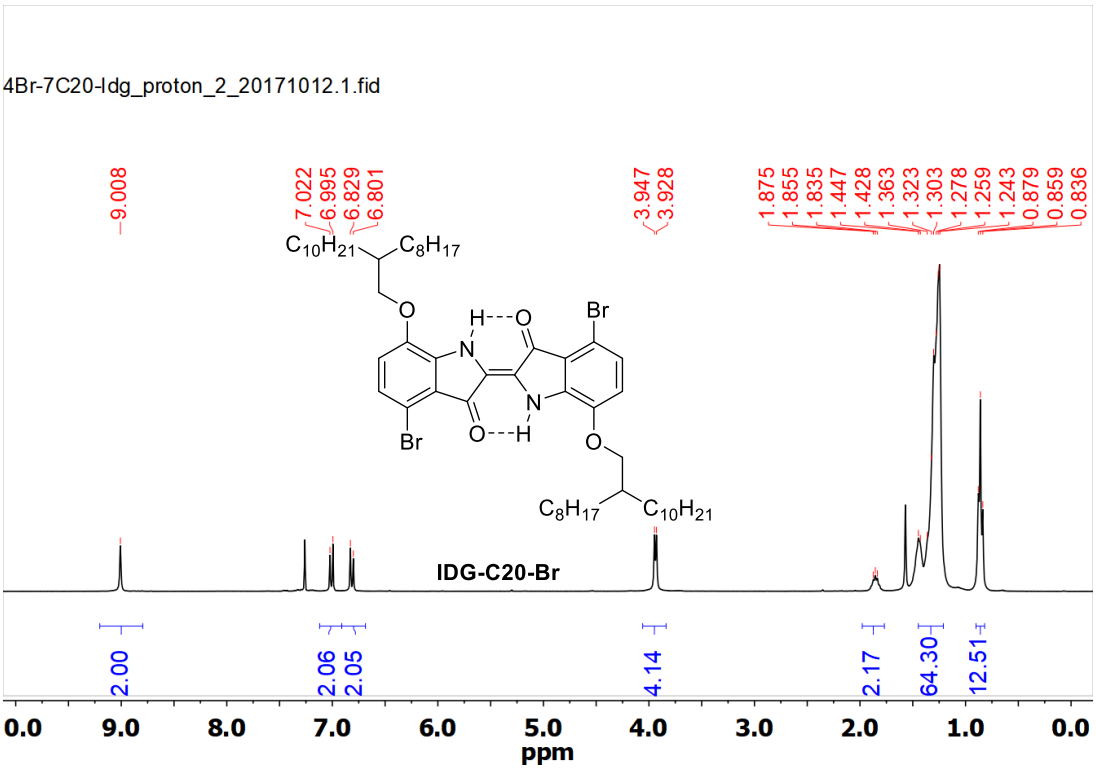

Figure B-5. 300 MHz ^{1}H NMR of **IDG-C20-Br** in $CDCl_3$.

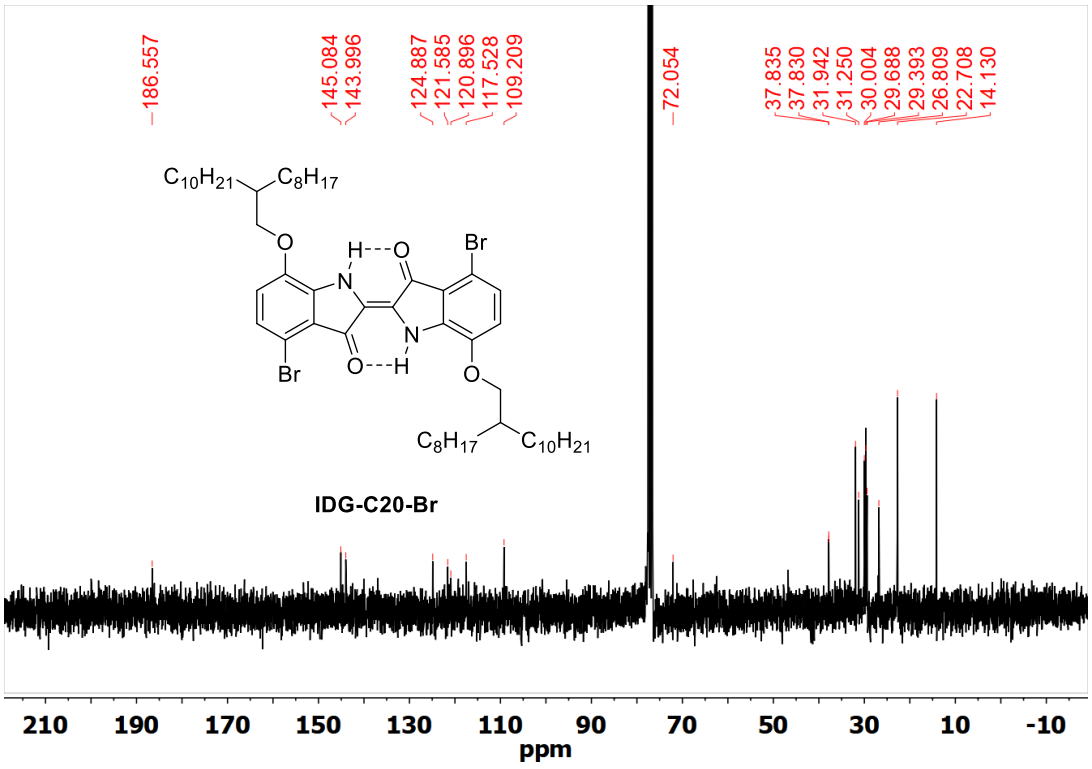

Figure B-6. 75 MHz ^{13}C NMR of **IDG-C20-Br** in $CDCl_3$.

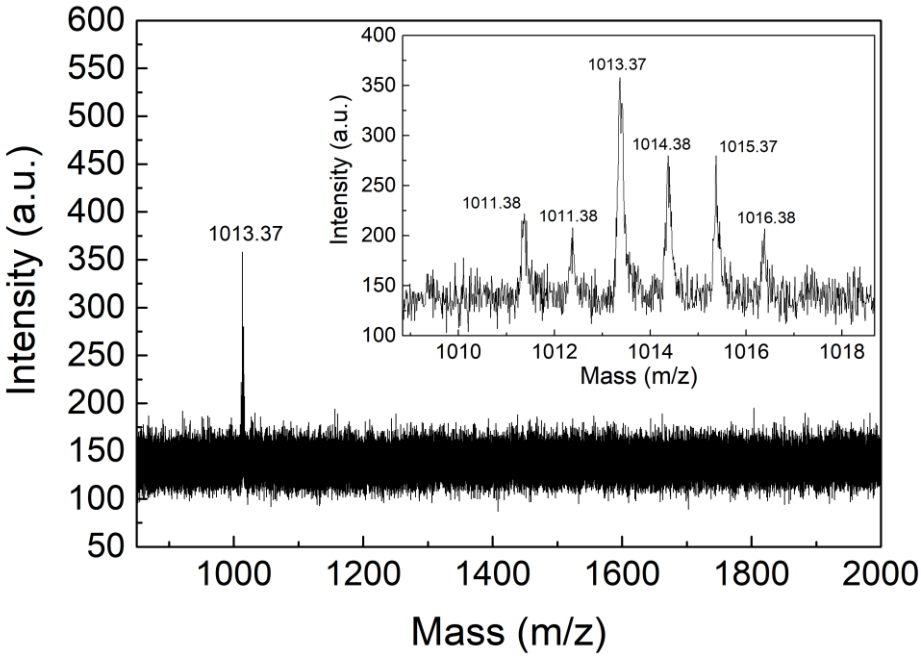

Figure B-7. MALDI-ToF MS spectrum of **Br-IDG-C20**.

Synthesis of polymer PIDG-T-C20 and PIDG-BT-C20

To a 25mL two-necked round-bottom flask, **4Br-7C20-IDG** (80 mg, 0.0790 mmol), P(*o*-tol)$_3$ (1.44 mg , 0.00473 mmol) and 5,5'-bis(trimethylstannyl)thiophene (32.4 mg, 0.0790 mmol) were added. One neck of the flask was fitted with a condenser and the other neck was stoppered with a rubber septum. The system was connected to argon atmosphere. The flask was then undergone a vacuum-purge cycle for three times and kept under argon atmosphere. Anhydrous chlorobenzene was added to dissolve all the solids before a solution of $Pd_2(dba)_3$ (1.08 mg , 0.00118 mmol) in chlorobenzene (1 mL) was added. The mixture was then stirred at 130 °C for 48 h. Upon cooling to room temperature, the viscous mixture was poured into methanol under stirring. The precipitate was collected and was purified by Soxhlet extraction using methanol, acetone and chloroform to afford polymer **PIDG-T-C20** as a dark blue film (68 mg, 92%). The synthesis of **PIDG-BT-C20** was carried out using a similar procedure using 5,5'-bis(trimethylstannyl)-2,2'-bithiophene as the donor building block and chlorobenzene as the final Soxhlet extraction solvent instead of chloroform. The final product obtained is a dark blue powder (72 mg, 90%).

Synthesis of Bis(2-ethylhexyl) 1,4-dioxo-3,6-di(thiophen-2-yl)pyrrolo[3,4-c]pyrrole-2,5(1H,4H)-dicarboxylate (DPPTh-EHC)

To a 100mL two-necked round bottom flask, 3,6-di(thiophen-2-yl)-2,5-dihydropyrrolo[3,4-c]pyrrole-1,4-dione (**DPPTh)** (500 mg, 1.66 mmol) and sodium hydride (200 mg, 8.32 mmol) were added. After the flask was purged with argon for 10 min, anhydrous THF (15 mL) was added via a syringe. The mixture was stirred for 1 hour under argon at room temperature before 2-ethylhexyl chloroformate (687 µL, 3.50 mmol) was added slowly via a syringe. The mixture was then heated to and maintained at 50 ºC for an additional 3 h before being cooled down to room temperature. A saturated sodium bicarbonate solution was added to quench the reaction. The mixture was then extracted with diethyl ether. The organic phase was washed with water, dried over anhydrous Na_2SO_4, and filtered. The filtrate was evacuated to remove the solvent. The crude product was purified by column chromatography using hexane/ethyl acetate (4:1) as the eluent to afford bis(2-ethylhexyl) 1,4-dioxo-3,6-di(thiophen-2-yl)pyrrolo[3,4-c]pyrrole-2,5(1H,4H)-dicarboxylate (**DPPTh-EHC**). Yield: 320 mg (31%). ^{1}H NMR (300 MHz, $CDCl_3$) δ 8.22 (d, *J* = 3.9 Hz, 2H), 7.64 (d, *J* = 5.0 Hz, 2H), 7.20 (t, *J* = 4.5 Hz, 2H), 4.29 (dd, *J* = 5.9, 1.7 Hz, 4H), 1.75 – 1.59 (m, 2H), 1.36 – 1.24 (m, 16H), 0.90 – 0.84 (m, 12H).^{13}C NMR (75 MHz, $CDCl_3$) δ 158.49, 150.39, 137.87, 133.91, 131.90, 129.52, 128.05, 110.46, 71.04, 38.51, 29.89, 28.72, 23.27, 22.78, 13.92, 10.77. (Figure B-8 & B-9)

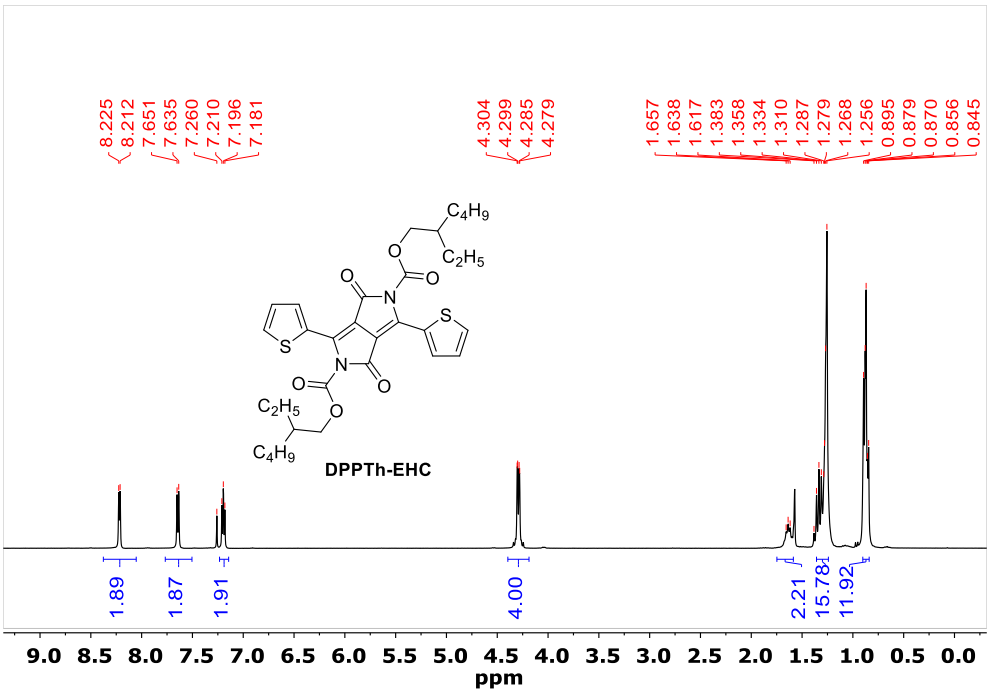

Figure B-8. 300 MHz ^{1}HNMR of **DPPTh-EHC** measured in $CDCl_3$.

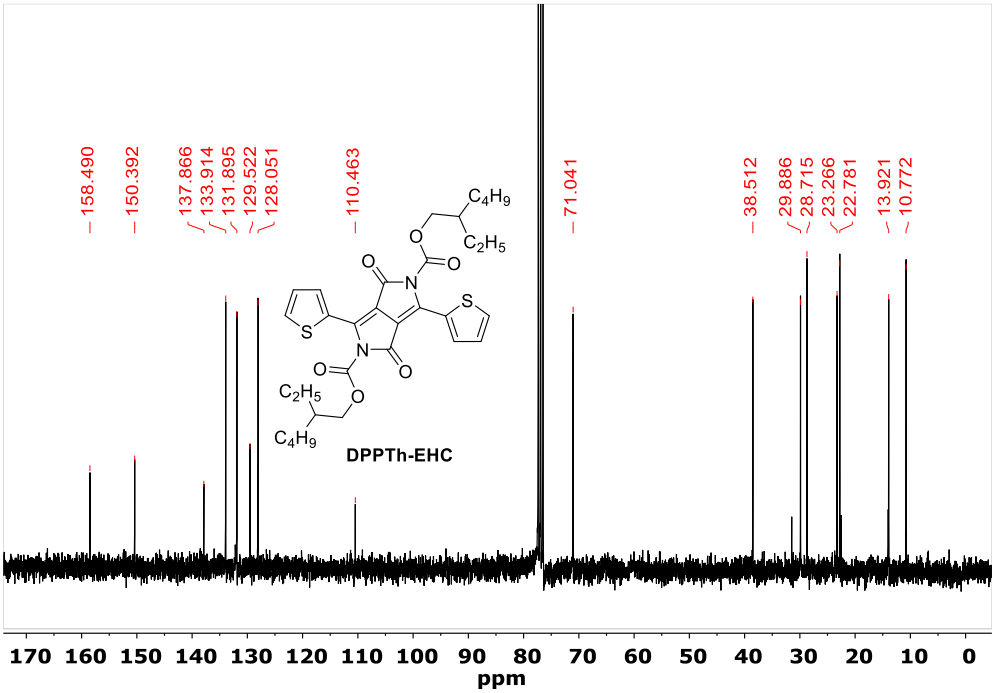

Figure B-9. 75 MHz ^{13}C NMR of **DPPTh-EHC** measured in $CDCl_3$.

Synthesis of Bis(2-ethylhexyl) 3,6-bis(5-bromothiophen-2-yl)-1,4-dioxopyrrolo[3,4-c]pyrrole-2,5(1H,4H)-dicarboxylate (Br-DPPTh-EHC)

To a 100mL two-necked round bottom flask were added 1,4-dioxo-3,6-di(thiophen-2-yl)pyrrolo[3,4-c]pyrrole-2,5(1H,4H)-dicarboxylate (**DPPTh-EHC**) (320 mg, 0.522 mmol) and chloroform (12 mL) under argon. *N*-Bromosuccinimide (NBS) (204 mg , 1.15 mmol) was added to the solution and then one drop of 48% hydrobromic acid (HBr) was added to the reaction mixture. The mixture was stirred at room temperature under argon for 1 h. Sodium sulfite solution was added to quench the reaction. The mixture was extracted with chloroform and washed with water. The chloroform portion was collected, dried over anhydrous Na_2SO_4, filtered, and evacuated to remove the solvent. The crude product was then recrystallized in chloroform/methanol mixture to afford bis(2-ethylhexyl) 3,6-bis(5-bromothiophen-2-yl)-1,4-dioxopyrrolo[3,4-c]pyrrole-2,5(1H,4H)-dicarboxylate (**Br-DPPTh-EHC**), Yield: 364 mg (90%). ^{1}H NMR (300 MHz, $CDCl_3$) δ 8.07 (d, J = 4.2 Hz, 2H), 7.16 (d, J = 4.2 Hz, 2H), 4.32 (d, J = 5.8 Hz, 4H), 1.81 – 1.61 (m, 2H), 1.50 – 1.16 (m, 16H), 1.01 – 0.78 (m, 12H). ^{13}C NMR (75 MHz, $CDCl_3$) δ 158.16, 150.40, 136.70, 134.57, 131.03, 130.73, 121.08, 110.58, 71.26, 38.58, 29.91, 28.73, 23.29, 22.82, 13.95, 10.79. (Figure B-10 & B-11)

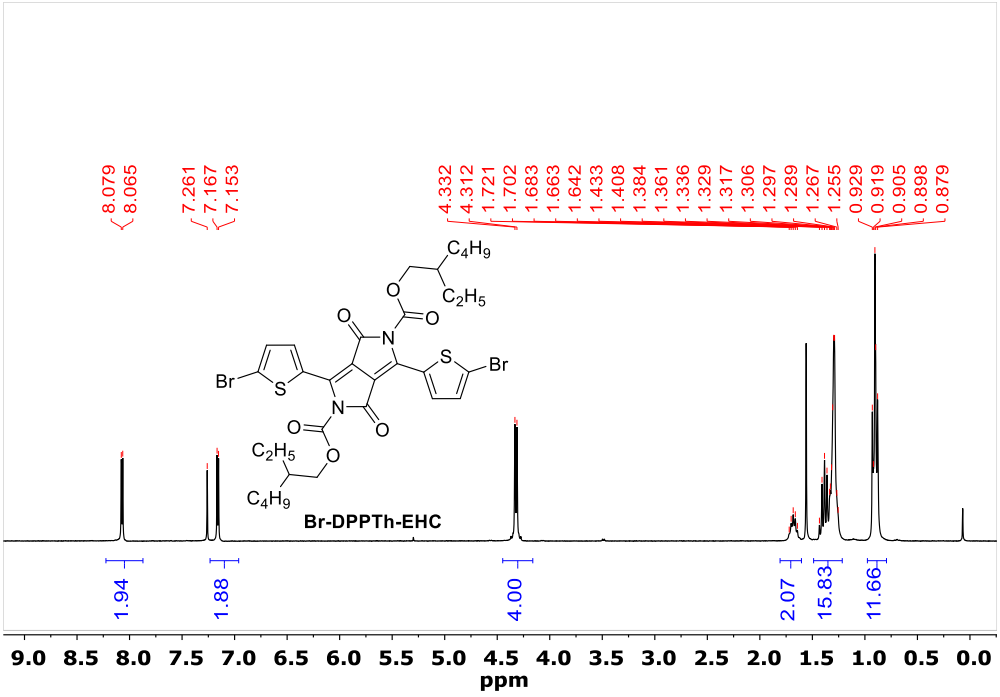

Figure B-10. 300 MHz ^{1}HNMR of **Br-DPPTh-EHC** measured in $CDCl_3$.

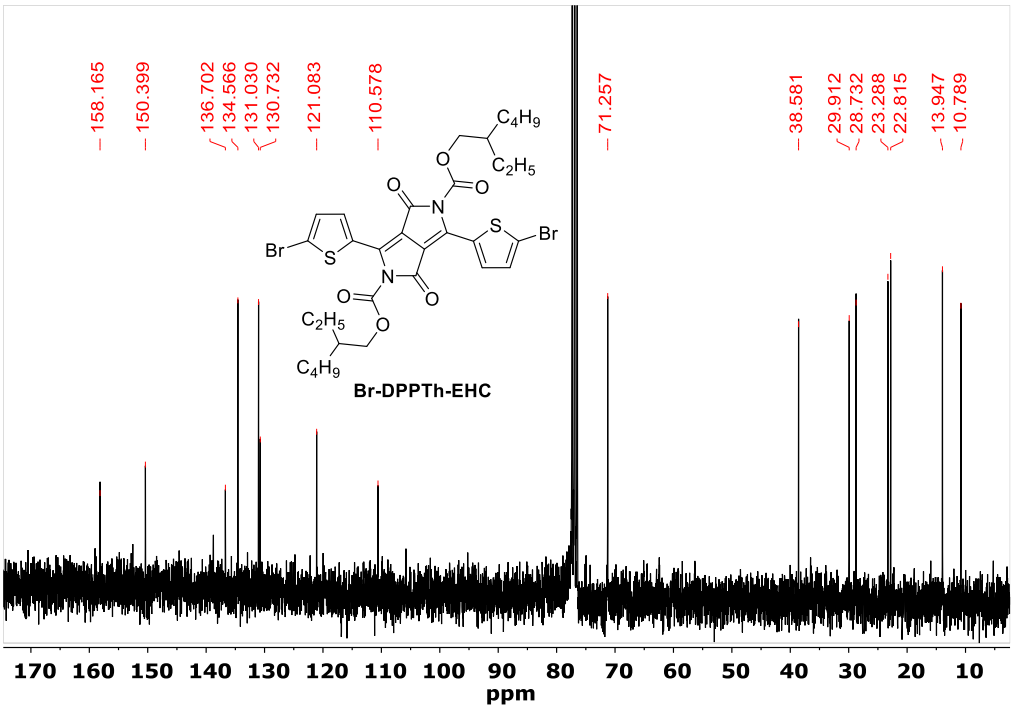

Figure B-11. 75 MHz ^{13}CNMR of **Br-DPPTh-EHC** measured in $CDCl_3$.

Synthesis of Poly[bis(2-ethylhexyl) 3-(3'',4'-bis(dodecyloxy)-[2,2':5',2''-terthiophen]-5-yl)-1,4-dioxo-6-(thiophen-2-yl)pyrrolo[3,4-c]pyrrole-2,5(1H,4H)-dicarboxylate] (PDEB)

To a 25mL two-necked round-bottom flask, bis(2-ethylhexyl) 3,6-bis(5-bromothiophen-2-yl)-1,4-dioxopyrrolo[3,4-c]pyrrole-2,5(1H,4H)-dicarboxylate (**Br-DPPTh-EHC**) (50.0 mg, 0.0649 mmol), P(*o*-tol)$_3$ (1.58 mg , 0.00519 mmol) and (3,3'-bis(dodecyloxy)-[2,2'-bithiophene]-5,5'-diyl)bis(trimethylstannane) (**C12-BTO-TMT**) (55.8 mg, 0.0649 mmol) were added. The system was evacuated and filled with argon for three times. Anhydrous chlorobenzene was added to dissolve all the solids before a solution of $Pd_2(dba)_3$ (1.19 mg, 0.00130 mmol) in chlorobenzene (1 mL) was added. The mixture was then stirred at 80 ºC for 48 h under argon. Upon cooling to room temperature, the viscous mixture was poured into methanol under stirring. The precipitate was collected and was purified by Soxhlet extraction using methanol, acetone and chloroform. The chloroform fraction was evacuated to remove the solvent to afford poly[bis(2-ethylhexyl) 3-(3",4'-bis(dodecyloxy)-[2,2':5',2"-terthiophen]-5-yl)-1,4-dioxo-6-(thiophen-2-yl)pyrrolo[3,4-c]pyrrole-2,5(1H,4H)-dicarboxylate] **PDEB** as a dark blue film. Yield: 60 mg (81%).

Synthesis of Poly[3-(3'',4'-bis(dodecyloxy)-[2,2':5',2''-terthiophen]-5-yl)-6-(thiophen-2-yl)-2,5-dihydropyrrolo[3,4-c]pyrrole-1,4-dione] (PDNB)

Polymer **PDEB** was spin-coated onto a substrate (glass, ITO-coated glass, SiO_2 (300 nm)/Si) at a concentration of 10 mg mL^{-1} in HPLC grade chlorobenzene at 700 rpm for 80 s. The substrate was then thermally annealed at 200 ºC in air for 20 min to afford the **PDNB** film. After the annealing, the substrate was cooled down to room temperature and the thin film was washed successively with deionized water, isopropanol, acetone and chloroform to obtain a **PDNB** film.

The **PDNB** flakes for the XRD measurement was prepared by annealing the **PDEB** flakes on a hotplate at 200 °C for 20 min in ambient air.

Synthesis of (Z)-6-bromo-3-((5-bromothiophen-2-yl)methylene)indolin-2-one (2a)

To a 100mL two-necked round bottom flask, 6-bromooxindole (2.00 g, 9.43 mmol) and 5-bromothiophene-2-carbaldehyde (**1a**) (1.80 g , 9.43 mmol) were added. One neck of the flask was fitted with a condenser and the other neck was stoppered with a rubber septum. The mixture was purged with nitrogen for 15 min. EtOH (25.0 mL) was added to the mixture and heated at refluxing temperature. Piperidine (2.15 mL) was added slowly with a syringe through the rubber septum. The mixture was then refluxed for 18 h under nitrogen atmosphere. The mixture was cooled to room temperature, and quenched by cold water. The yellow precipitate was filtered and washed successively with water, methanol and cold ethyl acetate. The final product (*Z*)-6-bromo-3-((5-bromothiophen-2-yl)methylene)indolin-2-one (**2a**) was a yellow powder and was used in the next step without further purification or characterization due to poor solubility in solvents. (2.17 g, 60%)

Synthesis of 2-ethylhexyl (Z)-6-bromo-3-((5-bromothiophen-2-yl)methylene)-2-oxoindoline-1-carboxylate (M1)

To a 100mL two-necked round bottom flask, (*Z*)-6-bromo-3-((5-bromothiophen-2-yl)methylene)indolin-2-one (**2a**) (1.00 g , 2.60 mmol) and sodium hydride (156 mg, 6.49 mmol) were added. One neck of the flask was connected argon atmosphere and the other neck was fitted with a rubber septum. The mixture was then vacuumed and purged with argon three times. Anhydrous THF was added to the mixture and the mixture was stirred at room temperature for 15 min or until the reaction mixture turned from a yellow suspension into a clear dark orange solution. 2-Ethylhexyl chloroformate (0.561 mL, 2.86 mmol) was added slowly into the reaction mixture using a syringe through the rubber septum. The reaction mixture was stirred for 1 h under argon atmosphere. Saturated $NaHCO_3$ solution was added slowly into the mixture to quench the reaction. The mixture was then extracted with diethyl ether and washed successively with water. The organic layer was collected and dried with anhydrous Na_2SO_4 salt. The solution was filtered and the solvent was removed. The crude product was purified by column chromatography using hexane : EA = 1 : 1 as the eluent to afford 2-ethylhexyl (*Z*)-6-bromo-3-((5-bromothiophen-2-yl)methylene)-2-oxoindoline-1-carboxylate (**M1**) as a light yellow powder. (0.954 g, 68%) ^{1}H NMR (300 MHz, Chloroform-*d*) δ 8.11 (d, *J* = 1.7 Hz, 1H), 7.60 (s, 1H), 7.48 – 7.40 (m, 1H), 7.37 (s, 1H), 7.32 (dd, *J* = 8.2, 1.7 Hz, 1H), 7.15 (d, *J* = 4.0 Hz, 1H), 4.38 (d, *J* = 5.9 Hz, 2H), 1.82 (p, *J* = 6.1 Hz, 1H), 1.55 – 1.25 (m, 8H), 1.07 – 0.85 (m, 6H). ^{13}C NMR (75 MHz, Chloroform-*d*) δ 164.23, 150.88, 138.81, 138.46, 138.28, 130.37, 129.19, 127.24, 123.95, 122.86, 122.56, 119.43, 118.64, 104.58, 69.97, 38.84, 30.33, 28.91, 23.71, 22.98, 14.08, 11.00. MALDI-TOF-MS calculated [M+Na^+]: 563.96; Found: 563.93 (Figure B-12, B-13 & B-14)

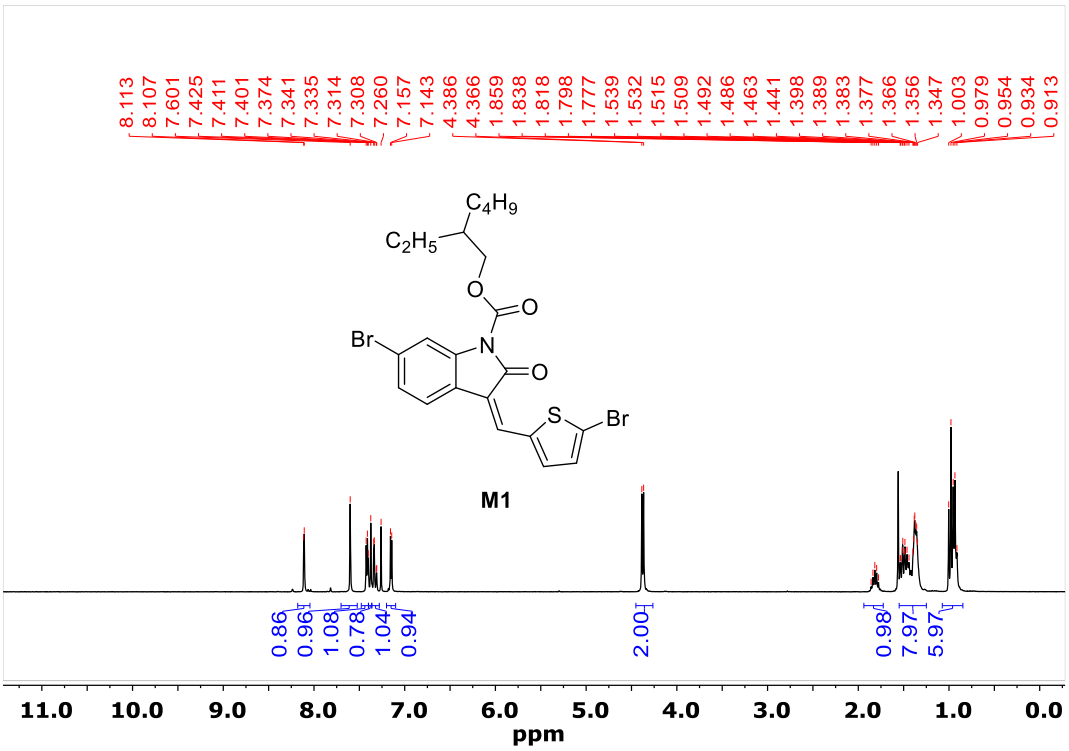

Figure B-12. [1]HNMR spectrum of compound **M1**.

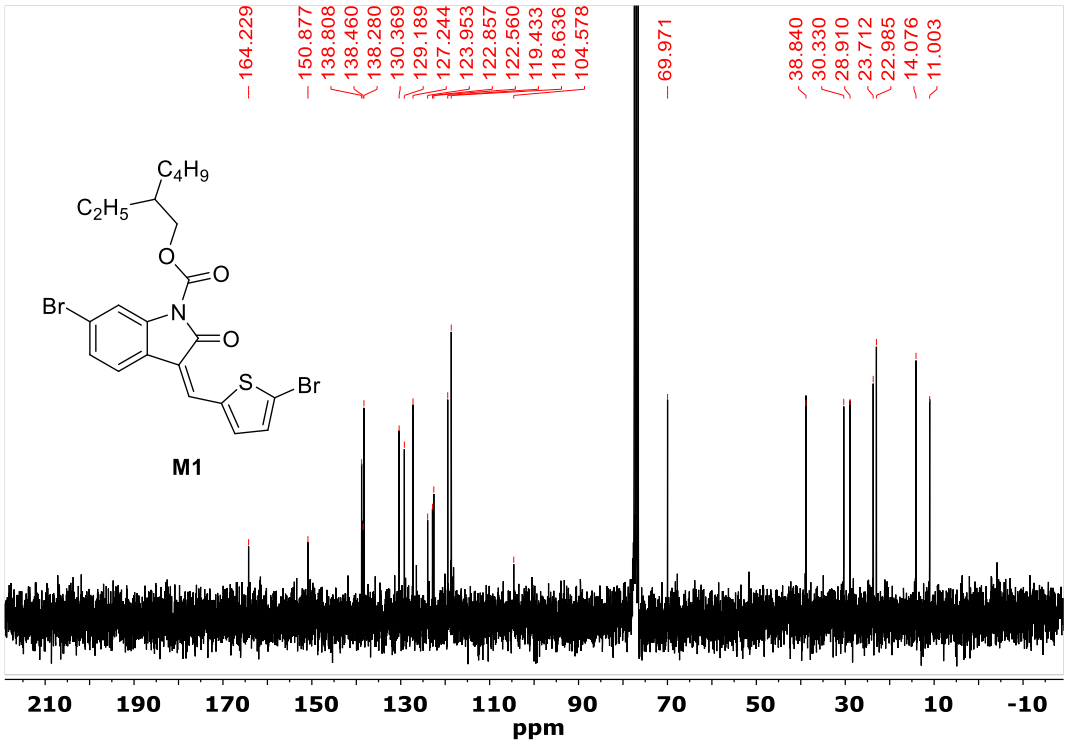

Figure B-13. [13]CNMR spectrum of compound **M1**.

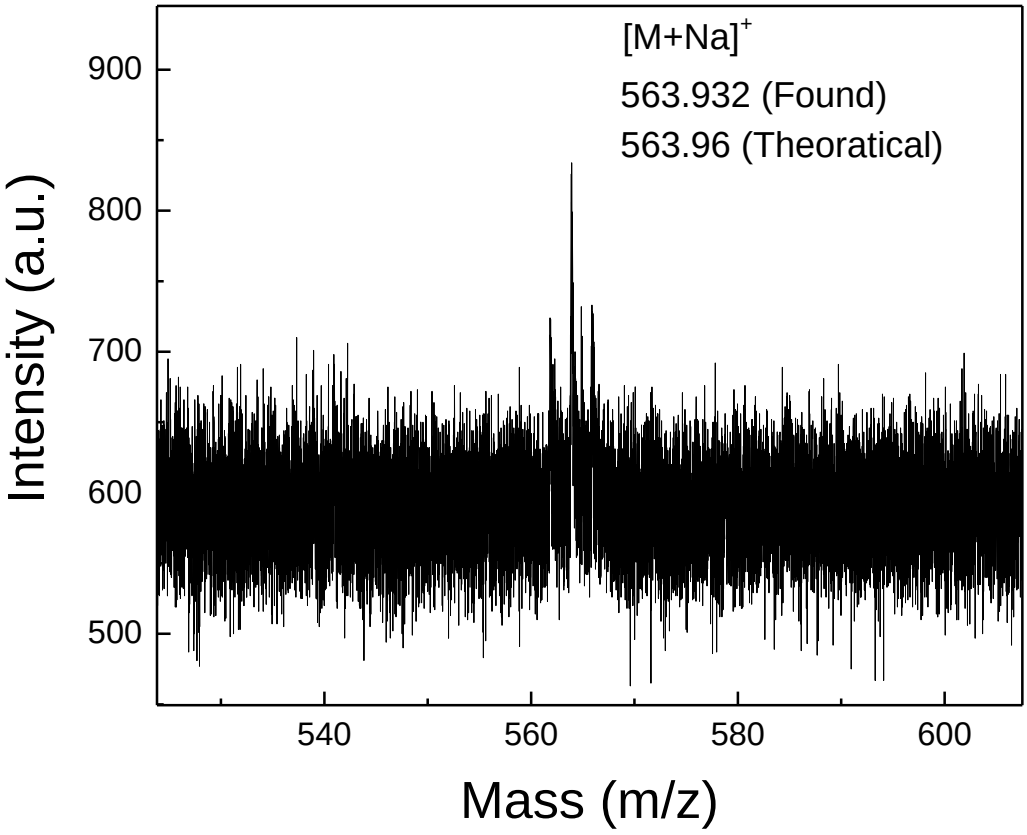

Figure B-14. MALDI spectrum of compound **M1**.

Synthesis of Poly[2-ethylhexyl 3-((3'',4'-bis(dodecyloxy)-[2,2':5',2''-terthiophen]-5-yl)methylene)-2-oxoindoline-1-carboxylate] (PTEB)

To a 25mL two-necked round-bottom flask, 2-ethylhexyl (*Z*)-6-bromo-3-((5-bromothiophen-2-yl)methylene)-2-oxoindoline-1-carboxylate (**3a**) (50.3 mg, 0.0930 mmol), P(*o*-tol)$_3$ (2.26 mg , 0.00744 mmol) and (3,3'-bis(dodecyloxy)-[2,2'-bithiophene]-5,5'-diyl)bis(trimethylstannane) (**M5**) (80.0 mg, 0.0930 mmol) were added. The system was evacuated and filled with argon for three times. Anhydrous chlorobenzene was added to dissolve all the solids before a solution of $Pd_2(dba)_3$ (1.70 mg, 0.00186 mmol) in chlorobenzene (~1 mL) was added. The mixture was then stirred at 80 ^oC for 24 h under argon. Upon cooling to room temperature, the viscous mixture was poured into methanol under stirring. The precipitate was collected and was purified by Soxhlet extraction using methanol, acetone and chloroform. The chloroform fraction was evacuated to remove the solvent to afford poly[2-ethylhexyl 3-((3",4'-bis(dodecyloxy)-[2,2':5',2"-terthiophen]-5-yl)methylene)-2-oxoindoline-1-carboxylate] (**PTEB**) as a dark blue film. (72.6 mg, 81%)

Synthesis of 3,4-dimethoxythiophene-2-carbaldehyde (2b)

To a 100mL two-necked round bottom flask, 3,4-dimethoxythiophene (**1b**) (1.50 g, 10.4 mmol) was added. One of the neck of the round bottle flask was stoppered by a rubber septum, while the other neck was fitted with a condenser. The whole system was connected to nitrogen atmosphere. Anhydrous THF (~6.00 mL) was added into the flask with a syringe through the rubber septum. The solution was then cooled to -10°C with ice/NaCl cooling bath purged under nitrogen for 15 min. Upon stirring, 2.5 M *n*-butyllithium (4.58 mL, 11.4 mmol) was slowly added into the cooled solution with a syringe through the rubber septum. The mixture was then stirred vigorously at -10°C for 30 min until a pale yellow slurry was given out. Dimethylformamide (DMF) (3.22 mL, 41.6 mmol) was then slowly added to the slurry with a syringe through the rubber septum. The mixture was then stirred at 0°C for 10 min, raised to room temperature and stirred for an additional 30 min. The reaction was quenched by pouring the mixture into ice with dilute HCl solution (0.5N). The crude product was then isolated by filtration and recrystallized in methanol to give 3,4-dimethoxythiophene-2-carbaldehyde (**2b**) as a brown powder. (1.65 g, 93%) ^{1}H NMR (300 MHz, Chloroform-*d*) δ 10.01 (s, 1H), 6.64 (s, 1H), 4.11 (s, 3H), 3.86 (s, 3H). (Figure B-15)

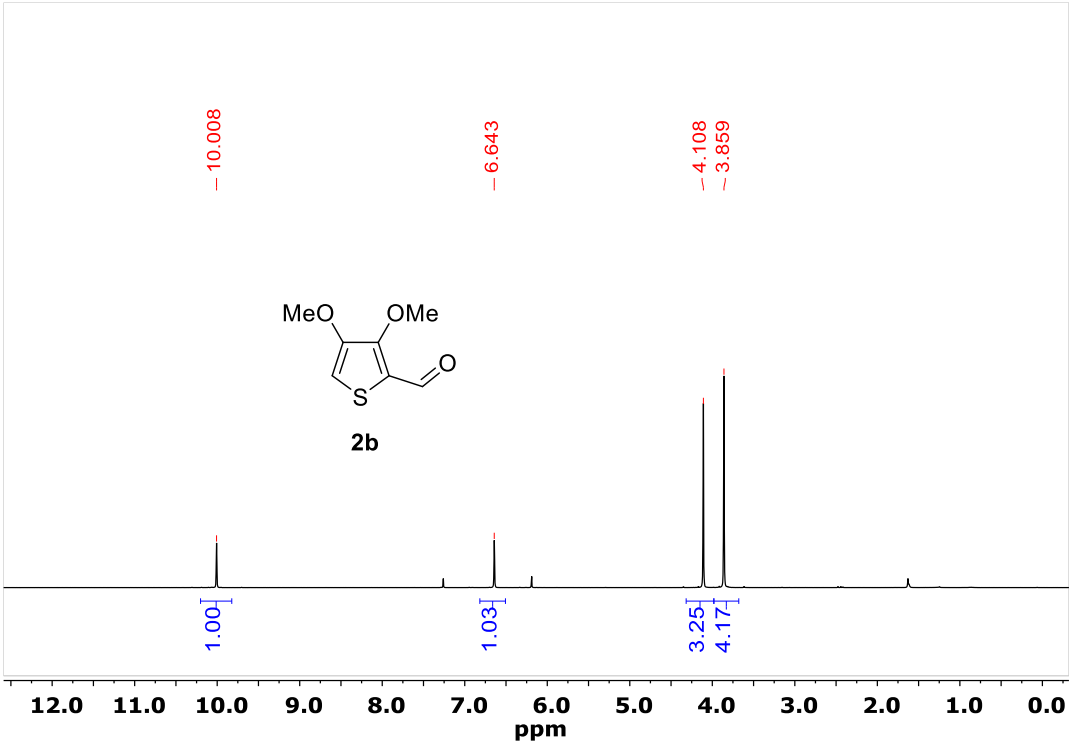

Figure B-15. ^{1}HNMR spectrum of compound **2b**.

Synthesis of (Z)-6-bromo-3-((5-bromo-3,4-dimethoxythiophen-2-yl)methylene)indolin-2-one (3b)

To a 100mL two-necked round bottom flask, 6-bromooxindole (850 mg , 4.01 mmol) and 3,4-dimethoxythiophene-2-carbaldehyde (**2b** (690 mg , 4.01 mmol) were added. One neck of the flask was fitted with a condenser and the other neck was stoppered with a rubber septum. The mixture was purged with nitrogen for 15 min. EtOH (10.9 mL) was added to the mixture and heated at refluxing temperature. Piperidine (0.912 mL) was added slowly with a syringe through the rubber septum. The mixture was then refluxed for 18 h under nitrogen atmosphere. The mixture was cooled to room temperature, and methanol was added to the solution. The precipitate was filtered and washed with MeOH and hexane to obtain an orange brown powder of (*Z*)-6-bromo-3-((5-bromo-3,4-dimethoxythiophen-2-yl)methylene)indolin-2-one (**3b**). (1.24 g, 84%) ^{1}H NMR (300 MHz, DMSO-d_6) δ 10.74 (s, 1H), 8.03 (d, *J* = 8.3 Hz, 1H), 7.78 (s, 1H), 7.37 – 7.13 (m, 2H), 7.03 (d, *J* = 1.9 Hz, 1H), 3.95 (s, 3H), 3.87 (s, 3H). (Figure B-16)

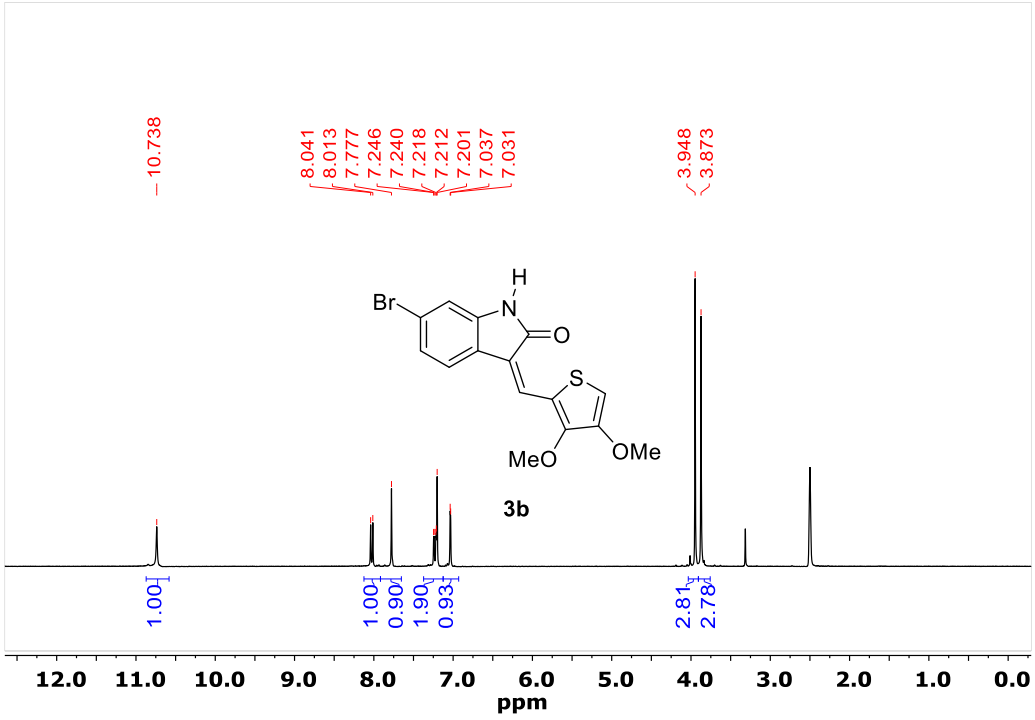

Figure B-16. ^{1}HNMR spectrum of compound **3b**.

Synthesis of 2-ethylhexyl 6-bromo-3-((3,4-dimethoxythiophen-2-yl)methylene)-2-oxoindoline-1-carboxylate (4b)

To a 100mL two-necked round bottom flask, (*Z*)-6-bromo-3-((5-bromo-3,4-dimethoxythiophen-2-yl)methylene)indolin-2-one (**3b**) (500 mg, 1.37 mmol) and sodium hydride (81.9 mg, 3.41 mmol) were added. One neck of the flask was connected argon atmosphere and the other neck was fitted with a rubber septum. The mixture was then vacuumed and purged with argon three times. Anhydrous THF (~8 mL) was added to the mixture and the mixture was stirred at room temperature for 15 min or until the reaction mixture turned from a yellow suspension into a clear dark orange solution. 2-Ethylhexyl chloroformate (0.295 mL, 1.50 mmol) was added slowly into the reaction mixture using a syringe through the rubber septum. The reaction mixture was stirred for 1 h under argon atmosphere. Saturated $NaHCO_3$ solution was added slowly into the mixture to quench the reaction. The mixture was then extracted with diethyl ether and washed successively with water. The organic layer was collected and dried with anhydrous Na_2SO_4 salt. The solution was filtered and the solvent was removed. The crude product was purified by recrystallization in MeOH/$CHCl_3$ solution to obtain orange brown solids of 2-ethylhexyl 6-bromo-3-((3,4-dimethoxythiophen-2-yl)methylene)-2-oxoindoline-1-carboxylate (**4b**), which consist of a mixture of inseparable geometric isomers in *Z*:*E* ≈ 1:1 ratio. (463 mg, 65%) ^{1}H NMR (300 MHz, Chloroform-*d*) δ 8.36 – 7.90 (m, 2H), 7.68 – 7.04 (m, 2H), 6.63 (d, *J* = 34.8 Hz, 1H), 4.36 (dt, *J* = 8.3, 4.2 Hz, 2H), 4.03 (dd, *J* = 18.7, 2.1 Hz, 3H), 3.89 (d, *J* = 4.5 Hz, 3H), 1.78 (dq, *J* = 12.0, 6.1 Hz, 1H), 1.55 – 1.14 (m, 8H), 1.09 – 0.81 (m, 6H). (Figure B-17)

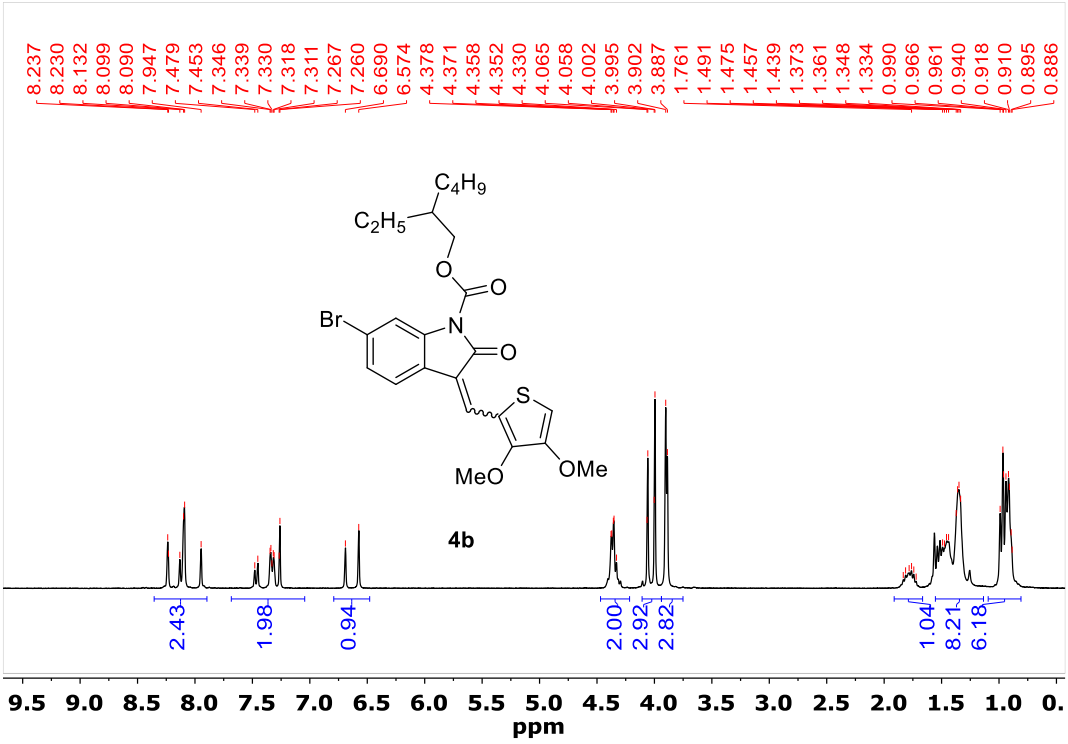

Figure B-17. [1]HNMR spectrum of compound **4b**.

Synthesis of 2-ethylhexyl 6-bromo-3-((5-bromo-3,4-dimethoxythiophen-2-yl)methylene)-2-oxoindoline-1-carboxylate (M2)

To a 50 mL round bottom flask, 2-ethylhexyl 6-bromo-3-((3,4-dimethoxythiophen-2-yl)methylene)-2-oxoindoline-1-carboxylate (**4b**) (400 mg, 0.766 mmol) was dissolved in 5.0 mL $CHCl_3$. The mixture was purged under nitrogen for 15 minutes. NBS was added slowly into the mixture and stirred for 15 min at room temperature. A catalytic amount of 47% HBr acid was added and the mixture was stirred for an additional 1 h. The mixture was then quenched by adding saturated sodium sulfite solution. The reaction mixture was extracted with diethyl ether and washed with water. The organic portion was collected and solvent was removed. The product was further purified by passing the solution through a short plug of silica. The solvent was removed and the product was recrystallized using MeOH/$CHCl_3$ solution to obtain orange brown solids of 2-ethylhexyl 6-bromo-3-((5-bromo-3,4-dimethoxythiophen-2-yl)methylene)-2-oxoindoline-1-carboxylate (**M2**) as a mixture of *Z*:*E* geometric isomers in 1:1 ratio. (408mg, 89%) ^{1}H NMR (300 MHz, Chloroform-*d*) δ 8.17 (dd, *J* = 40.1, 1.8 Hz, 1H), 8.06 – 7.28 (m, 3H), 4.44 – 4.26 (m, 2H), 4.21 – 3.80 (m, 6H), 1.78 (dq, *J* = 17.9, 6.1 Hz, 1H), 1.54 – 1.22 (m, 8H), 0.96 (ddd, *J* = 15.1, 7.5, 4.2 Hz, 6H). ^{13}C NMR of the compound was not shown because the spectrum does not give significant information to structural characterization due to the overlapping resonance signals of the two geometric isomers. MALDI-TOF-MS calculated [M^+]: 601.00; Found: 600.97 (Figure B-18 & B-19)

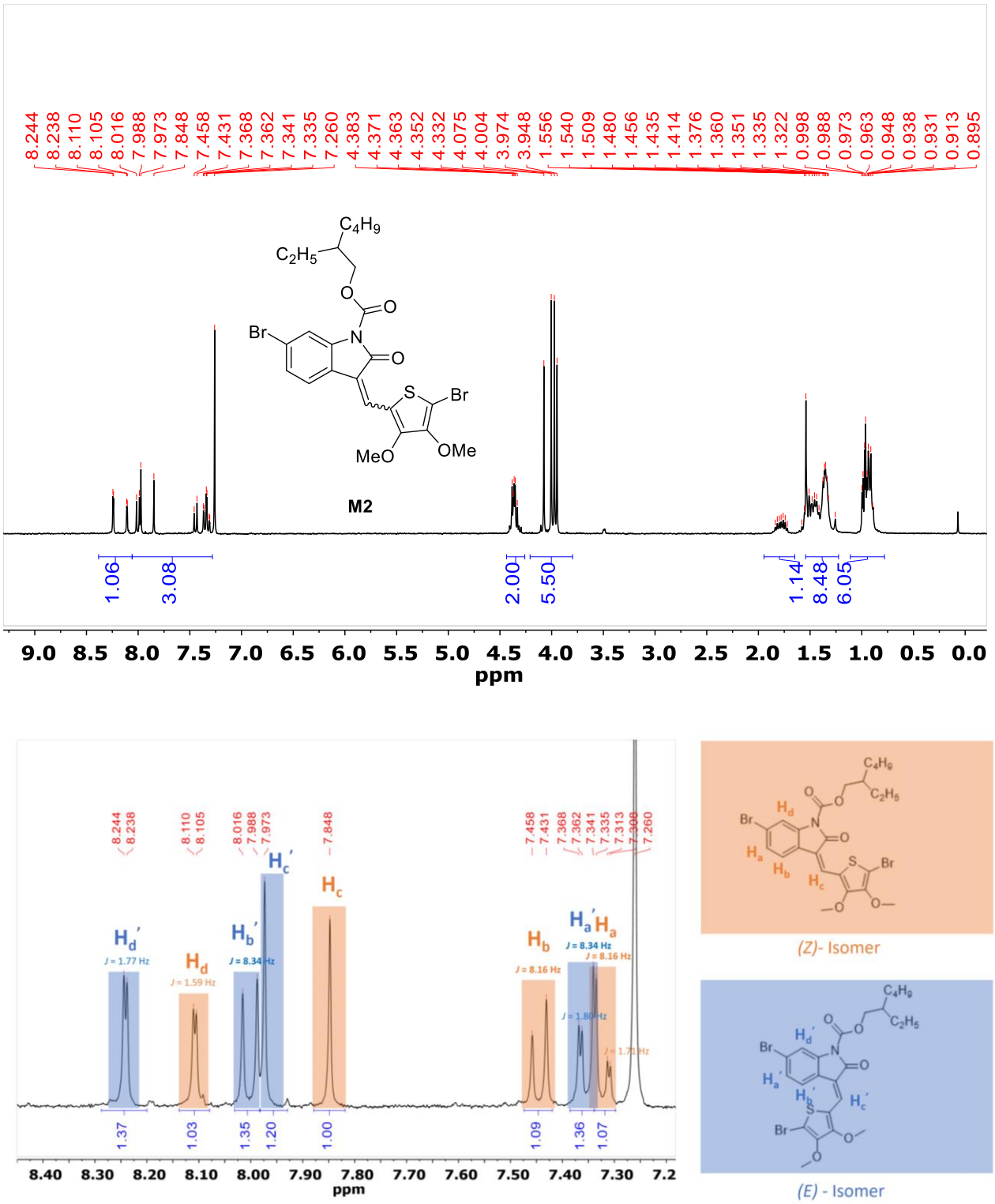

Figure B-18. [1]HNMR spectra of compound **M2** (top); Magnified [1]HNMR spectrum in the aromatic region and proton assignments of the (Z) and (E) isomers of compound **M2** (bottom).

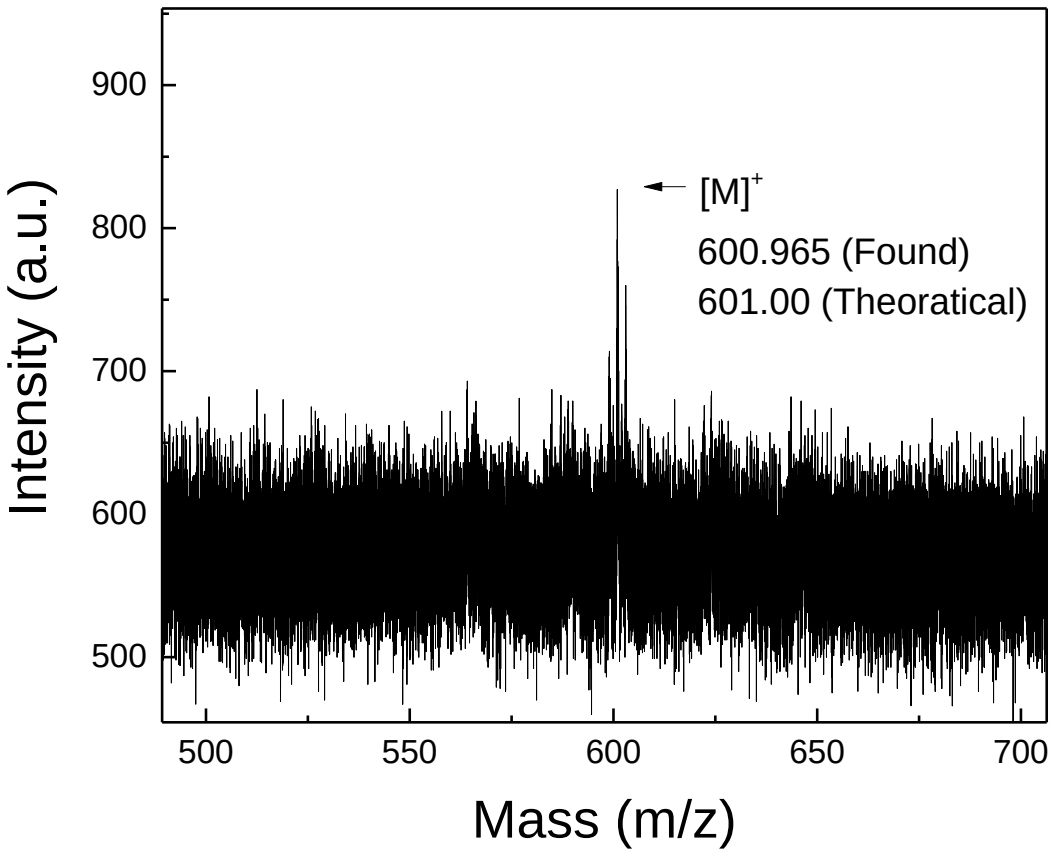

Figure B-19. MALDI spectrum of compound **M2**.

Synthesis of Poly[2-ethylhexyl 3-((3'',4'-bis(dodecyloxy)-3,4-dimethoxy-[2,2':5',2''-terthiophen]-5-yl)methylene)-2-oxoindoline-1-carboxylate] (PMEB)

To a 25mL two-necked round-bottom flask, 2-ethylhexyl 6-bromo-3-((5-bromo-3,4-dimethoxythiophen-2-yl)methylene)-2-oxoindoline-1-carboxylate (**5b**) (55.9 mg, 0.0930 mmol), P(*o*-tol)$_3$ (2.26 mg , 0.00744 mmol) and (3,3'-bis(dodecyloxy)-[2,2'-bithiophene]-5,5'-diyl)bis(trimethylstannane) (**M5**) (80.0 mg, 0.0930 mmol) were added. The system was evacuated and filled with argon for three times. Anhydrous chlorobenzene was added to dissolve all the solids before a solution of $Pd_2(dba)_3$ (1.70 mg, 0.00186 mmol) in chlorobenzene (~1 mL) was added. The mixture was then stirred at 80 ^oC for 24 h under argon. Upon cooling to room temperature, the viscous mixture was poured into methanol under stirring. The precipitate was collected and was purified by Soxhlet extraction using methanol, acetone and chloroform. The chloroform fraction was evacuated to remove the solvent to afford poly[2-ethylhexyl 3-((3",4'-bis(dodecyloxy)-3,4-dimethoxy-[2,2':5',2"-terthiophen]-5-yl)methylene)-2-oxoindoline-1-carboxylate] (**PMEB**) as a dark blue film. (85.2 mg, 94%)

Synthesis of 2,3-dihydrothieno[3,4-b][1,4]dioxine-5-carbaldehyde (2c)

To a 100mL two-necked round bottom flask, 3,4-ethylenedioxythiophene (**1c** or **EDOT**) (1.00 g, 7.03 mmol) was added. One of the neck of the round bottle flask was stoppered by a rubber septum, while the other neck was fitted with a condenser. The whole system was connected to nitrogen atmosphere. Anhydrous THF (~6.00 mL) was added into the flask with a syringe through the rubber septum. The solution was then cooled to -10^{o}C with ice/NaCl cooling bath purged under nitrogen for 15 min. Upon stirring, 2.5 M *n*-butyllithium (3.09 mL, 7.74 mmol) was slowly added into the cooled solution with a syringe through the rubber septum. The mixture was then stirred vigorously at -10^{o}C for 30 min or until a yellow solution was obtained. Dimethylformamide (DMF) (2.18 mL, 28.1 mmol) was then slowly added to the slurry with a syringe through the rubber septum. The mixture was then stirred at 0^{o}C for 10 min, raised to room temperature and stirred for an additional 30 min. The reaction was quenched by pouring the mixture into ice with dilute HCl solution (0.5N). The crude product was then isolated by filtration and recrystallized in cold hexane to give 2,3-dihydrothieno[3,4-b][1,4]dioxine-5-carbaldehyde (**2c**) as a white powder. (0.986 g, 82%) ^{1}H NMR (300 MHz, Chloroform-*d*) δ 9.91 (d, *J* = 1.2 Hz, 1H), 6.79 (d, *J* = 1.2 Hz, 1H), 4.36 (td, *J* = 3.7, 2.2 Hz, 2H), 4.27 (td, *J* = 3.7, 2.2 Hz, 2H). (Figure B-20)

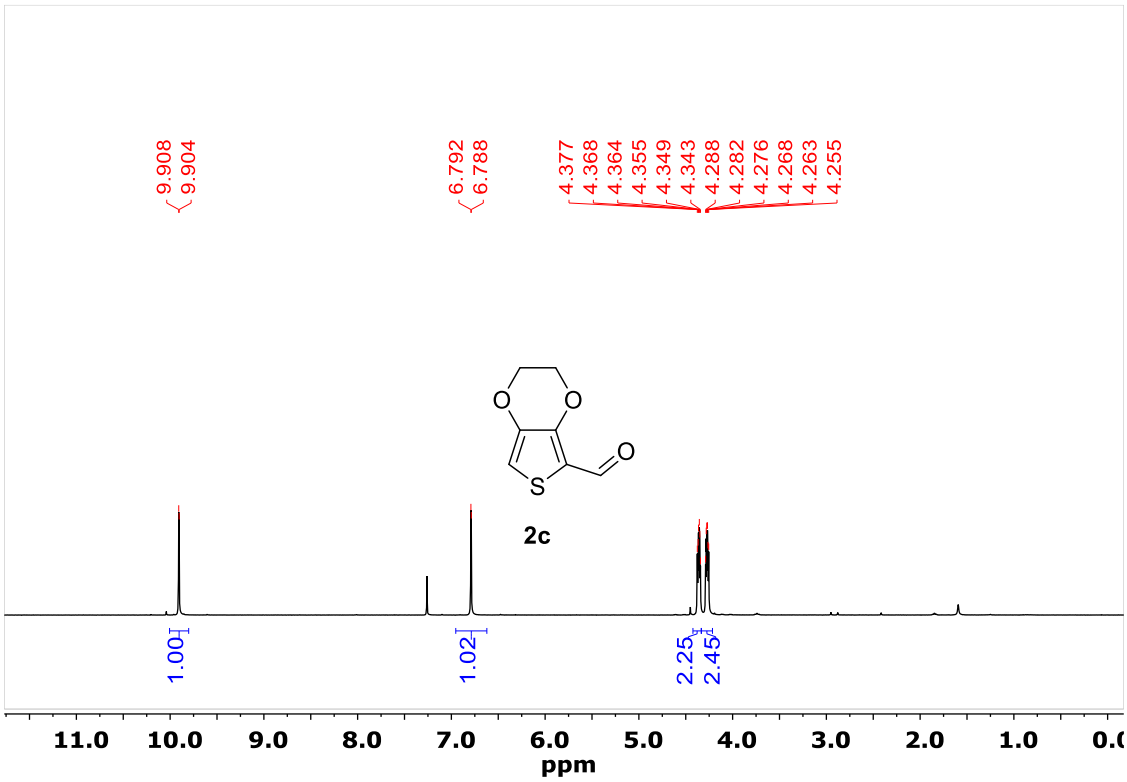

Figure B-20. [1]HNMR spectrum of compound **2c**.

Synthesis of 7-bromo-2,3-dihydrothieno[3,4-b][1,4]dioxine-5-carbaldehyde (3c)

To a 100mL round bottom flask, 2,3-dihydrothieno[3,4-b][1,4]dioxine-5-carbaldehyde (**2c**) (932 mg, 5.48 mmol) was dissolved in 5.0 mL THF. The mixture was purged under nitrogen for 15 minutes. N-bromosuccinimide (NBS) (1.07 g, 6.02 mmol) was added slowly into the mixture and stirred for 45 min at room temperature. The mixture was then quenched by adding cold saturated sodium sulfite solution. The reaction mixture was extracted with hexane and washed with water. The organic portion was collected and solvent was removed. The product was purified by recrystallization using cold hexane to obtain a white powder of 7-bromo-2,3-dihydrothieno[3,4-b][1,4]dioxine-5-carbaldehyde (**3c**). (1.20 g, 88%) ^{1}H NMR (300 MHz, Chloroform-*d*) δ 9.82 (s, 1H), 4.54 – 4.21 (m, 4H). (Figure B-21)

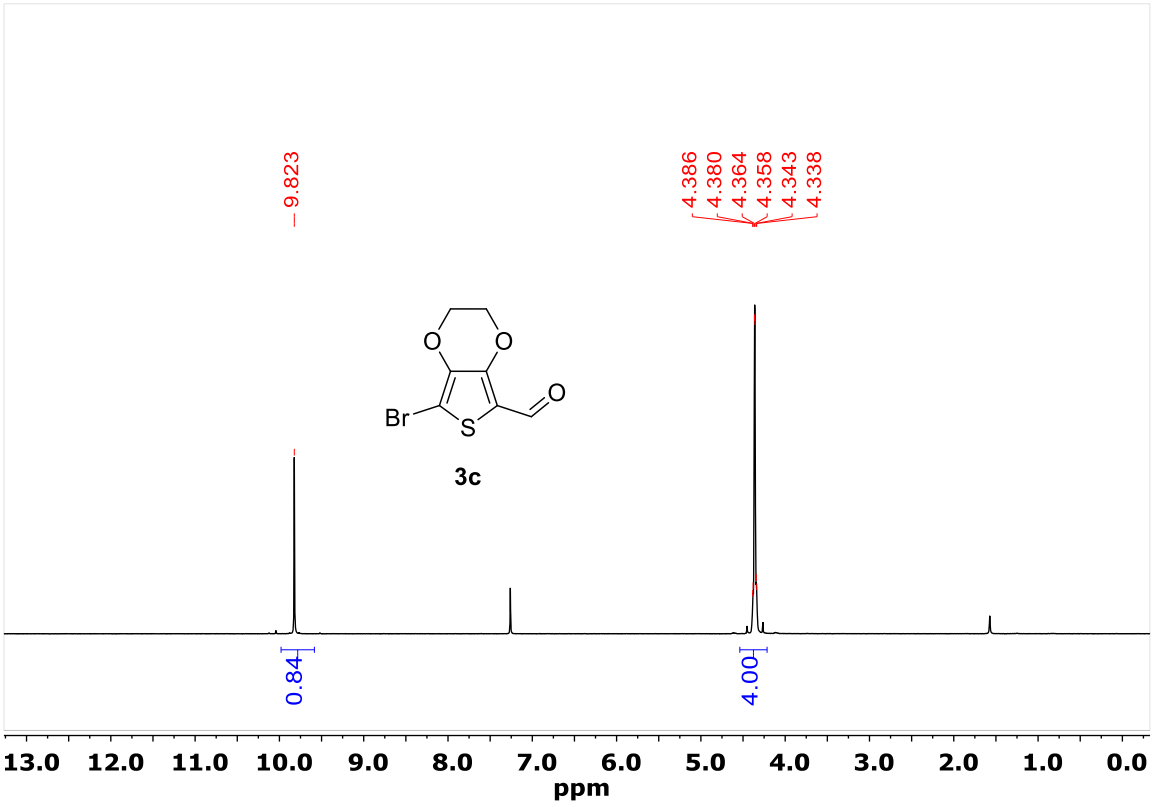

Figure B-21. ^{1}HNMR spectrum of compound **3c**.

Synthesis of (Z)-6-bromo-3-((7-bromo-2,3-dihydrothieno[3,4-b][1,4]dioxin-5-yl)methylene)indolin-2-one (4c)

To a 100mL two-necked round bottom flask, 6-bromooxindole (430 mg, 2.03 mmol) and 7-bromo-2,3-dihydrothieno[3,4-b][1,4]dioxine-5-carbaldehyde (**3c**) (505 mg , 2.03 mmol) were added. One neck of the flask was fitted with a condenser and the other neck was stoppered with a rubber septum. The mixture was purged with nitrogen for 15 min. EtOH (5.54 mL) was added to the mixture and heated at refluxing temperature. Piperidine (0.461 mL) was added slowly with a syringe through the rubber septum. The mixture was then refluxed for 18 h under nitrogen atmosphere. The mixture was cooled to room temperature, and methanol was added to the solution. The precipitate was filtered and washed with MeOH and hexane to obtain an brown powder of (*Z*)-6-bromo-3-((7-bromo-2,3-dihydrothieno[3,4-b][1,4]dioxin-5-yl)methylene)indolin-2-one (**4c**). (747 mg, 83%) ^{1}H NMR (300 MHz, DMSO-d_6) δ 10.75 (s, 1H), 7.76 (s, 1H), 7.58 (d, *J* = 8.1 Hz, 1H), 7.12 (dd, *J* = 8.1, 1.8 Hz, 1H), 6.97 (d, *J* = 1.7 Hz, 1H), 4.41 (ddd, *J* = 23.2, 6.5, 3.1 Hz, 4H). (Figure B-22)

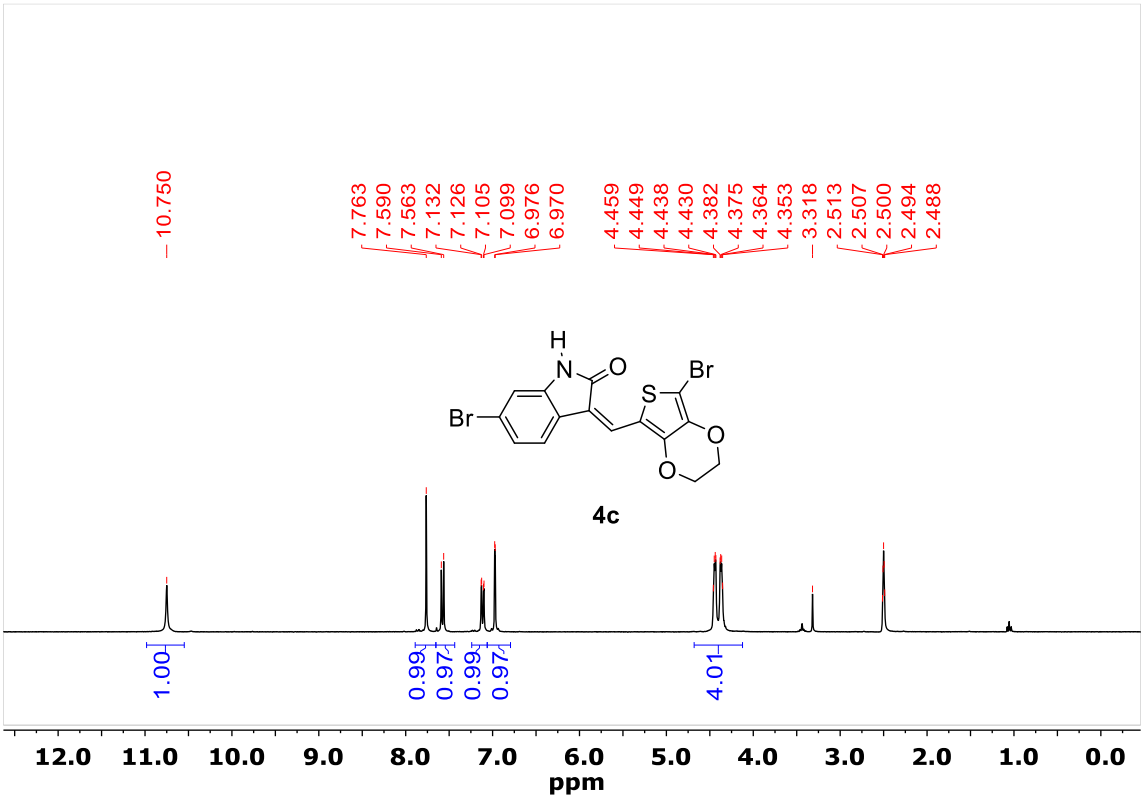

Figure B-22. ^{1}HNMR spectrum of compound **4c**.

Synthesis of 2-ethylhexyl (Z)-6-bromo-3-((7-bromo-2,3-dihydrothieno[3,4-b][1,4]dioxin-5-yl)methylene)-2-oxoindoline-1-carboxylate (M3)

To a 50 mL two-necked round bottom flask (*Z*)-6-bromo-3-((7-bromo-2,3-dihydrothieno[3,4-b][1,4]dioxin-5-yl)methylene)indolin-2-one (**4c**) (747 mg, 1.69 mmol) and sodium hydride (101 mg, 4.21 mmol) were added. One neck of the flask was connected argon atmosphere and the other neck was fitted with a rubber septum. The mixture was then vacuumed and purged with argon three times. Anhydrous THF (~12 mL) was added to the mixture and the mixture was stirred at room temperature for 15 min or until the reaction mixture turned from a yellow suspension into a clear dark orange solution. 2-Ethylhexyl chloroformate (0.364 mL, 1.85 mmol) was added slowly into the reaction mixture using a syringe through the rubber septum. The reaction mixture was stirred for 1 h under argon atmosphere. Saturated $NaHCO_3$ solution was added slowly into the mixture to quench the reaction. The mixture was then extracted with diethyl ether and washed successively with water. The organic layer was collected and dried with anhydrous Na_2SO_4 salt. The solution was filtered and the solvent was removed. The crude product was purified by recrystallization in MeOH/$CHCl_3$ solution to obtain brown solids of 2-ethylhexyl (*Z*)-6-bromo-3-((7-bromo-2,3-dihydrothieno[3,4-b][1,4]dioxin-5-yl)methylene)-2-oxoindoline-1-carboxylate (**M3**). (820 mg, 81%) ^{1}H NMR (300 MHz, Chloroform-*d*) δ 8.06 (d, *J* = 1.7 Hz, 1H), 7.75 (s, 1H), 7.37 (d, *J* = 8.2 Hz, 1H), 7.31 – 7.22 (m, 1H), 4.36 (p, *J* = 4.2 Hz, 6H), 1.81 (q, *J* = 6.2 Hz, 1H), 1.65 – 1.20 (m, 8H), 0.95 (dt, *J* = 12.6, 7.0 Hz, 6H). ^{13}C NMR (75 MHz, Chloroform-*d*) δ 164.63, 150.95, 145.55, 139.50, 137.98, 127.00, 123.82, 123.49, 121.56, 119.13, 118.42, 115.92, 114.52, 101.06, 69.83, 65.32, 64.73, 38.83, 30.33, 28.91, 23.71, 22.99, 14.09, 11.00. MALDI-TOF-MS calculated [M+Na^+]: 621.97; Found: 621.98 (Figure B-23, B-24 & B-25)

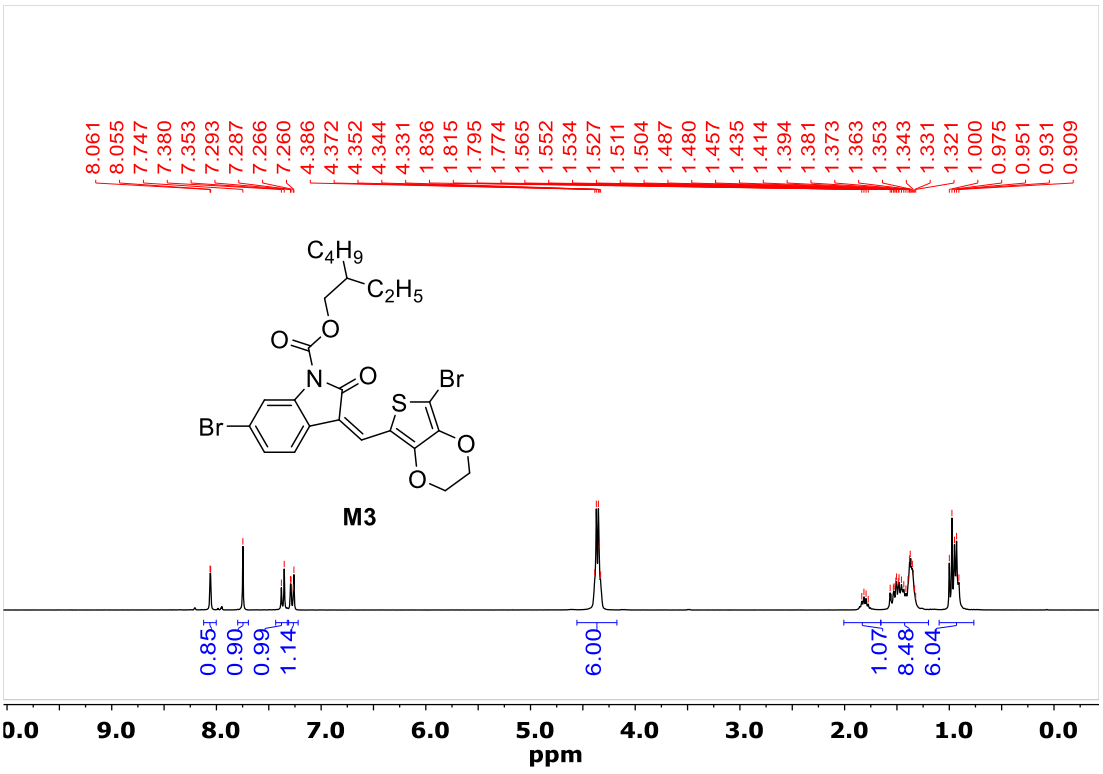

Figure B-23. [1]HNMR spectrum of compound **M3**.

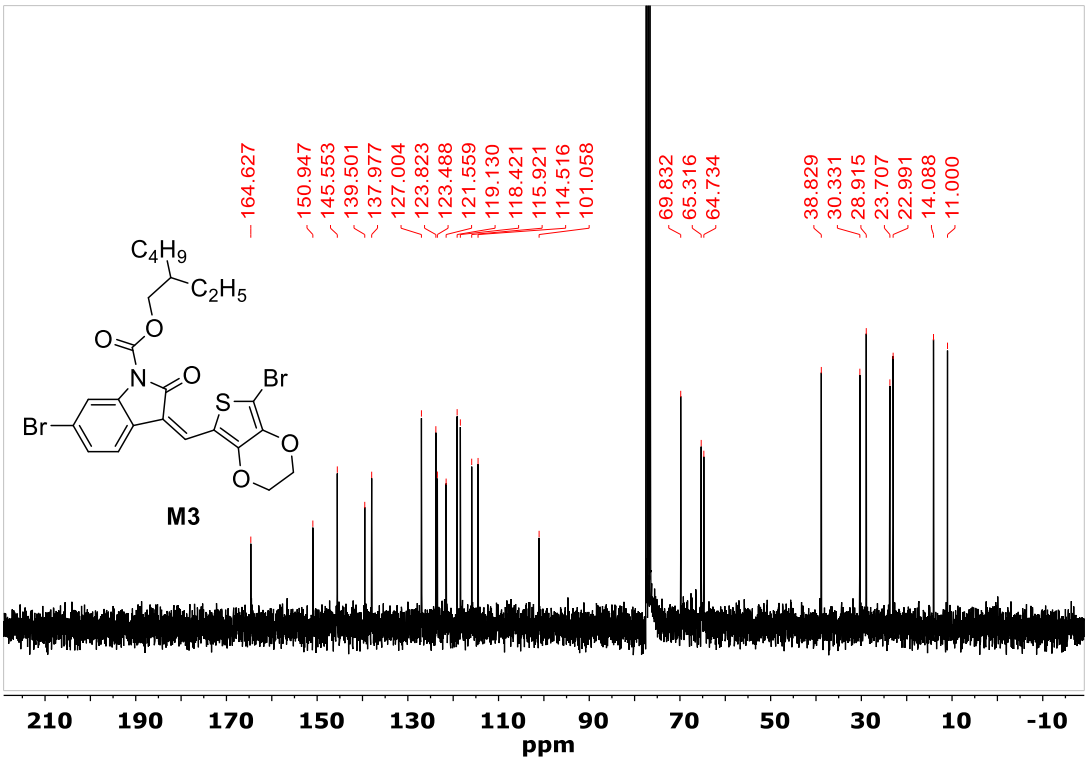

Figure B-24. [13]CNMR spectrum of compound **M3**.

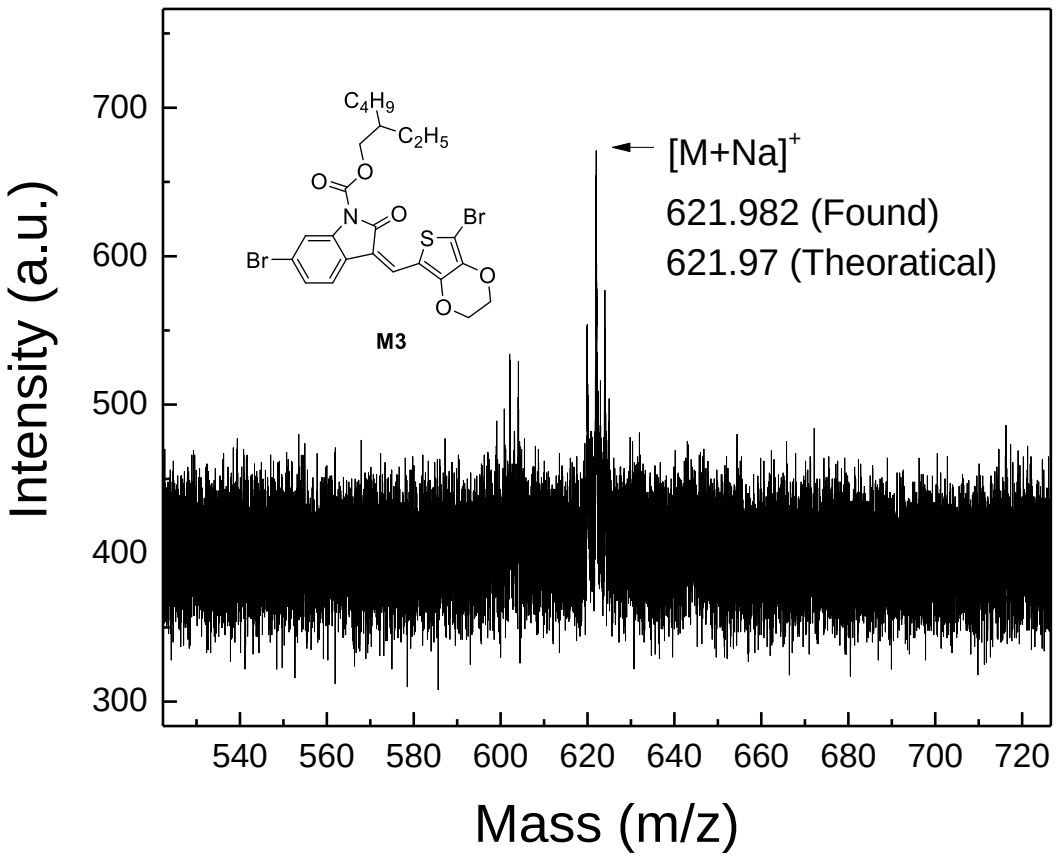

Figure B-25. MALDI spectrum of compound **M3**.

Synthesis of Poly[2-ethylhexyl 3-((7-(3,3'-bis(dodecyloxy)-[2,2'-bithiophen]-5-yl)-2,3-dihydrothieno[3,4-b][1,4]dioxin-5-yl)methylene)-2-oxoindoline-1-carboxylate] (PEEB)

To a 25mL two-necked round-bottom flask, 2-ethylhexyl (*Z*)-6-bromo-3-((7-bromo-2,3-dihydrothieno[3,4-b][1,4]dioxin-5-yl)methylene)-2-oxoindoline-1-carboxylate (**5c**) (69.6 mg, 0.116 mmol), P(*o*-tol)$_3$ (2.83 mg , 0.00930 mmol) and (3,3'-bis(dodecyloxy)-[2,2'-bithiophene]-5,5'-diyl)bis(trimethylstannane) (**M5**) (100.0 mg, 0.116 mmol) were added. The system was evacuated and filled with argon for three times. Anhydrous chlorobenzene was added to dissolve all the solids before a solution of $Pd_2(dba)_3$ (2.13 mg, 0.00232 mmol) in chlorobenzene (~1.2 mL) was added. The mixture was then stirred at 80 ^oC for 24 h under argon. Upon cooling to room temperature, the viscous mixture was poured into methanol under stirring. The precipitate was collected and was purified by Soxhlet extraction using methanol, acetone and chloroform. The chloroform fraction was evacuated to remove the solvent to afford poly[2-ethylhexyl 3-((7-(3,3'-bis(dodecyloxy)-[2,2'-bithiophen]-5-yl)-2,3-dihydrothieno[3,4-b][1,4]dioxin-5-yl)methylene)-2-oxoindoline-1-carboxylate] (**PEEB**) as a dark blue film. (85.6 mg, 76%)

Synthesis of 3,4-propylenedioxythiophene (1d or ProDOT)

To a 250mL round-bottom flask, 3,4-dimethoxythiophene (**1b**) (3.00 g, 20.8 mmol) and propan-1,3-diol (6.33 g, 83.2 mmol) and *p*-toluenesulfonic acid (0.396 g, 2.08 mmol) were added. Dry toluene (~ 50mL) was added and the solution was purged in nitrogen for 10 min. The solution was heated under reflux for 24 h. The reaction mixture was cooled to room temperature and water was added to quench the reaction. The solution was extracted by hexane and the solvent was reduced to minimum by distillation. The solution was then purified by flash column chromatography using pure hexane as eluent to afford 3,4-propylenedioxythiophene (**1d** or **ProDOT**) as a pale yellow oil. (1.98 g, 61%). ^{1}H NMR (300 MHz, Chloroform-*d*) δ 6.52 (s, 2H), 4.23 – 3.96 (m, 4H), 2.20 (p, *J* = 5.2 Hz, 2H). (Figure B-26)

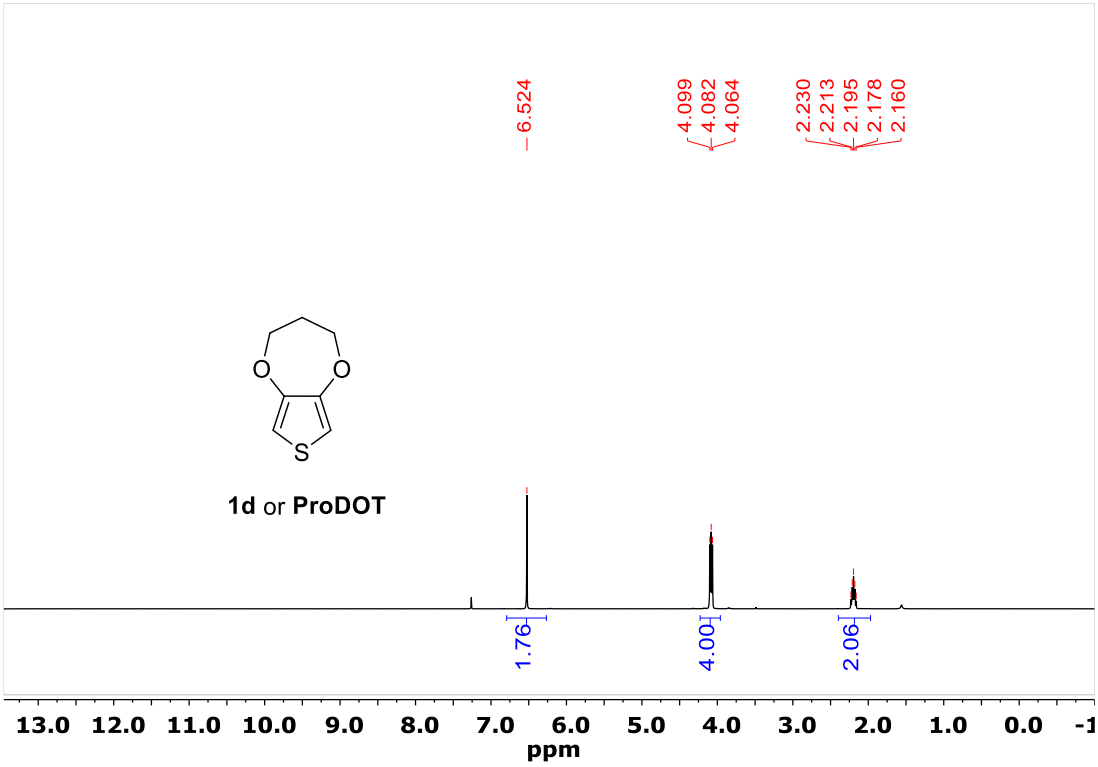

Figure B-26. ^{1}HNMR spectrum of compound **1d** or **ProDOT**.

Synthesis of 6,8-dibromo-3,4-dihydro-2H-thieno[3,4-b][1,4]dioxepine (2d)

To a 50mL round bottom flask, 3,4-propylenedioxythiophene (**1d** or **ProDOT**) (250 mg, 1.60 mmol) was dissolved in 3.0 mL THF. The mixture was purged under nitrogen for 15 minutes. N-bromosuccinimide (NBS) (627 mg, 3.52 mmol) was added slowly into the mixture and stirred for 15 min at 0^{o}C. The mixture was then quenched by adding cold saturated sodium sulfite solution.

The reaction mixture was extracted with hexane and washed with water. The organic portion was collected and solvent was removed. The product was purified by recrystallization using cold hexane to obtain a white powder of 6,8-dibromo-3,4-dihydro-2H-thieno[3,4-b][1,4]dioxepine (**2d**). (458 mg, 91%) ^{1}H NMR (300 MHz, Chloroform-*d*) δ 4.33 – 4.03 (m, 4H), 2.26 (tt, *J* = 6.2, 4.8 Hz, 2H). (Figure B-27)

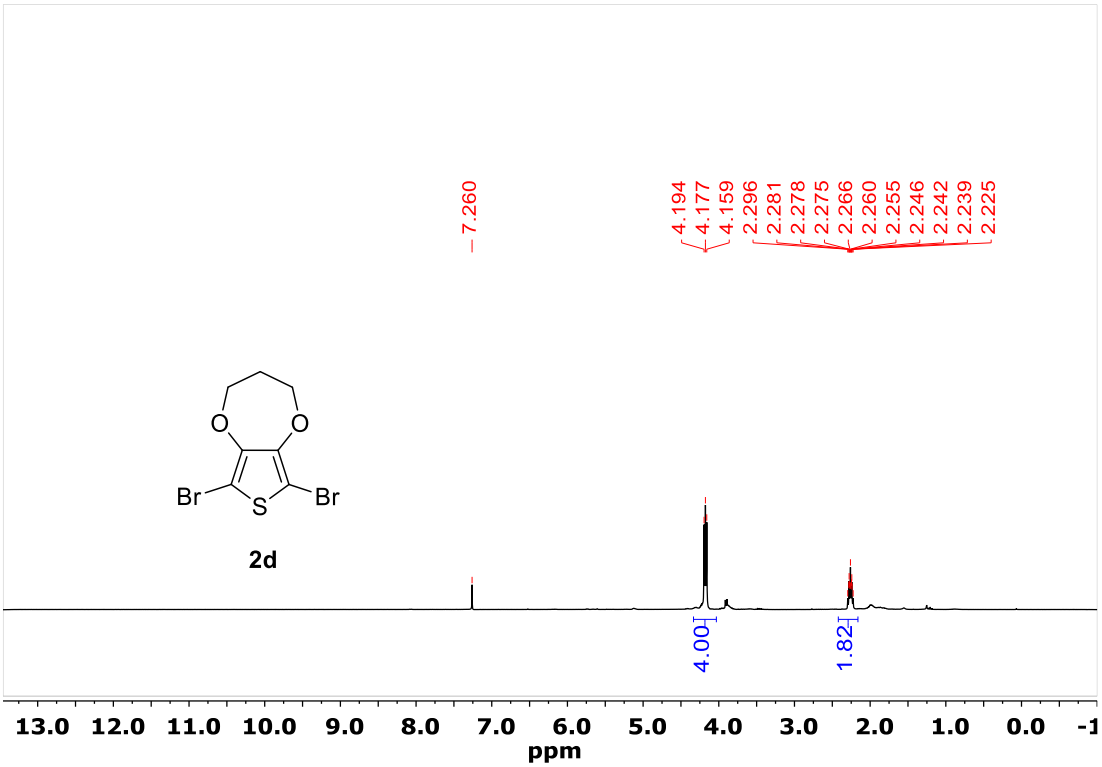

Figure B-27. ^{1}HNMR spectrum of compound **2d**.

Synthesis of 8-bromo-3,4-dihydro-2H-thieno[3,4-b][1,4]dioxepine-6-carbaldehyde (3d)

To a 100mL two-necked round bottom flask, 6,8-dibromo-3,4-dihydro-2H-thieno[3,4-b][1,4]dioxepine (**2d**) (443 mg, 1.41 mmol) was added. One of the neck of the round bottle flask was stoppered by a rubber septum, while the other neck was fitted with a condenser. The whole system was connected to nitrogen atmosphere. Anhydrous THF (~4.00 mL) was added into the flask with a syringe through the rubber septum. The solution was then cooled to -10°C with ice/NaCl cooling bath purged under nitrogen for 15 min. Upon stirring, 2.5 M *n*-butyllithium (0.621 mL, 1.55 mmol) was slowly added into the cooled solution with a syringe through the rubber septum. The mixture was then stirred vigorously at -10°C for 30 min or until a yellow solution was obtained. Dimethylformamide (DMF) (0.437 mL, 5.64 mmol) was then slowly added to the slurry with a syringe through the rubber septum. The mixture was then stirred at 0°C for 10 min, raised to room temperature and stirred for an additional 30 min. The reaction was quenched by pouring the mixture into ice with dilute HCl solution (0.5N). The crude product was then isolated by filtration and recrystallized in cold hexane to give 8-bromo-3,4-dihydro-2H-thieno[3,4-b][1,4]dioxepine-6-carbaldehyde (**3d**) (216 mg, 58%) ^{1}H NMR (300 MHz, Chloroform-*d*) δ 9.85 (s, 1H), 4.43 – 4.31 (m, 2H), 4.25 (t, *J* = 5.5 Hz, 2H), 2.45 – 2.25 (m, 2H). (Figure B-28)

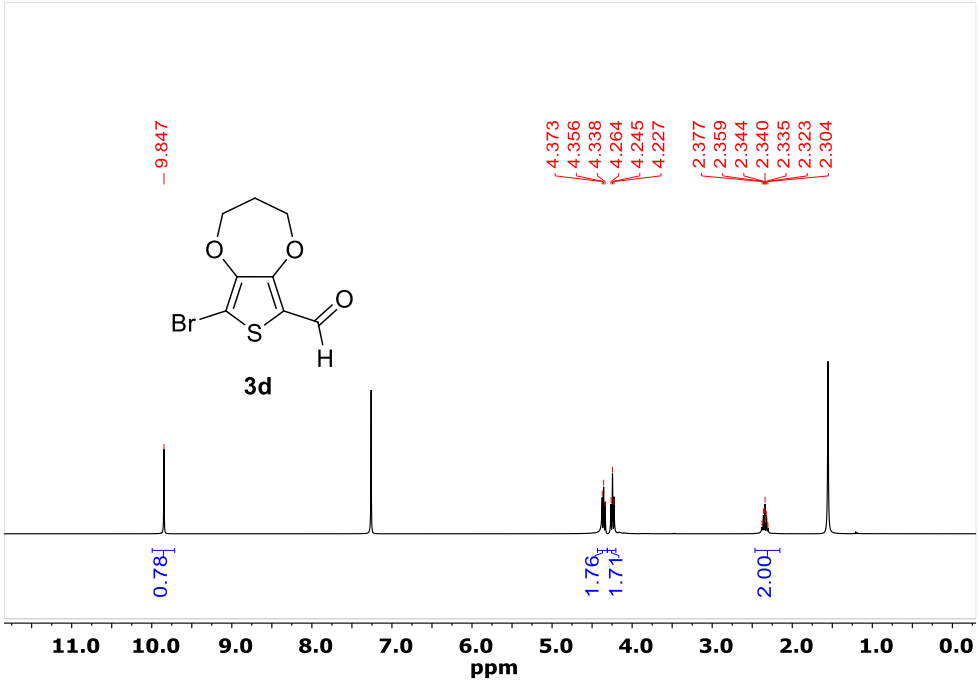

Figure B-28. ^{1}HNMR spectrum of compound **3d**.

Synthesis of (Z)-6-bromo-3-((8-bromo-3,4-dihydro-2H-thieno[3,4-b][1,4]dioxepin-6-yl)methylene)indolin-2-one (4d)

To a 100mL two-necked round bottom flask, 6-bromooxindole (173 mg , 0.817 mmol) and 8-bromo-3,4-dihydro-2H-thieno[3,4-b][1,4]dioxepine-6-carbaldehyde (**3d**) (215 mg , 0.817 mmol) were added. One neck of the flask was fitted with a condenser and the other neck was stoppered with a rubber septum. The mixture was purged wit h nitrogen for 15 min. EtOH (2.77 mL) was added to the mixture and heated at refluxing temperature. Piperidine (0.231 mL) was added slowly with a syringe through the rubber septum. The mixture was then refluxed for 18 h under nitrogen atmosphere. The mixture was cooled to room temperature, and methanol was added to the solution. The precipitate was filtered and washed with MeOH and hexane to obtain an orange powder of (*Z*)-6-bromo-3-((8-bromo-3,4-dihydro-2H-thieno[3,4-b][1,4]dioxepin-6-yl)methylene)indolin-2-one (**4d**). (173 mg, 46%) ^{1}H NMR (300 MHz, DMSO-d_6) δ 10.78 (s, 1H), 7.87 (s, 1H), 7.62 (d, *J* = 8.1 Hz, 1H), 7.15 (dd, *J* = 8.3, 1.8 Hz, 1H), 6.99 (d, *J* = 1.8 Hz, 1H), 4.31 (t, *J* = 5.2 Hz, 2H), 4.19 (t, *J* = 5.2 Hz, 2H), 2.37 – 2.14 (m, 2H). (Figure B-29)

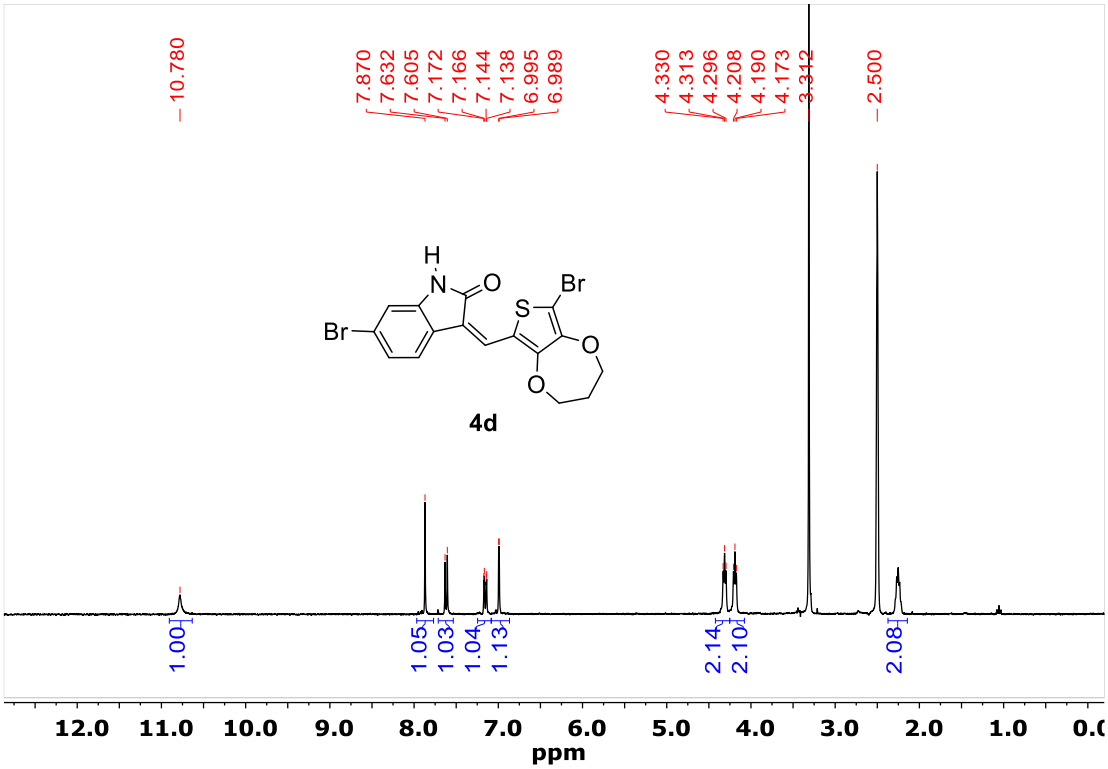

Figure B-29. ^{1}HNMR spectrum of compound **4d**.

Synthesis of 2-ethylhexyl (Z)-6-bromo-3-((8-bromo-3,4-dihydro-2H-thieno[3,4-b][1,4]dioxepin-6-yl)methylene)-2-oxoindoline-1-carboxylate (M4)

To a 50 mL two-necked round bottom flask (*Z*)-6-bromo-3-((8-bromo-3,4-dihydro-2H-thieno[3,4-b][1,4]dioxepin-6-yl)methylene)indolin-2-one (**4d**) (165 mg, 0.361 mmol) and sodium hydride (36.1 mg, 0.902 mmol) were added. One neck of the flask was connected argon atmosphere and the other neck was fitted with a rubber septum. The mixture was then vacuumed and purged with argon three times. Anhydrous THF (~7 mL) was added to the mixture and the mixture was stirred at room temperature for 15 min or until the reaction mixture turned from a yellow suspension into a clear dark orange solution. 2-Ethylhexyl chloroformate (0.0780 mL, 0.397 mmol) was added slowly into the reaction mixture using a syringe through the rubber septum. The reaction mixture was stirred for 1 h under argon atmosphere. Saturated $NaHCO_3$ solution was added slowly into the mixture to quench the reaction. The mixture was then extracted with diethyl ether and washed successively with water. The organic layer was collected and dried with anhydrous Na_2SO_4 salt. The solution was filtered and the solvent was removed. The crude product was purified by flash column chromatography using hexane:EA = 1:1 as eluent and the final product was recrystallized in MeOH/$CHCl_3$ solution to obtain orange brown solids of 2-ethylhexyl (*Z*)-6-bromo-3-((8-bromo-3,4-dihydro-2H-thieno[3,4-b][1,4]dioxepin-6-yl)methylene)-2-oxoindoline-1-carboxylate (**M4**) (190 mg, 86%) ^{1}H NMR (300 MHz, Chloroform-*d*) δ 8.07 (d, *J* = 1.7 Hz, 1H), 7.84 (s, 1H), 7.41 (d, *J* = 8.1 Hz, 1H), 7.29 (dd, *J* = 8.2, 1.8 Hz, 1H), 4.35 (dd, *J* = 7.8, 5.5 Hz, 4H), 4.25 (t, *J* = 5.4 Hz, 2H), 2.51 – 2.17 (m, 2H), 1.96 – 1.68 (m, 1H), 1.60 – 1.31 (m, 8H), 0.95 (dt, *J* = 13.1, 7.4 Hz, 6H). ^{13}C NMR (75 MHz, Chloroform-*d*) δ 164.64, 153.01, 150.95, 147.05, 138.11, 127.02, 124.95, 123.51, 121.72, 119.30, 118.44, 118.44, 116.64, 107.43, 71.75, 70.99, 69.85, 38.83, 32.83, 30.33, 28.91, 23.71, 22.99, 14.08, 11.00. MALDI-TOF-MS calculated [M^+]: 613.00; Found: 612.95 (Figure B-30, B-31 & B-32)

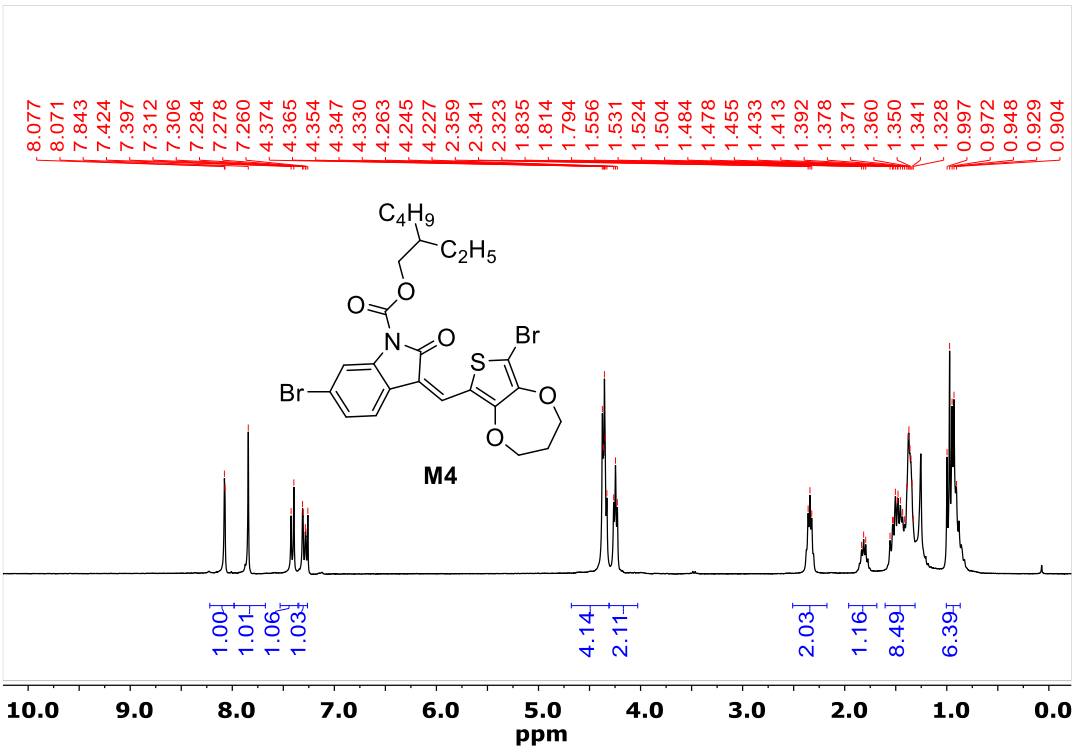

Figure B-30. [1]HNMR spectrum of compound **M4**.

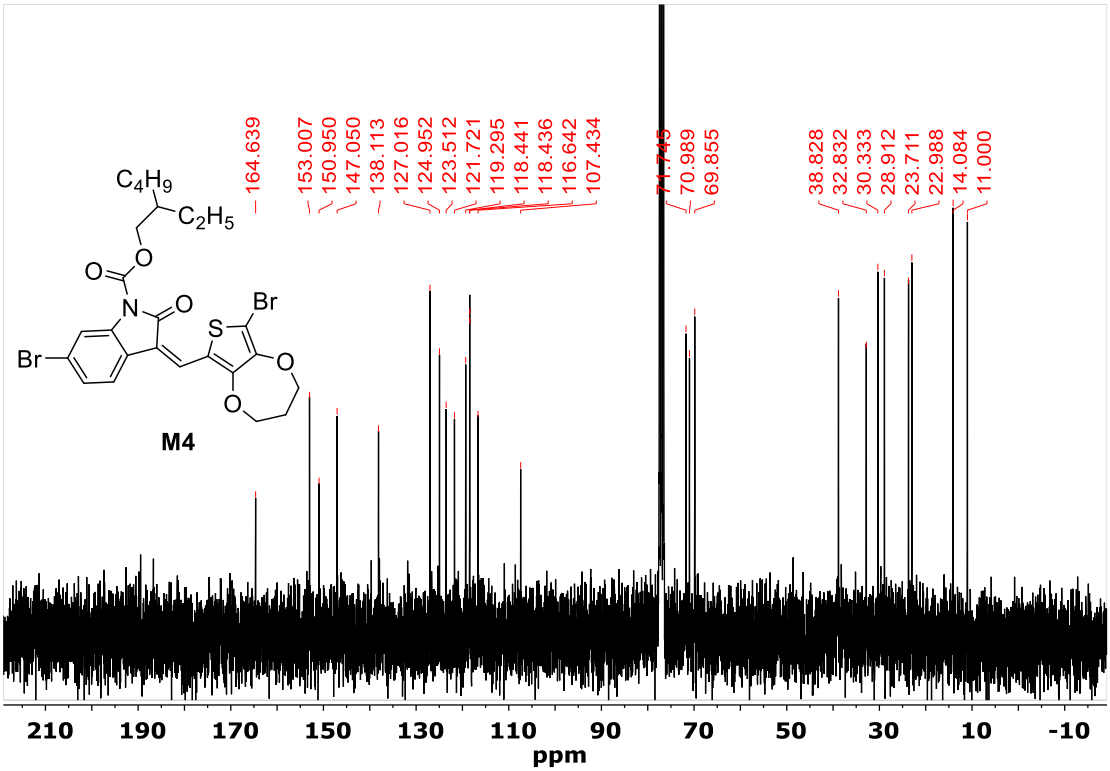

Figure B-31. [13]CNMR spectrum of compound **M4**.

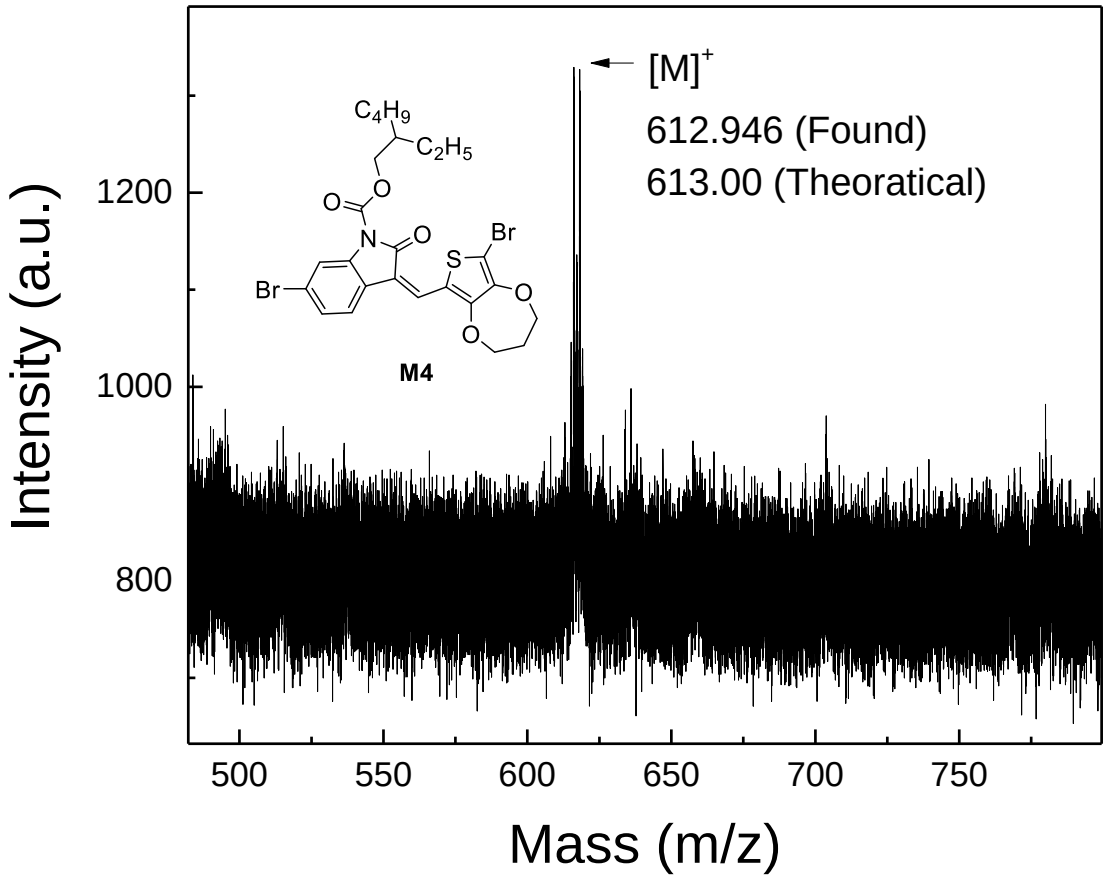

Figure B-32. MALDI spectrum of compound **M4**.

Synthesis of Poly[2-ethylhexyl 3-((8-(3,3'-bis(dodecyloxy)-[2,2'-bithiophen]-5-yl)-3,4-dihydro-2H-thieno[3,4-b][1,4]dioxepin-6-yl)methylene)-2-oxoindoline-1-carboxylate] (PPEB)

To a 25mL two-necked round-bottom flask, 2-ethylhexyl (*Z*)-6-bromo-3-((8-bromo-3,4-dihydro-2H-thieno[3,4-b][1,4]dioxepin-6-yl)methylene)-2-oxoindoline-1-carboxylate (**5d**) (42.8 mg, 0.0697 mmol), P(*o*-tol)$_3$ (1.70 mg , 0.00558 mmol) and (3,3'-bis(dodecyloxy)-[2,2'-bithiophene]-5,5'-diyl)bis(trimethylstannane) (**M5**) (60.0 mg, 0.0697 mmol) were added. The system was evacuated and filled with argon for three times. Anhydrous chlorobenzene was added to dissolve all the solids before a solution of $Pd_2(dba)_3$ (1.28 mg, 0.00140 mmol) in chlorobenzene (~1 mL) was added. The mixture was then stirred at 80 ^oC for 24 h under argon. Upon cooling to room temperature, the viscous mixture was poured into methanol under stirring. The precipitate was collected and was purified by Soxhlet extraction using methanol, acetone and chloroform. The chloroform fraction was evacuated to remove the solvent to afford poly[2-ethylhexyl 3-((8-(3,3'-bis(dodecyloxy)-[2,2'-bithiophen]-5-yl)-3,4-dihydro-2H-thieno[3,4-b][1,4]dioxepin-6-yl)methylene)-2-oxoindoline-1-carboxylate] (**PPEB**) as a dark blue film. (85.6 mg, 76%)

Appendix C: Theoretical Calculations

Theoretical calculations of model compounds were performed based on density functional theory (DFT) using quantum mechanical iteration methods included in software Avogadro 1.2.0., Gaussian 09, and Gaussian 16. A low level energy minimization of the model compounds was first performed by the Merck molecular force field (MMFF94s) method in Avogadro 1.2.0. Higher level geometry optimization and energy minimization of the model compounds were then performed using Gaussian 09 or Gaussian 16 using the B3LYP level of theory and the basis set 6-31G(d) under tight convergence to investigate the optimized geometry, molecular orbital (MO) energy levels, and electrostatic potential maps. Time-dependent density functional theory (TD-DFT) was performed by Gaussian 16 on geometry optimized model compounds to simulate the UV-Vis absorption spectra of model compounds.